OBSERVATION AND THEORY OF ELECTRON TEMPERATURE GRADIENT TURBULENCE IN LABORATORY PLASMA

By

SUSHIL KUMAR SINGH

PHYS06200704019

Institute for Plasma Research, Gandhinagar

A thesis submitted to the

Board of Studies in Physical Sciences

In partial fulfillment of requirements

For the Degree of

DOCTOR OF PHILOSOPHY

Of

HOMI BHABHA NATIONAL INSTITUTE

September, 2013

Homi Bhabha National Institute

Recommendations of the Viva Voice Board

As members of the Viva Voice Board, we certify that we have read the dissertation prepared by **Sushil Kumar Singh** entitled "**Observation and Theory of Electron Temperature Gradient Turbulence in Laboratory Plasma**" and recommend that it may be accepted as fulfilling the dissertation requirement for the Degree of Doctor of Philosophy.

PKaw ______________________________ Date: 10/1/14

Chairman: Prof. P. K. Kaw

RSingh ______________________________ Date: 10/1/14

Guide: Prof. R. Singh

______________________________ Date: 10.1.2014

Member: Prof. R. Jha

SMukherjee ______________________________ Date: 10/01/2014

Member: Dr. S. Mukherjee

______________________________ Date: 10/1/14

Member: Dr. L. M. Awasthi

Final approval and acceptance of this dissertation is contingent upon the candidate's submission of the final copies of the dissertation to HBNI.

I hereby certify that I have read this dissertation prepared under my direction and recommend that it may be accepted as fulfilling the dissertation requirement.

RSingh ______________________________ Date: 10/1/14

Guide: Prof. R. Singh

STATEMENT BY AUTHOR

This dissertation has been submitted in partial fulfillment of requirements for an advanced degree at Homi Bhabha National Institute (HBNI) and is deposited in the Library to be made available to borrowers under rules of the HBNI.

Brief quotations from this dissertation are allowable without special permission, provided that accurate acknowledgement of source is made. Requests for permission for extended quotation from or reproduction of this manuscript in whole or in part may be granted by the Competent Authority of HBNI when in his or her judgment the proposed use of the material is in the interests of scholarship. In all other instances, however, permission must be obtained from the author.

Sushil Kumar Singh

Sushil Kumar Singh

DECLARATION

I, hereby declare that the investigation presented in the thesis has been carried out by me. The work is original and has not been submitted earlier as a whole or in part for a degree/diploma at this or any other Institution/University.

Sushil Kumar Singh

Sushil Kumar Singh

Dedicated to

My Late Mother

ACKNOWLEDGEMENTS

First and foremost, I would like to express my deep sense of respect and gratitude to my thesis supervisor Prof. Raghvendra Singh. His deep knowledge and vision has fascinated me in both theory and experiment. During the early stage of the thesis, he taught me theoretical techniques. He has given me the complete freedom for doing my work and has rebuilt my self-beliefs. He has inspired me to think theoretical physics problem keeping in mind their realization in experiments. I humbly appreciate his motivating ideas and enjoyed fruitful discussions with him. I regard him as a great human being because of his simplicity, humbleness, down to earth attitude and a very kind and caring heart.

I am extremely thankful to my Doctoral Committee chairman Prof. P. K. Kaw, who has been a constant source of inspiration during my thesis work. His innovative ideas and academic discussion helped me a lot to complete my work. I truly inspired with his fundamental approach to tackle the research problem.

I am also thankful to Prof. S. K. Mattoo for his encouragement, guidance and motivation. I learnt a lot from him, especially experimental plasma physics and techniques. He has helped me from the beginning of my PhD and taught me about the perfection of the work. I am also thankful to Prof. Abhijit Sen for his academic help and support. I am also thankful to Prof. Dhiraj Bora for his encouragement and support.

I also owe a debt of my sincere gratitude to my Doctoral Committee member and LVPD division head Dr. L. M. Awasthi for his encouragement and support at each step of my work. He is always ready to help me whenever I need and provides me his constant moral support and independency. I spent sessions of very fruitful scientific discussion with him. He is like a mentor for me. I am also thankful to my other Doctoral Committee members Prof. R.

Jha and Dr. S. Mukherjee for their encouragement and critical discussions during the annual reviews. Prof. Jha has taught me many fruitful techniques about data analysis.

I specially thank to Mr P. K. Srivastava for his kind help in electronics, power supply and many other technical support for my experiment. My thanks are also due to Mr. A. K. Sanyasi, Dr. R. Kaur and Mr. R. Sugandhi for their supportive nature. The discussion session with these people has also proven fruitful for me. I would also like to thank Umesh, Arvind, Kalpesh, Avadhesh, Malhaar, Kunal, Amit, Dhaval, Santosh, Ruchita and Dakshesh for their kind help for carrying out my thesis work. I am also thankful to several other colleagues of LVPD and BETA laboratory who interacted and helped me either directly or indirectly.

I would also like to thank the academic committee and faculty members who taught me plasma physics and additional subjects during the course work. My thanks are due to Prof. Amita Das, Prof. R. Jha, Dr. R. Ganesh, Dr. S. Sengupta, Dr. Joydeep Ghosh, Dr, Prabal Chattopadhyay, Dr. N. Besai, Dr. P. K. Sharma, Dr. R. Srinivasan, Dr. D. Raju, Dr. Manoj Warior, Dr. S. K. Pathak, Dr. A. K. Chattopadhyay, Dr. Devendra Sharma, Dr. S. Pradhan, Dr. G. Ravi, Dr. Anita, Dr. Rajesh and Dr. Ramsubramanian for their valuable help in my thesis work.

I express my heartily thanks to my classmate friends Sanat, Rameswar, Pravesh, Nishant, Imran and Partha for providing me unforgettable cool ambience during first year course work. I cannot forget the significant help from Rameswar, Sanat and Pravesh at each moment during my PhD work. I would also like to thank my senior scholars, Pintu da, Manas, Rajneesh, Bhaskar, Vikrant, Subhash, Kishor, Maya, Sharad, Satya, Shekar, Jugal, Sunita, Vikram Naranag, Ashwin, Deepak, Gurudatt, Sita, Ujjwal, Prabal, Kshitish, Linthis, Bhavesh, Sanjay, Sunil and juniors Sayak, Manjit, Soumen, Aditya, Vikram Dharodi, Ved Prakash, Rana, Sandeep, Dushyant, Vara, Vibhu, Neeraj, Rupendra, Deepa, Chandrasekher, Akanksha, Mangilal, Meghraj, Vidhi, Harish, Samir and all first year scholars for providing me a friendly ambiance in the hostel as well as in scholar hall. My thanks are also due to all my TTP friends (list is too long!) for their respect and kind support.

I am also thankful to all employees from workshop, drafting section, computer centre, library, stores, purchase and administration for their co-operation and help during my entire duration of PhD. The name list is very long to write here for those for their useful contributions in the completion of my thesis work.

Finally, I would like to convey my heartily thanks and warm regards to my parents whose blessings, guidance and moral support helped me to achieve my goal of PhD. I have a great faith in my father for his patience and am thankful for allowing me to grow independently. I cannot forget the contribution of my sisters Neelu and Neetu, whose love and care carried me through from difficult situations in my life. I would also like to thank my best friends Srikrishna, Sachin, Kanhaiya, Laxmi Narayan and others for their significant help and encouragement throughout my personal and professional life.

Last but not least, I express my gratitude and great regard to Institute for Plasma Research, Thanks IPR!

Sushil Kumar Singh

Contents

Abstract

We present the experimental demonstration and theoretical model of Electron Temperature Gradient (ETG) turbulence in the finite beta laboratory plasma of Large Volume Plasma Device (LVPD). In magnetized plasma, the confinement problem starts with particle and thermal transport which becomes anomalous in nature due to small scale micro-instabilities. Recent numerical and experimental results reveal that ETG turbulence is more likely responsible for anomalous transport of plasma. The small scale nature of ETG mode inhibits its direct measurement in fusion devices whereas the basic plasma devices (linear and toroidal) provide conditions suitable to bring the scale length of the mode to measurable regime but faces problems because of the presence of ionizing hot and non-thermal electrons due to filamentary and other sources. The removal of unutilized primary ionizing and non-thermal electrons and control of radial gradient scale length in electron temperature are all achieved by placing a large Electron Energy Filter (EEF) in the middle of the LVPD. The EEF divides LVPD plasma region in source, filter and target plasma.

The electromagnetic ETG instability is investigated in the core plasma of the target region. We have established the turbulence by measuring the fluctuations (density, magnetic, temperature and potential), power-spectra, correlation, phase angle, propagation, wavenumber-frequency spectrum and beta scaling in suitable equilibrium plasma conditions for two EEF configurations, one for excitation and other of conformation of the ETG mode. The observed turbulence is characterized by broadband spectra in the lower hybrid range of frequencies following the power law. In the diagnostic, an electronically compensated Langmuir probe technique has been developed for accurate measurement of electron temperature and its fluctuations which are crucial parameters for turbulence study. Moreover, the experiment is performed for nonlinear coherent structures on a cross-field plane of core plasma in the background of ETG turbulence. The structures are determined from the conditional averaging technique of floating potential fluctuations taken by a poloidally separated array of Langmuir probes, moved to different radial locations with respect to reference probe. The experimental results will brief on size, lifetime, time evolution characteristic and nature of the observed structures.

The linear and nonlinear theory of coupled Whistler-Electron Temperature Gradient (W-ETG) mode is developed using two-fluid model applicable for LVPD plasma. The role of parallel and perpendicular magnetic field perturbations, non-adiabatic ion response and electron collisions are considered in the derived dispersion relations. The compared experimental and numerical results consisting of fluctuations level, frequency, correlation properties, phase velocity, mode characteristic and beta scaling of all fluctuation amplitudes are found in good agreement in accordance with electromagnetic ETG turbulence.

In addition to linear response, a theoretical model for secondary instabilities for long scale mode generation in the background of electromagnetic ETG turbulence is obtained using nonlinear fluid equations. The dispersion relation for zonal flows and streamers are obtained using the standard wave kinetic formalism. In the numerical results, zonal flows, zonal magnetic fields, electromagnetic streamers and pure magnetic streamers are shown to get excited by host turbulence. The interpretation of results obtained for nonlinear modes has also been discussed.

List of Figures

List of Tables

List of Publications

Peer Reviewed Journals:

1. **Theory of coupled Whistler-Electron Temperature Gradient mode in high beta plasma: Application to linear plasma device,**
   S. K. Singh, L. M. Awasthi, R. Singh, P. K. Kaw, R. Jha, and S. K. Mattoo
   Phys. Plasmas **18**, 102109 (2011).

2. **Experimental Observation of Electron Temperature Gradient Turbulence in a Laboratory Plasma,**
   S. K. Mattoo, **S. K. Singh,** L. M. Awasthi, R. Singh, and P. K. Kaw
   Phys. Rev. Lett. **108**, 255007 (2012).

3. **Investigations on ETG turbulence in finite beta plasma of LVPD ,**
   S. K. Singh, L. M. Awasthi, S. K. Mattoo, P. K. Srivastava, R. Singh, and P. K. Kaw
   Plasma Phys. Controlled Fusion **54**, 124015 (2012).

4. **Revisiting plasma hysteresis with an electronically compensated Langmuir probe,**
   P. K. Srivastava, **S. K. Singh,** L. M. Awasthi, and S. K. Mattoo
   Rev. Sci. Instrum. **83**, 093504 (2012).

5. **Performance of Large Electron Energy Filter in Large Volume Plasma Device,**
   S. K. Singh, P. K. Srivastava, L. M. Awasthi, S. K. Mattoo, R. Singh, and P. K. Kaw
   IPR/**RR-586**/2013, (under review, Review of Scientific Instrument, RSI: A131004R).

6. **Plasma Response to Electron Energy Filter in LVPD,**
   A. K. Sanyasi, L. M. Awasthi, S. K. Mattoo, P. K. Srivastava, **S. K. Singh,** R. Singh and P. K. Kaw
   Phys. Plasmas **20**, 122113 (2013).

7. **Investigations of Nonlinear Structures in Large Volume Plasma Device,**
S. K. Singh, L. M. Awasthi, S. K. Mattoo, R. Jha, P. K. Srivastava, R. Singh and P. K. Kaw
(Accepted for publication in AIP proceeding).

8. **Electromagnetic Secondary Instabilities of Coupled Whistler-ETG Turbulence,**
S. K. Singh, Rameswar Singh, L. M. Awasthi, R. Singh and P. K. Kaw
IPR/**RR-604**/2013, (To be submitted in Physics of Plasma).

9. **A 5 kA Pulsed Power Supply for large EEF solenoid in LVPD,**
P. K. Srivastava, **S. K. Singh,** L. M. Awasthi and S. K. Mattoo
(To be submitted).

International Conferences/Schools:

1. Electromagnetic Secondary Instability of Whistler-Electron Temperature Gradient Turbulence in Finite Beta Plasma,
S. K. Singh, Rameswar Singh, L. M. Awasthi, R. Singh and P. K. Kaw
Sokendai Asian Winter School and Toki Lectures on Simulation Science, 10-13 December 2013 at NIFS, Toki, Japan.

2. Observation of Electromagnetic Turbulence in the Energetic Electron Belt region of LVPD Plasma,
A. K. Sanyasi, L. M. Awasthi, S. K. Mattoo, P. K. Srivastava, **S. K. Singh,** R. Singh and P. K. Kaw
13th IAEA Technical Meeting on Energetic Particles in Magnetic Confinement Systems, 17-20 September 2013 at Beijing, China.

3. Experimental Observation of Coherent Structure in Finite Beta Plasma,
S. K. Singh, L. M. Awasthi, S. K. Mattoo, R. Jha, P. K. Srivastava, R. Singh and P. K. Kaw
The 6th ITER International School on RF Heating and Current Drive in ITER, 02-06 December 2012 at Ahmedabad, India.

4. Plasma Turbulence in the Complex Scenario of Near EEF Region,
A. K. Sanyasi, L. M. Awasthi, S. K. Mattoo, **S. K. Singh,** P. K. Srivastava, R. Singh and P. K. Kaw
International Conference on Complex Processes in Plasma and Nonlinear Dynamical System (ICCPPNDS), November 6-9, 2012 at Gandhinagar, India.

5. Investigations of Nonlinear Structures in Large Volume Plasma Device,
S. K. Singh, L. M. Awasthi, S. K. Mattoo, R. Jha, P. K. Srivastava, R. Singh and P. K. Kaw
International Conference on Complex Processes in Plasma and Nonlinear Dynamical System (ICCPPNDS-2012), 6-9 November 2012 at Gandhinagar, India.

6. Scaling of Electron Temperature Gradient with EEF For ETG Turbulence Study,
S. K. Singh, L. M. Awasthi, P. K. Srivastava, S. K. Mattoo, R. Singh and P. K. Kaw
39th European Physical Society Conference on Plasma Physics & 16th International Congress on Plasma Physics, 2-6 July 2012 at Stockholm, Sweden.

7. Revisiting Plasma Hysteresis with an Electronically Compensated Langmuir Probe,
P. K. Srivastava, **S. K. Singh,** L. M. Awasthi and S. K. Mattoo
8th General Scientific Assembly of the Asia Plasma and Fusion Association, 1-4 November 2011 at Guilin, China.

8. Experimental Observation of Electron Temperature Gradient Driven Turbulence in Laboratory Plasma,
S. K. Singh, S. K. Mattoo, L. M. Awasthi, R. Singh and P. K. Kaw
5th ITER International Summer School on MHD and Energetic Particles, 20-24 June 2011 at Aix en Provence, France.

9. LVPD Plasma for Studies on ETG Turbulence,
L. M. Awasthi, **S. K. Singh,** P. K. Srivastava, U. Dhobi, R. Singh, S. K. Mattoo and P. K. Kaw
52nd Annual Meeting of the APS Division of Plasma, Physics 8-12 November 2010 at USA.

10. Simon-Hoh Instability in High Beta Plasma,

S. K. Singh, L. M. Awasthi, S. K. Mattoo, P. K. Kaw and R. Singh

Sokendai Asian Winter School and Toki Lectures on Simulation Science 26-29 January 2010 at NIFS, Toki, Japan.

Chapter 1

Introduction

This thesis provides the experimental evidence of electron temperature gradient (ETG) driven turbulence in laboratory plasma of Large Volume Plasma Device (LVPD). The thesis includes major developmental and experimental efforts responsible for characterization of ETG turbulence. We have also developed theoretical models to explain these observations. In this chapter, we present motivation and a brief description, highlighting the contents of the thesis.

1.1 Overview and Motivation

An important issue encountered by the fusion community in magnetically confined plasma is the understanding of micro-turbulence, believed to play a crucial role in driving anomalously high level of transport, responsible for plasma loss. Even after more than five decades of active research, the causes of anomalous plasma transport in tokamaks are still an outstanding issue. The physics of particle and energy transport of ions and electrons has been studied separately in detail. It is well known that in Ohmically heated plasmas [1, 2] with Alcator scaling, the ion energy transport is neoclassical whereas electron energy transport remains anomalous. On the other hand, in auxiliary heated plasmas where most of the energy is deposited on ions, the ion thermal transport becomes anomalous. Ion temperature gradient (ITG) turbulence, trapped electron mode (TEM) and drift resistive ballooning mode (DRBM) are identified as the primary cause of heat and particle transport. However, these drift instabilities of ion Larmor radius ($\rho_s = c_s / \Omega_i$) scale (such as ITG, TEM, DRBM), the main drivers of all transport channels, are suppressed due to rapid formation of $\vec{E}\times\vec{B}$ shear /or Zonal flows [3] in the high confinement mode (H-mode) pedestal and internal transport barrier but electron energy transport remains anomalous. The interest is then again focused on the electron transport. Moreover, there is special interest in understanding of electron transport in a reactor scenario since the fusion alpha particles mainly heat the electrons. Thus the physics of anomalous electron transport [4, 5] across the confining magnetic field holds significant implication for fusion machines like ITER and advanced tokamak reactor. ETG turbulence is likely to play an important role in particle and electron thermal transport during the development phase of edge pedestal in H-mode plasmas due to the lack of ρ_s scale turbulence. Several theoretical and simulation studies support the analogy that anomalous electron transport may arise from an electron gyro scale ETG mode turbulence as sheared flow is inefficient in stabilizing these short scale modes [6-14].

The electron thermal transport driven by ETG turbulence was first studied by Lee et al. [15] and Guzdar et al. [7] using gyrokinetic theory in simple slab geometry. Further, investigation of instability was performed in toroidal geometry by Horton et al. [8] by employing fluid model. Later on Kim et al. studied the transition of instability from toroidal to slab geometry [16]. Moreover, ETG instability has also been studied in sheared slab geometry, reverse field configuration and with negative shear using gyrokinetic simulation. The experimental results of Tore Supra with hot electrons showed that electromagnetic ETG turbulence can provide satisfactory explanation of anomalous heat transport and confinement properties in the plasma [17, 18]. The observations and electron energy confinement analysis of the NSTX, TCV and MAST plasma support the conclusion that the ETG mode is able to explain a wide range of anomalous electron transport data [19, 20]. These experimental and simulation results suggest that the ETG turbulence is most likely a source for electron anomalous transport in plasma.

The ETG mode is a fast growing reactive and negative compressible mode driven by electron temperature gradient, which has wavelength and frequency of order $k_\perp\rho_e \le 1 << k_\perp\rho_i$, $\Omega_i < \omega << \Omega_e$ (where $k_\perp$ is the perpendicular wave vector, ρ_e and ρ_i are the Larmor radii of electron and ion respectively, Ω_i, Ω_e and ω are ion, electron gyro frequencies and the mode frequency respectively). In the electrostatic case, slab ETG mode is primarily driven by parallel compression of electron motion along the magnetic field. The compression effect in electron parallel motion will generate density ($\tilde{n}$) and temperature ($\tilde{T}_e$) perturbations. The density and potential ($\tilde{\phi}$) perturbations are out of phase due to the ion Boltzmann's shielding effect. This potential perturbation creates $\vec{E}\times\vec{B}$ drift, which brings cold electrons in a compressed region and thus lowering the pressure. The lowering the pressure ($\tilde{p}$) attracts more electrons along the line of force, further increasing the compression and thus shows negative compressibility ($\partial p/\partial n < 0$). This positive feedback loop leads to ETG instability [Fig. 1.1]. A similar feedback scheme also applies in case of toroidal ETG mode but the perpendicular compression of diamagnetic flux is non-zero due to inhomogeneous magnetic field. In both cases the compressibility is responsible for amplifying the temperature perturbation.

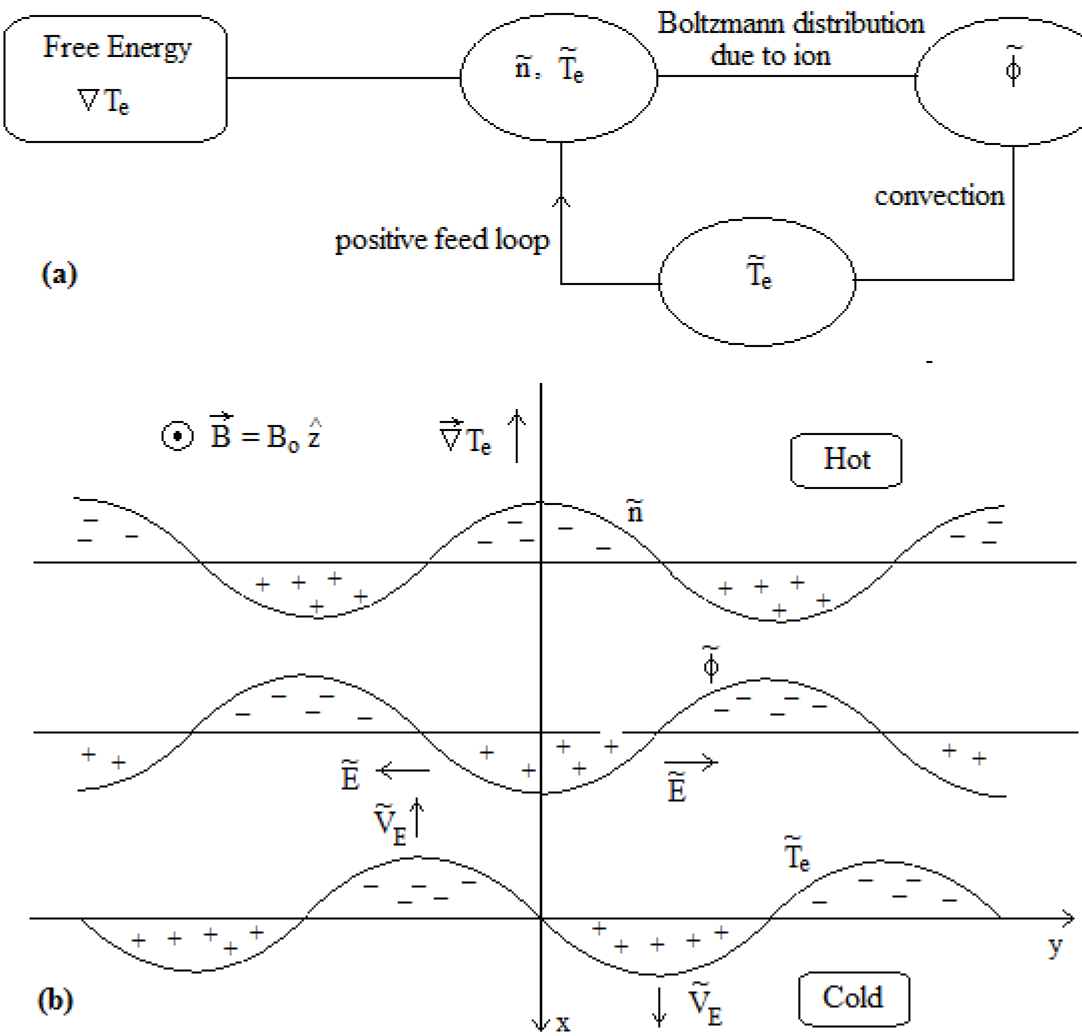

Figure 1.1: (a) Block diagram and (b) schematic of ETG instability mechanism.

The electrostatic ETG mode is excited when electron temperature gradient scale length exceeds the threshold value. The growth rate (γ) and frequency (ω) of the mode are typically $k_y\rho_e c_e / L_{T_e} \sim c_e / L_T$ (where c_e is the electron thermal velocity). The linear calculations of the ETG mode reveal a threshold in $\eta_e = L_n / L_{T_e}$, where L_n and L_{Te} are the density and electron temperature gradient scale lengths respectively. The threshold in η_e through negative compressible nature of the ETG mode can be understood more explicitly by using basic fluid equations. Considering linearized continuity, $\omega\tilde{n}_e - \omega_{*e}\tilde{\phi} - k_{\|}\tilde{u}_{\|e} = 0$, parallel momentum, $\omega\tilde{u}_{\|e} = -k_{\|}c_e^2(\tilde{\phi} + \tilde{p}_e)$, pressure equations, $\tilde{p}_e = \Gamma k_{\|}u_{\|e} / \omega + (1+\eta_e)(\omega_{*e} / \omega)\tilde{\phi}$ for electron dynamics along with adiabatic ion response, $\tilde{n}_i = -\tilde{\phi}$ within limit ($\omega < k_{\perp}c_i$, $T_e = T_i$), and by using quasi-neutrality condition ($\tilde{n}_e \simeq \tilde{n}_i = \tilde{n}$), we have obtained $\tilde{p}_e = [\Gamma + (\Gamma - 1 - \eta_e)\omega_{*e} / \omega]\tilde{n}$, where $k_{\|}$, ω_{*e} and $\tilde{u}_{\|e}$ are the parallel wave vector, electron diamagnetic frequency, perturbed parallel electron velocity respectively and $\Gamma = 5/3$ is the ratio of specific heat at constant pressure and constant volume. We can write compressibility,

$$\frac{\partial p_e}{\partial n} = \Gamma + (\Gamma - 1 - \eta_e)\frac{\omega_{*e}}{\omega},$$

Here we have taken $\partial p_e / \partial n = [< P_e > / < n >]\tilde{p}_e / \tilde{n} \approx \tilde{p}_e / \tilde{n}$. For a mode with frequency $\omega \simeq \omega_{*e}$ (electron direction), the necessary condition for the excitation of ETG mode (negative compressible mode, $\partial p / \partial n < 0$) is $\eta_e > \Gamma - 1 = 2/3$. The ETG mode will be unstable only if $\eta_e > \Gamma |\omega| / |\omega_{*e}| + \Gamma - 1$ or $\eta_e > \eta_{th} \sim 2$, which is the typical observed threshold value of ETG turbulence in tokomaks.

Recent experimental investigation of turbulence in linear devices like LVPD, CLM [21] and toroidal devices like NSTX [20], Tore Supra [18] have reported interesting observations on electron gyro scale fluctuations and their role on plasma transport [22] irrespective of having different plasma conditions. In LVPD, the difference is found in threshold condition which depends on plasma beta and Finite Larmor Radius (FLR) effect whereas in tokamak, it is decided primarily by the curvature effect. Also, the effect of magnetic shear is absent in linear devices in comparison to magnetically confined fusion devices. The large, finite axial length of LVPD plasma depicts similarity with tokamaks but differ as parallel loss in it dominates in contrast to tokamaks due to its toroidal symmetry. Apart from various dissimilarities, the major advantage to study ETG turbulence in LVPD lies in its simple geometry, reliable measurements and good realization of turbulence which becomes an extremely difficult task in tokamaks because of its small-scale nature, their complex geometries and restricted measurement capabilities. The major advantage with LVPD lies in flexibility to undertake detailed characterization of the turbulence for various plasma parameters such as temperature, density, magnetic field and floating potential fluctuations for different plasma beta through measurement of properties like correlations, threshold, phase angle, propagation direction, phase velocity beyond wave number and frequency spectra. The measurement of parallel wave number is also possible in LVPD which is very difficult task in tokamaks due to curvature in magnetic field lines. In addition, the leverage of exerting a modification in equilibrium profiles (density, electron temperature) in the core plasma has not only demonstrated ETG turbulence but also helped for its confirmation. Moreover, large scale structures like magnetic streamers can be easily observed in LVPD which is difficult to identify in tokamaks. Irrespective of various differences in LVPD and tokamaks, the fundamental physics of ETG turbulence remains the same because of similar scaling ($\rho_e / L_{T_e} << 1,\ \ \Omega_i < \omega < \Omega_e$). Also, a similarity in nature of turbulence is observed from the fact that mode approaches electrostatic nature with reducing plasma beta.

In the devices like LVPD and CLM, producing moderate density plasma at lower magnetic fields in order to bring the scale length of the ETG instability to conveniently measurable regime by making use of probes is not a difficult task but these devices are plagued by problems encountered in plasma production by the presence of ionising hot and non-thermal electrons due to radio frequency [20] and filamentary [23, 24] discharges. Each of these plasma production methods is a potential source of instability since they populate plasmas with energetic electrons, which acts as an additional source of free energy for driving fluctuations. Furthermore, the presence of energetic electrons makes the temperature measurement ambiguous and since gradient in electron temperature plays the prominent role in the excitation of ETG turbulence, it becomes hard to ascribe the origin of the turbulence unambiguously to ETG. It was observed that the accuracy of diagnostics cannot be improved to make a clear distinction on the source drivers of the plasma turbulence. Therefore, it becomes necessary to remove the primary energetic electrons from the plasma before carrying out ETG study. Past work on the concept of scavenging of the energetic electrons was carried out by Holmes, Mackenzie and others [25-32]. We verified the conjecture made by past investigators on electron temperature reduction in LVPD using a single cusp produced by two rows of permanent magnets, before actually designing a large scale magnetic filter capable of executing two major roles over the whole plasma cross section, 1) scavenging of energetic electrons and 2) providing a control on radial gradient scale length of electron temperature.

Based upon these observations, we have designed and installed a highly transparent ($\sim 82\%$) variable aspect ratio, rectangular solenoid, named as Electron Energy Filter (EEF) suitable to fit across the cross-section of LVPD in such a way that it divides the whole plasma into three regions of source, filter and target plasmas. The extremely localized perpendicular magnetic field of EEF removes energetic electrons all across the plasma in the target side and also enable a control over the radial scale length of electron temperature gradient by imposing different magnetic field configurations of EEF. We have investigated unambiguous controlled observations on ETG turbulence in finite beta ($\beta_e \sim 0.6$) in the core region of the target plasma of LVPD in two extreme EEF configurations. Apart from measuring spectral feature of turbulence such as joint wave number frequency spectrum, propagation and relationship with plasma parameters as earlier reported, we have carried out additional crucial measurements like temperature fluctuations, parallel wave number, correlation, cross-phase angle and beta scaling to characterize the ETG turbulence. In addition, we have also observed that the instability excited in LVPD is electromagnetic in nature and exhibits broadband spectra in lower hybrid regime following with power law. We have further developed theory for the ETG turbulence in finite beta plasma for LVPD and validated experimental results with theoretical predictions [33].

In the earlier work on ETG instability, most of the investigations are limited to the electrostatic limit [7-12] but the crucial aspects of electromagnetic ETG modes are still not well understood except few results from fluid and gyrokinetic simulations [13, 14]. In electrostatic case, ITG and ETG modes represent interchanged symmetry i.e. nearly isomorphism between the two modes for different space-time scales separated by $(m_i / m_e)^{1/2}$. Here, m_i and m_e are the mass of ion and electron respectively. In high beta regime, the isomorphism between ETG and ITG modes breaks down due to the presence of magnetic field perturbations. In this thesis, it is shown that when $\beta_e \sim 1$, perturbation along the magnetic field (δB_z) becomes important in ETG dynamics. For high beta, the ETG mode couples to whistler like perturbation in lower hybrid range, resulting into a coupled Whistler-ETG (W-ETG) mode. We have developed a linear theory of ETG mode in high beta inhomogeneous plasma using two-fluid model. The linear dispersion relation for W-ETG mode is derived by including non-adiabatic ion response and results show that the coupling of W-ETG mode is important when the plasma beta is high (i.e. $\beta_e > 0.2$). It is also seen that the beta effects related to δB_z destabilize the mode whereas, $\delta B_\perp$ resulting from parallel electron dynamics are shown to have stabilizing effect on ETG mode [33]. The detailed physics related to linear growth rate and threshold condition of W-ETG mode for different parametric regime are discussed and the numerical results are compared with experimental findings.

The experimental investigations on non-linear features of ETG turbulence are further carried out in the target plasma of LVPD. In the past, there has been a lot of interest bestowed by researchers in different aspect of dynamics involved with vortices and observations have conclusively shown signature of coherent structures, solitons, non-linear wave train, zonal flows, streamers, shocks, etc. [34-40]. In a non-linear regime, these instabilities are known to give rise to vortices of different scales in the plasma flow and thus enhance the heat and particle transport in plasma [41-43]. In our experiment, we have initiated investigations in the target plasma on non-linear coherent structures by using conditional averaging technique [34, 44]. In this method, certain condition is imposed on the amplitude of fluctuations observed in floating potential and plasma density of the reference probes in order to understand these structures. The structures are observed in poloidal cross-section using radially movable array of Langmuir probes [45-50]. These investigations are carried out in a limited band of poloidal cross-section and preliminary results indicate that non-linear radially elongated propagating structures with finite coherency are excited. These observations may have significant implications toward understanding electron transport in plasma in tokamaks [3, 12, 51]. Our observation confirms that we have non-linearity in our system but exact identification of the modes is not possible due to limited array size. For making further insight into the non-linear features of ETG turbulence, we have carried out a theoretical study of electromagnetic secondary instability for finite beta plasma.

Earlier work on nonlinear electromagnetic ETG was carried out using quasilinear approach [12-15, 17] and later simulation results were obtained which explain that temperature gradient driven perturbations evolve in the form of radially and poloidally elongated large scale structures called streamers [12, 51-54] and zonal flows [3, 55]. Streamers are radially pointed anisotrpic eddies in the poloidal plane wheras zonal flows (ZF) are poloidally extended radially propagating modes. These ZF strain and distort the radially elongated large scale streamers. Both structures constitute limiting cases of convective cell with finite radial and poloidal extent. The generation of these type of structures are based on modulational instability of isotropic turbulence [3]. Many results support the argument that zonal flows like structures suppress the turbulent heat transport whereas streamers like structures enhance the radial heat transport in plasma by convecting the plasma from higher temperature region to lower temperature region through mode coupling [17]. It has been noted that maximum growing mode with small mode number usually makes the largest contribution to transport. The observations on streamer like structures have been shown in fluid and gyrokinetic simulations [12, 51, 54]. The drift wave-zonal flow interaction have been investigated by many authors [13, 55-57]. The results reveal that a detail study of electromagnetic nonlinear structures is necessary to understand the actual mechanism of anamalous transport in the plasma. In this thesis, we also have studied the modulational instability of W-ETG mode to excite the long scale secondary instabilities and also shown that long scale modes such as ZFs, zonal fields and streamers are unstable in the background of W-ETG turbulence.

1.2 Thesis Organization

The remaining chapters of the thesis are organized as follows. In chapter 2, we focus on the developmental and experimental efforts made in the device. The major emphasis is given to the detail description of the EEF and its performance to LVPD plasma. These developments are made basically for meeting the purpose of producing plasma suitable for carrying out controlled ETG studies. The installation of EEF makes three significant changes in the characteristics of the plasma in a self-consistent manner. Firstly, energetic electrons are constrained to remain in the source and EEF region. Secondly, the electron temperature is reduced in the target region because of the transport of cold electrons and thirdly, a significant radial gradient in the electron temperature and density profiles are introduced by adjusting current density along the length of the solenoid. We have characterized plasma in the source and target region for different EEF activation currents and have established various equilibrium plasma profiles by varying the extent of charging area of EEF cross-section. We have also discussed briefly the experimental set-up of LVPD including its pumping system, magnet coil system, plasma source, power supplies and diagnostic system. A capacitor bank based 5 kA current power supply has been made for providing different current density in the EEF. In diagnostics, we make use of the cylindrical Langmuir probe to measure plasma density (n_0), electron temperature (T_e), floating potential (ϕ_f) and plasma potential (ϕ_p) [45-50]. The emissive probe [58] and B-dot probe [59] are also used to determine the plasma potential and diamagnetic flux. We have further developed compensated Langmuir probe and established a technique for direct measurement of electron temperature fluctuations [60]. In addition to this chapter, we have presented the detailed experimental results to understand the performance of EEF.

In chapter 3, we have demonstrated the first observations of ETG turbulence in finite beta laboratory plasma [61]. The observed instability is investigated in the core region of the target plasma. In the experimental results, ETG instability exhibits its direct dependence on electron temperature gradient and confirmation of the mode is seen by its absence when the electron temperature profile is made flat. These two scenarios of equilibrium profiles are achieved using two different EEF configurations. The finite beta effect in the plasma leads to electromagnetic nature of the instability. We consider spectral features such as power spectra, correlation**,** thresholds, and relationship with plasma parameters as key characteristics to define ETG turbulence. The β_e scaling of the density, magnetic field and temperature fluctuations and the correlation coefficients between various fluctuation quantities are also measured. We have also measured the phase velocity, parallel and perpendicular wave number-frequency spectrum of the fluctuations to characterize the turbulence. In order to explore the non-linear features of the turbulence, vortex like coherent structures has been investigated by using conditional averaging technique [36-40]. The structures are picked up by imposing certain conditions on the amplitude and slope on the fluctuations (density, potential) observed by the reference probe. The potential and density structures are observed in the cross-field plane of the core plasma by using an azimuthal array of radially movable Langmuir probes. We studied nonlinear characteristic of the time series of potential fluctuations such as probability density function (PDF), Skewness and Kurtosis. We briefly present the experimental results related to size, lifetime and time evolution characteristic of density and potential structures. The speculation and physical argument based on observations are also discussed.

In chapter 4, the basic fluid equations describing coupled W-ETG mode in finite β_e plasma are derived and subsequently analytical solution for different cases are presented. The theory is validated by making a comparison of the results obtained from linear dispersion relation with experimental observations. Theoretical interpretations based on mixing length argument are compared with the experimental results. The parametric dependence of growth rate of instability is discussed in detail using the linear dispersion relation for W-ETG mode. We also present numerical results related to collisional effect, non-adiabatic ions response and threshold condition of the electromagnetic ETG mode.

In chapter 5, we have studied the modulational instability of W-ETG mode to excite the secondary instabilities of zonal flows (ZF) and streamers and thus, seek how the secondary modes affect the evolution of W-ETG mode. We use wave kinetic equation (WKE) formalism [3], which relies on the spectral gap between two interacting modes. In our model, ZFs and streamers describe large scale slow wave compared to the small scale fast W-ETG mode. WKE technique is used to describe the W-ETG wave and fluid equations are used to describe the secondary modes. We have used quasilinear technique to evaluate the nonlinear terms in the dynamical equations of secondary waves and derive the nonlinear dispersion relation. The zonal flows, zonal magnetic fields and electromagnetic streamers are shown to get excited by W-ETG turbulence in high beta plasma. Wavenumber spectrum of secondary mode, effects of β_e and dependence on electron temperature gradient scale length are studied on growth rate of these modes.

Finally in chapter 6, we summarized our experimental and theoretical results. We have also presented the possibility for future investigations on problems like formation of coherent structures in the background of W-ETG turbulence. We will also like to do the control experiment (by varying the density and temperature profiles) to investigate particle and thermal transport in LVPD.

Chapter 2

Experimental Set-up and Diagnostics System

2.1 Introduction

In this chapter, a detailed description of the experimental set up and various subsystems is presented. The electron energy filter (EEF), 5kA power supply and the development of compensated Langmuir probe are some of the significant contributions made during this period. These developments are aimed for meeting the purpose of producing plasma suitable for carrying out controlled Electron Temperature Gradient (ETG) study. As described in the introduction, ETG study in basic devices is of great importance because of its direct relevance to plasma transport. The study of ETG is mainly confined to numerical and theoretical domains leaving apart one or two experimental attempts made in NSTX [19, 20] and CLM [21] devices. The complex geometry of fusion devices and extremely small scale length of the instability makes the measurement very difficult in those devices. The role of linear plasma devices, which are simple to operate, attains significance as production of moderate density plasma is possible at low magnetic fields. The use of weak magnetic field brings the scale length of the instability within the practically measurable limits and is measured by using conventional Langmuir probes that offers a clear incentive to study ETG turbulence in basic plasma devices such as Large Volume Plasma Device (LVPD) [24]. Although production of plasma of moderate density is simpler in linear devices but they suffer from the problem of very process of plasma production. The plasma in majority of linear devices is contaminated by the presence of ionising hot and non-thermal electrons emitted by hot filaments [21, 23]. The presence of these electrons in plasma with gradient in electron temperature confuses the interpretation of the results of the observed turbulence and makes its conclusion ambiguous. To address this problem, approach of first scavenging energetic electrons from the produced plasma and then exerting a control over the electron temperature gradient is adopted. For this purpose, we have made use of a specially designed EEF which not only removes energetic electrons all across the plasma in the target region but also enables a control over electron temperature gradient. In large sized devices like LVPD, use of large cable lengths for carrying probe signals are necessary and thus significant capacitive currents are evident to flow in the ramped probe circuitry used for electron temperature measurements in pulsed plasma. The measurement of the probe current is contaminated and thus makes it unreliable. Suitable ramped probe current measurement diagnostic is adopted in the LVPD to eliminate large capacitive currents by providing cable compensation to the Langmuir probe. The accurate measurements of electron temperature and its fluctuations are ensured since these are considered as the crucial parameters for studying ETG turbulence. The developed compensated Langmuir probe diagnostics has helped in greatly suppressing the capacitive cable charging current below noise level and signal to noise ratio is vastly improved. This diagnostic ensures a reliable measurement technique for electron temperature.

The detailed description of various subsystems is organized as follows. Section **2.2** describes the experimental set up of the device. Section **2.3** describes the construction and design of the EEF. The brief description for power supply of filaments, plasma discharge and EEF are presented in section **2.4**. The various diagnostics used are described in section. **2.5**. Data acquisition and control system are discussed in section **2.6**. Section **2.7** describes the electronically compensated Langmuir probe. Performance of EEF is discussed in section **2.8**. The chapter will conclude with a brief summary in section **2.9.**

2.2 Experimental Set up

The experimental set-up consists of LVPD chamber, its pumping system, magnet coil system for plasma confinement and multi-filamentary plasma source are described.

2.2.1 Vacuum Chamber, Pumping and Cooling System

The LVPD is a large double walled vacuum chamber having length 3 m and diameter 2 m. The device is made up of SS 304 material. The device chamber is divided in four parts where central cylinders are in two parts and are fixed to the support generated from the ground. The two ends of the device are parabolic dish shaped flanges mounted on a motorized movable platform.The vacuum sealing to all three major flanges is provided by double rubber O-ring with interspace pumping facility. The device is accessible either of its two ends. The vacuum chamber provides accessibility for various diagnostics and other operational necessities through 94 circular and 8 rectangular ports. One end of the device is dedicated to accommodating plasma source and pumping arrangement whereas the other end allows space for the end plate and arrangement for axial probe. There is large number of ports present on the two dish ends. The ports in the source side dish end are used for feeding electrical power for plasma source and discharge supply by means of water cooled current feed through.

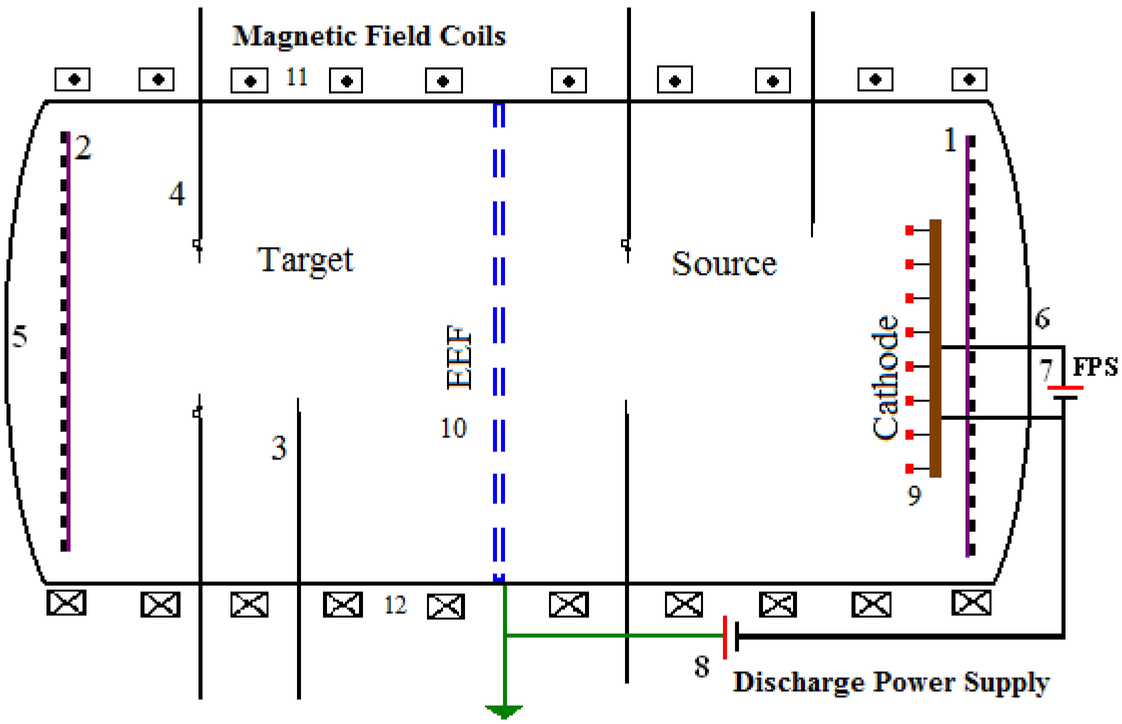

Figure 2.1: Schematic represents the layout of the internal components of LVPD. The numbers marked in the diagram represent namely, 1-2) end plates, 3) Langmuir probe, 4) a pair of B-dot and Langmuir probes, 5-6) dish ends, 7-8) filaments and discharge power supplies, 9) Multi-filamentary source 10) electron energy filter and 11-12) external magnetic field coils respectively.

The high vacuum pumping system of LVPD consists of three Diffstacks-rotary (2000 ltr/sec-42.5 m^3/h each) with one root-rotary (1750 m^3/h) pump combination. This pumping system smoothly takes the system to a base pressure of $1 \mathrm{x} 10^{-6}$ mbar. All the pumps are mounted on the movable platform connected to the pumping dish end. The conventional Pirani, Penning, and ionization gauge are employed to monitor the pressure of the device. The automatic pressure controller is used for gas feed during plasma discharges. A water cooling system capable of delivering about 600 LPM is used to cool vacuum vessel walls and cathode assembly below 60 °C and 100 °C respectively.

2.2.2 Plasma Confinement System

The plasma in LVPD is confined in both the axial and radial directions. The radial confinement of plasma is provided by a set of ten axially placed external copper coils garlanded around the chamber wall. The coils are made up of copper tubes housed inside FRP casted support structure. The magnet coil system is capable to produce uniform axial dc magnetic field of ~ 150 G by making use of magnet power supply (600V, 300A). The temperature of the coils is controlled by circulating cold demineralised water through them. The axial and radial variation of the magnetic field is uniform up to an extent of 3m and 1.5 m respectively with less than 1% ripple level. We can produce inhomogeneous magnetic field with the same power supply and magnet coils by feeding appropriate current and bypass the excess current through water cooled shunts across each coil. The details about the magnetic coils system are already described before by Mattoo et al. [24].

The axial confinement in LVPD is achieved by using a broken line cusp arrangements of water cooled samarium cobalt magnets of size ($50\,mm \times 9\,mm \times 13\,mm$) made on both ends of the device with an effective surface field of ~ 4kG. This enhances the confinement of primary electrons and subsequently helps in the density build-up.

2.2.3 Plasma Source

A large multi-filamentary Low Energy Electron Source (LEES) is used to produce plasma in LVPD by emitting electrons from it. The LEES is used as filamentary cathode consists of hairpin shaped 36 Tungsten filaments (diameter = 0.5 mm and length = 18 cm) having emission area 75 cm^2, mounted symmetrically on a rectangular ($130\,cm \times 80\,cm$) on a filament holder plate of copper. The filaments are mounted on a water-cooled multi-cusped copper plate holder having 4 kG Sm_2CO_5 magnets arranged in a line cusp. This plate along with another plate is kept at the other extreme end of LVPD to provide axial confinement to the plasma.

2.2.3.1 The plasma source (LEES)

The plasma source consists of an array of filaments arranged in a rectangular fashion inside the back plate in form of a rectangular box (L=1600mm, H=900mm and W=200mm) mounted in LVPD on the pumping side dish end. The continuous, multi-cusp, checker board confinement arrangement is mounted on all the surfaces of the box. The permanent magnets of Samarium Cobalt ($B_{surface}$~ 4kG) are used for the cusp arrangement. The magnets are arranged such that leakage of field is minimized at rectangular box corners. High purity electrolytic grade (ETP Grade) copper plates of thickness 1.2 mm are used for the side walls. The copper plates are efficiently cooled with cooling line brazed ETP grade copper tubes accommodated between the magnet channels. All the cooling lines were qualified for vacuum leak rate of better than 2 x 10^{-7} mbar litre/sec and compatible to pressure with 5 Kg/cm^2.

A total number of 36 hairpin shaped tungsten filaments are connected in parallel combination such that each filament carries 20A current at a voltage drop of 12 volts. These filaments are used as electron emitting cathode for which current is fed through water cooled copper tubes. The water cooled vacuum – air interface of the electrical feed through is rated for 750A DC. There is a provision of feeding current in 8 geometric sectors with positive and negative current feeds distributed in the entire rectangular plane for which 2 water inlet and out let copper tubing are used. Four sets are installed in the periphery (in a rectangular shape, made up of 4 “L”) and 4 sets are placed in the middle of the box for which 16 water cooled current carrying tubes are used. All the 16 arms are kept isolated from the main LEES box and from LVPD system using suitable ceramic isolators. The LEES assembly is mounted on movable RHS dish-end is electrically floating inside LVPD system.

The plasma can be produced for long discharge pulses of duration (~ 50 ms) and short pulses (~ 10 ms) over a repetition of 1s. The cooling arrangement is provided in such a way that both types of operations are possible without much increase in wall temperature. The wall temperature is not allowed to increase beyond 100ºC, to ensure safety of the permanent magnets mounted for the confinement system. The pulsed Argon plasma (duration~9.2 ms) is produced in the system by accelerating the primary ionising electrons emitted from the surface of hot tungsten filaments (cathode) due to negative bias discharge voltage, $V_{Dish} = -70VDC$ at a neutral pressure of 4×10^{-4} mbar in the presence of the ambient magnetic field ~6.2 G. The rectangular geometry is chosen to have a control on plasma density and electron temperature of the radial profiles by suitably making changes in the matrix of filaments. The cooling arrangement using brazed copper tube on the LEES system is designed for heat removal of the order of 45 kW of direct heat load due to tungsten (W) filaments. The electrical power feeding system connected to the LEES is capable of supplying 90 kW of power for pulse plasma operation.

The calculation for W filaments yields a current density of $J_c = 3.2A/cm^2$ at $T = 2200°K$, $A_c(W) = 1.2X10^6 Am^{-2}K^{-2}$. The total effective surface area of the filaments (36 filaments) is $S^{eff}_{filament} = 6.22X10^{-3}m^2$, in the ideal case the total current drawn from the filament array is expected to be, $I_{emission} = J_c X S^{eff}_{filament} \approx 200Amp$. This value is very close to the plasma discharge current of $I_d \approx 180Amp$ at an applied discharge voltage of 70 VDC where electron-neutral collision cross-section starts saturating. Calculations of I_d is empirical and its exact value cannot be derived directly from Child-Langmuir Law. It value is greatly modified by the filament configuration, position, anode cathode distance, anode configuration, applied discharge voltage, generation of electric field, gas pressure etc., hence the experimentally measured discharge current value is used for comparison. The discharge current calculations are done by balancing the production of the energetic electrons and loss rate of the ions.

2.3 Electron Energy Filter (EEF)

The electron energy filter, installed in LVPD is designed for the purpose of scavenging the energetic electrons present in the plasma and to exert a control on the gradient scale length of the electron temperature, a free energy source responsible for the excitation of ETG turbulence. Past research works [25, 62] have shown that the electron temperature of the plasma transported across the cusped magnetic field, produced by permanent magnets or the electromagnets [29, 30-32, 63-66], gets greatly reduced. It is also shown that the ratio of plasma density to the invested electrical power in the device is increased by the containment of primary ionizing electrons by the cusped magnetic field. Thus the characteristics of the plasma, both inside and outside the cusped magnetic field, is controlled by the perpendicular component of the magnetic field.

Based upon these observations, it can be argued that multi-pole cusped magnetic field across the plasma cross-section can be used to filter out energetic electrons to produce a plasma region devoid of non-thermal and primary ionizing electrons which is essential for carrying out ETG studies . However, producing cusp field all over the cross- section of the LVPD plasma by using permanent magnets is not a good solution. This is because the loss surfaces of the pole pieces introduce modulation in the plasma density in the volume of the plasma. This leads to a sizeable short scale perturbation to the plasma. This can be avoided only when extremely localized perpendicular magnetic field running across the cross-section is used and is provided by a device which does not present loss surfaces embedded in the volume of the plasma. The best choice is magnetic field produced by the coils placed outside the chamber of LVPD. It is very easy to show that making a provision of uniform magnetic field across a diameter of $2\,\mathrm{m}$ of LVPD plasma would require coils of enormous sizes. Such large size coils cannot localize magnetic field with a limited space in LVPD plasma. Further, making a provision for controlling the radial variation of magnitude of magnetic field in such a system does not seem to be a simple task. The alternative is to embed coil system in the plasma. The localization of the magnetic field with in a small volume of the plasma can be achieved by making use of a large aspect ratio solenoid. We designed and constructed a varying aspect ratio, highly transparent ($\sim 82\%$) solenoid snug fit to the entire cross section near middle of the LVPD. Since its function is to restrict transport of high energy electrons across the magnetic field, we call it Electron Energy Filter (EEF). Consequently, EEF carves out a plasma region, devoid of energetic electrons, from the source plasma. It consists of a solenoid with a circularly tapered rectangular cross-section [Fig. 2.2]. The design requirements and the details about its construction are described in the following subsections.

2.3.1 Design Drivers

1. Basic plasma devices usually have plasma, which is contaminated by the presence of primary ionising and non-thermal electrons. These electrons are potential sources of instabilities. LVPD is no exception to this experience. In this device the primary source of ionizing electrons is accelerated electrons boiled off from a set of hot filaments. These electrons eventually form a low-density tail with energy $< 70eV$ $(n_{e,tail} / n_{ec} \approx 0.1)$ attached to a cold population of high-density Maxwellian electrons ($n_{ec} \approx 3\times10^{11} cm^{-3}$, $T_e \approx 3eV$). Since energetic electrons in the source plasma have an isotropic distribution, the average parallel energy is $23eV$, 1/3 of the total energy $\sim 70eV$. This renders LVPD plasma, as it is produced, unsuitable for studies on ETG. No alternate prescription exists to produce plasma with the Maxwellian electron distribution. Consequently, there is no escape from that, the starting point has to be production of plasma by conventional methods. Thus, the first role of EEF is to scavenge energetic electrons from the whole body of the plasma to be used for the study of ETG.

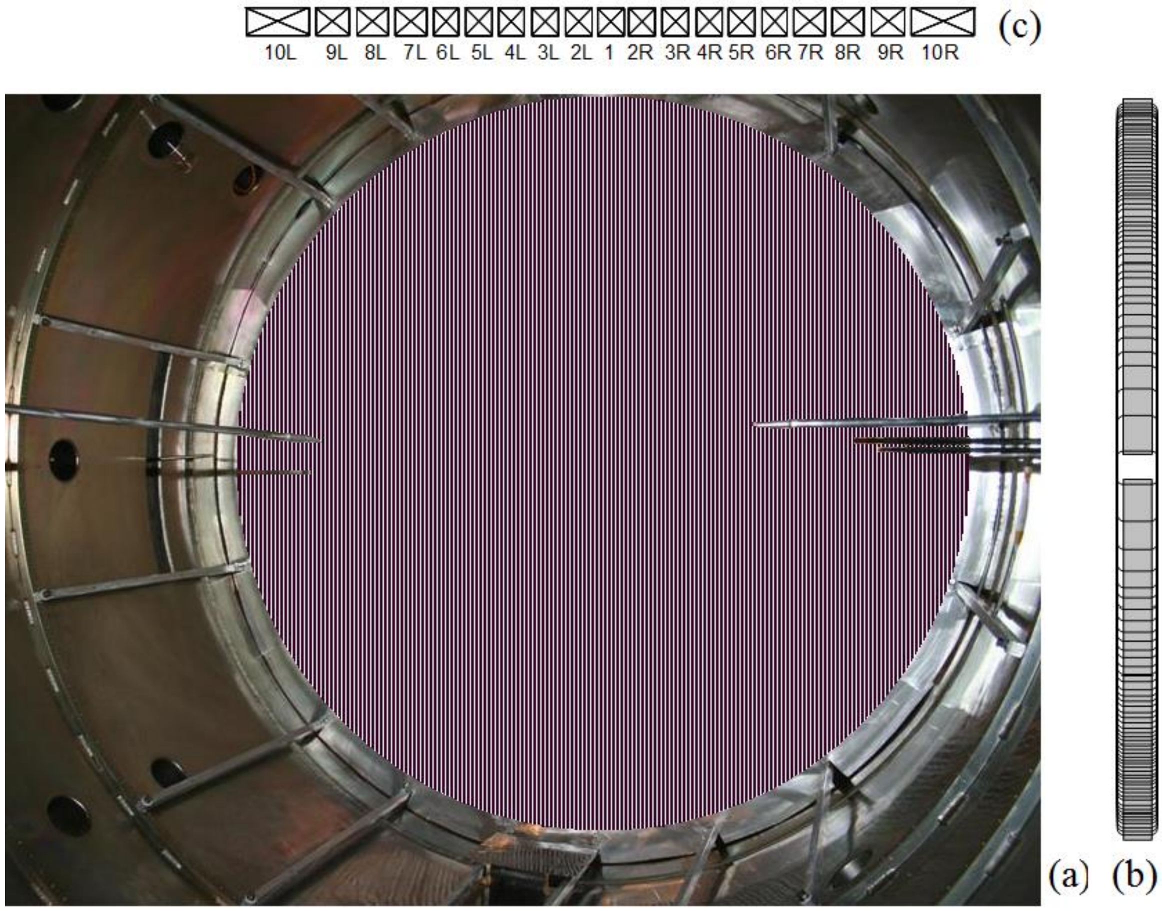

Figure 2.2: Shows (a) photograph of the EEF installed in LVPD, (b) the side view of its cross-section and (c) the top view showing the extent of respective coils. Note that there is no

leakage of plasma from the source to the target region through spaces outside of the physical boundaries of the EEF.

Since EEF occupies the full cross-section of LVPD, it divides the plasma into two regions, the source and the target. In the source region, plasma is produced by conventional methods and contains energetic electron. No plasma is produced in the target region. The plasma transported from the source region across the EEF fills the target region. Energetic electrons in the source part are restricted from entering in to the target region due to localized perpendicular magnetic field produced by EEF. The design issue is that while EEF isolates two plasmas one with energetic electrons and other without it, it has to occupy minimal axial extent. The axial extent of the source plasma has to be sufficient enough to allow significant ionization to occur by ionizing electrons with mean free path for ionization of a few meters. So EEF cannot be kept very close to cathode, the source of primary ionizing electrons. Also, target plasma has to be of sufficient axial extent to support studies of plasma turbulence consisting of modes with wavelength in the range of a few tens of cm. The LVPD is $3\,\mathrm{m}$ long device. Reserving few tens of centimetres of space for infrastructure of tungsten filaments for producing ionizing electrons, 1m for the source region and 1m for the target region and half a meter for the disturbed plasma region in and around the filter, it is clear that EEF width cannot be more than a few cm. It may be noted that the disturbed plasma region (~ 10-15 cm near EEF) on the target side of EEF cannot be used for any studies on ETG.

2. EEF should be highly transparent in order that it does not present itself as a large loss surface. It implies that it is to be built with extremely thin wires with diameter of the wire compatible with current capacity needed to produce the desired magnetic field within the solenoid. Ratio of turn-to-turn distance to the wire diameter has to be be kept high so as to attain high EEF transparency for plasma transport. This precludes use of actively cooled coils and energizing solenoid by DC current.

3. EEF operation should enable to introduce radial gradient in electron temperature. Magnetic field with in a long solenoid is largely uniform except near the edges for uniform turn current density. Since the electron temperature of the target plasma is solely determined by the plasma transport across the transverse magnetic field of the EEF which in turn is determined by the value of magnetic field with in the solenoid, a construct of EEF with uniform turn current density will not introduce gradient in electron temperature. So turn current density is

to be made non-uniform. This can be done by basing construction of the solenoid for EEF on use of serially placed several independent coils with independent current injection and return feed lines so that each coil can be energized by independent power supply. Such a solenoid built with parallel coils has built-in flexibility of operation to secure different field profiles. To secure scale length of the gradient in electron temperature of target plasma ranging from a few tens of cm to a few hundred cm, the solenoid may have to be operated by activating only some of the coils of the solenoid for short scale lengths with the same or different driving currents. It is possible that gradient in electron temperature in the target plasma may be simply controlled by the uniform current density using limited extent of the solenoid of EEF. There is no empirical evidence available for stating that the radial scale length of the solenoid magnetic field has one-to-one relationship with scale length of electron temperature in the target plasma. This correlation needs to be determined.

4. In order that solenoid does not perturb the plasma by drawing a large current, it is insulated by a vacuum compatible insulation.

5. Theoretical predictions indicate that $\eta_e = L_n / L_{Te}$ has to exceed a threshold value for exciting ETG turbulence in a laboratory plasma. The claim for ETG mode needs L_n to be very large compared to L_{Te}. Thus EEF should affect plasma density in the target region uniformly across its cross-section or at least produce L_n ~ several meters.

6. There should be flexibility in operation both in the selective charging of any one of the 19 elements of EEF or by feeding different current in them.

2.3.2 Construction

After working out physical and electrical parameters of the EEF solenoid, we built a square shaped prototype of 1m x 1m EEF. This was tested for its electrical performance and, more importantly, for the response of LVPD plasma. This led to some minor modifications which were duly incorporated in the EEF deployed in LVPD. The construction of the finally designed EEF solenoid is described below.

The large filter covers the whole cross-section of LVPD. The EEF is built on two rigid aluminium frames. Two frames are separated by 40 mm. Each frame consists of two semi-circles of radius of 940 mm. A semi-circle is formed from rectangular 2913 mm long aluminium bar of thickness ~ 10 mm and width ~ 40 mm. The width of the solenoid (40 mm) is sufficient to make field and plasma measurements within the EEF by deploying the field coils and Langmuir probes and its variants. The semi-circles are mounted on the support rings already provided in LVPD. Holes of 3.2 mm diameter are drilled along the width and dispersed over the circumference of the semicircles such that turn-to-turn distance of 12 mm remains uniform in the entire span. As indicated in figure 2.2(b) highlighting coil cross section, a turn of solenoid is formed by a wire passing through the directly opposite holes in the top and bottom semicircles of one set, going across to another set placed at 40 mm, passing through another pair of top and bottom holes, axially aligned with the pair in the first set, and finally returning to the first set at the next adjacent pair of holes to begin the next turn.

The entire EEF solenoid consists of 19 coil sets [Fig. 2.2 (c)] placed serially and electrically connected in parallel. This allows optimum use of available power supply. This solenoid has 155 turns of rectangular shape with uniform width of 40 mm but they have varying height and cross-section. The largest cross-section $(1848mm \times 40mm, coil 1)$ is at the centre of the solenoid and the smallest cross-section $(40mm \times 40mm, coils\, 10L \text{ and } 10R)$ is at the two ends. The space between two consecutive turns in a coil is 12 mm. The electrical length for each of 19 coils is kept same to ensure constancy of electrical resistance and dc voltage drop. Hence, numbers of turns in different coils vary, the smallest for the coil set at the centre (7 turns) and largest (14 turns) at the extreme ends of the solenoid. The uniform current is maintained in each set by restricting the potential drop to minimum at the connectors. This allows powering of 19 coils, connected in parallel, by a single power supply. It is also possible to inject non-uniform current in the coils from a single power supply by shunting coil currents. The cable used for winding coils is made up of Teflon coated silvered copper wire with a diameter of 2 mm and cross-section of $3.14 mm^2$ with effective resistance of $\sim 11.6 m\Omega / m$. The cable length of 485 m is used in winding the solenoid of 19 coils. The leads of each coil are taken outside LVPD chamber through a vacuum interface and terminated on a patch plate. Each coil offers a typical resistance of $\sim 350 m\Omega$. Total equivalent resistance offered by the parallel combination of all 19 coils is $18.5\, m\Omega$. The resultant inductance of the solenoid when 19 coils connected in parallel is $\sim 1.8\mu H$. Individual inductance of coils varied between 36 and $50\,\mu H$. The achieved design parameters of EEF are summarized in Table-2.1.

Table 2.1: Details about the design features of EEF

Size	Height and Span: 2m, Width: 40 mm
Material	Teflon insulated, 2 mm^2 silverized copper
Total turns	155 with turn-turn spacing 12 mm
Total sets	19 sets of 30 m each
Equivalent Resistance/Inductance	18.5 mΩ / 1.8 μH (at terminals) 20.5mΩ/ ~10μH (with transmission line)
Max. Current /Voltage	274A/96V (at individual terminals of coils) 5206A/ 106V (with transmission line)

The insulating cables are used to minimize the perturbation offered to plasma; hence direct contact of the conducting wire with the plasma is avoided. The cable is qualified for pulsed operation of $2kA$ for particular pulse duration ($\sim 20\,ms$). The measured transparency of EEF is 82%. The dimensions and aspect ratio of coils are chosen such that produced magnetic field follows the scaling of 1G/A when all coils are energized. Figure 2.2(a-b) shows installed EEF in LVPD and a schematic showing its cross section.

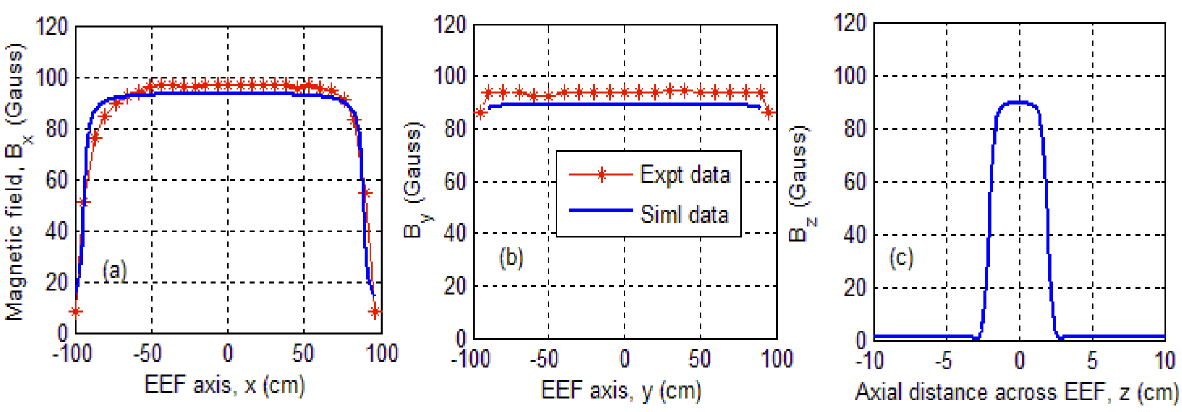

Figure 2.3: Shows field profiles of EEF magnetic field (a) along the axis of the solenoid, (b) perpendicular to its axis and (c) along the axis of LVPD.

The axial variation of the measured EEF magnetic field across its axis is shown in figure 2.3(c). It is seen that the magnetic field is nearly constant over the width of the solenoid, spills over a few cm outside towards both target and source side of the plasma. Beyond this region the magnetic field quickly decays to less than 1G at a distance of $\geq 50\,cm$. Thus plasma in the target region where ETG investigations are made, is largely unperturbed by the solenoid contributed magnetic field. Figures 2.3(a) and 2.3(b) show variation of the two components of the magnetic field with in the solenoid. The two components are: (1) the component along the length of the solenoid and (2) the component perpendicular to it. We note that the magnetic field is uniform over most of the length of the solenoid and falls rapidly near the ends when all coils are excited by the same amount of current of 100 A. The measured values are compared with the simulated values and a typical field pattern is shown in figure 2.3(a-b).

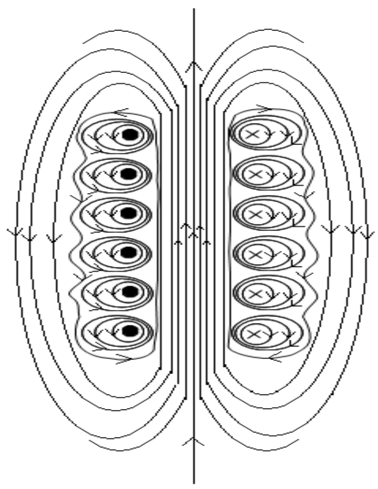

Figure 2.4: Shows the schematic of the typical magnetic field map when the coils in the solenoid are excited by uniform current. Here only some coils are shown for clarity.

Figure 2.4 shows the typical magnetic field map when a few coils in the solenoid are excited by uniform current. The field produced is divided into three regions. The inner region consists of closed field lines around each turn of the coils of the solenoid. This region is separated from the outer region by null points between the turns and a separatrix running around the turns of the solenoid. In the outer region, both the closed and open field lines exist. The open field lines encapsulate closed field lines, encircling all the 155 turns of the solenoid.

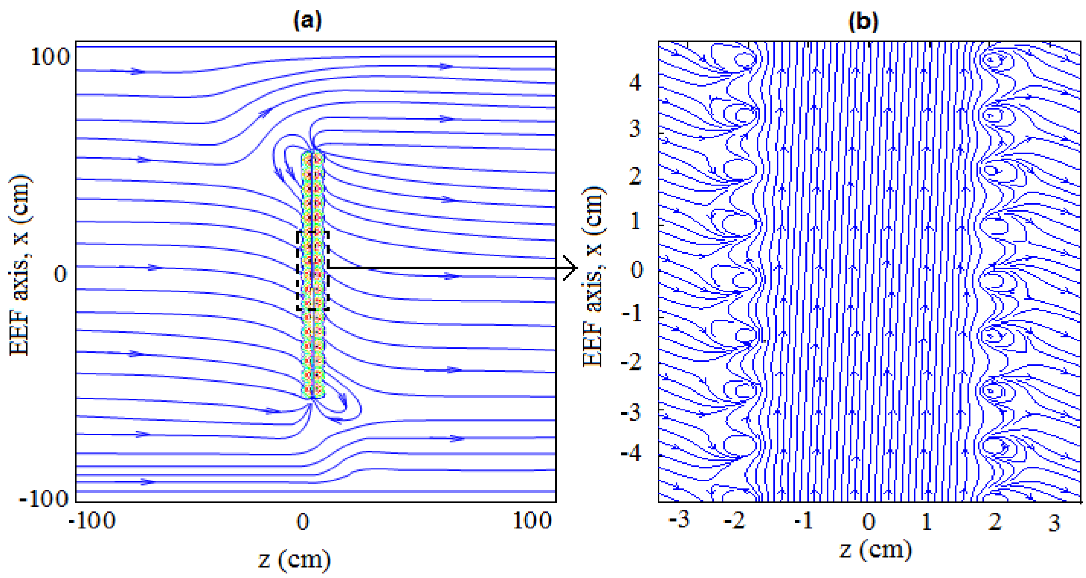

Figure 2.5: (a). Shows the schematic of combined magnetic field map of EEF magnetic field superimposed upon the uniform axial magnetic field of LVPD and (b) the zoomed view of the combined magnetic field inside EEF obtained numerically.

Figure 2.5 shows the schematic of the typical combined magnetic field pattern, when central thirteen coils (7L-1-7R) of solenoid [see Fig. 2.2] are energized along with the axial magnetic field of $6.2G$. Even when axial magnetic field is as small as $6.2G$, the field pattern undergoes a radical change. First, closed field lines encircling all the turns of the solenoid disappear. Secondly, open field lines run all across the device from the source to target regions through the free spaces between the turns of the coils of EEF. The field lines enter in the EEF solenoid by bending at 90 degrees and exit by taking another bend of 90 degrees. Thirdly, two oppositely positioned neutral lines appear just outside the entrance and exit of the EEF. Figure 2.5 shows a schematic representation of the solenoid field when all nineteen coils are energized.

A horn shaped coil is placed at each of two axial ends of the EEF to guide the magnetic field lines to the outside of LVPD to return from the other end. They help in preventing most of the field lines to return through the plasma volume. However, the leakage of field lines into the plasma between consecutive wires could not be avoided. It was observed that the measured leaked field perpendicular to the axial magnetic field of EEF is 1 G at 30 cm from the EEF.

2.4 Power Supply System

2.4.1 Filament and Discharge Power Supply

The filament and discharge power supplies are used for the plasma production in LVPD. The high current (1500A, 60V) filament power supply provides the power with 2% current ripple factor. The filaments are connected in parallel and are arranged in such a way that each filament carries $\sim 20\,\mathrm{A}$ current at a voltage drop of 12 volts. The filaments are biased at -70 V with respect to the chamber to accelerate the electrons using a pulsed discharge power supply.

A discharge power supply based on the capacitor bank of 1.8 F has been developed in the laboratory. The power supply consists of two paralleled connected high current IGBT switches (SKM500GA 123DS) for pulsed switching operation. The current is monitored through each IGBT to ensure equal sharing of current within 3% accuracy. A discharge current of $\sim 170\,\mathrm{A}$ is produced. The magnitude of discharge current depends on total load offered by a combination of electric load of plasma, current transport copper bars between power supply, cathode and the lead impedances. Hence plasma discharge is obtained under constant voltage mode. The rise and fall time of the power supply is $\sim 200\,\mu s$. Details about the filament and discharge power supplies are already reported [24]. This chapter have relevant details about the EEF power supply, built especially for meeting the requirement of the electron energy filter.

2.4.2 EEF Solenoid Power Supply

The power supply for EEF is a capacitor bank based static switch consisting of 10 IGBTs, connected in parallel, capable of providing a current ~5 kA for its operation. It rapidly sources 75 Coulombs available with a 200V rating capacitor bank of ~ 2.8 F. Power supply is made robust by ensuring 1) Equal current sharing, 2) Uniform power distribution during the pulsed operation of the IGBTs, 3) Safe commutation of power from ~ 9.5 μH inductive load circuit, 4) Minimization of power supply internal inductance <600nH by proper optimisation of power stack and 5) Making use of suitable snubber circuits for additional switch protection. This allows voltage protection against anticipated back emf in excess of 6 kV at turn off. The switch is operated on command and is electronically timed using an optically isolated computer controlled interface for both pulse width and pulse repetition frequency ≤ 1 Hz and duty cycle ≤ 01.5%. The supply has other specifications as : Rise time τ_{rise} ~ 41 μs (resistive load) and, decay time τ_{decay} ~ 9.4 μs, pulse duration with flat current $\Delta\tau_{pulsewidth}$ ~ 12 ms, current droop over the pulse duration < 20% and terminal voltage ≤ 150V. This type of switch can be treated as a module to build power supplies with larger current capacity and finds application in multi-kA discharge power supplies for pulsed plasma sources.

The constructed EEF is suitable for the pulsed operation. The fast rise time (τ_{rise}) becomes essential due a significant amount coulomb lost even during current build-up for the high current amplitude on the EEF's inductive load that draws charge from a limited coulomb reservoir of the capacitor bank. This necessitates a slight (~1.2ms) pre-trigger operation of the EEF to achieve its rated magnetic field before plasma discharge. EEF essentially appears an inductive load of ≤10 μH at the turn on/off of power supply and a resistive load of 20.5 mΩ at the flat top. Since load with its transmission line has inductance ≤ 8.2 μH, layout of the power supply within its own constitution and outside in relation to the location of the EEF becomes another essential parameter.

We have also undertaken simulation study using Pulse Forming Network(PFN) and Guillemin network but found this method of quick discharge of coulombs directly from a large capacitor bank as the best solution even though left with droop percentage of ≤ 20%. Although the droop control remains an issue with this scheme but in our case we have optimised it w.r.t. the performance of the plasma parameters within the droop percentage in the magnetic field produced by EEF. It was seen that the circuit design based on Pulse Forming Network(PFN) and Guillemin network are better options from the aspects of droop but are ignored because of the practical limitations of inductance and capacitance for large duration of pulsed operation(~few ms). We carried out a comprehensive simulation for capacitor bank, switch with snubber protection, transmission line along with solenoid load and results obtained for both, the pulse shaping and plasma parameters are found within acceptable limits of conducting experiments.

2.4.2.1 Circuit Overview

The high current amplitude (~ 5kA) is the design requirement for producing the magnetic field within EEF for ETG study in LVPD. In this topology, stored coulombs of charge in capacitor bank of main power are rapidly discharged to deliver high current across the load [Fig. 2.6].

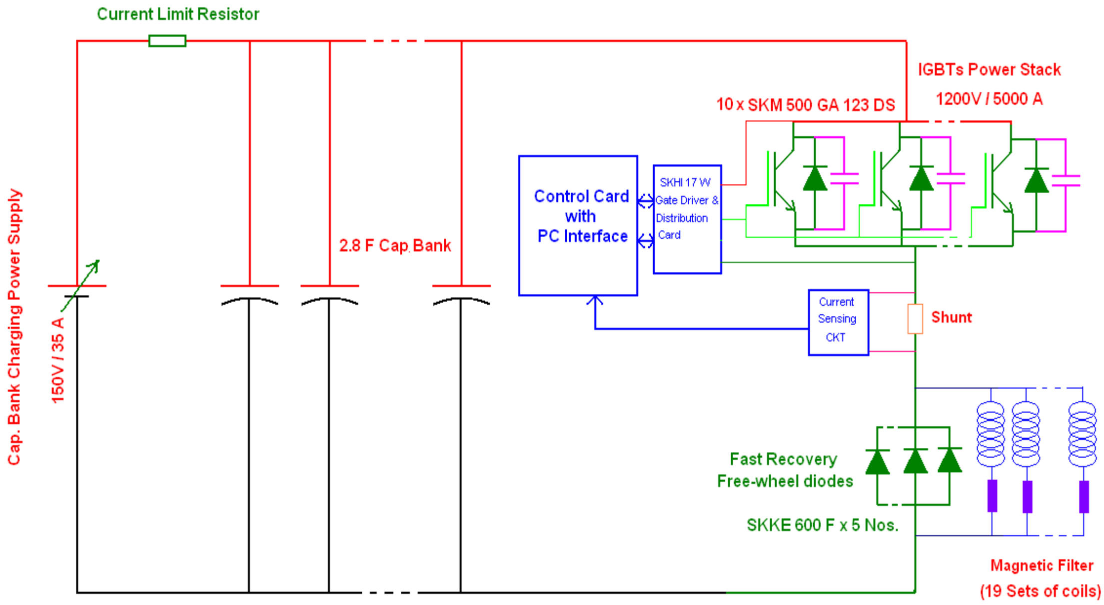

Figure 2.6: Pulse power supply topology adopted for high current system.

A capacitor bank of ~ 2.8 F is used to store the electrical energy, which is applied to the installed EEF through semiconductor switch. The semiconductor switch is made up of multiple insulated gate bipolar transistors (IGBTs) connected in parallel. IGBT's are robust devices for high current switching application. Once IGBT switches are turned ON for a pulse period of 7 – 12 ms, the entire voltage of capacitor bank is realized across the EEF resulting in the huge current. We have used 10 numbers of IGBTs connected in parallel having rating of 500A/1200V each to switch a current of 5kA from the power pack. The power supply produces a magnetic field which remains constant (droop within 20%) during the pulse duration (~12ms). The magnitude of the current in the solenoid is decided by the resistances offered by load, transmission line and power supplies internal resistance (~ 23.5 mΩ) and by the charging voltage of the capacitor bank (~125V). Multiple freewheeling diodes connected in parallel across the load terminals on the power stack serve to protect the switch from circulating inductive currents generated by the back e. m. f. at turn off. Similarly, the freewheeling diodes inside the IGBT modules and the snubber capacitors are mounted across IGBT to nullify the effect of own distributed inductance. The current monitoring circuit ensures a quick commutation of the switch for over current and short circuit conditions. A 3 phase servo controlled variac based transformer-rectifier power supply with rating of 35A/ 150 VDC is used to charge the capacitor bank, capable of handling transient loads. Two resistors of 1Ω/300W each are used in series to limit the maximum charging current of the capacitor bank. A brief description of various important subsystems/ components is given below.

(i) Capacitor Bank

The capacitance of the capacitor bank is chosen considering factors like cost, space and droop requirements for this application. The RC equations which govern the discharge of bank voltage to a resistive load essentially depict a drop from 90 % to 10% in within five RC time constants. The discharge voltage across the capacitor is proportional to its charge and has behaviour ($V=V_0e^{-t/RC}$) similar to the charge. The voltage and current delivering capacity reduces substantially in the fraction of RC time constant.

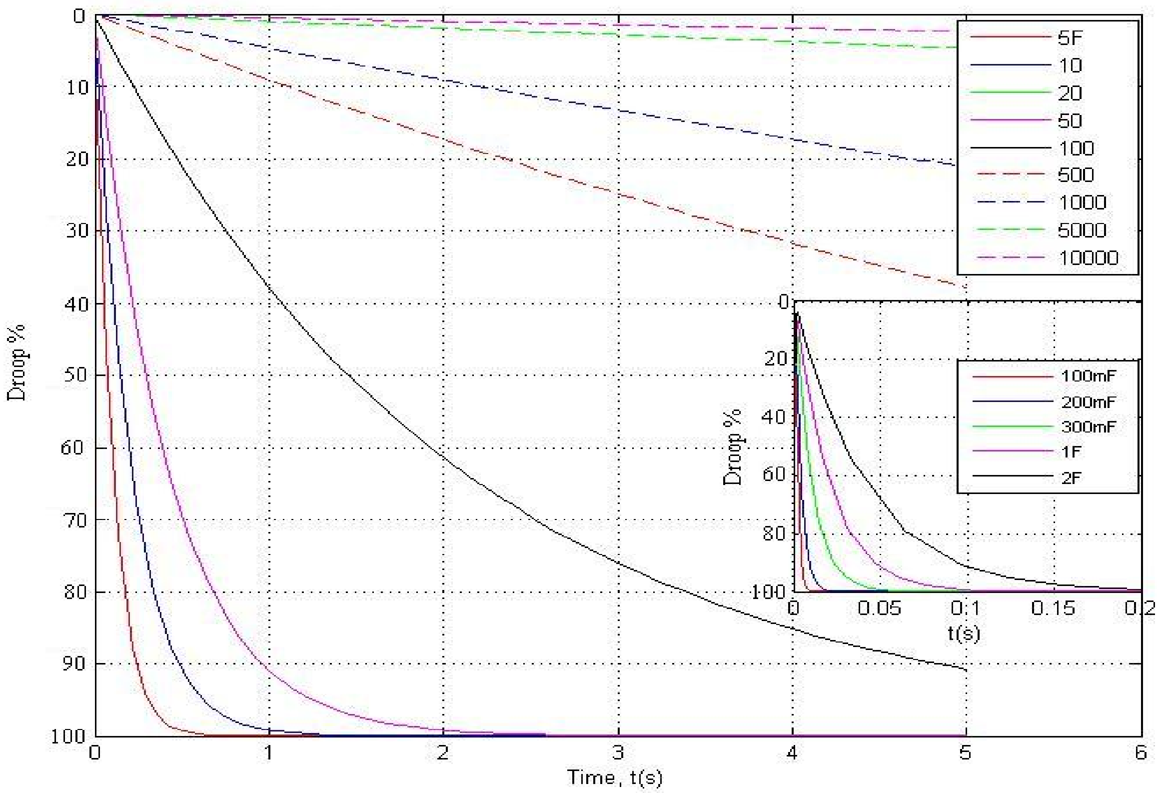

Figure 2.7: Droop percentage for different pulse duration.

The power supply is required to deliver 5 kA for 12ms on an expense of 60 coulomb of charge. We configured the capacitor bank in such a way that even after a depletion of 60 coulombs, a sufficient amount of charge should be left to sustain a minimum droop during the flat top of the discharge pulse.

A 2.77 F capacitor bank holds 346 coulombs when charged up to 125 V. This has shown that with expense of 60 coulombs from a total of 346 available, the droop percentage has been restricted to ~ 17 % which is within the allowed tolerance [see Fig. 2.7].

In figure 2.8, a comparison between the simulated and experimental current profiles when 5 kA current is injected across EEF load is shown before actually used it for plasma discharges.

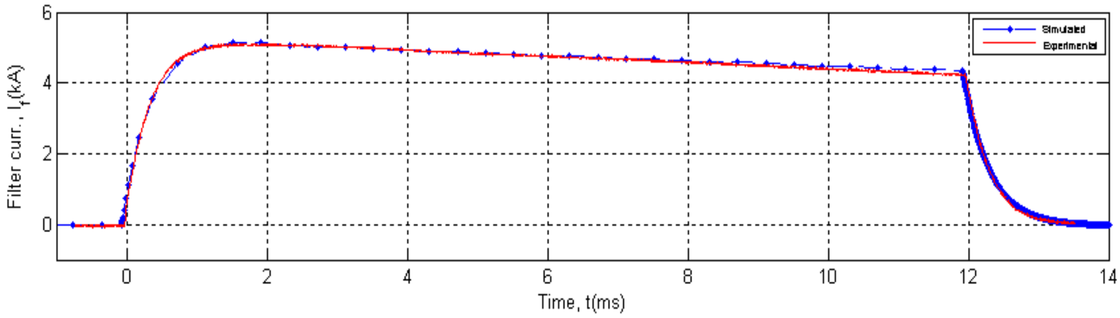

Figure 2.8: A comparison of the result obtained from the simulation and the actual load test of 5 kA power supply on EEF load.

This droop percentage is acceptable for carrying our ETG experiments as within this limit, the measured plasma parameters show negligible variation [see Fig. 2.9].

(ii) Control and Protection Circuit

The timing sequence of the EEF excitation is synchronized with the plasma discharge while satisfying various safety interlocks. The control card is designed in such a way that it allows both local and remote modes of operation. In local mode, the control card, on a given start command generates basic timing pulses required for the pulsed control operation of IGBTs switch through driver circuits while promptly monitoring and acting on fault generated in the circuits. The safety interlocks embedded in the control logic and are given priority over all other actions.

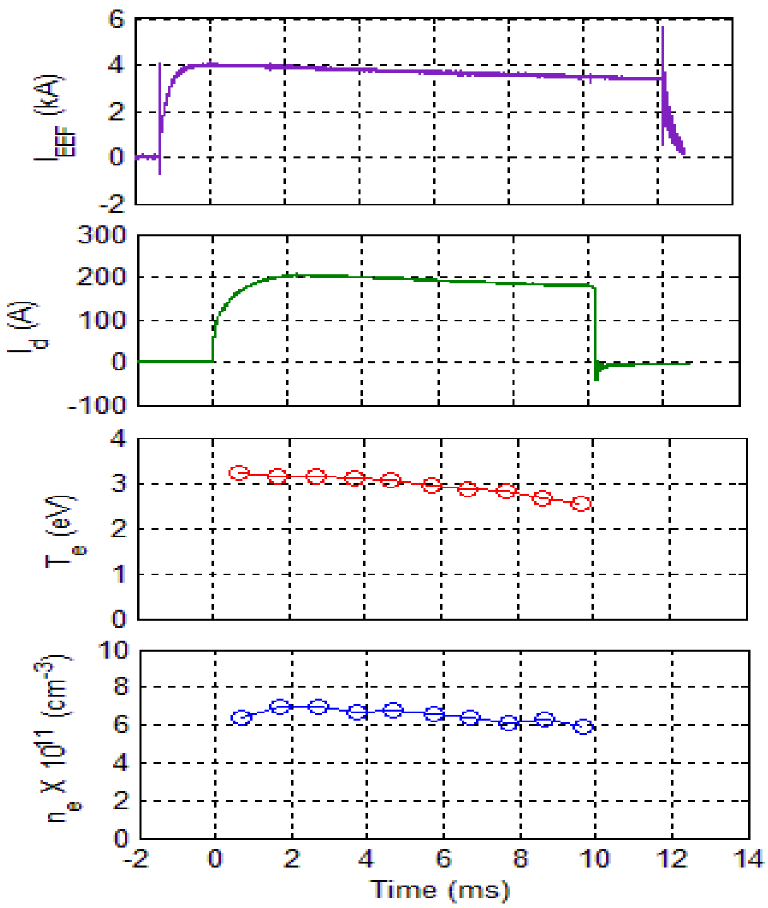

Figure 2.9: The temperature variation seen during the discharge pulse does not exhibit much variation. The overall change (≤ 15 %) is seen both in plasma density and electron temperature respectively.

A gate distribution card is wired for driving all 10 IGBTs with minimum jitter ensuring uniform driving amplitude and without time lag. This card is strategically mounted right above the IGBT power stack, to minimize the drive path to all the IGBT gates as similar value of series resistances are used in the charging path of the gate terminals.

(iii) POWER STACK

The power stack mainly consists of the IGBT switch, heat sink, fly back diodes and snubbing capacitors. A brief description of these is given below.

(a) Insulated Gate Bipolar Transistor (IGBT) Switch

IGBT switch is important for the power supply and needs special consideration during design and implementation. In order to meet our requirements, the design for current sharing with multiple devices is implemented. We have designed the IGBT power stack around Semikron make IGBT model SKM 500 GA 123 DS (1200V/ 500A), which is a robust device and has been extensively tested and used in the discharge supply of LVPD. A parallel combination of ten number of IGBT's of above mentioned make are used ensuring equal distribution of the path resistance for equal sharing of current by deploying circular multiplayer copper disk design for the current distribution. The stack has been proven for its ruggedness and the reliability with > 10^6 C of charge is pumped to the EEF while producing > 10000 plasma discharges.

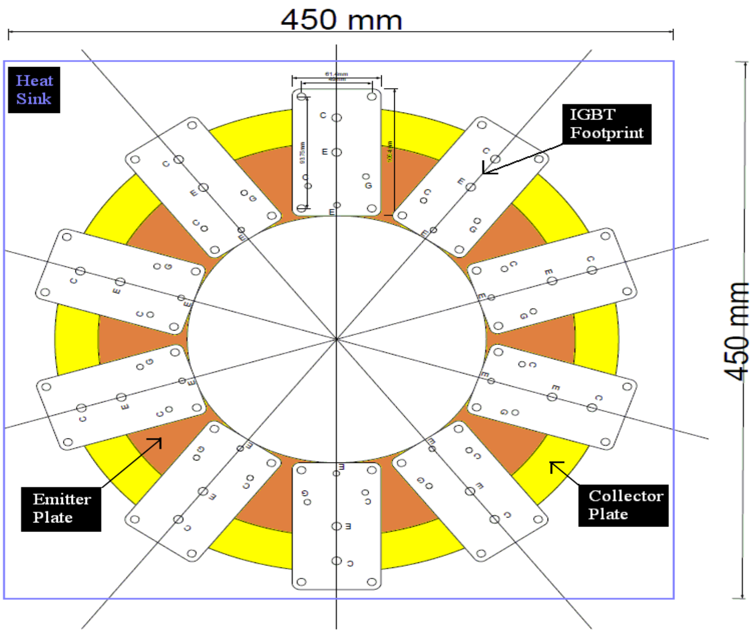

Figure 2.10: Layout of IGBT power stack on Heat Sink.

(b) Heat Sink

The layout of IGBT switch is shown in the figure 2.10. The IGBT's are arranged in a circular geometry and at equal distance from the centre. This is mounted on a rigid aluminium square heat sink of size 450 mm x 450 mm x 12 mm thick. A dissipation of 3 kW of power per IGBT in steady state results in 30 kW power dissipation on the stack. Considering a burst of 8 shots of duration 15 ms with a repetition rate of 1 Hz, we observe the rise in the temperature of heat sink that amounts to 3.6kJ of energy dissipation. The capacity of the designed heat sink allows a temperature rise of just 0.56 ^{o}C during this operation.

(d) Fly back diodes

Eight numbers of Semikron make fast recover diodes [Model SKKE 600F] are used to form fly back diode array for enhanced protection of the power supply against large inductive signals during turn off. A photograph showing arrangements of freewheeling diodes is shown in figure 2.11.

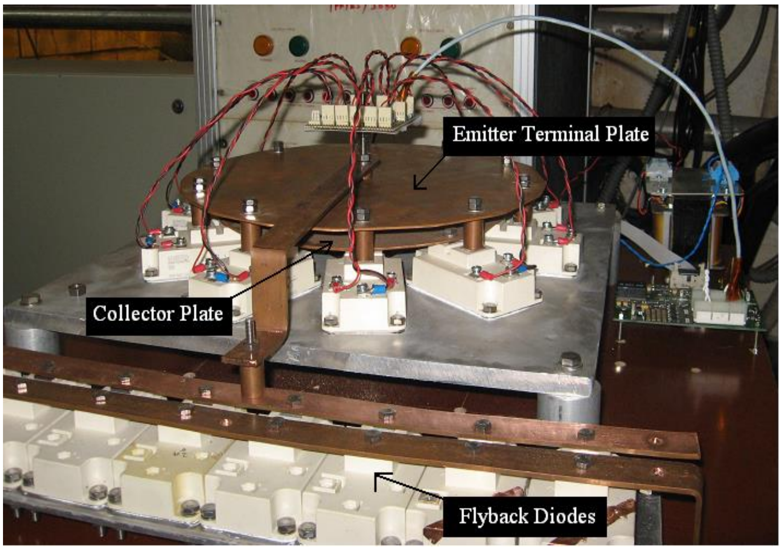

Figure 2.11: Picture showing output derived from the emitter terminal plate and negative of the power supply terminated on the flywheel diode array.

(e) Snubber Circuit

The power stack with distributed power loop inductance exhibits large back emf and capable of damaging the switch during fast commutation at high current amplitudes. This condition requires proper snubbing circuit to protect the switches. In the power stack designed here, in spite of its highly compact design, offers inductance amounting to ~590 nH. In a pilot experiment, the power stack at 10 % of rated current (~ 500A) @resistive load (R = 100 mΩ) and inductive load (R_L ~ 600 nH), a back emf of 600 V across the IGBT stack is observed.

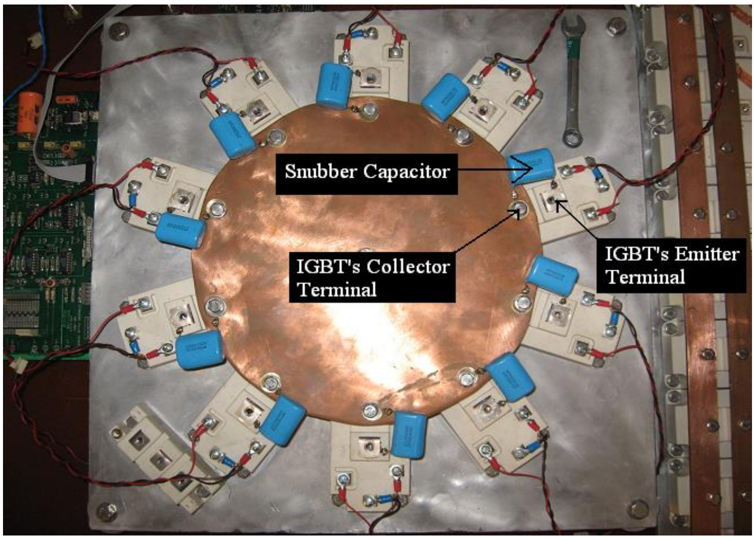

Figure 2.12: The photograph shows the mounting of snubber capacitors directly across the collector and emitter terminals of the IGBTs.

The snubber capacitors used are bipolar capacitors, mainly shares the maximum inductive energy from the load line of the switch at turnoff. In this power stack 8.2 μF/ 1500V radial leaded DPP type propylene film bipolar capacitors are deployed. It is mounted directly across the emitter and collector terminals of each IGBT that are capable of large peak currents for few hundreds of μs. The total capacitance applied across the power stack is 82 μF, which is sufficient enough to limit the electromotive force below 600V and allow dampening of total energy in < 800 μs to save the switch. It may also be noted that the IGBTs used (SKM 500 GA 123DS) have inherent fast recovering fly back diode connected across the collector and emitter terminals in reverse bias which provides enhanced protection against any reverse voltage appearing due to transients of inductive loads at turnoff [see Fig. 2.12].

2.5 Experimental Diagnostics

In LVPD, plasma parameters, like plasma density (n_0), electron temperature (T_e), floating potential (ϕ_f) and plasma potential (ϕ_p) are measured by using a cylindrical Langmuir probe. Emissive probe is also used to determine the plasma potential. Diamagnetic flux and magnetic fluctuations are measured by B-dot probe. The density and potential fluctuations are determined by single Langmuir probe whereas temperature fluctuations are obtained by four probes and compensated fast swept Langmuir probe. The details about these diagnostics are given below.

2.5.1 Langmuir Probe

The Langmuir probe [45-47] is a conventional electric probe for investigating plasma parameters using fundamental techniques. Some of the basic plasma parameters are obtained from ramped (I-V) characteristic of a Langmuir probe. The probe is a small conducting electrode and allows localized measurements in low temperature plasma [48, 59, 68]. The shape of probe can be a sphere, cylinder or planar and the probe dimension should be larger in comparison to the Debye length (λ_D) to minimize the sheath effect for the accurate measurement without making major perturbation in plasma.

2.5.1.1 Determination of Plasma Parameters using Langmuir Probe

The I-V characteristics of Langmuir probe can be obtained by sweeping the bias potential of the probe from negative to positive potential. The circuit diagram [Fig. 2.13(a)] and schematic of I-V characteristic [Fig. 2.13(b)] for a single Langmuir probe are shown. When probe bias potential (ϕ_B) is negative with respect to the plasma potential (ϕ_P), current drawn by the probe from the plasma is positive. Plasma potential is the potential at which the electron collection to the probe at electron thermal speed (C_e) as shown at point 4 in the figure 2.13. The electric field around the probe, confined to the ion sheath will prevent all the energetic electrons from reaching the probe, this causes effectively reducing of the electron current to zero. So, at this point the entire current collected by the probe is due to positive ions. This point is called ion saturation current I_{is} is given by

$$I_{is} = 0.5 n_i e A_p C_s \tag{2.1}$$

where n_i is the ion density at the sheath edge, A_p is collecting area of the probe, e is electron charge and C_s is ion sound speed or Bohm speed. Ion sound speed is the speed at which ions enter into the sheath and is given by $C_s = (kT_e / m_i)^{1/2}$, where T_e is electron temperature, k is Boltzmann constant and m_i is the mass of the ion.

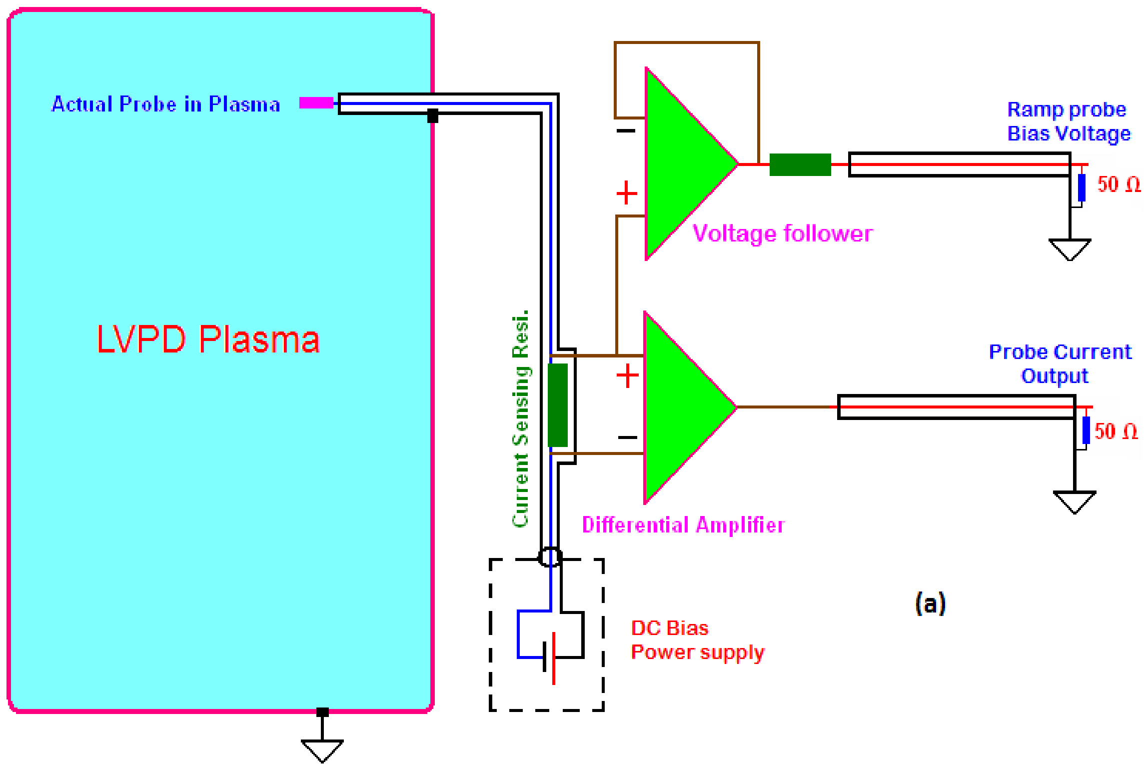

Figure 2.13 (a): The circuit diagram for the Langmuir probe circuit used in LVPD.

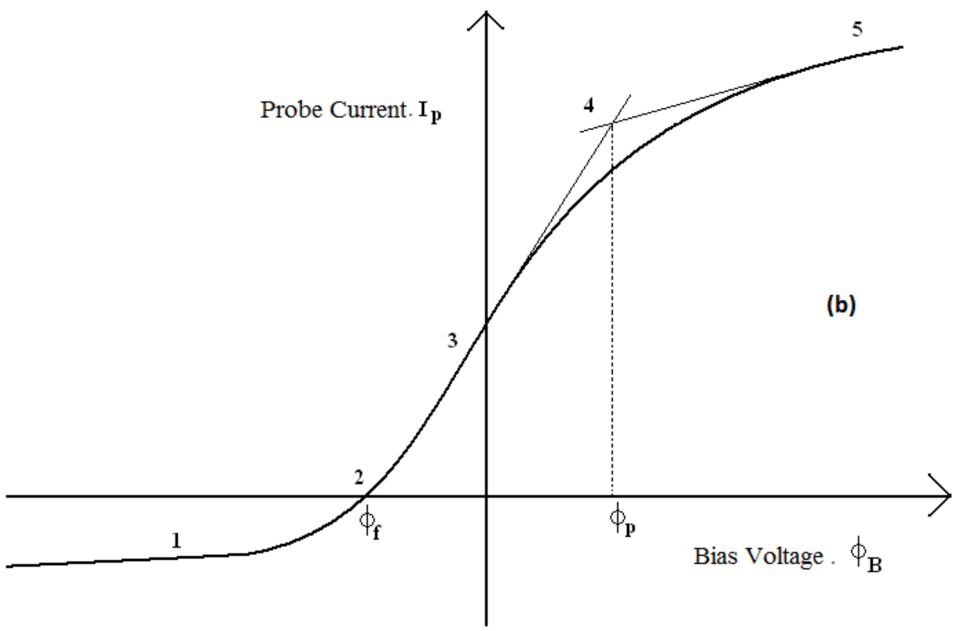

Figure 2.13 (b): The schematic of I-V characteristic for a Langmuir probe.

As the increase in probe bias (probe bias made more positive), attracts number of electrons which overcome the repulsive electric field. So negative (electron) current increases exponentially and overall current collected by the probe decreases. Eventually the electron current equals to $-I_{is}$ and total current becomes zero. This potential is known as floating potential (ϕ_f) represented at point 2 in the figure 2.13(b). The floating potential of the probe is measured across high impedance voltage measuring device.

The electron energy distribution function is associated with the I-V characteristic of the probe by sweeping the bias potential between ion to electron saturation region known as transition region (region between ϕ_f and ϕ_P) used to determine the electron temperature. The electron current at this region can be written as

$$I_e = I_{es} \exp\left(e\phi_B - e\phi_P\right) / k_B T_e \tag{2.2}$$

Here, $I_{es} = 0.25 n_e e A_P C_e$ is the electron saturation current. The inverse of the slope of the steep portion (between 2 and 4) of the graph between logarithm of the electron current and the potential on the probe will give the electron temperature

$$k_B T_e = \frac{e d\phi_B}{d(\ell n I_e)} \tag{2.3}$$

For the Maxwellian distribution of electron, the plasma temperature can be determined from the difference between plasma potential and floating potential.

$$\phi_P - \phi_f = \frac{1}{2}\left(\frac{k_B T_e}{e}\right) \ell n \left(\frac{2m_i}{\pi m_e}\right) \tag{2.4}$$

In the presence of energetic electrons, above equation cannot be used to determine electron temperature because of negative shifting in floating potential. After obtaining electron temperature and ion saturation current from logarithmic graph of I-V characteristic, plasma density can be calculated using equation (2.1). In our experiment, we have installed cylindrical Langmuir probe made of Tungsten wire (diameter~1mm and length~ 5mm) across the ambient magnetic field such that collecting surface area is normal to the magnetic field. Thus the effect of magnetic field is avoided in our measurements.

2.5.1.2 Determination of Electron Temperature Fluctuations

In the steady state plasma, temperature fluctuations can be obtained either using a single Langmuir probe swept with ramp voltage or using the triple probe method. In the novel way, we have obtained temperature fluctuations directly from the time series obtained for electron currents (I_{e1}, I_{e2}) and ion current (I_{s1}, I_{s2}) using a closely separated four-probe array of Langmuir probes. The probes are biased at voltage ϕ_1 and ϕ_2 for current measurements, both these potentials lies between plasma potential, ϕ_p and the floating potential ϕ_f and the ion saturation currents are measured by the other two probes, biased at fixed negative potential(-80V). The electron currents I_{e1} and I_{e2} are calculated by using the expression given below, $I_{p1} = I_{e1} + I_{s1}$ and $I_{p2} = I_{e2} + I_{s2}$, where I_{e1} and I_{e2} are defined as follows.

$$I_{e1} = I_{eo} \exp\left[\frac{-e(\phi_1 - \phi_p)}{kT_e}\right] \quad \text{and} \quad I_{e2} = I_{eo} \exp\left[\frac{-e(\phi_2 - \phi_p)}{kT_e}\right]$$

The ratio between I_{e1} and I_{e2} obtained using the above expressions gives the time series for the electron temperature as mentioned below.

$$kT_e = \frac{e(\phi_2 - \phi_1)}{\ln(I_{e1} / I_{e2})} \tag{2.5}$$

The mean of the obtained time series gives information about the electron temperature and the standard deviation of the time series provides the value of fluctuation in electron temperature. This method has precise advantages over the fast swept method as single Langmuir probe when used in sweeping mode can give an erroneous signal because of capacitive and hysteresis effects. We have made a validation of this technique by making measurements directly in the plasma and have shown distinctly that probe does not show any temperature fluctuations where they are not expected because of the prevailing non-ETG conditions. This method is used in ETG experiments for the measurements of temperature fluctuations. This has one more advantage over the fast ramped probe as this has a simple procedure of analysing the probe data for the estimation of temperature fluctuations. But one still needs a fast probe while measuring the electron temperature. To meet the purpose, we have also developed a cable compensated fast Langmuir probe.

2.5.2 Magnetic Probe

The detection of magnetic fluctuations in LVPD is made by using a bi-filar, single layered B-dot probe (N=30, diameter=10 mm and length=10 mm). The output voltage (V_{ind}), of the probe is given by

$$\oint_c \vec{E}.d\vec{l} = -\frac{d}{dt}\int_A \vec{B}.d\vec{A} \tag{2.6}$$

$$V_{ind} = -NA\dot{B} \tag{2.7}$$

Equation (2.7) implies that V_{ind} depends linearly on the number of turns (N), the coil area (A) and the time derivative of the fluctuating magnetic field B. If the time dependency of B is harmonic, the induced voltage would be

$$V_{ind}(\omega) = -NAB_o\omega\cos(\omega t) \tag{2.8}$$

It scales linearly with the frequency. In order to gain high sensitivity, the number of windings and the area can be chosen in such a way so that a minimum perturbation is produced in plasma.

2.5.2.1 Design of Magnetic Probe

The B-dot probe can be designed either in a single axis or 3-axis as per requirement of magnetic field fluctuations study [59]. It picks up very weak magnetic field fluctuations in the form of electro motive force generated across its windings. The coil is wound in such a way that it strongly attenuates the common mode electrostatic pickups which otherwise tend to interfere with the magnetic signals. The schematic of the magnetic probe is shown in figure 2.14.

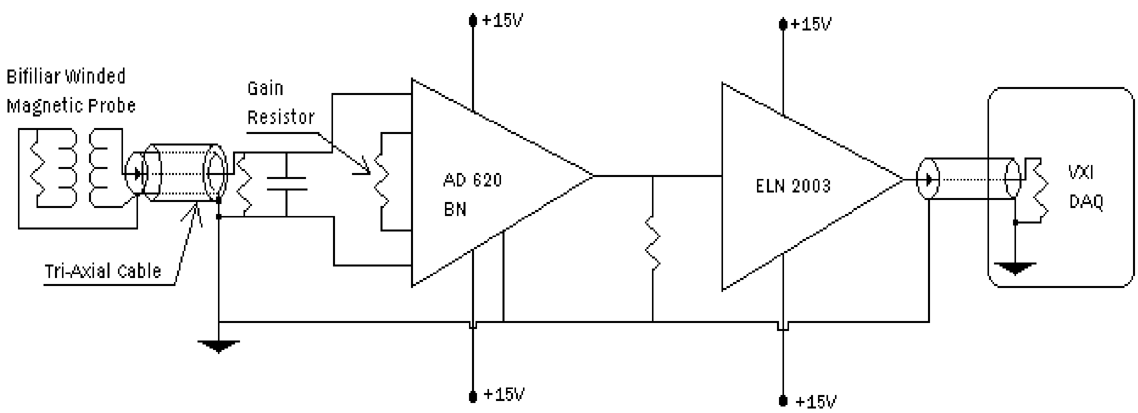

Figure 2.14: The schematic of the B-dot probe circuitry.

The probe contains a bifilar winding made on a ceramic bobbin (diameter=10 mm, length=10 mm). An enamelled copper wire of (diameter =0.10 mm) is used for winding. As shown in figure 2.15, two wires A – A' and B – B' are interlaced and wound together from one end of the bobbin to the other end. This ensures that same magnetic flux lines are intercepted by both the coils yielding exactly equal signal for any given condition or orientation. A transmission line with characteristic impedance of 50 Ω is used to take the signal to the data acquisition. The probe is provided with a cover made up of high temperature, vacuum compatible kapton tape for providing insulation from plasma. A tri-axial cable is used for the probe to avoid plasma charging of the cable carrying the probe signal.

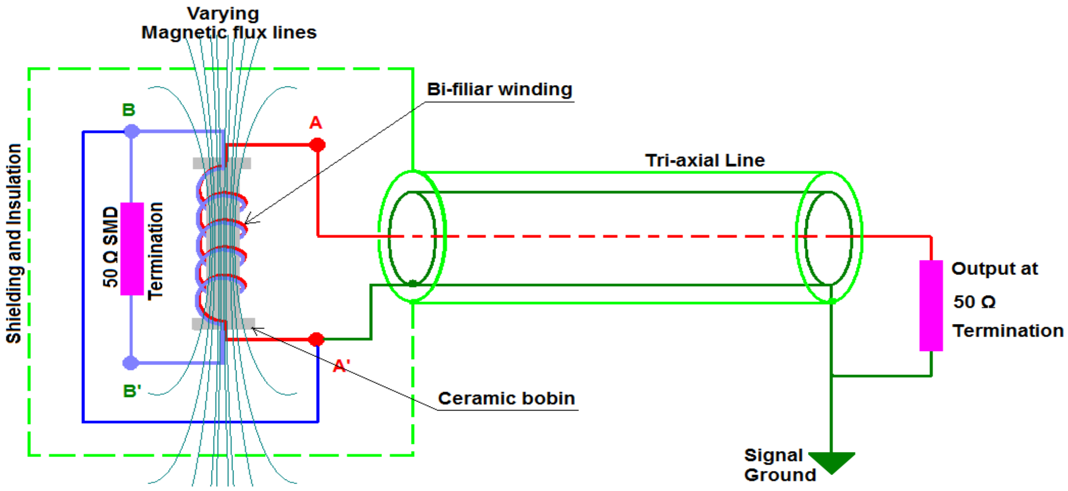

Figure 2.15: Design of centre tapped coil based magnetic probe.

2.5.2.2 Calibration and Frequency Response of the Magnetic Probe

The probe is calibrated for its frequency response. As can be seen from equation (2.8), the output voltage from the probe is the function of frequency, therefore we calibrated it for the frequency spectrum between 10 kHz to 10 MHz. For this purpose, we have made use of a Helmholtz coil (radius = 85 mm, no. of turns = 1) for producing a uniform magnetic field.

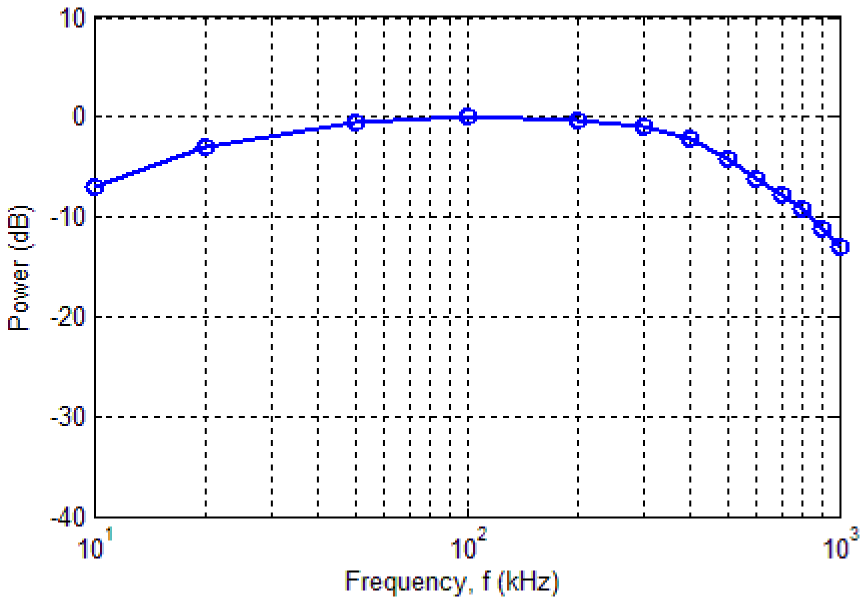

Figure 2.16: The frequency response curve of the B-dot probe.

In this method, a constant current is fed to the Helmholtz coil at different frequencies and therefore a constant magnetic field is produced at the centre of the coil. The output signal of the pick-up coil is normalized with the injected current and input frequency. The frequency response curve of magnetic probe is shown in figure 2.16. The profile indicates that probe response is reasonably good for the frequency range between 10-500 kHz.

2.5.3 Emissive Probe

An emissive probe [58, 69-72] is used to measure the plasma potential. An emissive probe is essentially a hot tungsten wire inserted into the plasma to measure the floating potential and plasma potential. Usually three methods are used for measurement of plasma potential but commonly zero current bias method [58] is used for our experiment. In this method, the floating potential of emissive probes tends to saturate as probe temperature is increased and saturated potential is interpreted as plasma potential. The schematic diagram of the emissive probe used is shown in figure 2.17.

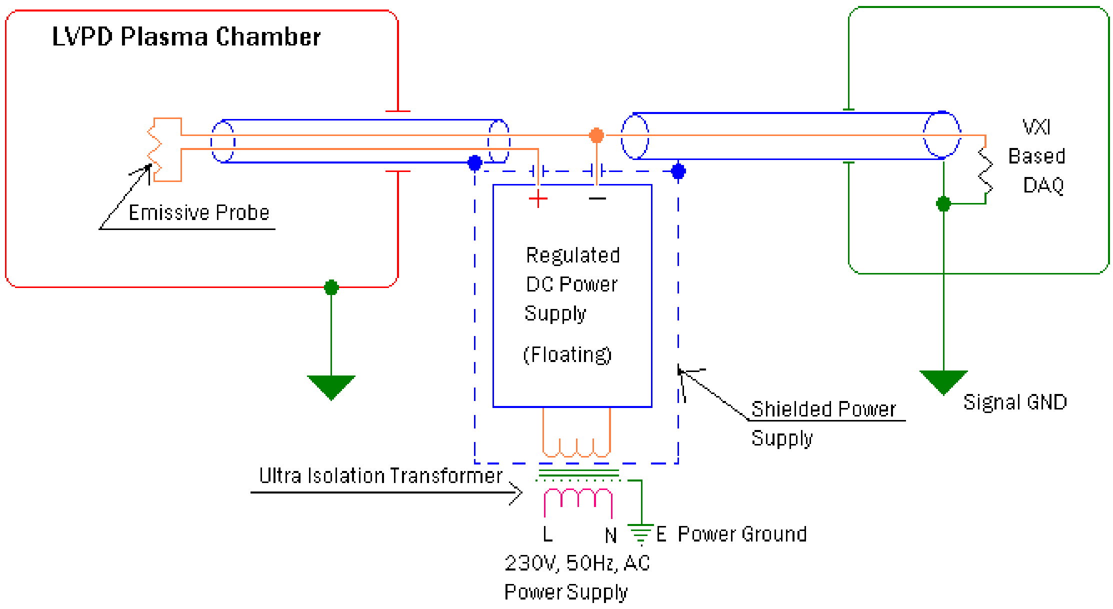

Figure 2.17: The emissive probe circuitry used in LVPD for the measurement of plasma potential.

The emissive probe used in LVPD is made up of a tungsten wire (diameter=0.1 mm and length=10mm) shaped in a semi-circle, where the two ends are inserted through two holes in a cylinder of the ceramic mould with a plug in arrangement for electrical connections. The probe bias cable is terminated to other ceramic mould mounted to the probe shaft end. Electrical connections within ceramic guides along with replaceable tungsten tip are taken care by using gold plated connectors. The emissive probe is heated sufficiently by a floating power supply of rating 5A/ 30V with respect to the plasma potential to allow thermionic emission of electrons. The floating potential measured by the emissive probe increases and finally the saturated value of it gives the plasma potential. We carried out measurements using this probe for ETG experiments.

2.6 Data Acquisition and Control System

We have a VXI based data acquisition system [73] wherein the Chassis and slot “0” controller are from National Instruments and digitizers are from Tektronix. There are four Tektronix make TVS641A Digitizer modules. Each module has four fast analog channels with a total capacity of simultaneous acquiring 16 channels up to 30 k record length on each channel. Digitizers possess analog bandwidth up to 250 MHz and up to 1 GHz sampling rate best even for single shot events. The auto advance acquisition mode of this module offers the additional advantage of scaling down the time interval between consecutive pulses and also offers flexibility over triggers, record length, gain, and sampling rate. The VXI mainframe provides powers, back plane and cooling for resident module. All the VXI data acquisition modules and controller module share the single VXI bus. All these modules are controlled by the MXI slot "0" controller and reside on a PCI slot of a standard Server PC with Windows 2000 Professional operating system programmed in C language. This computer controls the whole VXI system. Our VXI data acquisition modules are message based because the modules have their own command processing time. The effective transfer rate is 500 Kbytes/s irrespective of the operating system. All the signal conditioned data are stored in Server PC and retrieved from data based by network connection to other computer for analysis purpose.

2.7 Electronically Compensated Langmuir Probe

As discussed in section 2.5.1, Langmuir probes are used in experimental plasma devices to measure several plasma parameters and their fluctuations. A probe biased at specific voltage and the floating probes are utilized to measure fluctuations in the plasma density and floating potential respectively. However, measuring electron temperature or its fluctuation requires probe to be rapidly swept over a wide voltage range such that capacitive current of signal due to cable charging does not contaminate measurements. This assumes significance in our case because of the large diameter of the device. For high sweep frequencies, capacitive currents become several tens of mA for cable length of 10m. This leads to error not only in the measurement of current collected by the probe but also to the hysteresis during ramp up and down of the bias voltage. Amount of hysteresis is shown to decrease with the increase of the ramp period. This phenomenon affects the interpretation of the results [74-76]. Thus collected probe current from the plasma can be measured only when cable-charging current is subtracted from the total probe current. Although L. Giannone et al. [77] have demonstrated a technique for subtracting capacitive current from the probe current. In this technique, the cable charging current is measured from another dummy Langmuir probe, which is not exposed to the plasma. This probe has the same cable length and is biased by the voltage ramp derived from the same generator but isolated from each other. A difference circuit results in the measure of the probe current. However, the demonstrated technique still leaves a residue of 5 mA of capacitive current. The residue was reduced to 3 mA in the works of Hidalgo et al. [74]. It is clear that such compensated probes would not be suitable for experiments where ion saturation current of Langmuir probe needs to be kept of the order of hundreds of micro-amperes.

In our experimental observation, we found that while electronic differencing circuit is good enough for low frequency sweeps (≤10 kHz), magnetic difference circuit yields compensation to the level of residual capacitive current of not more than 20μA for a cable length of 11.5 m for sweep frequency at 100 kHz [see Figs. 2.18(a-b)] [60]. The recipe is in balancing out the last pF. This circuit is made up of ferrite core transformer and is referred as magnetic compensation scheme. We have adopted the electronic compensation scheme for DC to ~10 kHz sweep periods and a magnetic compensation scheme (using Ferrite core based differential transformer) for sweep frequencies ranging between 10 kHz ≤ f ≤ 3 MHz.

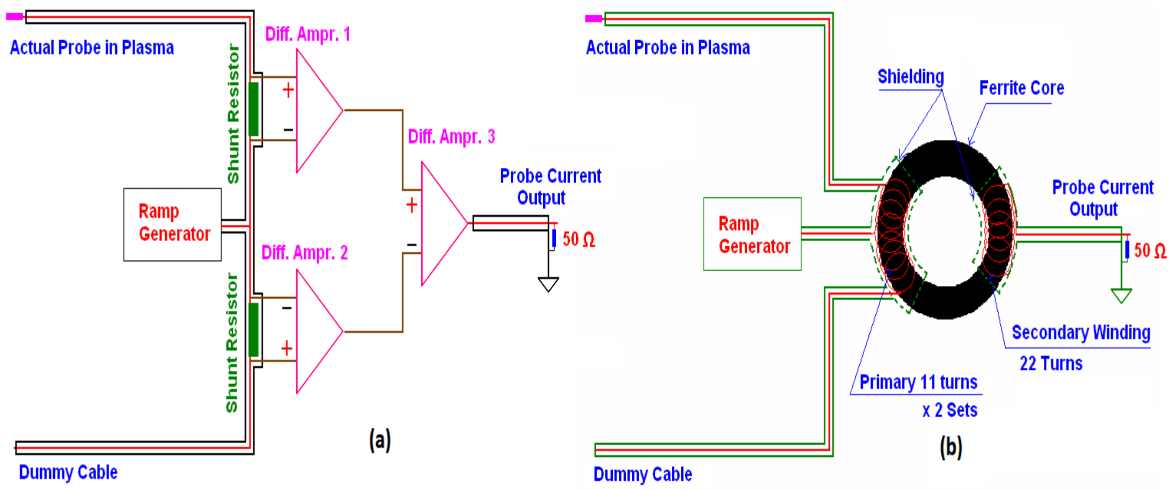

Figure 2.18: Schematic showing cable compensation schemes used for (a) electronic compensation scheme using IC LF356 and (b) magnetic compensation scheme using ferrite core transformer design.

2.7.1 Probe Compensation Schemes

A comparison of semiconductor OPAMP ICs based electronic subtraction scheme with magnetic subtraction schemes for compensation is made in this section. The electronic compensation scheme [Fig. 2.18(a)] makes use of a differential amplifier (IC LF356) with flat wide bandwidth frequency response from DC to ~ 3 MHz with gain bandwidth of 5 MHz. The response of an uncompensated probe when it is immersed in the plasma is shown in figure 2.19. The figure 2.19(c-f) can be interpreted that plasma is exhibiting hysteresis behavior whereas figure 2.20(c-f) shows hysteresis disappears due to cable compensation of capacitive current.

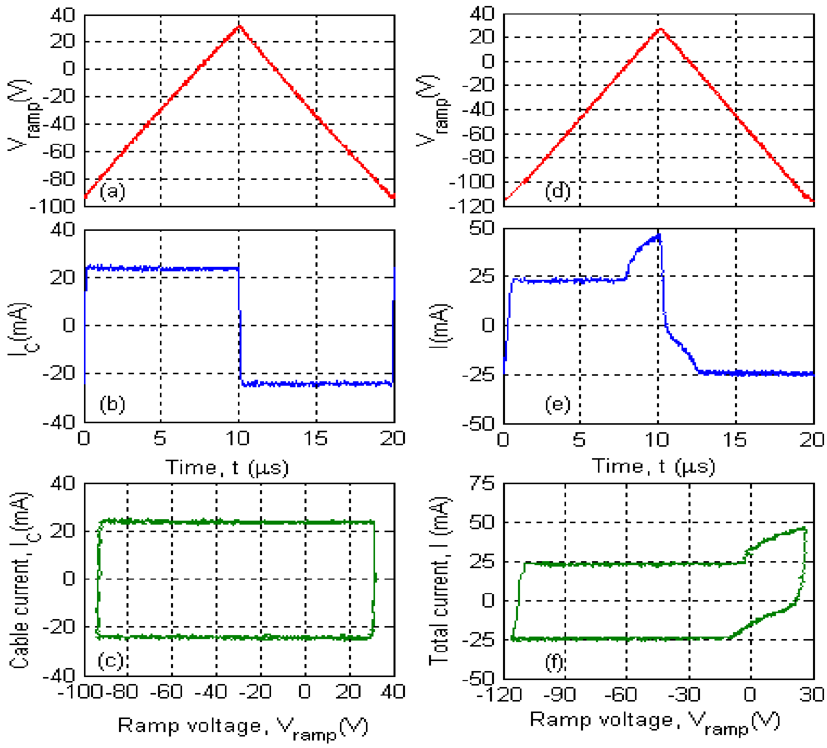

Figure 2.19: The measurement of cable charging for sweep frequency, f~50 kHz for uncompensated cable in vacuum and plasma is shown in (a-c) and (d-f) respectively. It clearly demonstrates that the hysteresis exhibited by the cable charging could have been attributed to the plasma.

In the experimental procedure, a common ramp bias is applied to both the Langmuir probes, one exposed to plasma and other unexposed so called as dummy probe [Fig. 2.20(a)]. Both the probes are having equal cable lengths. The calibrated shunt resistors of 50 Ω are used to record the current by making use of two differential amplifiers 1 and 2 and their outputs are inputted to a third differential amplifier. It is observed that the output from the third amplifier becomes zero when neither of the Langmuir probes is exposed to the plasma and cable capacitances are perfectly balanced [Fig. 2.20(c)]. Measured Langmuir probe current when it is not compensated is as shown in figure 2.20(b). In this case the dummy probe is not used.

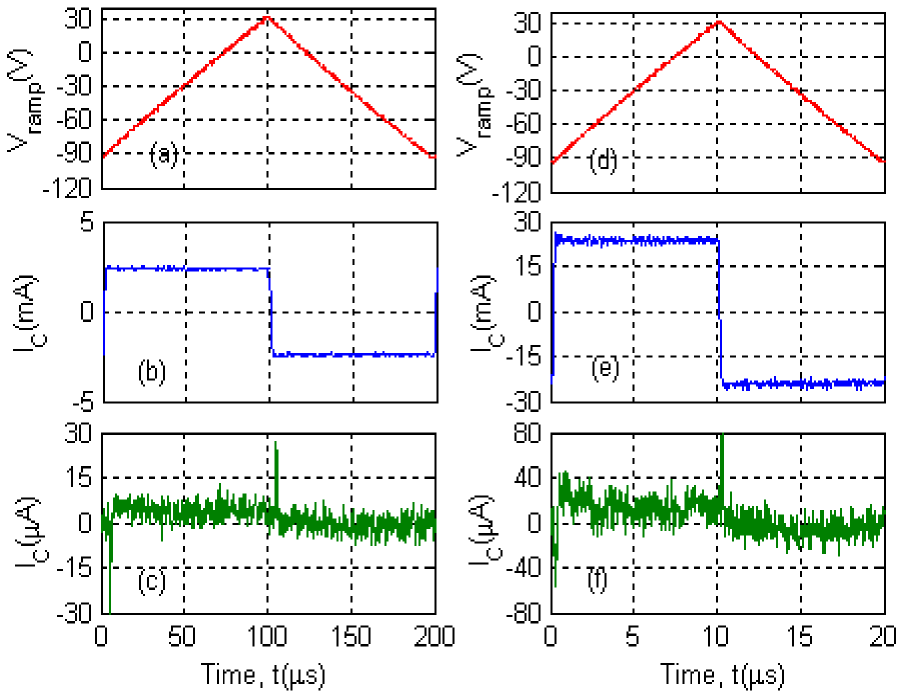

Figure 2.20: A demonstration of the effectiveness of the cable compensation in eliminating the cable charging effect when a long cable ~ 11.5 m is used. The sweep frequencies used for electronic compensation and magnetic compensation schemes are 5 kHz and 50 kHz respectively. The responses for the applied ramps show that a significant improvement in the sensitivity is achieved by eliminating the undesired cable charging currents.

After balancing out the cable charging current, the diagnostic Langmuir probe is exposed to the plasma. Figure 2.21(f) shows that the balancing can be adjusted to last pF which contributes about 20μA. The choice of signal connection hardware is important for balancing as can be seen in figure 2.22. Its significance can be envisaged from the fact that any component in the transmission line circuitry has its signature on the measured current. The current measurement for triangular bias voltage of 100$V_{pk\text{-}pk}$ at ramp frequency ~100 KHz for different cable lengths of 25, 50, 75 and 100 cm respectively is carried out to exhibit the same. The transmission line comprises of cable of RG 58C/U make along with BNC female, ‘I’ and ‘T’ connectors, all having characteristic impedance of 50 Ω. In the present figure emphasis is also made to show that capacitive switching current signature obtained from the smallest transmission line elements cannot be neglected for making such measurements which otherwise has insignificant distributed capacitance.

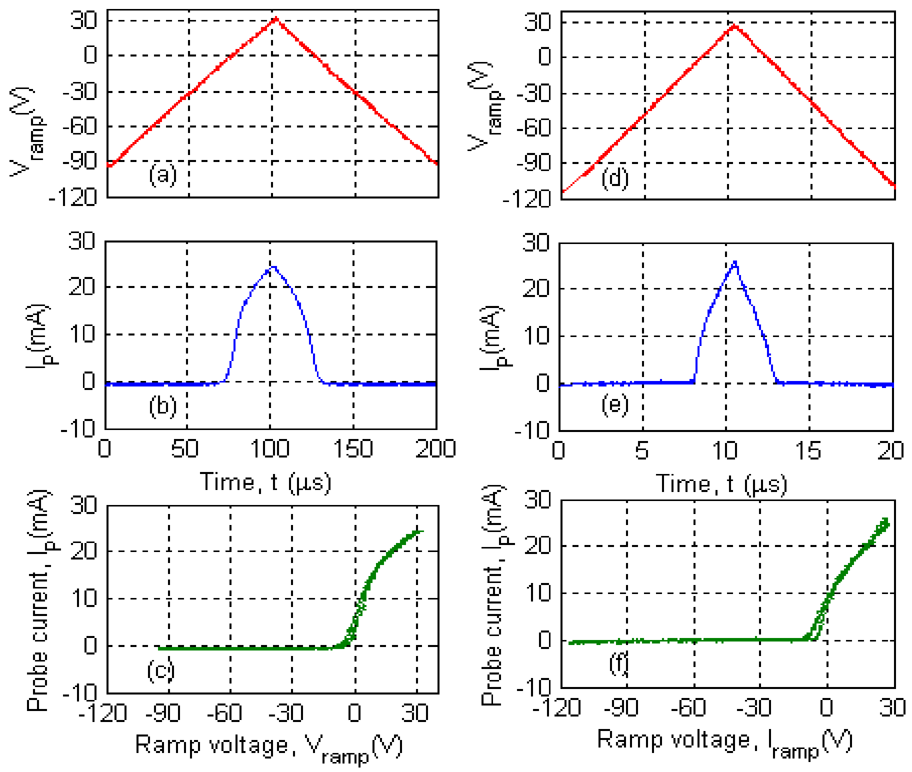

Figure 2.21: Response of probe is shown in figure (a-c) and (d-f) respectively for both electronic and magnetic compensation schemes when used in steady state of plasma produced.

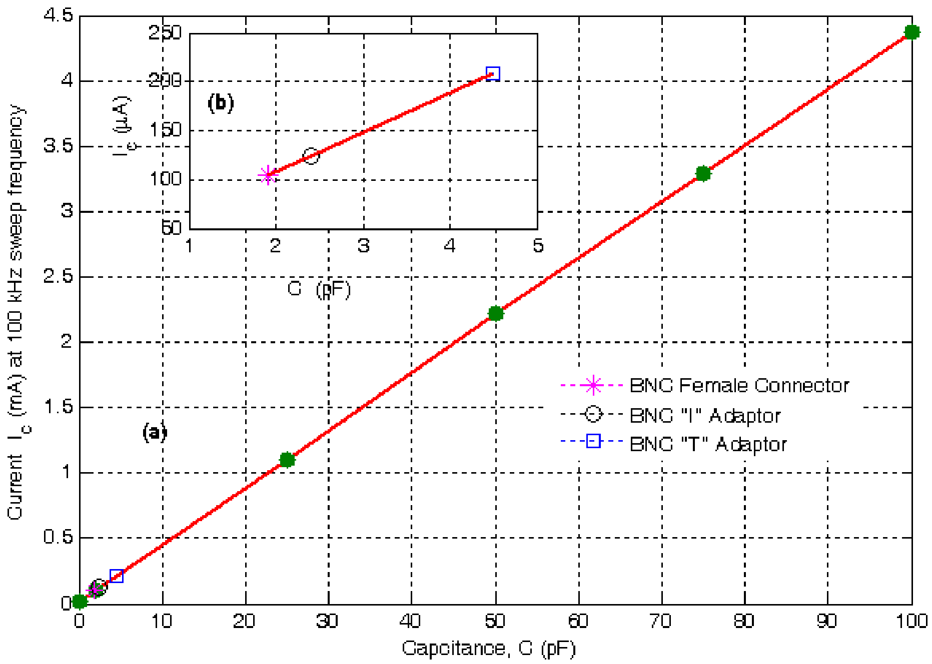

Figure 2.22: Residual capacitive current amplitude for (a) cable capacitance values □100pf to a triangular sweep frequency of 100 KHz at 100 Vpk-pk in the main plot, and inset plot (b) shows charging current measured for Z_0=50 Ω BNC female connector, BNC 'I' and BNC 'T' adaptors at same sweep frequency.

The measured probe current is shown in figure 2.21(b). The resultant difference current at the output of amplifier 3 becomes non-zero. This represents the plasma current measured by the Langmuir probe. The frequency response of the measured plasma current for the same plasma parameters as a function of ramp frequency is shown in figure 2.23 It is noted that the power spectra of the measured probe current in plasma is reliable for ramp frequency less than 10 kHz. For frequency greater than 10 kHz, the measured plasma current is not independent of ramp frequency. Further investigations led to that loss in frequency response arises from the effect due to loss of CMRR with the increased ramp frequency. Consequently, an alternative in difference circuit using a vector flux subtraction of magnetic circuits sharing the same magnetic path has been investigated.

The scheme based on magnetic circuits is shown in figure 2.18(b). The magnetic circuit makes use of a high frequency Ferrite core. The common magnetic path of the Ferrite core is linked to the inputs from two Langmuir probes, actual probe and dummy probe, in such a manner that the induced voltage on the third linkage corresponds to the difference in their currents. Hence a differential transformer is built on the Ferrite core.

A circular shaped ring is made from Manganese-Zinc (μ_r = 3450 H/m) Ferrite. The ring has inner and outer diameters of 28, 45 mm and thickness of 11 mm. It has a core inductance of index AL ~ 3570 nH/N^2 where N is the number of turns, effective magnetic path length ~ 11.4 x 10^{-3} m. A center-tapped primary (11 turns each) is wound in the toroidal cross-section of a Ferrite core. Similarly, a secondary is also wound with a total of 22 turns. The primary and secondary windings are magnetically coupled. Separate electrostatic shields are provided to both primary and secondary windings. The ramp voltage is applied at the center of the primary winding while both the measurement cables are connected to the two ends of this winding. When the ramp voltage sweep appears at the two ends connected to the cable without exposing either of the Langmuir probes to the plasma, a current of I_c is injected to the circuits in response to the applied voltage. These charging currents in two cables pass through the half primary windings. They produce an equivalent magnetic flux in response to the changing current, which is in the opposite direction. Since there is an exactly equal and opposite excitation of magnetic field in the core and are linked to the secondary winding, there is no electro motive force (emf) induced in the secondary as the vector sum of both the fluxes cancel out each other as demonstrated in figure 2.20(f). When the Langmuir probe is exposed to the plasma, the probe collects plasma current. It flows through the one primary winding along with the cable charging current. This additional current generates an equivalent magnetic flux due to changing additional current and is detected as an EMF across the secondary winding as seen in figure 2.21(e).

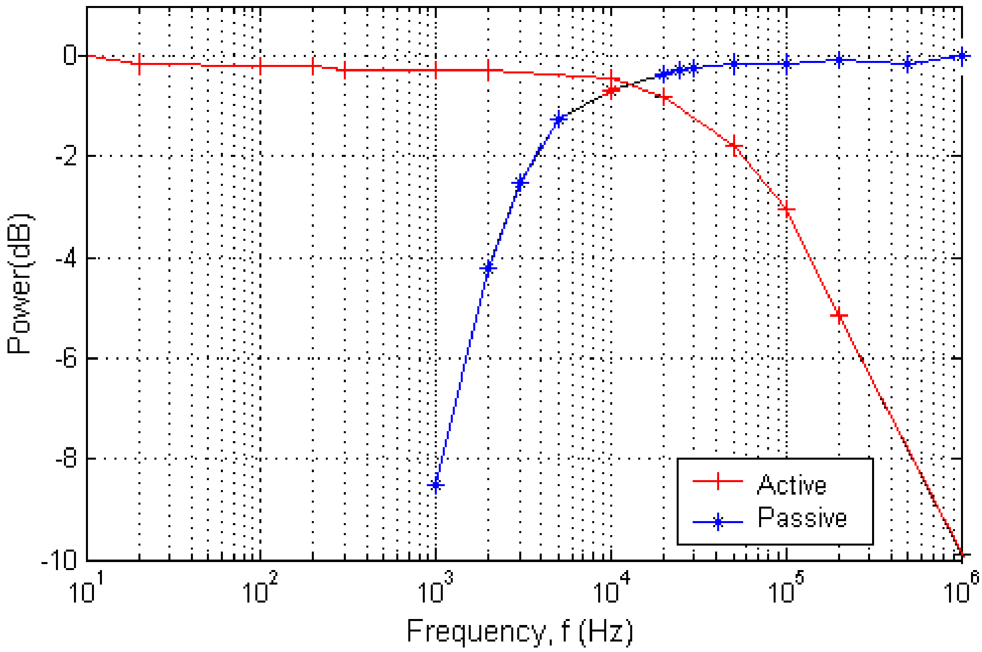

Figure 2.23: An exhibition of the frequency response for both electronic compensation (active) and magnetic compensation (passive) schemes is shown.

The probe current is thus recorded irrespective of the presence of large cable charging current due to the differential action of the Ferrite core despite high frequency. The secondary winding is designed for 50 Ω loads and hence no effect of swept frequencies is seen and this avoids loading of the signal because of the cable lengths. Some of the other important considerations include proper optimization of Ferrite transformers for the primary and secondary turns. Small number of turns makes this transformer to suffer in sensitivity at lower frequencies while larger number of turns limits its high frequency response. In the latter situation, coil winding becomes a self-integrator for higher harmonics. Similarly, numbers of turns in secondary winding are also optimized. The choice of ferrite material is made to meet the desired range of frequencies and a suitable cross section is chosen so as to accommodate the linear magnetization flux well below the saturation.

2.7.2 Experimental Observation

The experiments are carried out in LVPD plasma by sweeping the probe cable with a triangular ramp of 150 $V_{(pk\text{-}pk)}$ at frequency of ~ 50 KHz. The cable charging current, $I_{c\ (pk\text{-}pk)}$ is ~ 24 mA. This current is much higher than the ion saturation current and is comparable to the electron current. The corresponding ratios of ion and electron current to cable current are 4.2×10^{-2} and 1 respectively. Such a large dynamic range in current measurement leads to greater errors in the readings of ion saturation current. Ion saturation current is used for both the measurement of plasma density and electron temperature and determination of floating potential suffers a shift depending upon whether cable charging current is in or out of phase the ion saturation current. Thus the hysteresis effect is bound to exist in probe current measurement.

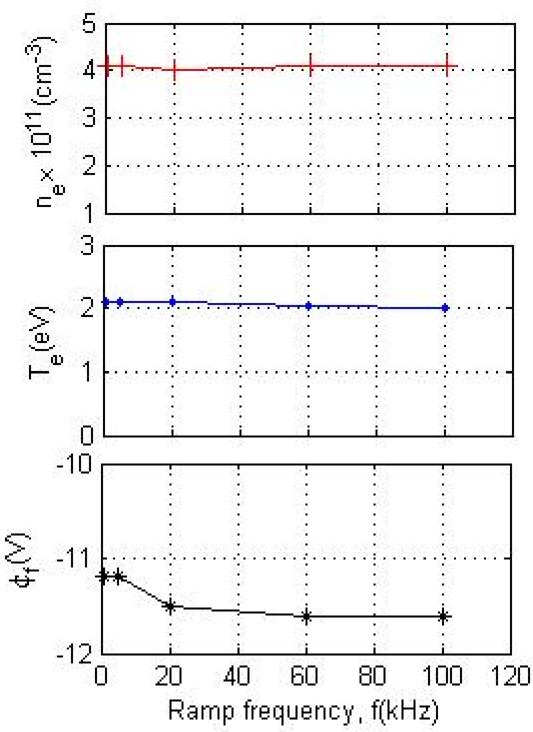

Figure 2.24: Shows the measurements of plasma density, ne, electron temperature, T_e and floating potential, ϕ_f for different frequencies of ramp voltage. The measured parameters exhibit almost constant values even when the probes are swept over a wide range of frequencies.

Figure 2.21(d-e) shows the voltage and current waveforms obtained for swept probe ($\Delta V \sim -100$ to $20\,V$) with sweep frequency of 50 kHz. When the length of cable for transport of signal is as large (11.5 m), hysteresis appears. Figure 2.21(f) is a plot of measured current against the ramped voltage in order to deduce the hysteresis information, which does not exhibit significant amount of hysteresis. The measurement of current also shows that the fast ramped cables exhibit hysteresis even without the plasma discharge as shown in figure 2.19(a-c). Reactance of the cable leads to ramp voltage exhibiting a hysteresis.

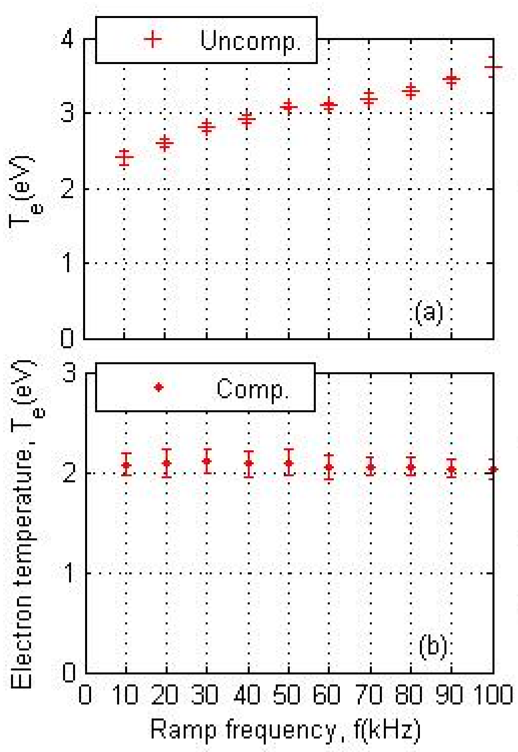

Figure 2.25: The uncompensated and compensated probe measurement of mean electron temperature in the steady state of target plasma is shown in (a-b). The electron temperature obtained using compensated probe exhibits a distinct advantage over uncompensated technique over the entire range of ramped frequencies.

The measurements of plasma density, electron temperature and floating potential at different frequencies of ramp voltage are shown in figure 2.24. The observation suggests that the measured plasma parameters exhibit no variation when the probe is swept over a wide range of frequencies and thus makes these measurements independent of ramp period. It is to be noted here that the temperature measurements become almost free of cable charging and hence have shown an improvement in measurement by 45 %. This measurement becomes extremely important as gradient in electron temperature provides a free energy source to the excited fluctuations. Any measurement error here can lead to major errors in the measurement of fluctuations. We have made an attempt to compare the fluctuation levels obtained by the two techniques [Fig. 2.25]. The probe is swept with a frequency of 40 kHz and the correction in fluctuation level is observed by 30 % as can be seen in figure 2.25(c-d). It may be noted that this technique provides a suitable facility to enable us to measure both the plasma parameters and their ac counter parts with good accuracy. This allows us to make measurements till sweep period of $\Delta t \sim 10\mu s$.

2.8 Performance of Electron Energy Filter

In this section, the performance of EEF in LVPD plasma is discussed. The EEF is utilized to remove primary energizing and non-thermal electrons from the plasma and allows control over the scale length of radial gradient of electron temperature and plasma density in the target plasma for ETG studies [78]. The detail experimental results regarding its application are discussed below.

2.8.1 Experimental Results

The experimental results are presented in two parts. The results of first subsection are focussed on scavenging of energetic electrons through measurements of floating potential profiles and I-V characteristics of Langmuir probe with and without EEF. The results associated with control of gradient scale lengths of electron temperature and plasma density for different EEF currents and for different EEF configurations are presented in the second subsection.

2.8.1.1 Floating potential of plasma with and without EEF

To understand the role of EEF, it is important to compare the characteristics of the plasma without EEF with that of the plasma when EEF is physically embedded and energized. Since emphasis is on the removal of energetic electrons, we have chosen the parameter of floating potential as an indicator of energetic electrons. Temporal profiles [Fig. 2.26(b-c)] of floating potential over the discharge period are measured at different radial positions in the device at half way from the cathode. From these traces, peak and steady state values of floating potential are noted and plotted in figure 2.27(a-b). It can be seen that the peak floating potential during the formation of discharge current profile undergoes a sharp reduction and its value reduces from- 45V to - 30V at the axis of LVPD when EEF is energized. The reduction in the floating potential considerably decreases in the plasma near the edge compared to its value in the core plasma. However, as the steady state in the discharge current is achieved, the decrease in floating potential is nearly the same at all the radial location with a marginally more decrease at locations away from the axis and from the plasma edge. We have assessed the performance of the EEF by response of the plasma produced in LVPD to it. Response of the plasma is characterised by the changes in the plasma parameters (n_e, T_e, ϕ_f) brought about by the presence of the EEF in LVPD with and without current injected into it. These parameters are measured in all regions, namely source, target and filter for the same discharge parameters (V_d ~ 70V, I_d ~ 200A). These measurements are benchmarked against the characteristics of the plasma when EEF is not physically embedded in LVPD. Figure 2.26(a) shows Langmuir probe traces when EEF is not embedded (trace 1) in LVPD whereas, Langmuir probe traces (2 and 3) are shown for source and target regions after EEF is embedded and energized. These are taken at a position (z = 30 cm) from EEF where influence of its magnetic field is not as strong as it is within the filter plasma. This implies that the EEF has not affected plasma formation in the source region. This is indicated by the similarity of Langmuir probe trace in the source region to the same when EEF was not embedded in LVPD.

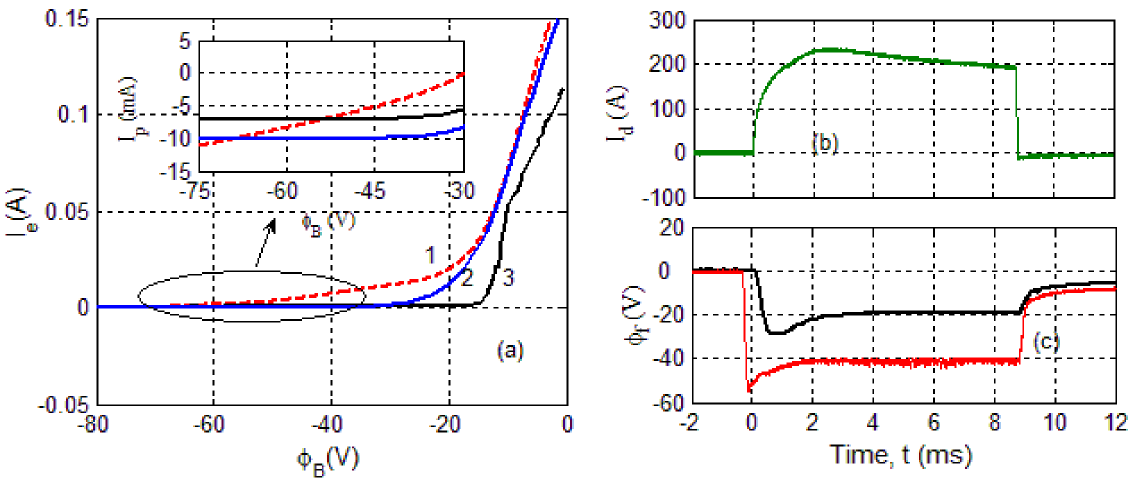

Figure 2.26: Shows in (a) the I-V characteristics obtained by fast swept Langmuir probe, after subtracting ion-saturation current and the curve is marked as 1 for plasma when EEF is not

embedded physically and as 2 for the source plasma and 3 for the target plasma when it is physically embedded and energized. The inset shows the zoomed view of ion saturation currents for the three cases. In figure (c), time profile of floating potential is shown for plasma without (continuous) and with EEF embedded and energized (dashed) during the plasma discharge period (figure b). Note that the peak potential, an indicator of energetic electrons is considerably reduced. Steady state value also shows a significant reduction thus exhibiting a clear demonstration of scavenging of energetic electrons.

On the other hand Langmuir probe trace in the target region is different. Main deviation appears in the electron collection region. It is seen that the long tails corresponding to the presence of non-thermal and primary ionizing electrons are absent in this trace (trace 3). The value of ion-saturation current is reduced (inset) in the source region with respect to the same when EEF is not embedded in LVPD. Ion saturation current is an order of magnitude smaller in the target region in comparison to the same in the source region.

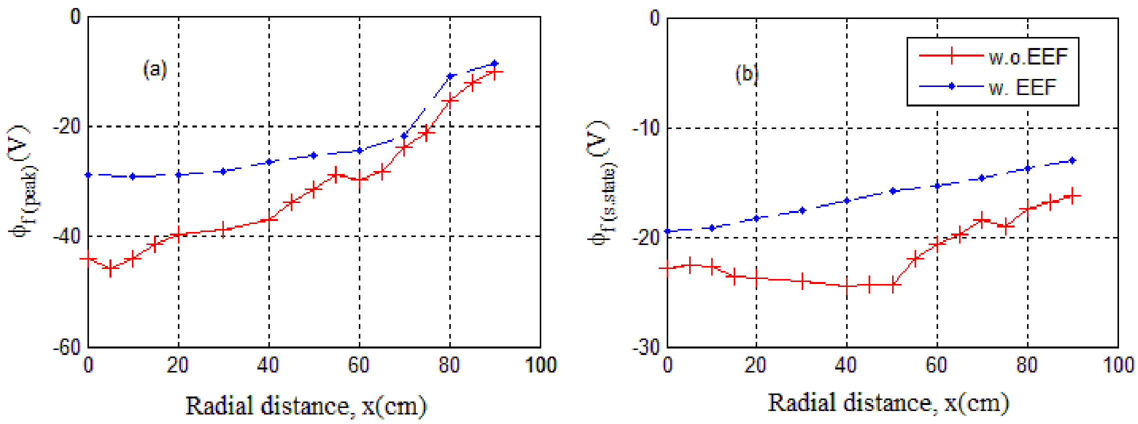

Figure 2.27: Shows the radial profile of floating potential for its (a) peak and (b) steady state values for two different cases when EEF is embedded and when it is not. A distinct reduction in the potential values over the entire plasma cross-section is observed. This confirms that the presence of embedded, energized EEF reduces the energetic population over the entire plasma volume.

Figure 2.26(b-c) shows the temporal evolution of floating potential, measured by a Langmuir probe in target plasma over the discharge period. It can be seen that highly energetic electrons, ~ 50 eV for the plasma without EEF and ~ 30 eV with EEF, are present in the plasma during its formation. During the flat top of the discharge pulse, EEF causes floating potential to drop by 25 volts. This demonstrates scavenging of energetic electrons by EEF. We have also carried out another check by making a comparison between the radial profile of electron temperature obtained by using a fast swept compensated Langmuir probe and the temperature obtained by using the expression, $\phi_p = \phi_f + 5.4T_e$, where ϕ_p and ϕ_f are the plasma and floating potential respectively [31].

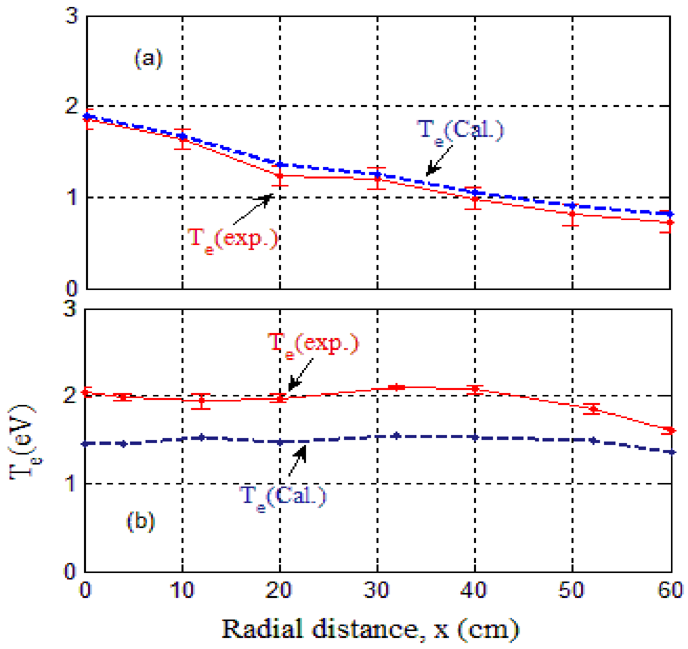

Figure 2.28: Shows a comparison made between the electron temperature values obtained in the plasma of target region in LVPD by the swept Langmuir probe and the calculated electron temperature using the expression $\phi_p = \phi_f + 5.4T_e$, where ϕ_f and ϕ_p are the measured floating and plasma potentials. Note a close agreement between the measured value of T_e and that calculated from the expression in (a) where EEF is energized and deviation in (b) where EEF is not energized.

The measurements of plasma potential and floating potential are carried out separately using cold Langmuir and hot emissive probes. Figure 2.28(a) corresponds to when EEF is embedded and energized in plasma and figure 2.28(b) correspond to when EEF is not energized. We note a close agreement between two methods of measurement of electron temperature in figure 2.28(a). Figure 2.28(b) shows the electron temperature for LVPD plasma for unenergized EEF as predicted by the potential-temperature equation. The predicted value of electron temperature is not in agreement with the measured value indicating presence of a good fraction of tail electrons. On the other hand, as noted earlier, when EEF is used to scavenge hot electrons, the measured electron temperature in the target plasma is in excellent agreement with the predicted value [Fig. 2.28(a)]. This is another evidence in support of the argument that the energetic electrons are absent in the target plasma.

2.8.1.2 Control of EEF size and excitation current

Figure 2.29(a) represents electron temperature profile with EEF current when all the 19 coils are excited. The excitation current is varied up to 2kA. Electron temperature is measured on the axis of LVPD in the target region. It shows that the electron temperature in the target plasma decreases as excitation current in EEF is increased. The change in the value of electron temperature observed is from 3 eV to ~1.5 eV. For excitation current >1.5 kA, electron temperature in the target plasma is not significantly reduced and attains a saturation value of 1.5 eV.

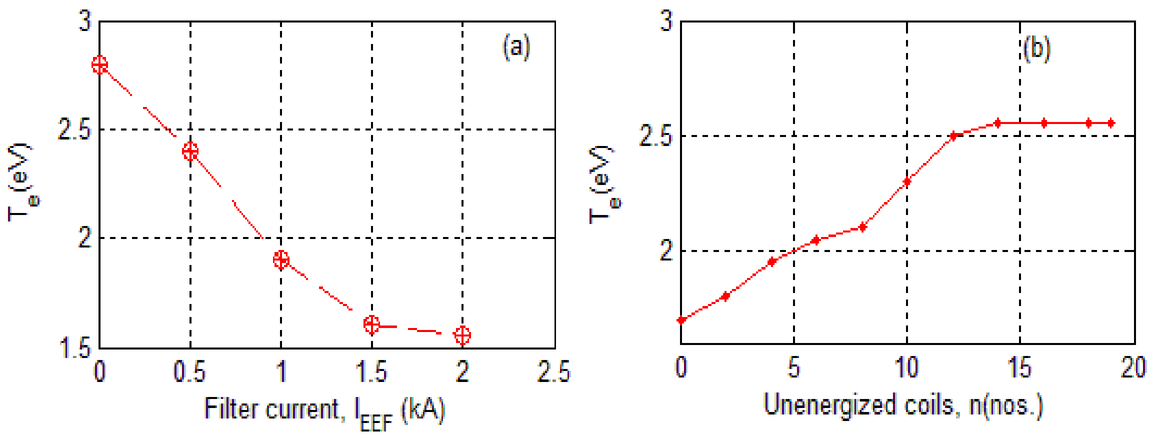

Figure 2.29: Shows the change in (a) electron temperature at x=0, the radial centre of target plasma with the variation in EEF current when all 19 coils are energized. This has also been demonstrated in (b) that electron temperature can be varied in the device if magnetic field can be varied by selectively unenergizing of the EEF coils.

In figure 2.29 (b), we have excited selected coils of EEF. The first point (n=0) refers to providing the current in all the coils and last point (n=19) to zero current in all the coils. In between points are obtained by taking out one coil at a time from both the extreme ends of EEF solenoid from driving current circuit. Thus the performance of EEF is obtained with 10L- 1- 10R coils comprising of 19 coils, where L and R corresponds to the left and right side coils with respect to coil number 1, i.e., the central coil. We note from figure 2.29(b) that electron temperature at the axis of the target plasma can also be varied by the extent of the EEF. However, it may be noted that extent of the EEF also affects the radial variation of electron temperature in the target plasma. Hence variation of current profile across the extent of EEF provides a control on the radial profile of electron temperature in the target plasma. The characterization of source and target plasma of different EEF current is discussed below.

(i) Characterization of source plasma:

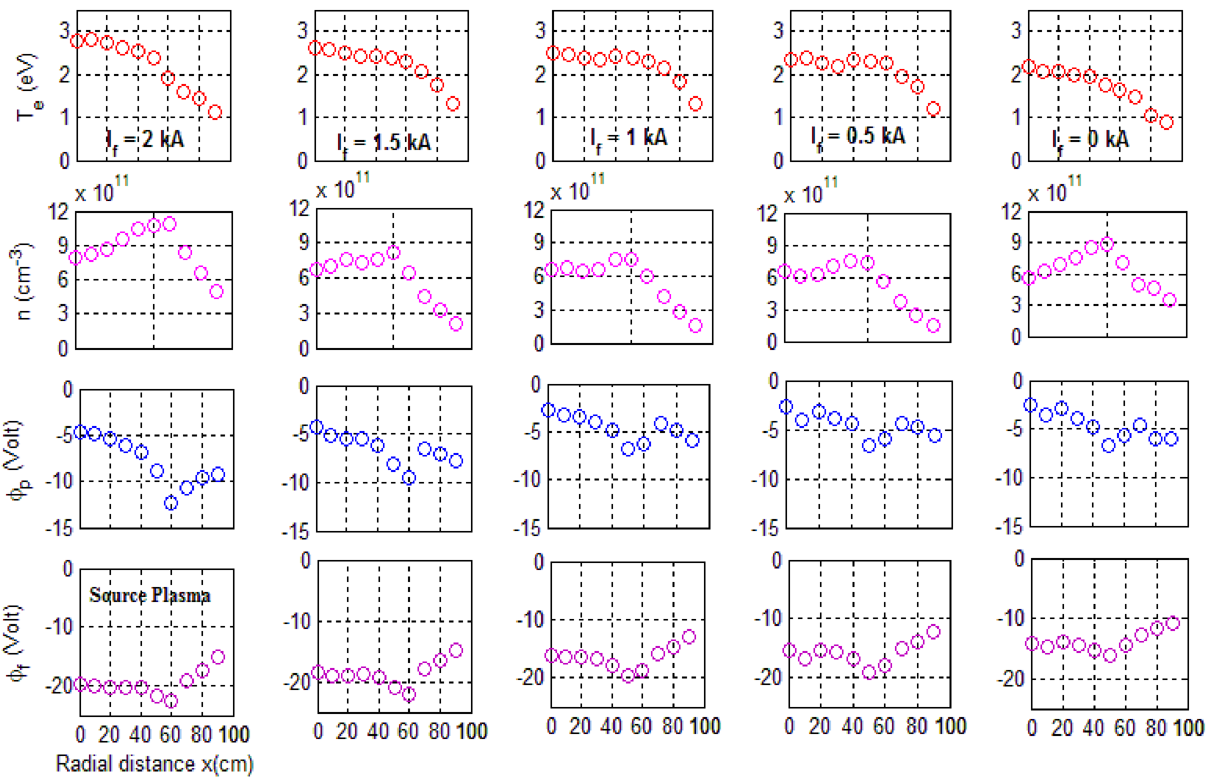

Figure 2.30: Shows the radial profiles of electron temperature, plasma density, floating potential and plasma potential in the source plasma where embedded EEF is energized to different currents. The source plasma distinctly identifies the presence of the electron source when EEF is energized to higher magnetic fields. The temperature profile remains unaltered over a large variation of EEF current and only when current exceeds 1.5 kA, gradient in electron temperature exhibits a noticeable change. The plasma density shows a hollow profile in the core but enhancement at the location of filament.

We have plotted electron temperature, plasma density, plasma potential and floating potential of the source plasma as a function of radial distance in figure 2.30. These measurements are made at 30 cm away from the axis of EEF. It can be seen in figure 2.30, that electron temperature remains largely flat in the central region of the source plasma. Moreover, the electron temperature remains unaffected when the strength of the magnetic field in the EEF is varied by exciting it with the current varying in the range of 0- 2 kA. On the other hand, the EEF magnetic field seems to affect the value of plasma density and its radial profile. This may be due to increased confinement of primary ionizing electrons because of increasing magnetic field of EEF. Hollowness in the plasma density profile is attributed to the fact that the source function of primary ionizing electrons is located at (90cm vertical x 130 cm horizontal) rectangle**.** The floating potential remains nearly constant over the current but its magnitude increase by ~ 3 volts when EEF current varies from 0 to 2kA. A notable dip (increased negative floating potential) is observed to occur at radial location of 65 cm. This corresponds to the position of the filaments on the cathode. Although floating potential remains constant over the central region, the floating potential decreases in the plasma edge. This is seen even in the plasma potential and electron temperature, indicating that a radial electric field is established at the plasma edge.

(ii) Characterization of target plasma and control on gradient scale length:

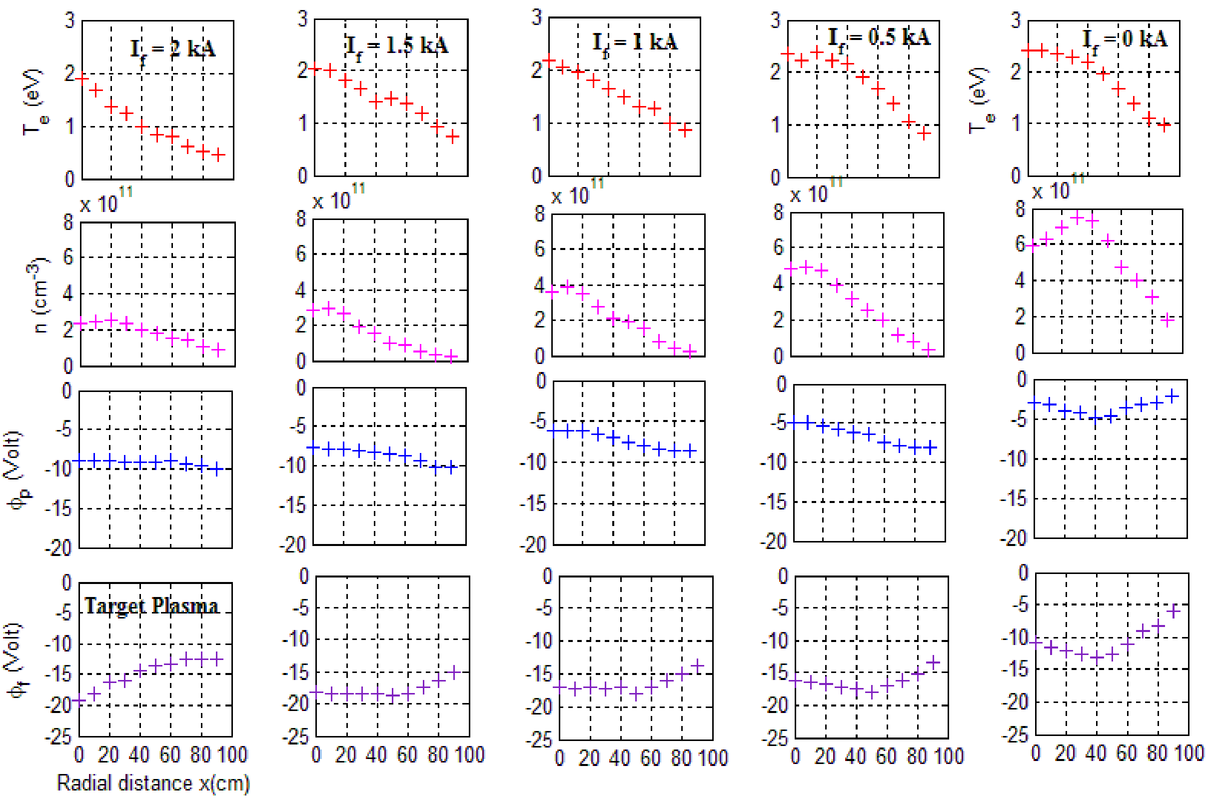

Figure 2.31: Shows the radial profiles of electron temperature, plasma density, floating potential and plasma potential in the target plasma where embedded EEF is energized to different currents. The graded electron temperature profile gradually develops with the increase in EEF current. The density profile shows diminishing effect of energetic electrons as presence of filament location is not visible. The core density plasma profile shows flattening with increasing EEF current.

Figure 2.31 shows that characteristics of the target plasma are at variance with the same for the source. First, we note that the electron temperature does not remain flat in the central region. When EEF is not excited, the electron temperature is constant in the central region. When current in EEF is increased, the region over which electron temperature is flat shrinks and the region over which gradient exists, expands. Finally, at EEF current of 2kA, the whole of the plasma exhibits graded electron temperature. The plasma density is flattened with the increasing magnetic field of EEF unlike the plasma density profile of the source which is hollow. This seems to indicate that primary ionizing electrons are not crossing over to the target region. As discussed earlier, we have attributed hollowness in the profile of plasma density to the rectangular spatial form of the source function of primary ionizing electrons. The appearance of the gradient in electron temperature is correlated with the disappearance of the electric field in the central. This is reflected in the extension of central region over which plasma potential is constant. The gradient in electron temperature is mirror reflected in the floating potential.

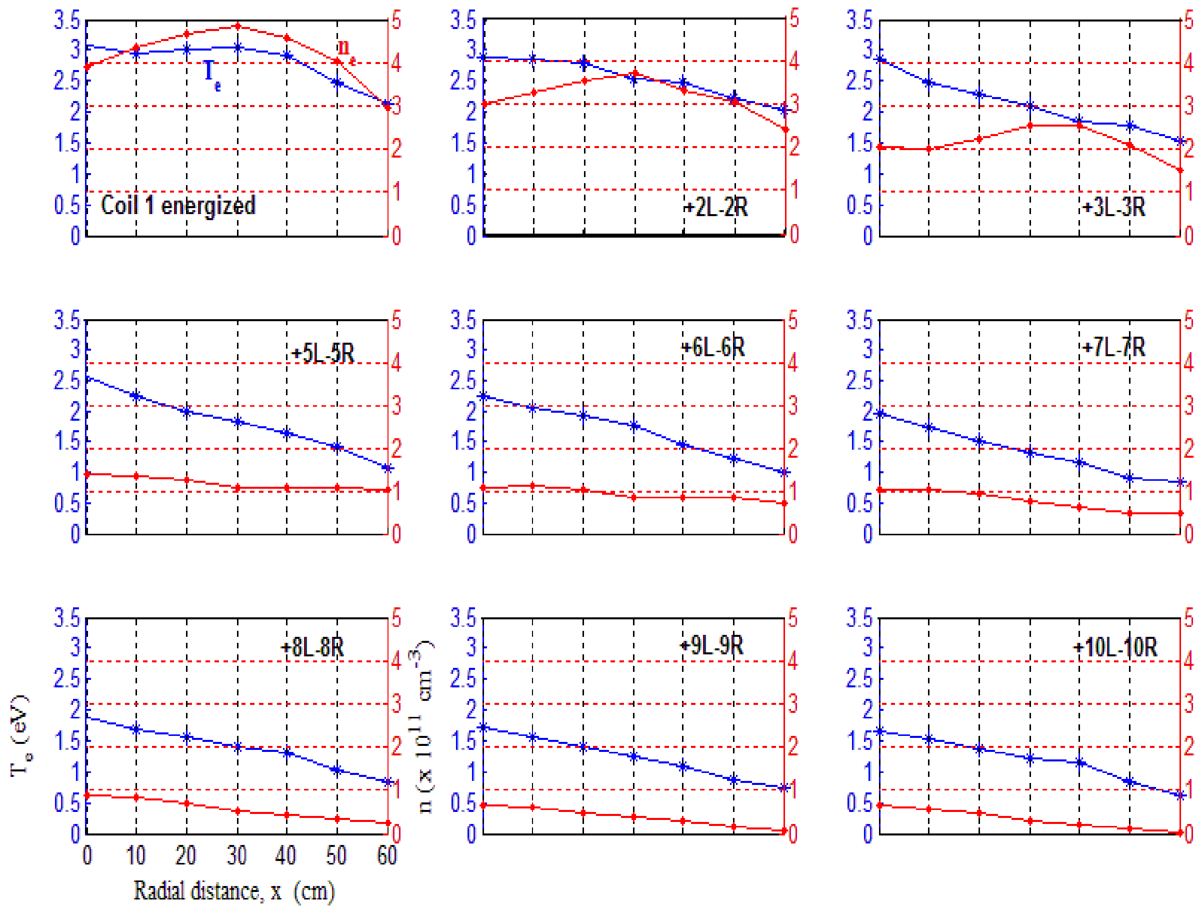

Figure 2.32: Shows the radial profiles of electron temperature and plasma density in target plasma for different configurations for which EEF is energized. The current is kept same for all configurations. Sign '+' means the addition of indicated coils with the previous configuration.

Figure 2.32 shows electron temperature and plasma density profiles in target plasma for different configurations of the EEF. An attempt is made to understand how the plasma profiles and their gradient scale lengths can be correlated with the extent of EEF. The excitation cross-section of the EEF is sequentially increased by adding coils on both sides of the central coil, the coil **1** in the EEF. The variation in radial profiles for electron temperature and plasma density is observed till the cross section includes 7L/7R coils and thereafter profiles remains mostly unaltered. Many configurations of the coils in the EEF solenoid are found suitable for carrying out ETG studies.

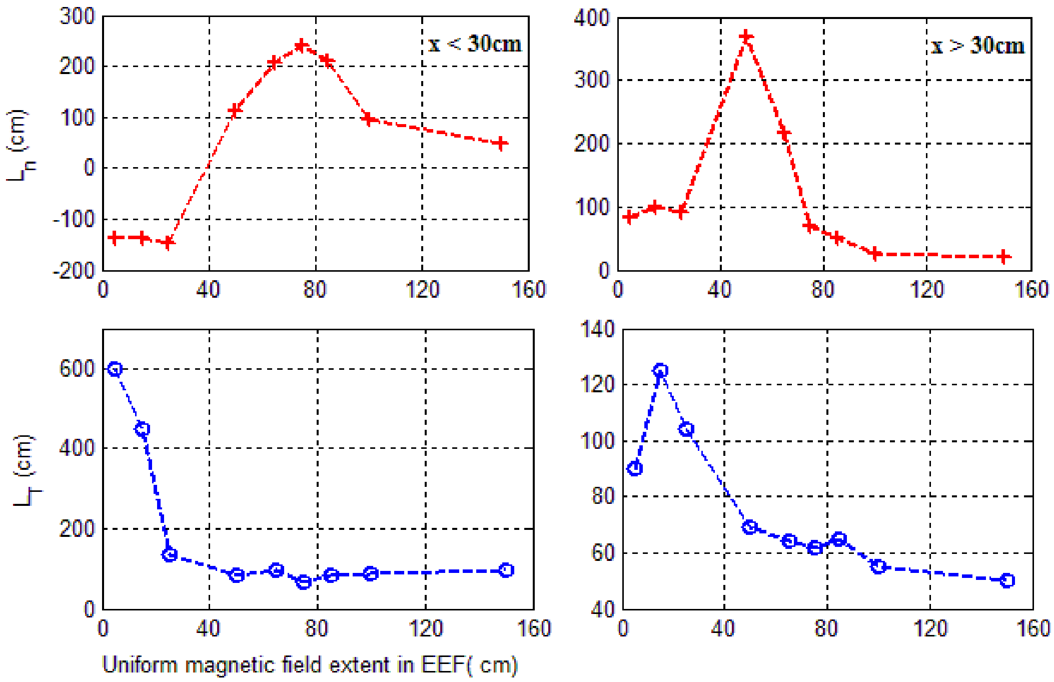

Figure 2.33: Shows the scale length of the gradient in electron temperature and density in the target plasma for the regions x < 30 cm and x > 30 cm with respect to the extent of length of uniform field of EEF. The uniform field extent is expanded over the entire cross-section of EEF along its axis by charging current in 19 coils. The variation in gradient scale length is observed till 7L- 7R coils are charged whereas no change is effected till the whole EEF is charged.

The scale length in the gradients of plasma density (L_n) and electron temperature (L_{Te}) are calculated from the measured radial profiles of density and electron temperature [Fig. 2.32]. In order to state that plasma is hollow for some configuration of EEF, we have calculated L_n and L_{Te} separately for plasma regions with x< 30 cm and x>30 cm respectively. The gradient in plasma density and electron temperature profiles are examined for identifying suitable combination of L_n and L_{Te} for satisfying the condition for excitation of ETG turbulence. The scale lengths are shown in figure 2.33. The temperature gradient scale length, $L_{Te} \sim [(1/T_e)(dT/dx)]^{-1}$ can be effectively varied from 50 to 600 cm by changing parameters (number of coils, current in the coils and positions of coils used in the solenoid) of the EEF. This figure projects several combinations possible for carrying out ETG study in LVPD. Again, not much variation is observed beyond 7L/7R coils. We have observed that the condition for ETG instability to excite, i.e., $\eta_e > 1$, is satisfied within the 1m radial extent of excited EEF. There are various other combinations possible for producing such plasmas and a detailed study for plasma characterization from the perspective of understanding the role of transport in developing such profiles is underway..

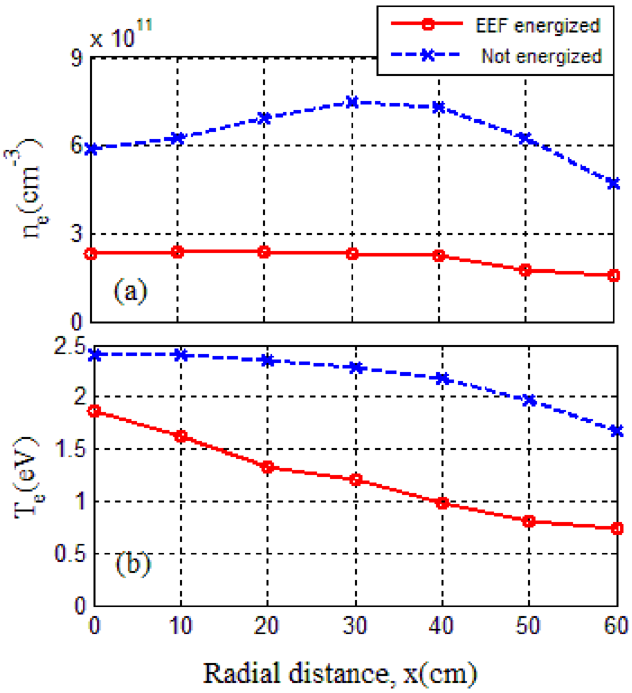

Figure 2.34: Shows the radial profiles of (a) plasma density and (b) electron temperature in the target region of LVPD for the cases, when thirteen coils (7L- 7R) of EEF are energized and when all 19 coils of EEF are not energized.

Out of various combinations of equilibrium profiles of plasma density and electron temperature obtained for different configurations of EEF, the two profiles, shown in figure 2.34, are chosen for the study of ETG turbulence. Figure 2.34(a) has profiles for plasma density and figure 2.34(b) for electron temperature, which are found suitable (when EEF is energized) and not suitable (when EEF is not energized) for the excitation of ETG turbulence. The profiles with activated EEF give values of L_n and L_{Te} such that their ratio, $L_n/L_{Te} > 2/3$. Briefly, two configurations are distinguished by hollow plasma density profile with flat electron temperature and flat density profile with graded electron temperature. ETG was observed for the profiles in figure 2.34(a-b) when EEF is energized but not observed in the case when EEF is not energized [33, 78].

2.8.2 Discussion on collisional diffusion of electrons across EEF magnetic field

For LVPD parameters of $T_e\,(average) \sim 1.0\; eV$, $n_e = 3\times10^{11} cm^{-3}$, the electron- ion collision frequency for cold electrons, $\nu_{ei} = n_i \sigma v_e = 1.3\times10^7 s^{-1}$ and the mean free path for collisions, $\lambda_f^c \sim 3cm$. These electrons travel an average distance ~ 600 cm in EEF and suffer ~ 200 collisions. During the process of collisions**,** perpendicular distance travelled by these electrons is ~ 3 cm and thus are subsequently transported across EEF field. On the other hand, the $23eV$ fast electron suffers collision with neutrals with collision frequency, $\nu_{en} = n_n \sigma v_e = 1.0\times10^6 s^{-1}$ and mean free path, $\lambda_f^h = 200cm$. As the gyro radius, $\rho_{eh} \sim 0.08\; cm$, they suffer effectively 3 collisions and travel only ~ 0.24 cm within EEF. Consequently fast electrons are transported along the axis of EEF and may be getting lost to the wall of LVPD. This explains why electron temperature is reduced in the target plasma and energetic electrons are inhibited from getting transported across this region**.**

2.9 Conclusion

In summary, this chapter highlights developmental effort carried out for making the device and the measurement system suitable for ETG turbulence studies in LVPD. The major emphasis has gone into the development of the largest electron energy filter, its power supply, developing compensated Langmuir probe technique for accurate measurement of electron temperature and its fluctuation. The EEF has performed its assigned role. First, it scavenges energetic electrons and secondly it exerts a control on the scale length of electron temperature and plasma density of target plasma. The scale length of the gradient of electron temperature is effectively varied from 50 to 600 cm and electrons are scooped out. Thus the requirements for carrying out unambiguous experiments on ETG turbulence are satisfied. The detailed study and experimental demonstration of ETG turbulence are discussed in the next chapter.

Chapter 3

Experimental Investigation of ETG Turbulence in the LVPD

3.1 Introduction

In this chapter, we have discussed the observations on ETG driven turbulence in the core region of finite beta ($\beta_e \sim 0.2-0.6$) LVPD plasma. It has been already shown in the previous chapter that different electron temperature gradient scale lengths are obtained by either varying the magnetic field of electron energy filter (EEF) or by exciting different extent of it [78]. Out of various scales obtained, turbulence is studied for two extreme configurations of EEF, the first one is in which the ETG turbulence is excited and the second one in which it gets suppressed. The finite beta effect in the plasma leads to electromagnetic nature of the instability and is described by wave number-frequency spectra of magnetic fluctuation (δB_z). The measurement of electron temperature fluctuations (δT_e) and spectral features of fluctuations such as power spectra, correlation, threshold condition, beta scaling and the crucial relationship with plasma parameters are considered to characterize the ETG turbulence. A comparison of the parallel wave number (k_z) and perpendicular wave number ($k_\perp$) for density fluctuations shows that the observed instability satisfies the condition $k_z / k_\perp << 1$. Moreover, in this chapter, we have also discussed about non-linear coherent structures observed in core plasma, in the background of ETG turbulence. The structures are determined by using conditional averaging technique [34, 35, 79-85] imposed on the amplitude of floating potential fluctuation ($\delta\phi_f$) and ion saturation current fluctuation (δI_s) signals taken by the reference probe and an array of Langmuir probes. We have observed non-Gaussian probability distribution functions (PDF) that includes higher order moments like variance, skewness and kurtosis. The conditional averaging technique is applied to pick up those eddies from the turbulent data, which satisfies certain imposed conditions on amplitude and slope over time series of the reference probe. Observations have shown the existence of vortex like coherent structures with dipole nature.

The remaining part of the chapter is organized as follows: The experimental setup is described in section 3.2. The experimental investigation on ETG turbulence is discussed in section 3.3. Section 3.4 describes investigation of nonlinear structures. The summary and concluding remarks are given in section 3.5.

3.2 Experimental Setup

The plasma in target region of LVPD is characterized by typical plasma parameters such as plasma density, $n_e \sim 3\times10^{11}\,cm^{-3}$, electron temperature, $T_e \sim 2\,eV$ and the applied ambient field, $B_z \sim 6.2\ G$. A schematic diagram of the experimental set up and details about basic plasma parameters are shown in figure 3.1 and table 3.1 respectively. The pulse Argon plasma ($\sim 9.2\,ms$) is produced by using the multi-filamentary source and therefore possibility of presence of energetic electrons cannot be ruled out. A signature of this was already reported by Awasthi et al. (2010), in LVPD where they have shown typical electron temperature as $T_{ec} = 8\ eV$ and hot component as $T_{eh} = 17-20\ eV$ respectively. The presence of long tail in I-V curve obtained by Langmuir probe and existence of high edge temperature $\sim 6\ eV$ are some of the signatures pointing to the presence of energetic electrons [23]. The mere presence of these electrons open up possibility of exciting other instabilities along with electron temperature gradient (ETG) instability and thus bring ambiguity in identification of ETG turbulence.

In the present experiment, we have first dressed the plasma so that energetic electrons are almost eliminated and secondly altered the scale lengths of gradient in electron temperature. For this purpose, we have employed an electron energy filter. The EEF is a device, which embeds transverse magnetic field, localised around the filter region. As we discussed earlier, the source function for primary ionising electrons resides in the source region whereas the target plasma has no source function and is filled with the plasma that diffuses across the EEF region from the source region. Also, the EEF not only allows transport of electrons across its own magnetic field with dependence on its energy but also trap or provide loss pathways for energetic electrons. The EEF enables to remove bulk of the energetic electrons and helps in setting up gradient in electron temperature in target plasma [33, 78]. The detail description and performance of EEF is already discussed in the previous chapter. The dominance of the magnetic component of the EEF field along the axis of LVPD is realized only within $z \le 5$ cm and its magnitude becomes a fraction of the ambient magnetic field in the target region considered for turbulence study. This ensures that the measurements carried out for turbulence studies remain unaffected by EEF produced magnetic field.

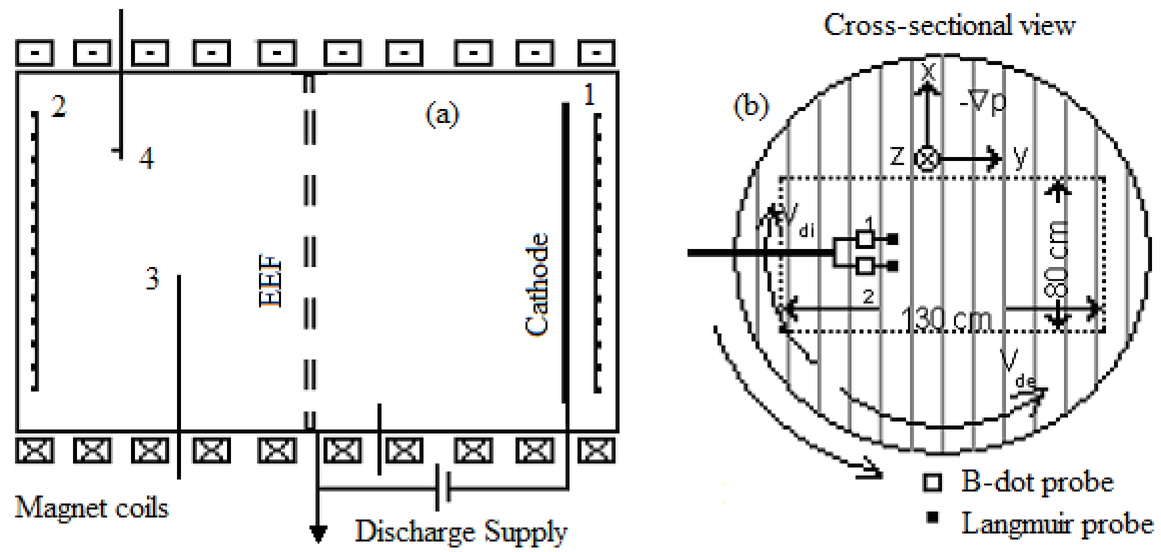

Figure 3.1: (a) The layout of the internal components of LVPD. The marked numbers represent namely, 1) back plate, 2) end plate, 3) Langmuir probe and 4) a pair of B-dot and Langmuir probe. (b) The cross-sectional view shows both electric, magnetic probes and different drift directions. The dotted rectangular contour (130 cm x 80 cm) represents the filament locations in the source region whereas vertical lines on it represent the coils of the EEF.

In the diagnostic, electron temperature and plasma potential are measured using fast swept Langmuir probes ($\Delta t = 20 \mu s$) whereas the plasma density is measured by keeping probe at fixed bias ($-80\ V$) and floating potential is measured by the high impedance probe. The fluctuation components of plasma parameters are captured using band pass filter (300 Hz-300 kHz). The temperature fluctuations are estimated using two Langmuir probes. The

Langmuir and the B-dot probes are mounted on large numbers of SS304 shafts, discretely placed along the device length. An array of five Langmuir and four B-dot probes is used for determining the phase velocity of the observed eddies at different radial distances. The radially movable probes are used to pick up data over the complete radial extent of the device. The Langmuir probes and B-dot probes are used for making both DC and fluctuation measurements. The respective distances between the consecutive Langmuir and B-dot probes are kept as 1.5 and 2.2 cm respectively. The probe signals are acquired in National Instruments make VXI system. The mean and fluctuating plasma parameters are acquired at a sampling rate of $1MS/s$ and $500kS/s$ with record length of 15k points and 8k points respectively. The data acquired is made available for further processing as well for analysis purpose through network interface.

Table 3.1: Basic plasma parameters in the core region of target plasma.

Plasma Density, n_e	3×10^{11} cm^{-3}
Electron Temperature, T_e	2.0 eV
Ion Temperature, T_i	0.2 eV (assumed)
Floating Potential, ϕ_f	-17 eV
Plasma Potential, ϕ_P	-8 eV
Ambient Magnetic Field, B_z	6.2 G
EEF Magnetic Field, B_{EEF}	155 G
Electron Thermal Velocity, C_e	5.9×10^7 cm/s
Ion Thermal Velocity, C_i	6.9×10^4 cm/s
Ion Acoustic Velocity, C_s	2.2×10^5 cm/s
Electron diamagnetic drift velocity, V_{de}	5.0×10^5 cm/s
Ion Larmor Radius, ρ_i	46.6 cm
Electron Larmor Radius, ρ_e	0.54 cm
Ion Larmor Radius, ρ_s	1.5×10^2 cm
Electron cyclotron frequency, Ω_e	1.1×10^8 rad/sec
Ion cyclotron frequency, Ω_i	1.5×10^3 rad/sec
Electron plasma frequency, ω_{pe}	3.1×10^{10} rad/sec
Ion plasma frequency, ω_{pi}	1.1×10^8 rad/sec
Ion-neutral collision frequency ν_{in}	3.2×10^3 sec-1
Electron-neutral collision frequency, ν_{en}	3.0×10^5 sec-1
Electron Debye Length, λ_D	1.9×10^{-3} cm
Skin Depth, $\lambda_s = c/\omega_{pe}$	9.7×10^{-1} cm
Plasma Beta, $\beta_e = 2\mu_0 n_e T_e / B_z^2$	~ 0.6

3.3 Study of ETG Turbulence

Out of various configurations of EEF, we have restricted our measurements to two extreme cases for studying mean plasma parameters and their ac components in the core region of LVPD. The core plasma is characterized by flat density and gradient in electron temperature (Fn_eGT_e) and by hollow density and flat electron temperature (Hn_eFT_e) for EEF active and inactive cases respectively. Now onwards this terminology will be cited throughout the thesis. Various drift directions are obtained from the mean plasma profiles and are shown in the cross-sectional view of the device for the Fn_eGT_e plasma [Fig. 3.1]. We found that the electron diamagnetic drift velocity and $\vec{E} \times \vec{B}$ drift velocity are in the same direction and both are opposite to the ion diamagnetic drift velocity.

3.3.1 Equilibrium Plasma Profiles for ETG Studies

In an attempt to alter the electron temperature profile, the observations are focussed on two scenarios of the EEF. We now discuss the equilibrium profiles of mean plasma parameters for Fn_eGT_e case. We have divided the plasma into two regions. The region for $x < 50\ cm$ is defined as core plasma and the remaining region beyond it as edge plasma. The profile of plasma density (n_e) is flat and that of the electron temperature (T_e) is steeper in the core plasma. The floating potential (ϕ_f) measured by a Langmuir probe is negative with respect to the vessel, indicating preferential confinement of electrons. We have observed that there is a significant reduction in the peak of floating potential, which may be considered as a signature for the reduction in the population of energetic electrons. The observations also exhibit a significant reduction in both peak and bulk potential of the plasma produced because of the presence of magnetic filter in comparison to the plasma produced in the LVPD using a narrow source [23]. The core region of target plasma is dominated solely by the gradient in electron temperature whereas the outer region is dominated by the pressure gradients [Fig. 3.2]. In the core region for Fn_eGT_e case, radial profiles of plasma density and plasma potential (ϕ_p) are typically flat and electron temperature gradient has scale length, $L_{Te} \sim 50\,cm$. In the core region for the Hn_eFT_e case, filter exhibits a flat temperature and hollow density profiles whereas radial profile of ϕ_p represents significant gradient. In the edge region ($x \geq 50\ cm$), the pressure gradient dominates for both the configurations of the magnetic filter. We can physically understand the equilibrium profiles by the following qualitative argument.

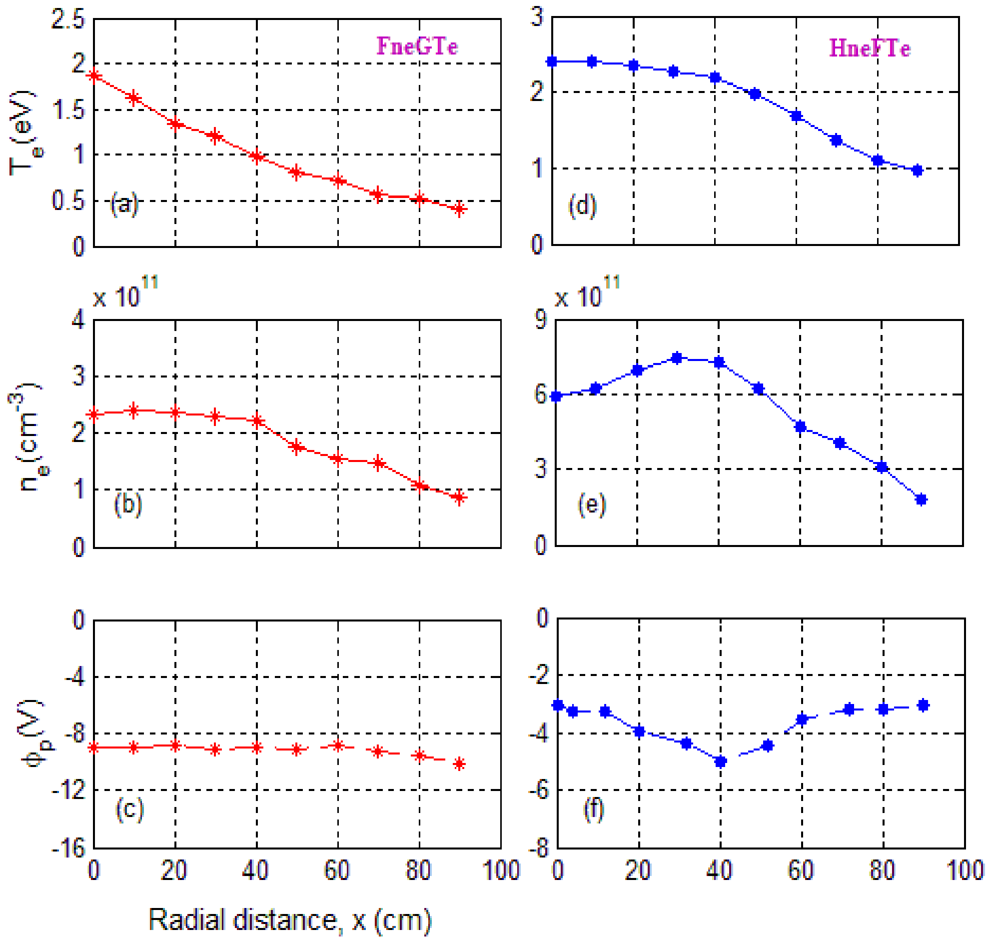

Figure 3.2: Radial profiles of mean plasma parameters, (a, d) electron temperature, T_e, (b, e) plasma density, n_e and (c, f) plasma potential, ϕ_p for two configurations of EEF active and inactive respectively. It is seen that the finite electron temperature gradient of scale length, $L_{Te} \sim 50\,cm$ exists only in the core region of LVPD plasma for filter active condition.

In the core region, near the axis, both electrons and ions are well confined by the applied magnetic field, however as ion gyro radii, $\rho_i \sim 45\,\mathrm{cm}$ so that the density is flattened on that scale whereas because of small electron gyro radius, the electron temperature exhibits significant gradient. In the outer shell of LVPD, the ions remain unconfined and in successive collisions move radially outward, leaving the plasma with a negative potential. Quasi-neutrality is maintained by the flow of electrons along the electric field. In the outer shell, turbulence may be dominated by the pressure gradient.

3.3.2 Fluctuations, Power Spectrum and Correlation Analysis

We now describe the experimental results on plasma fluctuation, e.g., scaling of fluctuation amplitude for Fn_eGT_e and Hn_eFT_e configurations. The measurement of the power spectrum, correlation properties of the fluctuations are described in below.

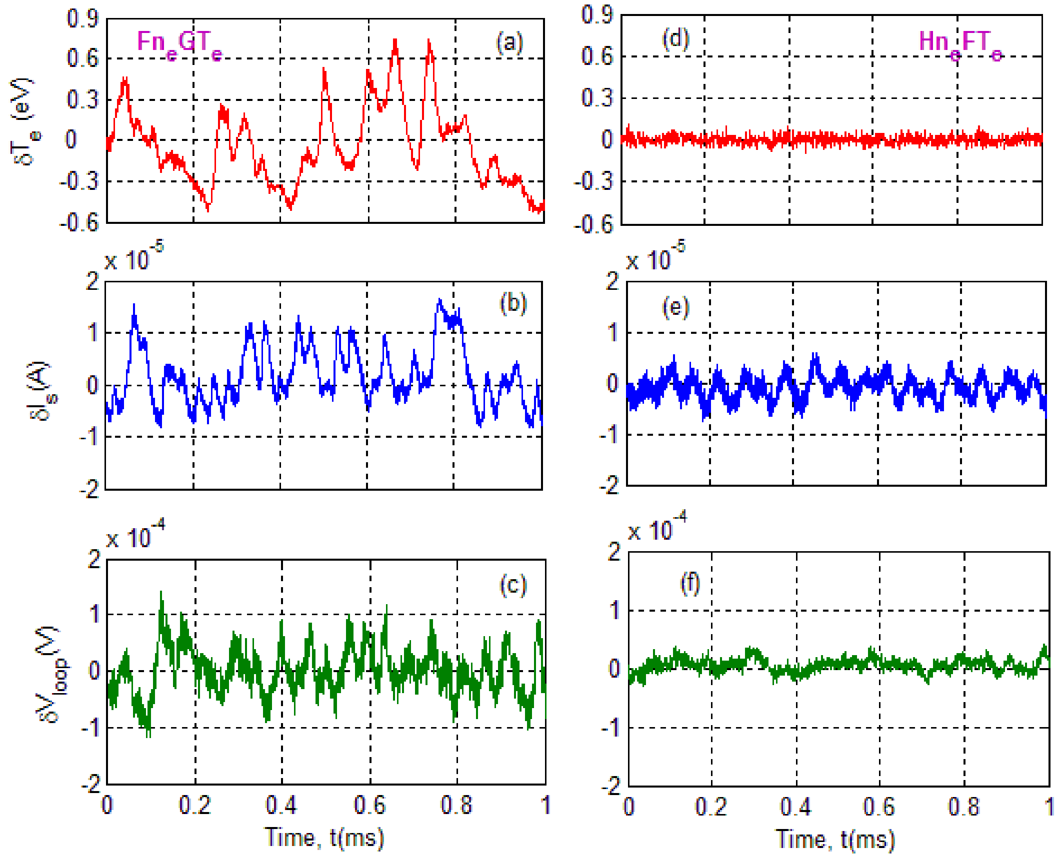

Figure 3.3: Time series for fluctuations are shown for the EEF active (a-c) and inactive (d-f) cases. At the radial centre in target plasma, the fluctuations exist only in the case of FneGTe and suppresses to the level of noise for HneFTe case.

Figure 3.3 displays the time series profiles of fluctuations for Fn_eGT_e and Hn_eFT_e plasmas in the core region. It may be noticed that fluctuations in temperature, density and magnetic field are present in the Fn_eGT_e case and these get suppressed for the Hn_eFT_e case. The core plasma for filter active case supports turbulence of ETG nature while for Hn_eFT_e case, no such signatures are seen.

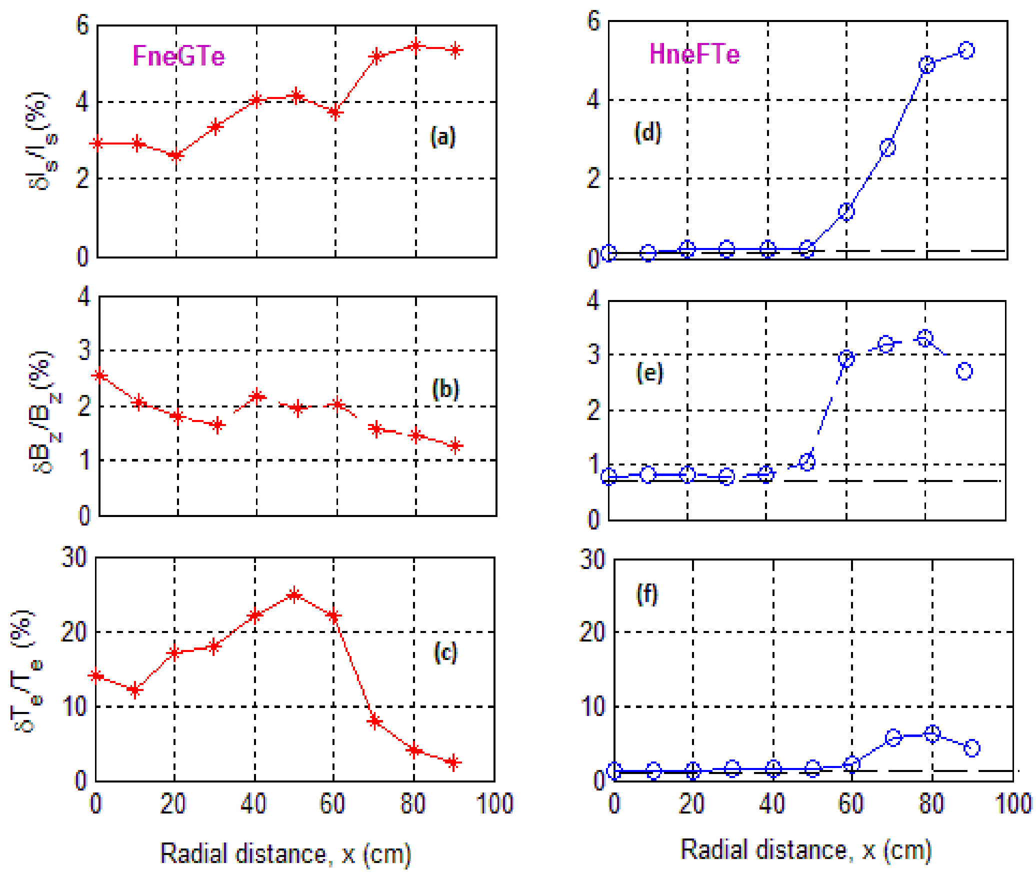

Figure 3.4: Radial profile showing comparison of normalized fluctuations in ion saturation current ($\delta I_s / I_s$), magnetic field ($\delta B_z / B_z$) and electron temperature ($\delta T_e / T_e$) for both FneGTe and HneFTe cases.

The radial profiles of normalized density ($\delta n_e / n_e$), magnetic field ($\delta B_z / B_z$) and electron temperature fluctuations ($\delta T_e / T_e$) are shown in figure 3.4. They have been measured at the applied axial magnetic field of 6.2 G for both types of plasmas. It is observed that for FneGTe, the fluctuation amplitudes are higher and the values obtained for $\delta T_e / T_e$, $\delta n_e / n_e$ and $\delta B_z / B_z$ are $\sim 13\%$, $\sim 4\%$ and $\sim 2\%$ respectively. These fluctuations reduce to noise level for HneFTe. The noise level is shown with a dashed line. In fact, the level of fluctuations increases toward the edge region where plasma is dominated by gradients in mean profiles. Noticeably, the temperature fluctuation remains of the order of noise level and the reason assigned to this is the absence of gradient in electron temperature in that region. Moreover, the presence of magnetic fluctuations reveal that observed turbulence is electromagnetic in nature. The significant magnetic fluctuation appears only when the plasma beta

($\beta_e = 2\mu_0 n_e T_e / B_z^2$) exceeds a critical value $\beta_{e,cr} \sim 0.1$ [see Fig. 3.8]. The plasma beta is controlled experimentally by varying discharge current through variation in filament temperature and has the effect of converting purely electrostatic fluctuations into partially electromagnetic ones. The fluctuation amplitudes of δB_z, δI_s and δT_e at one radial location is obtained for determining their dependences on the plasma beta. The detail experimental results of beta scaling on the fluctuations are discussed in section 3.3.4. It may be noted that, even though the density gradient and velocity shear are present in Hn_eFT_e case, the absence of gradient in electron temperature does not allow the ETG mode to get destabilized. The results from simulation also show that hollow density profile and $E \times B$ velocity shear can destabilize the ETG mode for certain threshold conditions but only when $\nabla T_e < 0$ [84]. Thus we have clear empirical evidence for ∇T_e driven turbulence, which is electrostatic in low β_e plasma and gets coupled to an electromagnetic mode when the plasma beta is high ($\beta_e \geq 0.1$).

The important characteristic features like power spectra and cross-correlation function are necessary to identify the instability. In this regard, we have measured correlation coefficients between various physical quantities and the results are shown in figure 3.5. The obtained result supports the case for ETG turbulence. The cross correlation function between the density (δn_e) with potential ($\delta\phi_f$) fluctuations, electron temperature (δT_e), with potential ($\delta\phi_f$) fluctuations and density (δn_e) with magnetic field fluctuations (δB_z) are found strongly anti-correlated. The correlation coefficients obtained are $C(1.5,0) \sim -0.8$, $C(2,0) \sim -0.7$ and $C(2.2,0) \sim -0.7$ respectively. These measurements are carried out using four probes at different axial locations. We assume that there may be slight de-correlation spatially as probes are not seeing the same magnetic field line. The observed turbulence exhibits broad band spectra with significant power between the frequencies $\leq 2-20\ kHz$ [Fig. 3.5]. It follows a power law of $1/\nu^{1.8}$ for $\nu \leq 10-80 kHz$ for density fluctuation. The observed frequency of the mode lies in the lower hybrid range of frequency ($\Omega_i < 2\pi\nu << \Omega_e$) and it indicates that the basic instability driving the turbulence is the only ETG driven mode.

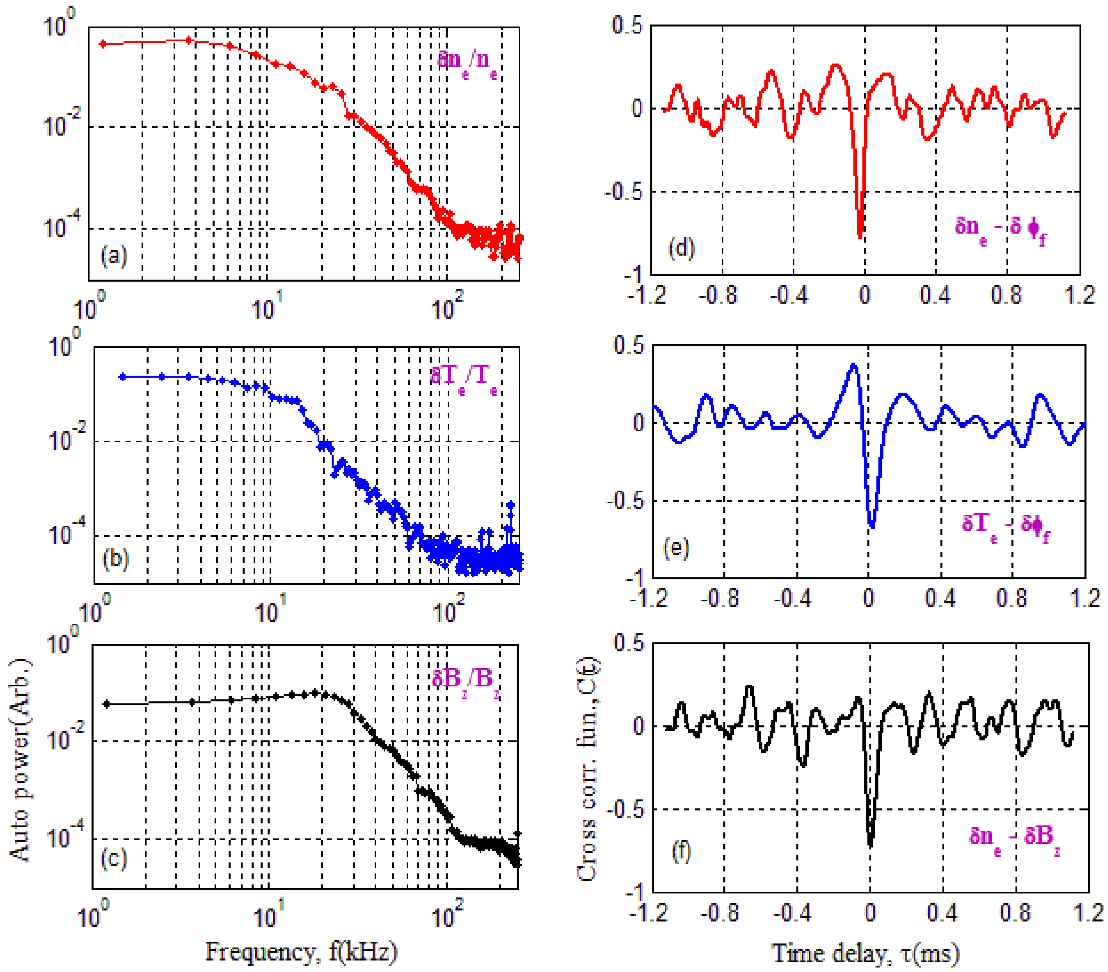

Figure 3.5: Auto-power spectrum of fluctuations (a) density, δn_e (red), (b) electron temperature, δT_e (blue) and (c) magnetic field, δB_z (black) are shown in target plasma for Fn_eGT_e. The cross-correlation between (d) $\delta n_e - \delta\phi_f$, (e) $\delta T_e - \delta\phi_f$ and (f) $\delta n_e - \delta B_z$ exhibits strong anti-correlation.

3.3.3 Spectral Features of the Observed Turbulence

The experimental results obtained by carrying out spectral analysis of the turbulence data are discussed below. These include wave number-frequency spectra and propagation characteristics of the fluctuations.

3.3.3.1 Wave Number-Frequency Spectrum and Phase Velocity

The wave number-frequency spectrum, $S(k,\omega)$ is determined for δn_e and δB_z fluctuations and is shown in figure 3.6. We have used data obtained from probes separated in the vertical direction with probe spacing between two consecutive probes as 1.5 cm for the density fluctuations and 2.2 cm for the magnetic fluctuations. The spectrum peaks at $\omega \approx 10\,krad/s$ and $k_\perp \approx 0.12\,cm^{-1}$ for the δn_e and at $\omega \approx 40\,krad/s$ and $k_\perp \approx 0.15\,cm^{-1}$ for the δB_z fluctuations. The spectrum also exhibits a spectral width in frequency, $\Delta\omega/\omega \approx 2.5$ and wave number, $\Delta k/k \approx 2$ for the density fluctuations. The magnetic field fluctuation exhibits spectral widths as, $\Delta\omega/\omega \approx 2$ and $\Delta k/k \approx 3$ respectively. The plasma fluctuation exhibits long wavelength ~ 50 cm. The phase shift observed corresponds to the velocity, $V_{2,1} \approx 2.8\times10^5\,cm/s$ in the electron diamagnetic drift direction with same order of magnitude as for the electron diamagnetic drift velocity ($V_{de} \approx 5\times10^5\,cm/s$). We have used probe identifiers for correct assessment of drift direction [see Fig. 3.1 (b)].

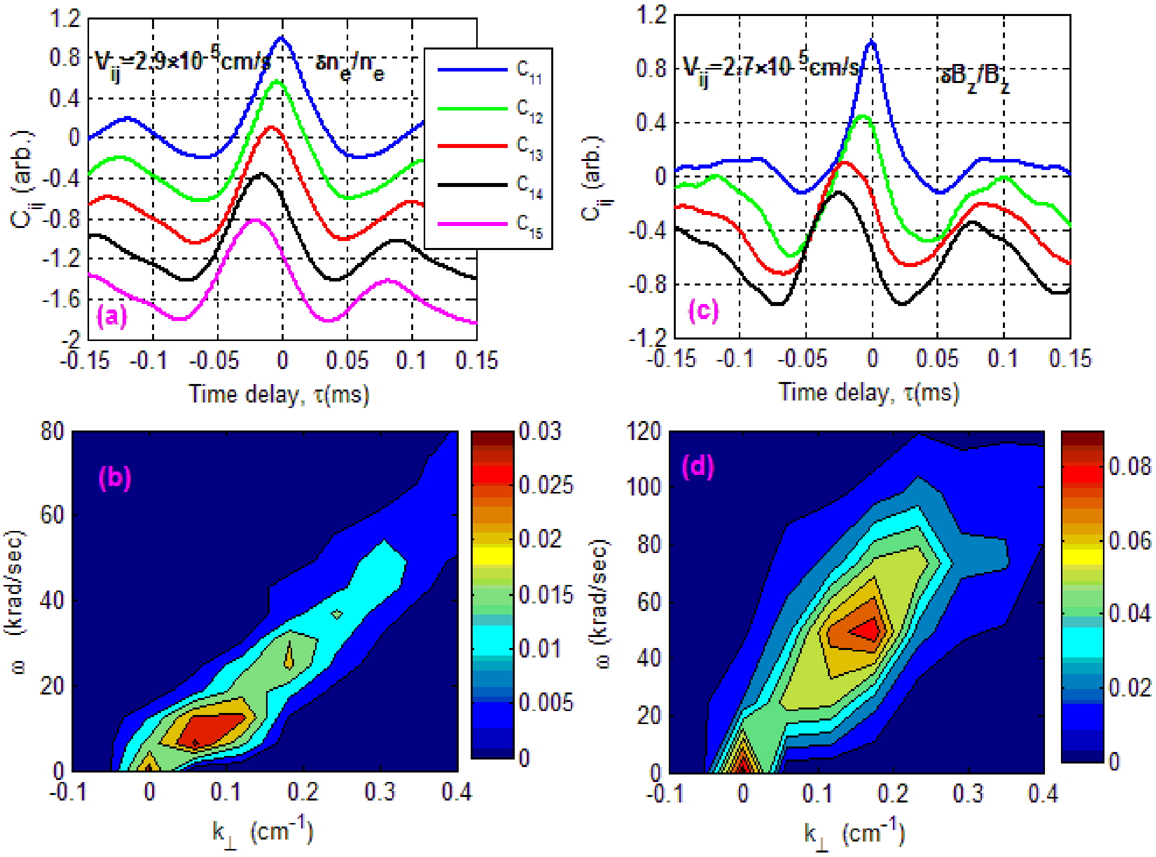

Figure 3.6: Cross- correlation function is shown for fluctuations in both density (a) and magnetic field (c). The contour plot of the joint wave number- frequency spectrum for (b) density and (d) magnetic field fluctuations are shown. The observation is made at $x = 30cm$ for the applied magnetic field $(B_z) \sim 5G$.

3.3.3.2 Measurement of Parallel Wave Number

We have also carried out measurements for axial wave number (k_z) of the observed mode and for this purpose an array consisting of axially separated Langmuir probes are mounted on an axial shaft. The probe separation between consecutive probes is kept 20 cm. The cross correlation function between various Langmuir probes (with increasing probe separation) and frequency- wave number ($\omega - k_z$) spectra for the δI_s fluctuations are obtained from a set of four axially separated Langmuir probes.

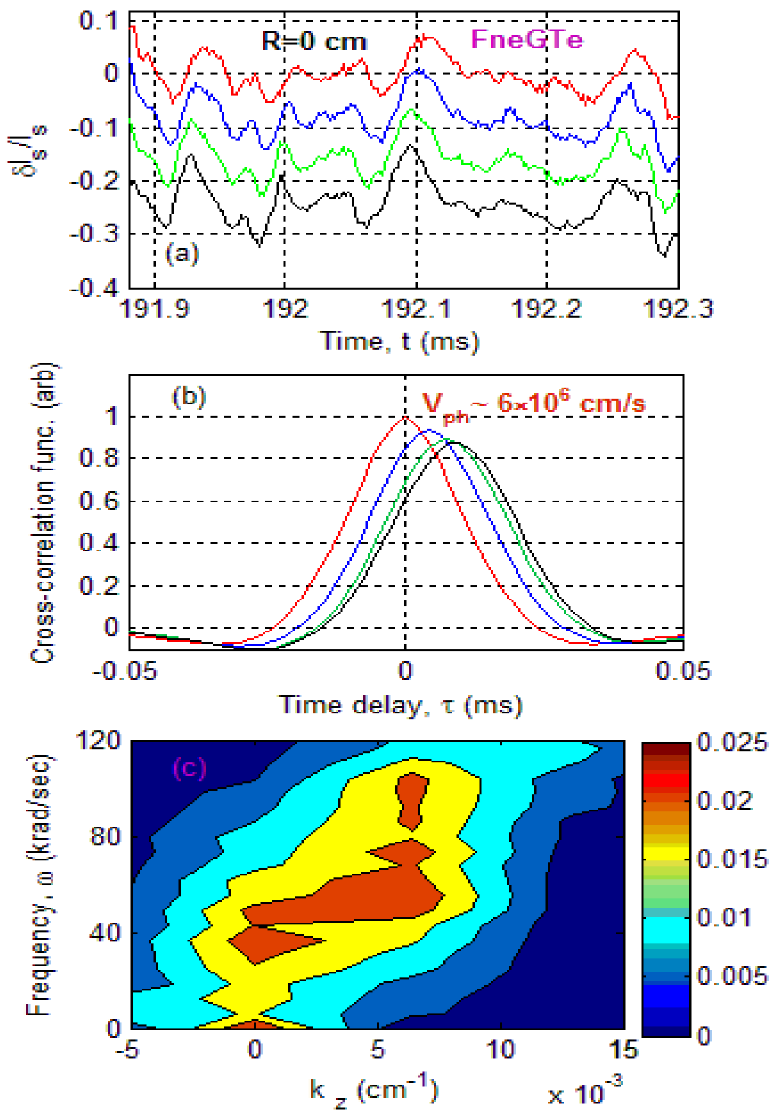

Figure 3.7: Time series profiles (a) to determine axial propagation for density fluctuations (b) by using cross- correlation function whereas the joint wave number- frequency spectrum shown in (c). Result exhibits $k_z \sim 0.008\,cm^{-1}$ for $\omega \approx 60\,krad/s$.

The contour plot of frequency-wave number spectrum $S(k_z, \omega)$ is shown in figure 3.7 for a pair of probes axially separated apart by 20 cm. The typical obtained value of parallel wave number is $k_z \sim 0.008 cm^{-1}$ with corresponding frequency, $\omega \approx 60 krad/s$. This satisfies the condition $k_z / k_\perp << 1$ and thus exhibits a good agreement with the suggested theory for ETG turbulence. The estimated axial phase velocity for the density fluctuation is $V_{ph} \sim 6 \times 10^6 cm/s$.

3.3.4 Discussions I

We have demonstrated that a plasma without high energy electrons and with free energy source present only in the form of electron temperature gradient can drive low frequency ($\omega << \Omega_{ce}$), short scale ($k_\perp \rho_e \leq 1$) fluctuations in density, temperature, potential and magnetic field with the appropriate correlations. We have experimentally demonstrated that in a plasma with Fn_eGT_e, the fluctuations in δT_e, δn_e and δB_Z exhibits strong signatures of electron temperature gradient driven turbulence. We now present a quantitative analysis of these experiments. The frequency ordering of the ions in ETG dynamics is given by the expression $\Omega_i \sim \nu_{in} < \omega \leq k_\perp c_i$, where $\Omega_i \sim 2 \times 10^3$ rad/s, $\nu_{in} \sim 3 \times 10^3$ s^{-1} and $\omega \sim 2 \times 10^4$ rad/s are the ion gyro, ion-neutral collisional and the characteristic frequency of observed mode respectively. In these scales, the role of ions is considered as mobile, warm, collisionless and unmagnetized.

We have also verified experimentally that the condition of $k_z / k_\perp << 1$ is satisfied and the mode disappears when the electron temperature gradient becomes sufficiently weak. This is as unambiguous demonstration of the ETG turbulence as one can make in a laboratory experiment and is more complete than any other identification of ETG modes in the current literature. It is also seen that experimentally obtained normalized gradient, $\eta_{e,\exp} \sim 6$ is found to be greater than the theoretical critical gradient for this plasma, $\eta_{e,\,th} \sim 1.5$. The theoretical critical gradient for ETG mode has been discussed in the next chapter. Note that the $E \times B$ rotation shear has weak effect on ETG mode since the shearing rate is much smaller than the growth rate of ETG mode in LVPD plasma [53, 84].

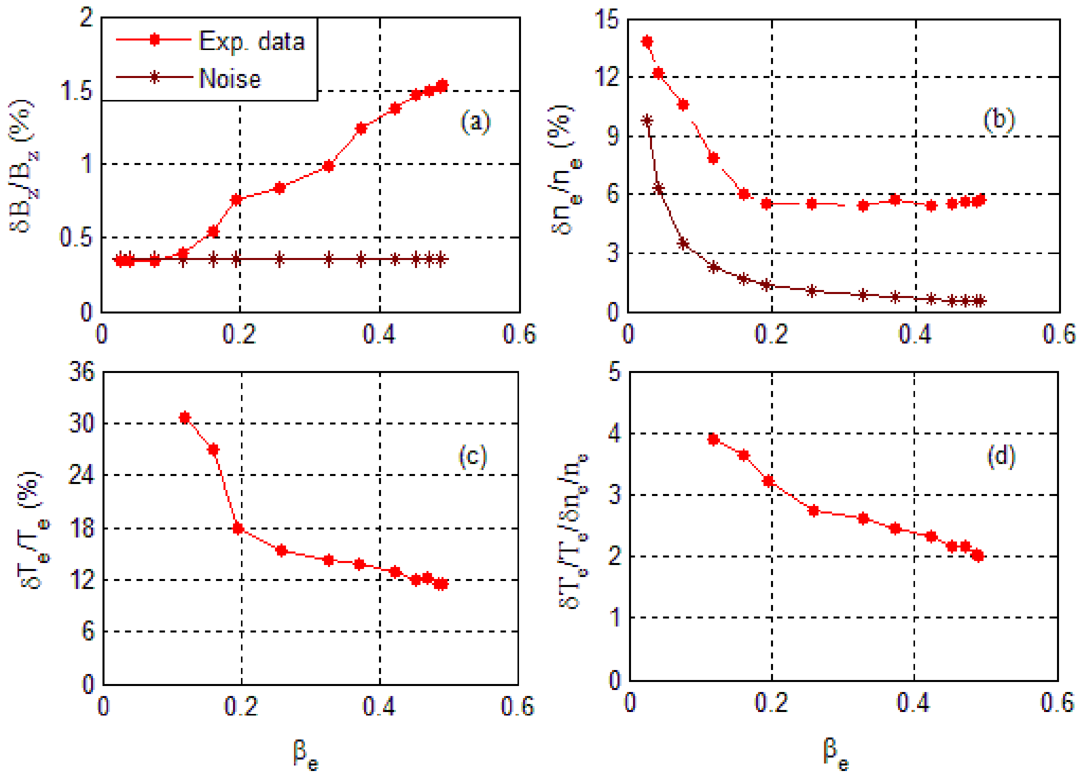

Figure 3.8: Shows the profiles of beta scaling with experimentally observed normalized fluctuations of (a) magnetic field (b) density (c) electron temperature and (d) ratio of electron temperature to density fluctuations.

Figure 3.8 shows the variation of observed $\delta B_z / B_z$, $\delta n_e / n_e$, $\delta T_e / T_e$ and ratio of normalized temperature to density fluctuations along with the noise as a function of β_e. The results show that magnetic fluctuations increases but density fluctuations decreases with β_e [Fig. 3.8(a-b)]. The temperature fluctuations and ratio of $\tilde{T}_e$ and $\tilde{n}_e$ amplitudes both decrease with β_e are shown in [Fig. 3.8(c-d)]. For $\beta_e < 0.1$, the value of $\delta B_z / B_z$ is close to the noise level and mode becomes electrostatic in nature. The comparison of beta scaling of these observed fluctuations with theoretically estimated fluctuations amplitudes using the mixing length argument are discussed in the next chapter where the estimated values are close to the experimental observations.

Till now, we have discussed about observations relevant to the linear regime of ETG turbulence. The observations regarding non-linear aspect of turbulence will be discussed in the following section.

3.4 Investigation of Non-linear Structures

In order to explore the non-linear features of the turbulence, vortex like coherent structures is investigated by using conditional averaging technique. The experiment is again performed in the core of the target plasma of LVPD where observations for linear ETG studies are carried out [33]. We have investigated the non-linear structures (density and potential structures) in x-y cross-section, perpendicular to the axial magnetic field by using an azimuthal array of radially movable Langmuir probes from the vertical direction [Fig. 3.9], to collect data on grid points spread over this region [85]. A reference probe is installed in the same poloidal plane. However, probe arrays covering the whole cross section are too complex to build and would create a strong perturbation to the plasma [83]. Keeping this in mind, we have restricted our studies in the one quarter of core plasma region where conditions suitable for ETG turbulence exist. We have observed non-Gaussian probability distribution functions (PDF) associated with higher order moments like variance, skewness and kurtosis and these parameters are estimated. The conditional averaging technique is applied to pick up those eddies from the turbulent data, which satisfies the certain imposed conditions on amplitude ($\tilde{\phi}_c > 1.5\sigma$) and slope ($d\tilde{\phi}_c / dt > 0$) on the fluctuation data of reference probe. Here σ is the standard deviation of the fluctuation data. The probes are aligned azimuthally but the movement is restricted to radial direction. The cross-correlation and conditional averaging techniques are used to obtain the correlation length, correlation time and also to pick up similar eddies to determine the dynamical behaviour of the selected structures [34-35, 44].

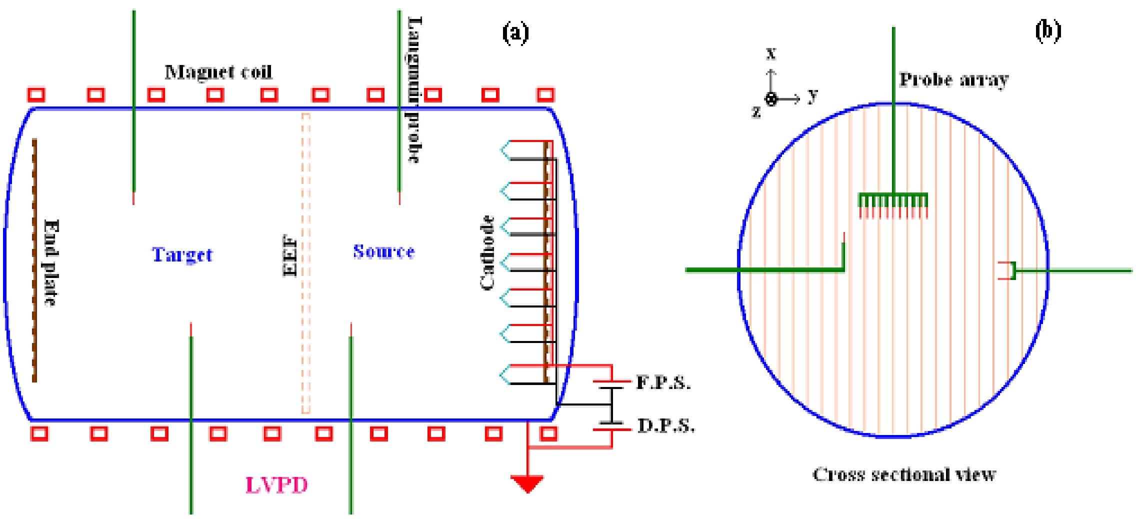

Figure 3.9: (a) A schematic diagram describing experimental setup used for carrying our non-linear studies in core region of target plasma. Both the anode plate and the end plates have multi-cusped magnetic mirrors mounted on them and are electrically grounded along with the vacuum vessel. (b) In cross-sectional view, an array of Langmuir probes inserted from the top along with reference probes (horizontal) is shown. These probes are used for the measurement of density and potential fluctuations.

The radial profiles of the plasma density, electron temperature and plasma potential in the mid plane of the target plasma cross section are determined in figure 3.2 (a-c). As discussed before in the section 3.3.1, the density profile is flat and exhibits a sharp gradient in electron temperature for FneGTe case in the core region. This region is free of electric field as the plasma potential profile remains nearly constant. The fluctuation for conditional averaging are acquired in a grid having poloidal extent of ~ 8 cm and a radial length of 30 cm. Langmuir probe array having equal poloidal separation of 1 cm is installed from a vertical port and is moved to different grid locations by moving it from x=10 to 40 cm with a step resolution of 1 cm. Data is acquired with respect to a reference (fixed) probe, aligned to the probe array [see Fig. 3.9(b)]. The data are sampled at the rate of 5 MS/s with record length of 15k points after band pass filtering between 300 Hz to 300 kHz.

3.4.1 Data Analysis Techniques

Before attempting conditional averaging technique, the data are subjected to standard analysis of probability distribution function (PDF), cross-correlation and S(k,ω) spectrum [33, 44]. The conditional averaging technique is employed to obtain the spatial and temporal behaviour of the organized structures in the presence of the turbulence. The conditional average technique is based on satisfying certain conditions imposed on the fluctuation data and ensemble average of newly generated sub series gives rise to conditionally averaged time series which is considered a physically relevant quantity. In the turbulent plasma, this method of data analysis has been used to investigate two-dimensional structures in a plane perpendicular to the magnetic field. Using this technique, the localized small structures embedded in random fluctuations can also be observed.

In order to perform conditional averaging, the data of ion saturation current fluctuation (δI_s) and floating potential fluctuation ($\delta\phi_f$) are acquired in the reference probe and are subjected to a condition imposed for amplitude. Those structures are then picked up which satisfy the condition on amplitude ($\tilde{\phi}_c > 1.5\sigma$) and also they should contain a positive slope $d\tilde{\phi}_c / dt > 0$. The data is picked up from all other probes at different radial locations for the time window ($t_c - 5\tau$ *to* $t_c + 5\tau$), where t_c is the instant at which the above condition is satisfied with respect to the reference probe, and $\tau \geq$ correlation time. The overlapping of the data is avoided by skipping the searched time series by 10τ time steps with respect to time t_c when the last condition on the reference probe was satisfied.

These conditionally chosen sub series are considered independent realization of the time series of density and potential fluctuations at the selected probe in the interval $(-5\tau, 5\tau)$. The ensemble average of these provides a conditionally averaged time series at the selected probe position. The procedure is repeated for all grid points where data are recorded simultaneously with the reference probe. The above procedure of data analysis is used for the determination of structures. The figure 3.10 shows conditionally averaged time series of floating potential and ion saturation current at the two reference probe simultaneously.

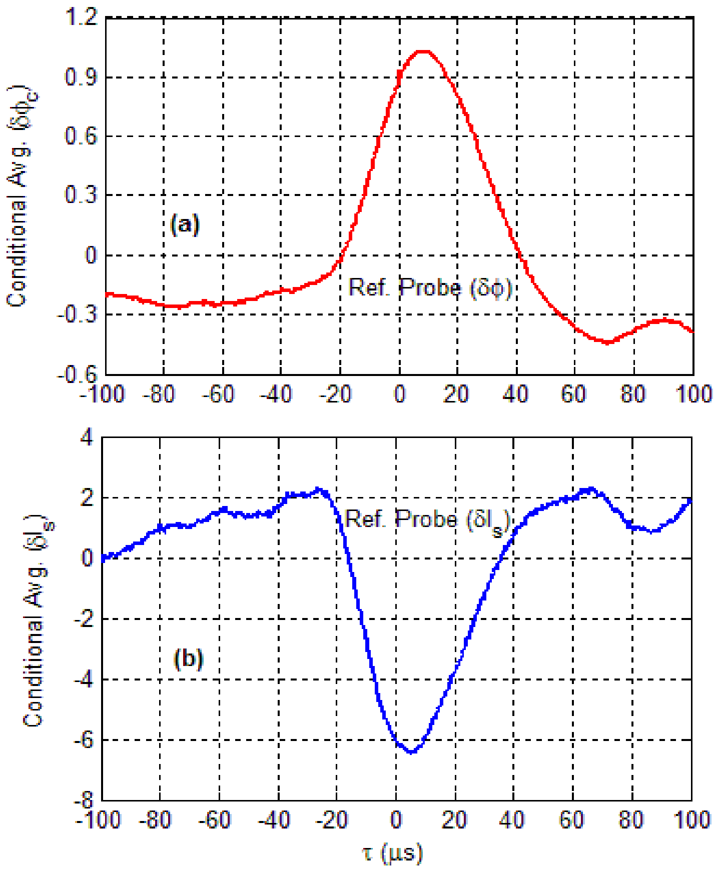

Figure 3.10: The typical conditional averaged time series of (a) floating potential and (b) ion saturation current fluctuations picked up at a fixed radial location by using two reference probes. The averaged time series of potential fluctuation is found anti-correlated with the averaged density fluctuation.

3.4.2 Experimental Results

The time series of potential fluctuations picked up by the reference probe and that the movable probes are used to obtain the cross-correlations between the reference probe and the grid points [see Fig. 3.11]. Typical correlation time obtained varies between 15 to 25 μs in different radial locations whereas the poloidal correlation length is ~ 16 cm. The cross-correlation function reveals that the potential fluctuations propagate poloidally in the direction same as that of electron diamagnetic drift velocity. The poloidal phase velocity of fluctuation is $\sim 3\times10^{5}\,cm/s$ and typical value of $k_y \approx 0.4\,cm^{-1}$ [see Fig. 3.12(a)]. It should be noted that neither the correlation function nor the spectral density can characterize the non-linear aspect of the turbulence. The coherency profile of density fluctuation with frequency indicates that modes exhibits coherency $\leq$ 40 kHz [Fig. 3.12(b)].

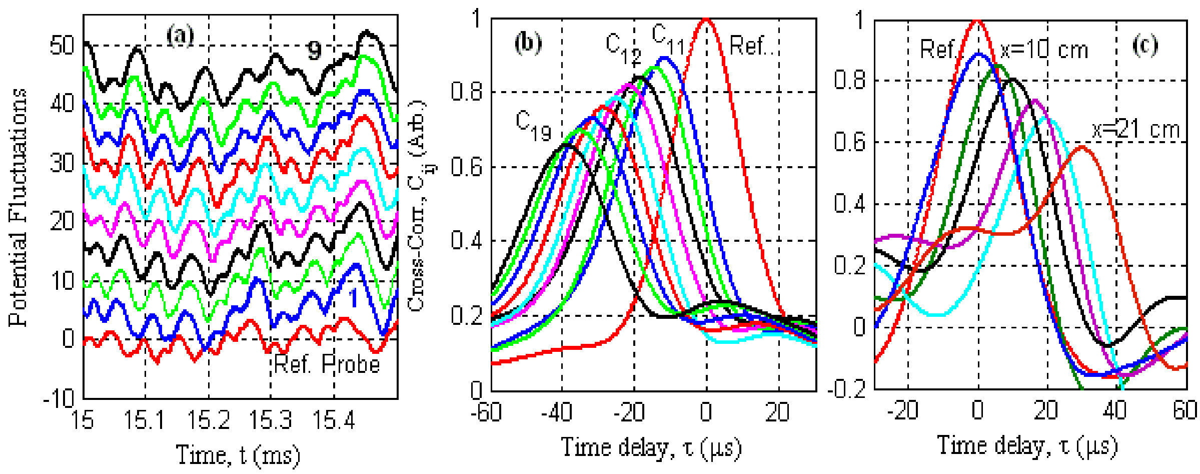

Figure 3.11: (a) Represents the time series of potential fluctuations of Langmuir probe array along with reference probe and (b) the cross-correlation function between the probes of the array with respect to the reference probe. The C11 represents here the auto-correlation of the reference probe and is separated by 2 cm in poloidal direction w. r. t the first probe of the probe array. The poloidal correlation length is ~16 cm. (c) shows the radial cross-correlation function for potential fluctuations w. r. t. reference probe. The reference probe is kept at x

=10 cm whereas the other probes is moved in radial direction at step of 1 cm. The typical value of radial correlation length obtained is ~ 18 cm.

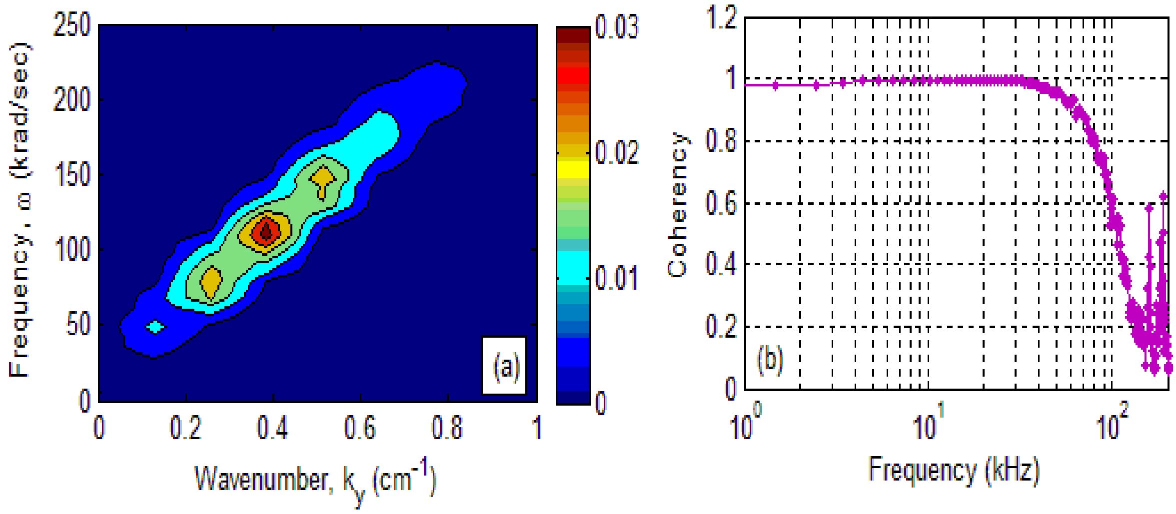

Figure 3.12: Shows the frequency-wave number spectra, $S(k_y, \omega)$ of density fluctuation. The typical wave number $(k_y) \sim 0.4\ cm^{-1}$ is obtained by making use of a pair of probes poloidally separated by 1cm. The profile of coherency with frequency has been shown in figure 3.12 (b).

The nonlinearity of the structure can be determined in terms of the higher order moments of probability distribution function and the conditional averaged fluctuations which are sensitive to non-linearity in the data. We have determined the probability density function of fluctuation data at various locations covering the whole cross-section of target plasma. The Standard deviation (σ), Skewness (S) and Kurtosis (K) at various grid locations vary in the ranges 0.03 - 0.1, 0.1- 0.5, and 2.6- 3.0 respectively. The positive value of skewness indicates the asymmetry in the distribution function [see Fig. 3.13]. The results indicate that probability distribution function is more asymmetric near the centre of the plasma column where temperature gradient is strong.

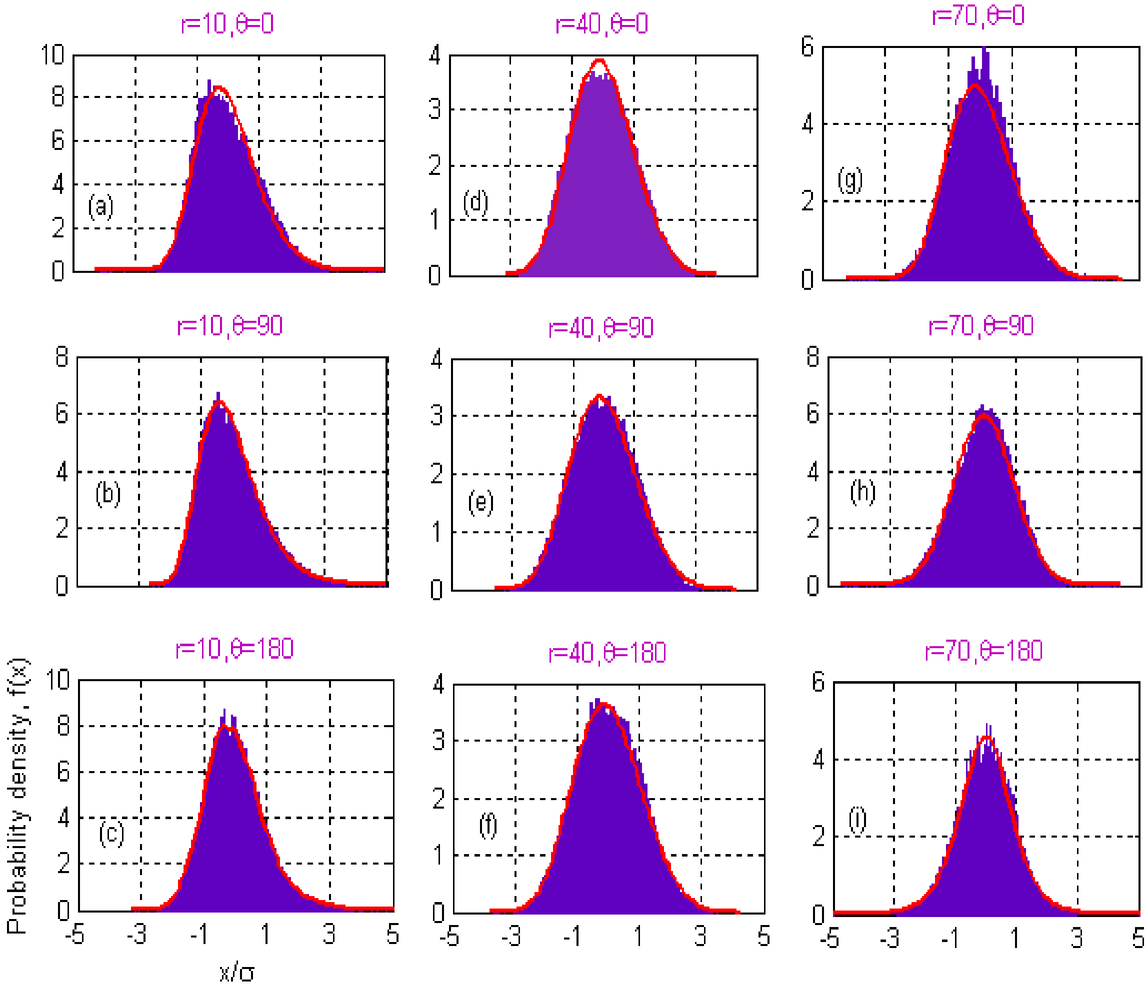

Figure 3.13: The probability distribution function (PDF) of density fluctuations are shown in target plasma both in the core and the edge regions. The core region (Fig. 3.13a-3.13f) shows more asymmetry and the same gets reduced in the edge region (Fig. 3.13g-3.13i). The positive skewness (0.7 at r=10cm and 0.15 at r=40cm) is an indication of the presence of non-linearity in the distribution i.e. non-Gaussian distribution in core plasma whereas in edge plasma probability distribution is almost symmetric (skewness is 0.05 at r=70cm).

A more extensive analysis of the density and potential fluctuation has been performed using conditional averaging technique. The conditionally averaged time series of poloidally separated probes (in the array) as shown in figure 3.14(a) indicates that the peaks of the averages move in the poloidal direction. Figure 3.14(b) shows the conditional averaged time series of one of the probe (in the array) at different radial distances. It indicates that the peak moves along the radial distance.

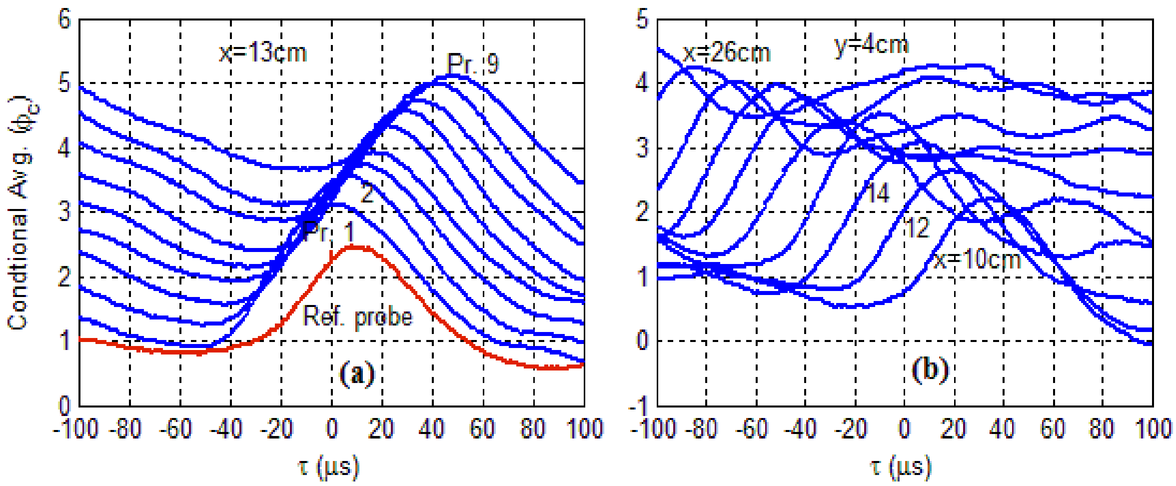

Figure 3.14: (a) The temporal history of floating potential obtained from the probe array by using the conditional average technique, (b) The temporal history of floating potential for a probe at different radial distances.

The conditional structures of potential fluctuation on 31 x 09 matrix points are determined by the analysis described before. Figure 3.15(a) shows potential contours when the condition is applied on floating potential at the first reference probe. On the other hand, when the condition is applied on density fluctuation at the second reference probe, the potential structure obtained is shown in figure 3.15(b). It is obvious that density and potential structures are anti-correlated. This corresponds to an important feature of ETG turbulence.

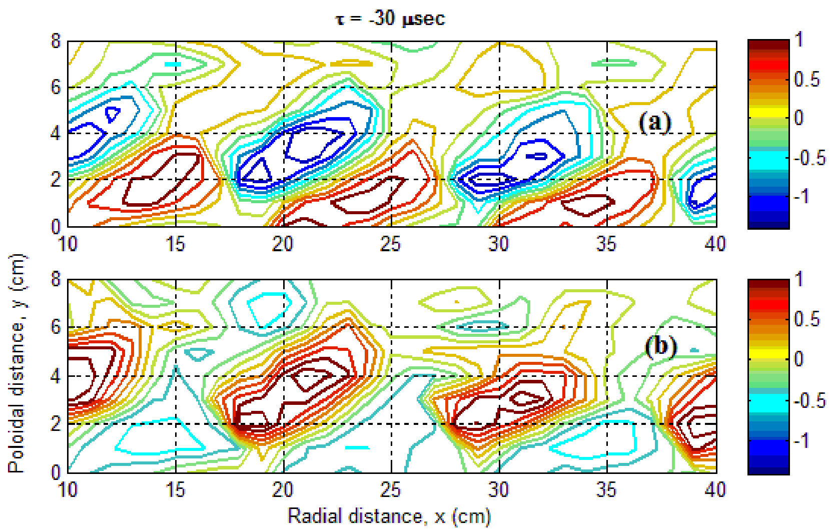

Figure 3.15: Snap shot of potential structures obtained by array of probes at x-y grid points using conditionally averaged data by applying the conditions on two reference probes. Figure 3.15 (a) represents the snap shot of potential structures when condition is applied on the time series of potential fluctuation of the reference Probe 1 and in (b) when condition is applied on density fluctuation (Ref. Probe 2). These snap shots are taken at same time (-30 μs) and exhibits anti-correlation.

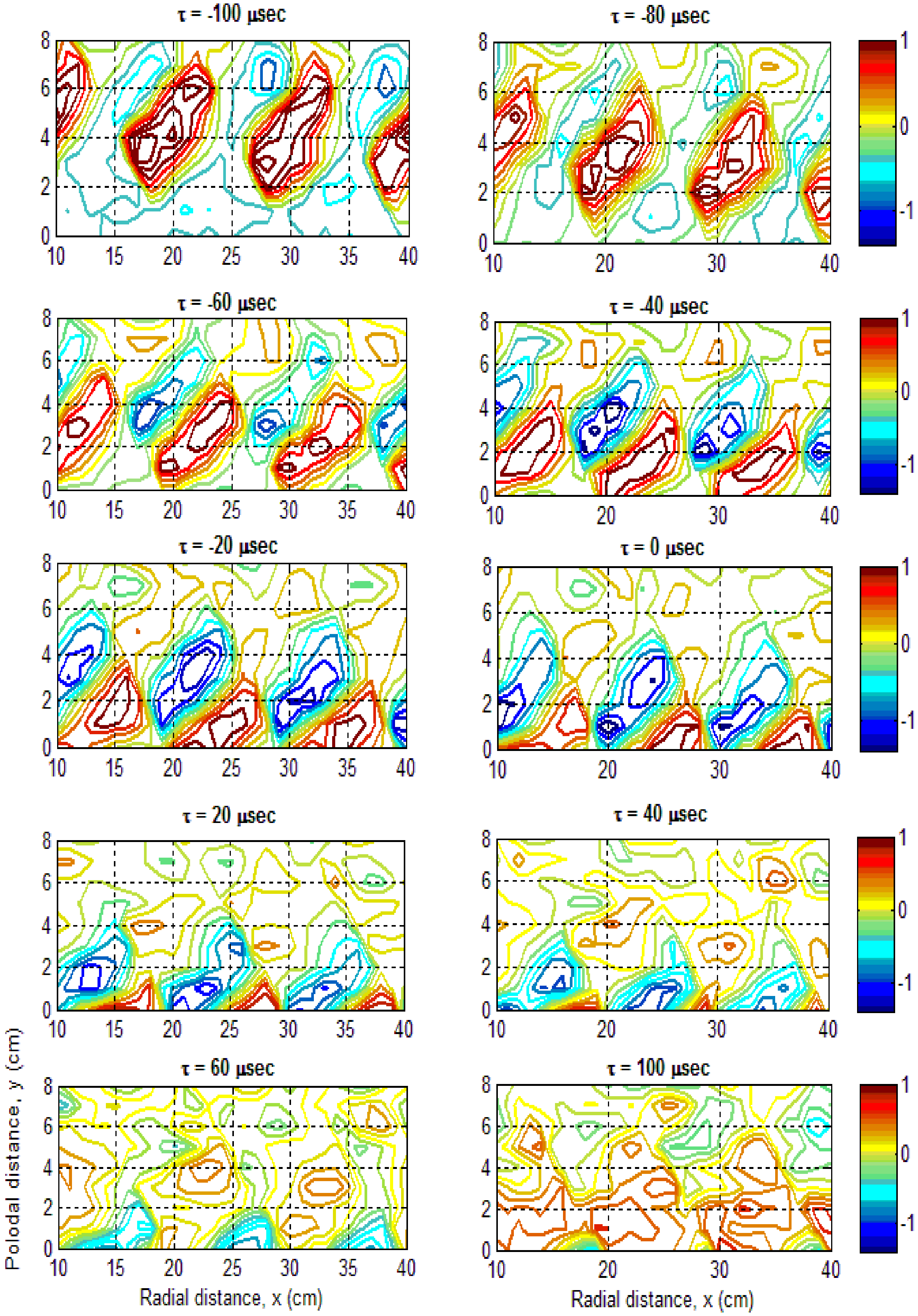
τ = -100 μsec
τ = -80 μsec
τ = -60 μsec
τ = -40 μsec
τ = -20 μsec
τ = 0 μsec
τ = 20 μsec
τ = 40 μsec
τ = 60 μsec
τ = 100 μsec
Polodal distance, y (cm)
Radial distance, x (cm)
Radial distance, x (cm)

Figure 3.16: The time evolution of potential structures in poloidal (x-y) plane from –100 to +100 μs at step of 20 μs. The structure moves both in radial as well as in azimuthal direction and shows an elongation in the radial direction.

3.4.3 Discussions II

The snap shots obtained from the evolution of contour plots of conditionally averaged potential fluctuations are shown in figure 3.16 and are used for the characterisation and evolution of short scale non-linear structures. The consecutive time delay between each contour plot is kept constant i.e. 20 μs. The ratio of sizes of these structures in radial (x- axis) and poloidal (y-axis) directions is ~ 2, showing a radially stretched structure. The typical sizes obtained in radial and poloidal directions are 7- 8 cm and 4-5 cm respectively. The size, lifetime and evolution of density and potential structures are observed as identical but the important observation in the form of anti-correlation is seen for the density and potential structures. These observations thus indicate that the observed structures are coherent in nature and exhibits weak nonlinearity as shown by skewness ~0.3 and kurtosis ~2.8. We have found that the small sized structures are obtained once conditional averaged technique is applied and the possible reason for their detection may be the conditions imposed as well as limited size of probe array. This allows picking up of only those structures having higher wave numbers and high coherency and resides in higher frequency side of the spectrum. The presence of long scale structures with lower wave-number is not observed due to the limitations of the array size. However, the size of structure and its life time (coherence time) are explainable as follows: We assume the fluctuation phase velocity $\sim 3\times10^5\, cm/s$ and coherence time is ~25 μs. This gives the structure size of ~ 7.5 cm which is in the observed range. Although, there may have some poisoning effect because of the influence of poloidal component on radial propagation but as probe array is vertical and is inserted from the top side of cross-section so other effects in measurements like probe shaft sagging, misalignment are ruled out. An interesting observation is seen in the form of small structures developing into bigger ones by merging and over a long time these bigger structures again disintegrate into the smaller ones periodically. We have observed that during this time only large structure survives for longer time before they finally disappear after breaking. The obtained structures maintain certain periodicity with dipole character and are observed at different regions in the x-y plane. These structures are coherent in nature. Furthermore, we have repeated the analysis of the data and have looked into the evolution of picked up structures for different imposed conditions i.e. for $\tilde{\phi}_c > 1.0\sigma$ and $\tilde{\phi}_c > 2.0\sigma$ along with $d\tilde{\phi}_c / dt > 0$ on the reference probe. We have noticed that the dynamical characteristics of structures are very similar in comparison with above results.

3.5 Summary and Conclusions

In summary, a conclusion can be made that we have successfully produced plasma in LVPD devoid of free energy sources other than required for driving ETG mode. This includes absence of both gradients in plasma density and energetic electrons. A unique signature of ETG turbulence is observed in core plasma by representation of plasma turbulence in the parameter of radial gradient in electron temperature. Important signatures other than spectral features of ETG turbulence have been measured. The key characteristics to define the turbulence are spectral features, correlations, thresholds, beta scaling and relationship with plasma parameters. The correlation coefficients between various physical parameters like electron temperature, plasma density, magnetic field and floating potential are measured and found anti-correlation between them. The ETG instability is observed for the first time in a new operating paradigm of finite beta plasma in a laboratory device. These laboratory observations have significant implications for understanding electron transport in tokamak fusion plasmas. Although ETG instability of high beta plasma is not known to exist in present day fusion plasmas, it may be important in alternate magnetic concepts [86-89]. These observations may also be relevant to such instabilities in magnetospheric plasma, when the plasma beta is high [90]. Finally, the experiments showing the efficacy of the EEF are also relevant to the physics of negative ion formation and electron extraction in negative ion sources for high energy heating neutral beams [91].

In the non-linear aspect of the turbulence, vortex like coherent structures has been investigated in the core plasma. These observations are made in the region suitable for ETG turbulence in LVPD. The non-Gaussian characteristic of the potential and density fluctuations has been observed by means of skewness and kurtosis associated with PDF. The motion of the vortices is visualised in terms of long scale and short scale eddies obtained by conditional averaging method of data analysis. The spectral analysis reveals that linear wavelength of the mode is ~ 15 cm but this probe array is not able to see it because of its limited size. The lifetime of structure is 60-80 μs which is 3-4 times greater than correlation time (~20 μs). The important observation in the form of anti-correlation is seen for the density and potential structures. These observations thus indicate that the observed structures are coherent in nature and exhibits weak nonlinearity. Based on experimental results, we speculate that these nonlinear modes are not the primary modes but look like secondary modes having short wavelength. These secondary modes are alternative dipole structures which are localized vortices in radial direction excited by tertiary instability like Kelvin-Helmholtz (K-H) modes. The radial extents of these structures are larger than poloidal extent and thus looks like streamers dominated structures [3, 10-14, 52, 92, 93]. A detail investigation on these speculations over whole poloidal cross-section of core plasma is needed to confirm the exact nature of structures and will be addressed in future study.

The detailed theoretical models on linear and non-linear aspects of ETG mode with finite beta effect are discussed in the coming chapters. Moreover, a comparison of the experimental results on ETG turbulence with that obtained from the linear dispersion relation have also been presented in the next chapter.

Chapter 4

Theory of Coupled Whistler-ETG Mode: Application to LVPD Plasma

4.1 Introduction

In the last chapter, we have given the detail experimental results in which the ETG turbulence in finite beta plasma is demonstrated by using EEF as controlling agent. It is shown that the results were consistent with electromagnetic ETG instability. In this chapter, we present a theoretical model of ETG mode in high beta plasma to explain the experimental results of LVPD plasma.

ETG mode is widely recognized as one of possible candidate for anomalous electron transport in fusion plasma [4, 5]. The physics of anomalous electron transport across the confining magnetic field holds significant implication for improvement of confinement scheme in reactor scenario [86-94]. Several theoretical and simulation works [7, 12-15, 53-54, 94-96] have revealed that the turbulence driven by electron temperature gradient is the main source for the observed anomalous electron thermal transport in fusion machine. For this view, there are indirect pieces of evidence such as observations of threshold in electron temperature gradient and bursty nature of transport events, which are consistent with linear and nonlinear characteristics of the ETG mode [12-13, 54, 94-98]. However, direct confirmation of the existence of the ETG turbulence in fusion devices is a very difficult diagnostic exercise because ETG turbulence has extremely small-scale lengths (i.e., $k_{\perp}\rho_e \sim 1$

and $\rho_e \sim \mu m$ in Tokamak) due to presence of high magnetic fields. This has prevented securing direct measurements of correlations among different parametric components of fluctuations as well as characteristics of turbulence spectrum. Further, fusion devices have complex geometries, which restrict measurement and have limited control over the parameters that govern the turbulence. Linear plasma devices LVPD, on the other hand, provide a simplified geometry, a good realization of turbulence and control of some experimental parameters because they are operated at lower plasma density and magnetic field to bring scale length of turbulence in the measurable limits. Thus there is a clear incentive to develop theoretical understanding of ETG instability in basic plasma devices such as LVPD.

In this chapter, we focus our study in two fold objectives, first is to develop a general theory of ETG mode in high beta plasma and second is to use it for explaining experimental results presented in previous chapter. An interesting and well known feature of ETG modes in high beta plasma is that in the electrostatic limit, the slab or toroidal ETG modes have the same property as the corresponding ITG modes [86, 98] except that the dynamical roles of electrons and ions are interchanged. When electromagnetic effects are included, the ion - electron interchange symmetry breaks down. This is because the magnetic perturbations alter the electron dynamics; as a result, the parallel dynamics of ions and electron are no longer symmetric. It is well known that, Whistler and lower hybrid ETG modes lie at two ends of the frequency spectrum and these two modes can get coupled in high beta inhomogeneous plasma. This coupling of modes gives rise to a new-coupled whistler-electron temperature gradient (W-ETG) mode. In our experimental observations, it has been noted that the coupling of W-ETG mode is important when the beta of plasma is high (i.e. $\beta_e \geq 0.2$). It is also noted that the beta effects related to parallel magnetic field perturbation (δB_z) destabilize the mode whereas the electromagnetic effect associated with parallel electron dynamics are shown to be stabilizing effect on ETG mode [8, 12, 14, 94-95]. Initial part of the chapter includes the detailed parametric studies of the growth rate and frequency in which the threshold value of ETG instability have been determined. In the later sections, the numerical results are compared with experimental results observed for ETG turbulence in LVPD plasma [33, 61, 99].

The chapter is organized as follows. Detail derivations of model equations governing W-ETG mode are given in Sec. 4.2. Linear dispersion relation including both magnetic flutter and parallel magnetic field perturbations is given in Sec. 4.3. The physics of coupled W-ETG mode is presented in Sec. 4.4. The summary of experimental results is given in Sec. 4.5 and a comparison of theory with experiment is presented in Sec. 4.6. The conclusions of the chapter are summarized in Sec. 4.7.

4.2 Basic Governing Equations of W-ETG Mode

We first present the basic equations for the whistler–electron temperature gradient (W-ETG) mode including effects of magnetic flutter perturbations ($\delta B_\perp$) and parallel magnetic field perturbations (δB_z). The relevant space and frequency orderings of the W-ETG mode are:

$$\begin{aligned} &k_\perp \rho_e \le 1 << k_\perp \rho_i \ , \quad \Omega_i < \omega << \Omega_e \\ &\omega < \omega_{*T} , \quad \omega / k_\perp < c_i , \quad k_z R \sim 1 \end{aligned} \tag{4.1}$$

Here $k_\perp (k_z)$ is the perpendicular (parallel) wave vector of the mode, ω is the mode frequency, ρ_j is the Larmor radius, c_j is the thermal velocity, Ω_j is the cyclotron frequency, where $\rho_j = c_j / \Omega_j$, $c_j = \sqrt{T_j / m_j}$ $\Omega_j = eB / m_j c$, $j = e, i$ (corresponding to electron and ion respectively), R is the length of plasma along mean magnetic field. We will also use the other standards notations as follows: $\lambda_{De} = \sqrt{(T_e / 4\pi n_e e^2)}$ is the Debye's length, $\omega_{*T} = \eta_e \omega_*$, $\omega_* = k_\theta v_{*e} = k_\theta (\rho_e c_e / L_{n_e})$, $\eta_e = L_{n_e} / L_{T_e}$, $L_{n_e}^{-1} = -(d \ln n_e / dx)$, $L_{T_e}^{-1} = -(d \ln T_e / dx)$.

4.2.1 Ion dynamics:

In this section we present a brief description of ion dynamic in the background of W-ETG mode. Here, we drive the nonadiabatic ion response from fluid theory for W-ETG mode in the lower-hybrid regime. In the limits $\Omega_e > \omega >> \Omega_i$, $k_\perp \rho_i >> 1 \ge k_\perp \rho_e$ the ions are unmagnetized and if the perpendicular phase velocity of W-ETG mode is not much smaller than the ion thermal velocity (i.e. $\omega / k_\perp < c_i$), the ion inertia effect in the perpendicular ion dynamics become important. The governing equations for ion in W-ETG regime are:

Momentum equation

$$m_i n \frac{\partial \vec{v}_{i\perp}}{\partial t} = -en_i \vec{\nabla}_\perp \phi - T_i \vec{\nabla}_\perp n_i \qquad (4.2)$$

Continuity equation

$$\frac{\partial n_i}{\partial t} + n_i \vec{\nabla}_\perp \cdot \vec{v}_{i\perp} = 0 \qquad (4.3)$$

By linearizing equations (4.2-4.3), we get

$$\tilde{n}_i = -\frac{\tau_e \tilde{\phi}}{(1-\omega^2 / k_\perp{}^2 c_i{}^2)} \qquad (4.4)$$

Equation (4.4) is valid for W-ETG mode in lower-hybrid limit (i.e., $\omega \sim \omega_* > \Omega_i$) and for the perpendicular phase velocity of W-ETG mode is much smaller than the ion thermal velocity (i.e., $\omega / k_\perp < c_i$), we can also recover the adiabatic ion response from Eq. (4.4) (i.e. $\tilde{n}_i = -\tau_e \tilde{\phi}$). Note that in W-ETG dynamic, the density perturbation is out of phase with potential perturbation due to ion Boltzmann shielding effect. Here $\tilde{n}_i = \delta n_i / n_i$ and $\tilde{\phi} = e\delta\phi / T_e$ are the normalized density and potential perturbations and $\tau_e = T_e / T_i$.

4.2.2 Electron dynamics:

The electron dynamics of the W-ETG mode is described by the Braginskii's fluid equations. For $\nu_e << \Omega_e$, the electron collision with ion and neutral can be neglected in the perpendicular momentum equation but it is retained in the parallel momentum equation. The basic equations for electron are:

Continuity equation:

$$\frac{\partial n_e}{\partial t} + \vec{\nabla}.(n_e \vec{v}_{e\perp}) + \nabla_z (n_e v_{ez}) = 0 \tag{4.5}$$

Momentum equation:

$$m_e n_e \frac{d\,\vec{v}_e}{dt} = -en_e\vec{E} - \nabla p_e - en_e \frac{\vec{v}_e \times \vec{B}}{c} - m_e n_e \nu_{en} \vec{v}_e \tag{4.6}$$

Energy equation:

$$\frac{3}{2} n_e \frac{dT_e}{dt} + p_e \vec{\nabla}.\vec{v}_e = -\vec{\nabla}.\vec{q}_{e*} \tag{4.7}$$

Here, $\vec{q}_e^{\,*} = -\left(\frac{5P_e}{2m_e\Omega_e}\right)\hat{e}_z \times \vec{\nabla}_\perp T_e$ is the diamagnetic heat flow, and the derivative is defined as $\frac{d}{dt} = \frac{\partial}{\partial t} + \rho_e c_e \hat{e}_z \times \vec{\nabla}\tilde{\phi} \cdot \vec{\nabla}$. In the limit $\Omega_i << \omega < \Omega_e$ and from equation (4.6), the perpendicular electron drift velocities including modification due to magnetic field perturbation (δB_z) along the mean field ($\vec{B} = B\,\hat{e}_z$) are,

$$\vec{v}_{e\perp} = (\vec{v}_E + \vec{v}_{*Pe})(1 - \frac{\delta B_z}{B_z}) + \vec{v}_{pe} + \vec{v}_\pi \tag{4.8}$$

Where the drift velocities are defined as

$\vec{v}_E = \frac{c}{B^2}\vec{E} \times \vec{B}$ the ExB drift,

$\vec{v}_{*Pe} = -\frac{c}{eB}\hat{e}_z \times \frac{\vec{\nabla} p_e}{n_e}$ the diamagnetic drift,

$\vec{v}_{pe} = -\frac{c^2 m_e}{eB^2}\frac{d\vec{E}_\perp}{dt}$ the polarization drift

$$v_\pi = -\frac{c}{eB}\hat{e}_z \times \frac{\nabla.\vec{\pi}}{n_e} \qquad \text{the stress tensor drift,}$$

where $\hat{e}_z$ is the unit vector along the magnetic field.

We also use the Ampere's law, which may be written as

$$\vec{\nabla}\times\vec{B} = \frac{4\pi}{c}\vec{j} \approx -\frac{4\pi e n_e}{c}\vec{v}_e \tag{4.9}$$

Next, we combine the above equations to obtain a set of three linear, coupled equations that form the basis of the theory. The contribution of the $\vec{E}\times\vec{B}$ drift flux in the continuity equation can be expressed as

$$\begin{aligned}
\nabla.\left[(n_e\vec{v}_E)\left(1-\frac{\delta B_z}{B}\right)\right] &\approx \frac{n_e c}{B}\begin{bmatrix}(\vec{E}_\perp\times\hat{e}_z).\dfrac{\vec{\nabla}n_e}{n_e}-(\vec{E}_\perp\times\hat{e}_z).\dfrac{\vec{\nabla}B}{B}\\ +\hat{e}_z.\vec{\nabla}\times\vec{E}_\perp-\vec{E}_\perp.(\vec{\nabla}\times\hat{e}_z)\end{bmatrix}\left(1-\frac{\delta B_z}{B}\right)\\
&-\frac{n_e c}{B}(\vec{E}_\perp\times\hat{e}_z).\frac{\vec{\nabla}\delta B_z}{B}\\
&\approx n_e(\vec{v}_{*e}.\vec{\nabla})\tilde{\phi}-n_e\frac{\partial\delta\tilde{B}_z}{\partial t}+n_e\rho_e c_e(\hat{e}_z\times\nabla\tilde{\phi}.\nabla\tilde{n}_e-\hat{e}_z\times\nabla\tilde{\phi}.\nabla\delta\tilde{B}_z)
\end{aligned} \tag{4.10}$$

where $\tilde{n}_e = \delta n_e / n_e$, $\delta\tilde{B}_z = \delta B_z / B$, are the normalized density, potential, parallel magnetic field perturbations. Here we have neglected the effects of the electromagnetic shielding of $E_\perp$ since $\omega << k_\perp c$ (c is the velocity of light). The sum of compression of particle fluxes due to polarization and stress tensor drifts can be expressed

$$\begin{aligned}
\nabla\cdot(n_e\vec{v}_{pe}+n_e\vec{v}_\pi) &\approx n_e\rho_e^2\left(\frac{\partial}{\partial t}+\vec{v}_{*Pe}\cdot\vec{\nabla}\right)\nabla_\perp^2\tilde{\phi}+n_e\rho_e^3 c_e\,\hat{e}_z\times\vec{\nabla}\tilde{\phi}\cdot\vec{\nabla}\nabla_\perp^2\tilde{\phi}\\
&+n_e\rho_e^3 c_e\vec{\nabla}\cdot\left[(\hat{e}_z\times\vec{\nabla}\tilde{\phi}\cdot\vec{\nabla})\vec{\nabla}_\perp\tilde{p}\right]
\end{aligned} \tag{4.11}$$

Here the last two terms in right hand side correspond to the nonlinear Reynolds Stresses and $\vec{v}_{*Pe} = (1+\eta_e)v_{*e}, \quad v_{*e} = \rho_e c_e / L_n$. The compression of diamagnetic flux, including parallel magnetic perturbation, can be expressed as

$$\nabla.\left(n_e \vec{v}_{*Pe}(1-\frac{\delta B_z}{B}) \right) \approx -n_e(1+\eta_e)\vec{v}_{*e}\cdot\vec{\nabla}\delta\tilde{B}_z + n_e\rho_e c_e \hat{e}_z \times \vec{\nabla}\tilde{p}_e \cdot \vec{\nabla}\delta\tilde{B}_z \tag{4.12}$$

The above equation is assisted by additional equations like $\vec{B} = \vec{\nabla}\times\vec{A}$ and $\vec{\nabla}\cdot\vec{A} = 0$ related to the vector potential $\vec{A}$. Ampere's law may now be written as

$$\nabla_\perp^2 \vec{A} = -\frac{4\pi}{c}\vec{J} \approx \frac{4\pi e n_e}{c}\vec{v}_e \tag{4.13}$$

The parallel component of this equation can be rewritten as

$$\frac{\tilde{J}_z}{en_e} = -\frac{c_e^2 c^2}{\omega_{pe}^2}\nabla_\perp^2 \frac{\tilde{A}_z}{c} \tag{4.14a}$$

From equation (4.9), the term $\nabla_z J_z$ in continuity yields linear and nonlinear term and can be expressed as:

$$\frac{1}{en_e}\nabla_z \tilde{J}_z = -\frac{c_e^2 c^2}{\omega_{pe}^2}\nabla_z \nabla_\perp^2 \frac{\tilde{A}_z}{c} + \frac{\rho_e c_e^3 c^2}{\omega_{pe}^2}\hat{z}\times\vec{\nabla}\frac{\tilde{A}_z}{c}\cdot\vec{\nabla}\nabla_\perp^2 \frac{\tilde{A}_z}{c} \tag{4.14b}$$

Here $\tilde{A}_z = e\delta A_z / T_e$, $\tilde{A}_\perp = e\delta A_\perp / T_e$ are the normalized parallel and perpendicular vector potential associated with perpendicular and parallel magnetic field perturbations, respectively and $\omega_{pe} = \sqrt{4\pi n_e e^2 / m_e}$ is the plasma frequency. The perpendicular component of vector potential $A_\perp$ and parallel magnetic field perturbation δB_z satisfy the equation

$$\begin{aligned} \nabla^2 \delta\vec{A}_\perp &= -\vec{\nabla}\times\delta\vec{B} \approx \hat{z}\times\vec{\nabla}\delta B_z = -\frac{4\pi}{c}\delta\vec{J}_\perp \\ &\approx \frac{4\pi e n_e}{c}(\delta v_E + \delta v_{*pe}) = \frac{4\pi e n_e}{c}\rho_e c_e \ \hat{z}\times\vec{\nabla}(\tilde{\phi} - \tilde{p}_e) \end{aligned} \tag{4.15}$$

For $k_z << k_\perp$, equation (4.15) yields a relation between δB_z, $\delta\phi$, δp_e, which can be written as

$$\delta\tilde{B}_z \approx \frac{\beta_e}{2}(\tilde{\phi} - \tilde{p}_e) \tag{4.16}$$

where $\beta_e = \dfrac{8\pi n T_e}{B^2}$ is the ratio of electron plasma pressure to the magnetic pressure. The electron continuity equation (4.5) with various electron drifts has the following form:

$$\begin{aligned}\frac{\partial}{\partial t}\delta n_e + \nabla.\left[(n_e\vec{v}_E)\left(1-\frac{\delta B_z}{B}\right)\right] + \nabla.\left[n_e\vec{v}_{*Pe}\left(1-\frac{\delta B_z}{B}\right)\right] + \nabla\cdot(n_e\vec{v}_{pe} + n_e\vec{v}_\pi) \\ = \frac{1}{e}\nabla_z \delta J_z\end{aligned} \tag{4.17}$$

Combining equations (4.10-4.14) and equation (4.17), we get

$$\begin{aligned}&\frac{\partial}{\partial t}\tilde{n}_e + \vec{v}_{*e}.\vec{\nabla}\tilde{\phi} - \frac{\partial}{\partial t}\delta\tilde{B}_z - (1+\eta_e)\vec{v}_{*e}\cdot\vec{\nabla}\delta\tilde{B}_z + \rho_e^2\left(\frac{\partial}{\partial t} + \vec{v}_{*Pe}.\vec{\nabla}\right)\nabla^2\tilde{\phi} + \frac{c_e^2 c}{\omega_{pe}^2}\nabla_z\nabla_\perp^2\tilde{A}_z \\ &= -\rho_e c_e \hat{e}_z \times \nabla\tilde{\phi}.\nabla\tilde{n}_e - \rho_e^3 c_e \hat{e}_z \times \vec{\nabla}\tilde{\phi}\cdot\vec{\nabla}\ \ \nabla_\perp^2\tilde{\phi} + \rho_e^3 c_e \vec{\nabla}\cdot\left[(\hat{e}_z \times \vec{\nabla}\tilde{\phi}\cdot\vec{\nabla})\vec{\nabla}_\perp \tilde{p}_e\right] \\ &+ \frac{\rho_e c_e^3 c}{\omega_{pe}^2}\hat{e}_z \times \vec{\nabla}\tilde{A}_z \cdot \vec{\nabla}\nabla_\perp^2\tilde{A}_z + \rho_e c_e\, \hat{e}_z \times \nabla(\tilde{\phi} - \tilde{p}_e).\nabla\delta\tilde{B}_z\end{aligned} \tag{4.18}$$

In the left hand side of continuity equation (4.17), the third and the fourth linear terms and last two terms in right hand result from compression of $\vec{E}\times\vec{B}$ and diamagnetic drifts modified by δB_z perturbation (see Eqs. 4.10 and 4.12) and the others are standard linear and nonlinear terms

To eliminate $\tilde{A}_z$ wave vector from equation (4.18), we use electron parallel momentum equation

$$n_e m_e\left(\frac{\partial}{\partial t} + \vec{v}.\vec{\nabla}\right)v_{ez} = -n_e e E_z - \nabla_z p - n_e m_e \nu_e\, v_{ez} \tag{4.19}$$

Writing parallel operator $\nabla_z = \nabla_z^{(0)} + (\delta B_r / B).\nabla_r$, $E_z = -\nabla_z \phi - (1/c)\partial A_z / \partial t$ and using equation (14) in equation (4.19), we get

$$-\left(\frac{\partial}{\partial t} + \nu_e\right)(\frac{\tilde{J}_z}{en_e}) - c_e{}^2(\frac{\partial}{\partial t} + \vec{\text{v}}_{*\text{pe}} \cdot \vec{\nabla})(\frac{\tilde{A}_z}{c}) - c_e{}^2\vec{\nabla}_z(\tilde{\phi} - \tilde{p}_e)$$
$$= -c_e{}^3\rho_e\,\hat{e}_z \times \vec{\nabla}\tilde{\phi} \cdot \vec{\nabla}(\frac{\tilde{A}_z}{c}) + c_e{}^3\rho_e\,\hat{e}_z \times \vec{\nabla}(\tilde{p}_e) \cdot \vec{\nabla}(\frac{\tilde{A}_z}{c}) + c_e\rho_e\,\hat{e}_z \times \vec{\nabla}\tilde{\phi} \cdot \vec{\nabla}(\frac{\tilde{J}_z}{en_e}) \tag{4.20}$$

Eliminating $\tilde{J}_z$ in equation (4.20) from equation (4.14), we get

$$\left[\left(1-\lambda_s^2\nabla_\perp^2\right)\frac{\partial}{\partial t} - \nu_e\lambda_s^2\nabla_\perp^2 + (1+\eta_e)\vec{v}_{*e} \cdot \vec{\nabla}\right](\frac{\tilde{A}_z}{c}) + \nabla_z[(\tilde{\phi} - \tilde{n}_e - \tilde{T}_e]$$
$$= c_e\rho_e\,\hat{e}_z \times \vec{\nabla}(\tilde{p}_e - \tilde{\phi}) \cdot \vec{\nabla}(\frac{\tilde{A}_z}{c}) + c_e\rho_e\lambda_s^2\,\hat{e}_z \times \vec{\nabla}\tilde{\phi} \cdot \vec{\nabla}\nabla_\perp^2(\frac{\tilde{A}_z}{c}) \tag{4.21}$$

Here $\lambda_s = c/\omega_{pe}$ is the skin depth and ω_{pe} is the plasma frequency. We next write the evolution equation for electron temperature perturbation from electron energy equation

$$\frac{3}{2}n_e\frac{d}{dt}T_e + p_e\vec{\nabla}_\perp.\vec{v}_{\perp e} + p_e\nabla_{\|}v_{\|e} = -\vec{\nabla}.q_{e*} \tag{4.22}$$

Where $q_{e*} = -(5p_e/2m_e\Omega_e)\hat{e}_{\|} \times \vec{\nabla}T_e$, the diamagnetic heat flows. The linearize energy equation can be written as

$$\frac{\partial\tilde{T}_e}{\partial t} + (\eta_e - 2/3)\vec{\text{v}}_* \cdot \vec{\nabla}\tilde{\phi} - \frac{2}{3}\frac{\partial\tilde{n}_e}{\partial t} = -\rho_e c_e\,\hat{e}_z \times \nabla\tilde{\phi} \cdot \vec{\nabla}\tilde{T}_e + \frac{2}{3}\rho_e c_e\,\hat{e}_z \times \nabla\tilde{\phi} \cdot \vec{\nabla}\tilde{n}_e \tag{4.23}$$

In all the above equations the effect of inhomogeneous magnetic field ($\nabla_x B_{0z}$) has been neglected. This completes the derivation of the basic equations governed the W-ETG mode.

4.3 Derivation of Linear Dispersion Relation of W-ETG Mode and Analytical Solutions

In this section we drive the linear dispersion relation of W-ETG mode. Linear equations that we need for W-ETG mode in lower-hybrid regime are

$$\tilde{n}_i = -\tau_e^* \tilde{\phi}; \qquad \tau_e^* = \frac{\tau_e}{(1-\omega^2 / k_\perp{}^2 c_i{}^2)} \tag{4.24}$$

$$\begin{aligned} &\frac{\partial}{\partial t}\tilde{n}_e + \vec{v}_{*e}.\vec{\nabla}\tilde{\phi} - \frac{\partial}{\partial t}\delta\tilde{B}_z - (1+\eta_e)\vec{v}_{*e}\cdot\vec{\nabla}\delta\tilde{B}_z \\ &\qquad + \rho_e^2\left(\frac{\partial}{\partial t} + \vec{v}_{*Pe}.\vec{\nabla}\right)\nabla^2\tilde{\phi} + \frac{c_e^2 c}{\omega_{pe}^2}\nabla_z\nabla_\perp^2\tilde{A}_z = 0 \end{aligned} \tag{4.25}$$

$$\delta\tilde{B}_z \approx \frac{\beta_e}{2}(\tilde{\phi} - \tilde{n}_e - \tilde{T}_e) \tag{4.26}$$

$$\left[\left(1-\lambda_s^2\nabla_\perp^2\right)\frac{\partial}{\partial t} - \nu_e\lambda_s^2\nabla_\perp^2 + (1+\eta_e)\vec{v}_{*e}\cdot\vec{\nabla}\right](\frac{A_z}{c}) + \nabla_z[(\tilde{\phi} - \tilde{n}_e - \tilde{T}_e] = 0 \tag{4.27}$$

$$\frac{\partial\tilde{T}_e}{\partial t} + (\eta_e - 2/3)\vec{\mathrm{v}}_*\cdot\vec{\nabla}\tilde{\phi} - \frac{2}{3}\frac{\partial\tilde{n}_e}{\partial t} = 0 \tag{4.28}$$

We take perturbation as $\tilde{f}(r,t) = \tilde{f}\exp\{-i(\omega t - \vec{k}\cdot\vec{r})\}$ and assuming quasi-neutrality approximation ($\tilde{n}_e \simeq \tilde{n}_i$), the linear coupled equations are transformed into three coupled equations for $\tilde{\phi}$, $\tilde{A}_z$, $\tilde{T}_e$

$$\begin{aligned} &\left[\omega\tau_e^* + \omega_* + k_\perp^2\rho_e^2(\omega-\omega_{*pe}) + \frac{\beta_e}{2}(\omega-\omega_{*pe})(1+\tau_e^*)\right]\tilde{\phi} \\ &\qquad - \frac{\beta_e}{2}(\omega-\omega_{*pe})\tilde{T}_e - (\frac{c_e{}^2\lambda_s{}^2}{c})k_z(k_\perp{}^2\tilde{A}_z) = 0 \end{aligned} \tag{4.29}$$

$$\left[\left(1-\lambda_s^2\nabla_\perp^2\right)\omega+i\nu_e\lambda_s^2 k_\perp^2-\omega_{*pe}\right](\frac{\tilde{A}_z}{c})-k_z\left[(1+\tau_e^*)\tilde{\phi}-\tilde{T}_e\right]=0 \tag{4.30}$$

$$\omega\tilde{T}_e - \left[(\eta_e-\frac{2}{3})\ \omega_* - \frac{2}{3}\tau_e^*\omega\right]\tilde{\phi}=0 \tag{4.31}$$

Eliminating $\tilde{\phi}$, $\tilde{A}_z$, $\tilde{T}_e$ from above equations (4.29-4.31) then the linear dispersion relation for W-ETG can be written as

$$\begin{aligned}&\omega\left[\omega\tau_e^*+\omega_{*e}+k_\perp^2\rho_e^2(\omega-\omega_{*pe})+\frac{\beta_e}{2}(1+\tau_e^*)(\omega-\omega_{*pe})\right]\\&\quad-\frac{\beta_e}{2}(\omega-\omega_{*pe})\left[(\eta_e-\frac{2}{3})\omega_{*e}-\frac{2\tau_e^*}{3}\omega\right]\\&\qquad=k_z^2c_e^2\ \ k_\perp^2\rho_e^2\left[\frac{(1+\tau_e^*)\omega-(\eta_e-\frac{2}{3})\omega_{*e}+\frac{2\tau_e^*}{3}\omega}{\left\{\omega(\frac{\beta_e}{2}+k_\perp^2\rho_e^2)+i\nu_e k_\perp^2\rho_e^2\right\}-\frac{\beta_e}{2}\omega_{*pe}}\right]\end{aligned} \tag{4.32}$$

Here, first term in the square bracket on the left hand side of equation (4.32) corresponds to rate of change of density, the second term represents the change in density due to $\vec{E}\times\vec{B}$ convection, third term results from polarization and stress tensor drifts, fourth and fifth terms correspond to finite compression of $\vec{E}\times\vec{B}$ and diamagnetic drifts modified by δB_z perturbation (see Eq. 4.10 and Eq. 4.12) in a homogeneous magnetic field. The last term in the right hand side of equation (32) is corresponding to parallel compression of electron flow including finite β_e effects associated with $\delta B_\perp$ perturbations. We now describe a few special limits of the generalized dispersion relation (4.32).

4.3.1 Whistler mode:

We can recover the whistler wave from equation (4.32) by just considering plasma is homogeneous and collisionless (i.e., $\omega_{*e}=\omega_{*pe}=0$, and $\nu_e=0$). In the limit $\omega<k_\perp c_i$, where ions are adiabatic ($\tilde{n}_i=-\tau_e\tilde{\phi}$), a simple dispersion relation of whistler mode can be written as

$$\omega^2 \ \frac{\beta_e}{2}\left[\frac{2\tau_e}{\beta_e}+\frac{2}{\beta_e}k_\perp^2\rho_e^2+(1+\frac{5\tau_e}{3})\right]=k_z^2c_e^2 \ \ k_\perp^2\rho_e^2\,\frac{2}{\beta_e}\left[\frac{1+\dfrac{5\tau_e}{3}}{1+\dfrac{2}{\beta_e}k_\perp^2\rho_e^2}\right] \tag{4.33}$$

In order to compare the whistler wavelength with skin depth, we replace electron Larmor radius with skin depth (i.e., $\rho_e^2 = 0.5\beta_e\,\lambda_s^2$), equation (4.33) can be re-written as

$$\omega = \frac{(k_z k_\perp \lambda_s^2)\Omega_e}{(1+k_\perp^2\lambda_s^2)}\left[1+\frac{2\tau_e}{\beta_e(1+5\tau_e/3)}+\frac{k_\perp^2\lambda_s^2}{(1+5\tau_e/3)}\right]^{-\frac{1}{2}} \tag{4.34}$$

Equation (4.34) is the real frequency of whistler wave modified due to following effects: (i) thermal correction (τ_e), which results from adiabatic ion motion, (ii) β_e correction, which is the product of δB_z perturbation results from compression of $\vec{E}\times\vec{B}$ drift, and (iii) finite Larmor radius effect from electron polarization drift.

4.3.2 ETG mode:

From a generalized dispersion relation presented in equation (4.32), we can also recover the frequency and growth rate of simple electrostatic ETG mode by taking $\beta_e \approx 0$, $k_\perp^2\rho_e^2 << 1$, and $\omega \sim \omega_{*e} < \omega_{*Te} = \eta_e\omega_{*e}$ limits, then equation (4.32) yields

$$\omega_r = (1/2)[\eta_e\omega_{*e}k_z^2c_e^2/\tau_e]^{1/3}, \tag{4.35a}$$

$$\gamma = (\sqrt{3}/2)[\eta_e\omega_{*e}k_z^2c_e^2/\tau_e]^{1/3} \tag{4.35b}$$

Note that when β_e is large (i.e., $\beta_e \geq 1$ and $\delta B_z \neq 0$), in that situation we find that both the Whistler and ETG couple each other and giving rise to a new mode the W-ETG mode. The physics of coupled W-ETG mode will be discussed in next section.

4.4 Physics of Coupled W-ETG mode

We now show that when the magnetic gradient and curvature effects are absent, the long wavelength 'toroidal' ETG - like mode can be excited, because coupling of the slab ETG mode with the Whistler mode at high β_e leads to a similar compression physics that works in toroidal electron temperature gradient (ETG) mode. Theoretically, ETG modes have two branches: (i) slab ETG mode [7, 15] driven by the parallel compression of electron fluid, and (ii) toroidal ETG mode [12-14, 54, 94-95] driven by finite compression of diamagnetic flux arising due to inhomogeneous magnetic field in tokamak. In both cases the compressibility is responsible for amplifying the temperature perturbations. In the electrostatic limit, the slab or toroidal ETG modes have the same property as the corresponding ITG modes except that the dynamical roles of electrons and ions are interchanged. The electromagnetic effect can be significant if perpendicular wavelength of the mode is above the electron gyro radius and this effect yield the ion - electron interchange symmetry breaks down. This is because the magnetic perturbations alter the electron dynamics. As a result, the parallel dynamics of ions and electron are no longer symmetric.

4.4.1 Slab ETG mode:

In low β_e plasma, the slab mode is primarily driven by parallel compression of electron motion along the magnetic field. The compression effect in electron parallel motion will generate temperature and density perturbations. The density perturbation is an out of phase to potential perturbation via ion Boltzmann shielding effect. This potential perturbation creates $\vec{E}\times\vec{B}$ drift, which brings cold electrons in a compressed region and thus lowering the pressure. The lower pressure attracts more electrons, further increasing the compression. This positive feedback loop leads to instability of growth $\gamma \sim (\sqrt{3}/2)[\eta_e \omega_{*e} k_z^2 c_e^2/\tau_e]^{1/3}$ [Eq. 4.35].

4.4.2 Toroidal ETG mode:

A similar feedback scheme also applies in case of toroidal ETG mode but the perpendicular compression of diamagnetic flux is non-zero due to inhomogeneous magnetic field. The electron temperature perturbation takes place in finite compressibility of diamagnetic flux,

$$\vec{\nabla}_{\perp} \cdot (n_e \vec{v}_{*pe}) \approx (n_0 \rho_e c_e / R) \partial_y (\delta n / n_0 + \delta T_e / T_{e0}) \tag{4.36}$$

Here $|-\nabla_x B / B|^{-1} \approx R$ is the magnetic scale length. The evolution of toroidal ETG mode perturbations in plasma can be best understood in a simplified case where density is flat, $\beta_e = 0$, $k_{\perp}\rho_e < 1$, and $\omega > k_z c_e$ otherwise these effects determine the frequency and threshold of toroidal ETG mode. The governing equations of ETG mode are: (1) the continuity equation, where the density perturbation couples only with electron temperature perturbation along with ions Boltzmann relation (i.e. $\tilde{n}_e = -\tau_e \tilde{\phi}$), and (2) the temperature perturbation evolves via $\vec{E} \times \vec{B}$ convection of mean temperature in electron energy equation. This simple set of equations can be written as:

$$\text{(i) } \tilde{n}_e = -\tau_e \tilde{\phi} \qquad \text{(ii) } \omega \tilde{n} = (2L_n / R) \omega_* \tilde{T}_e, \qquad \text{(iii) } \omega \tilde{T}_e = \eta_e \omega_{*e} \tilde{\phi} \tag{4.37}$$

Here, the form of inhomogeneous magnetic field is taken as $B_z(x) = B_z(1 - x/R)$, R is the major radius of tokamak. Combining above equations, we get the growth rate, $\gamma \sim k_y \rho_e c_e \sqrt{2} / \sqrt{RL_{Te}}$. This is the maximum growth of toroidal ETG mode [12].

4.4.3 W-ETG mode:

Interestingly, even without magnetic gradient and curvature effects the toroidal ETG like mode can be excited in a high $\beta_e > 0.2$ regime at the long wavelength end through coupling of ETG modes with Whistler mode. The development of W-ETG mode in plasma could be understood as follows: when β_e is high, the electron perpendicular $\vec{E} \times \vec{B}$ and v_{*pe}, the diamagnetic drifts will significantly modify due to finite parallel magnetic fluctuation δB_z and have the form of $\vec{v}_{\perp e} = (\vec{v}_{E\times B} + \vec{v}_{*pe})(1 - \delta B_{\parallel} / B)$. For $k_{\parallel} / k_{\perp} < 1$, $k_{\perp} L_{pe} > \beta_e / 2$, and $\beta_e > 0.2$, the perpendicular electron current can be expressed as $J_{\perp} = -en_e(v_{E\times B} + v_{*e})$, which yields $\delta B_z / B \approx (\beta_e / 2)(e\delta\phi / T_e - \delta p_e / p_{e0})$. This shows the importance of coupling of ETG mode to Whistler waves. The reverse coupling is seen in the continuity equation (4.25) through terms $\partial_t \tilde{n}$ and $(\partial_t + v_{*pe}\partial_y)\delta\tilde{B}_z$, which comes from

$$\vec{\nabla} \cdot n_e(\vec{v}_{E\times B} + \vec{v}_{*pe}) = n_e(\beta_e / 2)(\partial_t + v_{*pe}\partial_y)(\delta n_e / n_0 + \delta T_e / T_{e0} - e\delta\varphi / T_e) \tag{4.38}$$

We note the similarity in temperature perturbations produced in electron continuity equation by finite diamagnetic compressibility due to non-zero $\nabla_x B$ effect (as shown in Eq. 4.36) and finite diamagnetic compressibility due to δB_z perturbation effect, in both cases their response to the temperature perturbations, which are responsible for temperature gradient driven mode, in continuity equations emerge in same phase. Quantitatively, it can be shown from generalized dispersion relation (4.32) that this coupling is important when $k_z L_{Te} \sim \beta_e$ i.e., for lower frequency and longer wavelength Whistler mode perturbations in high β_e plasma. Moreover W-ETG mode is unstable only when the electron temperature gradient crosses a threshold value, $\eta_e > 2/3$.

4.5 Summary of Experimental Results of the ETG Turbulence

In the preceding chapter, the relevant basic parameters of LVPD plasma are shown in table-3.1. The observed crucial parameters in low magnetic field indicate that turbulence at gyro radius scale can be measured with convenience in LVPD but becomes extremely difficult to measure in tokamaks. In the radial profile of mean plasma parameters [Fig. 3.2], it was observed that the density profile was flat and the temperature profile was steeper in the core region ($r \le 50\,cm$) in the case when EEF is activated. The time series measurements and radial profile of electron temperature (δT_e), ion saturation current (δI_s) and the magnetic field (δB_z) perturbations were also presented in the two EEF configurations [Fig. 3.3]. It was seen that all fluctuation amplitudes in the core region were large for steeper temperature gradient and they reduced significantly to noise level for flat temperature profile [Fig. 3.4]. The fluctuation characteristics also changed from electrostatic to electromagnetic for increasing plasma beta ($\beta_e \geq 0.2$) [Fig. 3.8]. It was observed that normalized density fluctuations ($\delta I_s / I_s$) were anti-correlated with potential fluctuation ($e\delta\phi / T_e$) and magnetic fluctuation ($\delta B_z / B_z$) whereas temperature fluctuation ($\delta T_e / T_e$) is also anti-correlated with potential fluctuations [Fig. 3.5]. In addition, the frequency and wavelength spectra were broad band followed with power law and found in lower hybrid range of frequency ($\Omega_i < \omega << \Omega_e$) with long wavelength ($k_\perp \rho_e < 1$). The joint wave number – frequency spectrum [Fig. 3.6], $S(k_\perp, \omega)$ for δn_e and δB_z show peak at frequency, $\omega \approx 20$ krad/s and wave-number, $k_\perp \approx 0.15$ cm^{-1} having phase velocity (~ 3 x 10^5 cm/s) in the same direction as the electron diamagnetic drift velocity (~5 x 10^5 cm/s). Moreover, the parallel wave number is found very small ($k_z \sim 0.008 cm^{-1}$) satisfying the condition $k_z / k_\perp << 1$ with axial phase velocity $\sim 6 \times 10^6 cm/s$ [Fig. 3.7].

4.6 Comparison of Theory with Observation

In this section, we try to compare the above summarized experimental observations with numerical results including evaluation of fluctuation levels with beta scaling. We now present a comparison of these results as following.

4.6.1 Numerical Results and Discussion

In the numerical results, the plots of growth rate, real frequency as a function of wave number, plasma beta and temperature gradient scale length from linear dispersion relation derived from fluid theory are shown. The typical value of basic plasma parameters of the experiment are: $T_e \approx 2\ eV$, $n_e \approx 3 \times 10^{17} m^{-3}$, the applied axial magnetic, $B \approx 6G$, $\beta_e \sim 0.6$, $L_{Te} \sim 0.5m$, $\nabla_r \ln n_e = \nabla_r \ln B \approx 0$ in the core region, and electron Larmor radius $\rho_e = c_e / \Omega_e \approx 0.5 \times 10^{-2}\, m$. The model predictions that are comparable to experimental observations are as follows: (i) fluctuation frequency and wave number, (ii) magnitude of fluctuation levels, namely $\tilde{\phi} \sim 1.5$ %, $\tilde{n}_e \sim 4\%$ and $\tilde{B}_z \sim 2\%$, (iii) $\tilde{n}_e$ are out of phase with $\tilde{\phi}$ and $\tilde{B}_z$, and (iv) $\tilde{T}_e$ and are out of phase with $\tilde{\phi}$. The fluctuation frequency is in the lower hybrid range, namely, $\Omega_i < \omega << \Omega_e$ and the wave number satisfies the condition $k_\perp \rho_e < 1 << k_\perp \rho_i$. The experimental frequency ordering reveals that electrons are magnetized whereas ions are typically unmagnetized and collisionless. These experimental conditions are also in agreement with theoretical prediction of the W-ETG mode.

We introduce the normalized parameters: $\hat{\beta} = \beta_e / 2$, $\varepsilon_T = R / L_T$ and $\varepsilon_n = R / L_n$, $\hat{\omega} = R\omega / c_e$, $\hat{\nu}_{en} = \nu_{en} R / c_e$, $\hat{k} = k_\perp \rho_e = k_y \rho_e$, $\hat{k}_z = k_z R$, $\tau_e = T_e / T_i$, $\hat{\gamma} = R\gamma / c_e$ and $\tau_e^* = \tau_e [1 - \tau_e \hat{\omega}^2 \hat{\rho}_e^2 m_i / \hat{k}_\perp^2 m_e]^{-1}$, where $R = 300\ cm$ is axial length along the ambient magnetic field. In the limit $\omega / k_\perp \le c_i$, the ion inertia effect becomes important and the ion Boltzman's relation takes the form $\tilde{n}_i = -\tau_e \tilde{\phi} / (1 - \omega^2 / k_\perp{}^2 c_i{}^2) = -\tau_e^* \tilde{\phi}$. Therefore, we rewrite the generalized dispersion relation (32) for ETG mode as:

$$\begin{aligned} &\hat{\omega}\left[\hat{\omega}\tau_e^* + \varepsilon_n \hat{k}_y + \hat{k}_\perp^2(\hat{\omega} - (\varepsilon_n + \varepsilon_T)\hat{k}_y) + \hat{\beta}(1+\tau_e^*)[\hat{\omega} - (\varepsilon_n + \varepsilon_T)\hat{k}_y]\right] \\ &\qquad - \hat{\beta}\left[\hat{\omega} - (\varepsilon_n + \varepsilon_T)\hat{k}_y\right]\left[(\varepsilon_T - \frac{2\varepsilon_n}{3})\hat{k}_y - \frac{2\tau_e^*}{3}\hat{\omega}\right] \\ &\qquad\qquad = \hat{k}_z^2 \hat{k}_\perp^2 \frac{\left[[(1+\frac{5\tau_e^*}{3})\hat{\omega} - (\varepsilon_T - \frac{2\varepsilon_n}{3})\hat{k}_y]\right]}{\left[\hat{\omega}(\hat{\beta} + \hat{k}_\perp^2) + i\hat{\nu}_{en} k_\perp^2 - \hat{\beta}(\varepsilon_n + \varepsilon_T)\hat{k}_y\right]} \end{aligned} \tag{4.39}$$

Fig. 4.1 shows normalized linear growth $\hat{\gamma}$ as a function of wave number $\hat{k}$ for various values of β_e keeping other parameters fixed at $\tau_e = 2$, $\hat{k}_z = 0.5$, $\varepsilon_T = 6$ and $\varepsilon_n = 0$. It shows that the $\hat{\gamma}$ increases with increasing β_e and has maximum growth around $\hat{k} < 0.5$. Simultaneously, the peak of the growth rate moves towards higher $\hat{k}$ when $\beta_e = 0$. This also indicates that the electromagnetic nature of the instability changes to purely electrostatic.

As shown in gyro kinetic simulations [11], the linear theory of ETG shows that the growth of the instability peaks at $k_\perp \rho_e \sim 0.3 - 0.5$ and non-linear theory suggests its peaking at ~ 0.2. This shows the importance of kinetic and non-linear effects. The global kinetic code results and nonlinear feature such as inverse cascade process (e.g., generation of W-ETG streamers, zonal flows which could explain the shift of peak growth rate to longer wavelength) will be presented in next chapter.

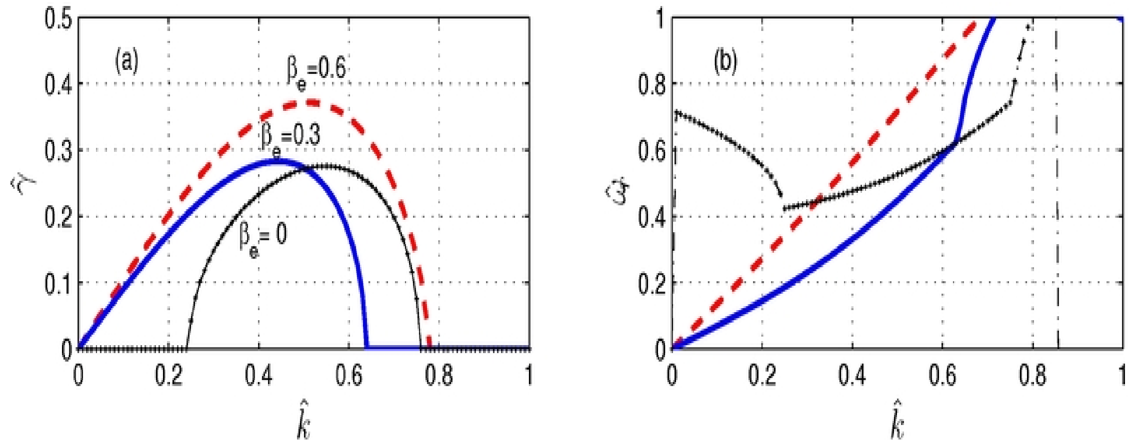

Figure 4.1: The growth rate ($\hat{\gamma}$) and real frequency of mode ($\hat{\omega}$) versus $\hat{k}$. In this plot and other plots, $\hat{k}_y = \hat{k}_\perp = \hat{k}$.

Fig. 4.2 illustrates the growth $\hat{\gamma}$ and frequency $\hat{\omega}$ as a function of beta β_e for various values of ε_T for parameters $\tau_e = 2,\ \hat{k}_z = 0.5, \hat{k}_y = 0.5,\ \varepsilon_n = 0$. The growth rate decay for beta $\beta_e = 0 - 0.2$; this is a standard feature of electrostatic ETG mode where the beta effect arises through $\delta B_\perp$ perturbation has the stabilizing effect. When $\beta_e > 0.2$, the coupling of parallel magnetic field δB_z perturbation with other fluctuating plasma fields becomes important. In this case, ETG mode couples with whistler wave. Also note that for β_e greater than critical value, there is threshold value of β_e for each ε_T before which growth increases and decreases thereafter. It also illustrates that as ε_T increases, threshold value of β_e decreases i.e. peak of the growth increases but shifts towards lower β_e. There is a band of β_e for each ε_T before which mode is like electrostatic and becomes electromagnetic after the critical value.

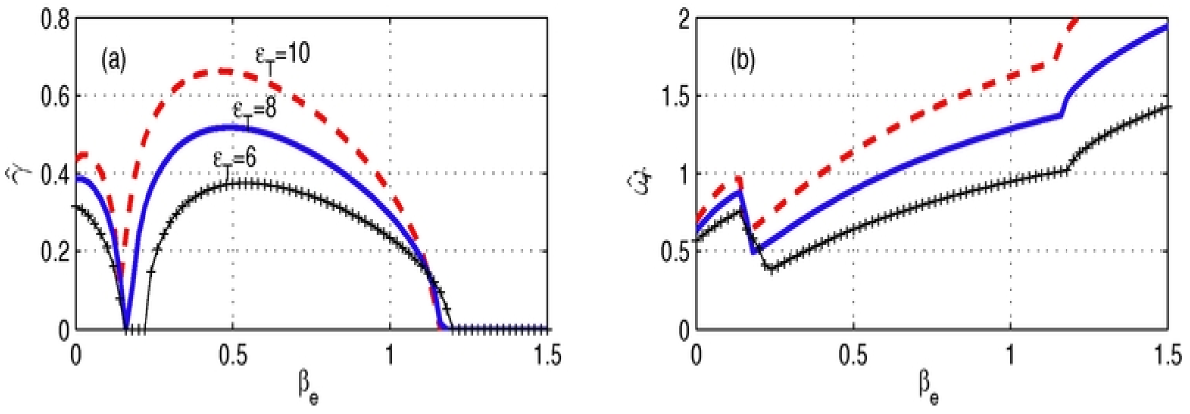

Figure 4.2: The growth rate ($\hat{\gamma}$) and real frequency of mode ($\hat{\omega}$) versus β_e for different values of ε_T .

Fig. 4.3 shows the growth and real frequency as a function of temperature gradient scale length (ε_T) for various value of density gradient scale length (ε_n) with fixed parameters $\tau_e = 2,\ \hat{k}_z = 0.5, \hat{k}_y = 0.5,\ \beta_e = 0.6$. The results indicate that growth of mode increases with increasing value of ε_T. The profile shows a threshold in ε_T for each value of ε_n and numerical critical gradient ($\eta_{e,\,th} \sim 1.5$) for excitation of the mode is found less than experimentally obtained gradient ($\eta_{e,\exp} \sim 6$) for this plasma condition. The result is consistent with the standard threshold of ETG mode where the mode is stable if $\eta_e(\varepsilon_T / \varepsilon_n = L_n / L_T) < 2/3$. It is also noted that mode does not exhibit any growth for $\varepsilon_T = 0$ irrespective of the value of ε_n.

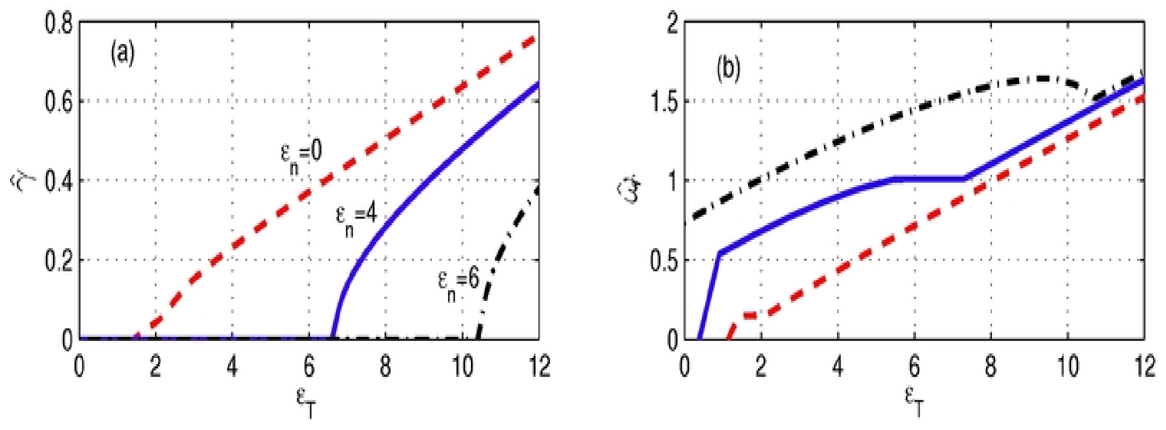

Figure 4.3: The growth rate ($\hat{\gamma}$) and real frequency ($\hat{\omega}$) versus ε_T for various value of ε_n .

Fig. 4.4 illustrates the role of ion inertia on W-ETG mode. The growth rate of W-ETG mode reduces when ion are non-Boltzmann (ion inertia effect is important). Ion inertia effect in W-ETG dynamic is significant when the perpendicular phase velocity of mode is order of ion thermal velocity $\omega / k_{\perp} \leq c_i$.

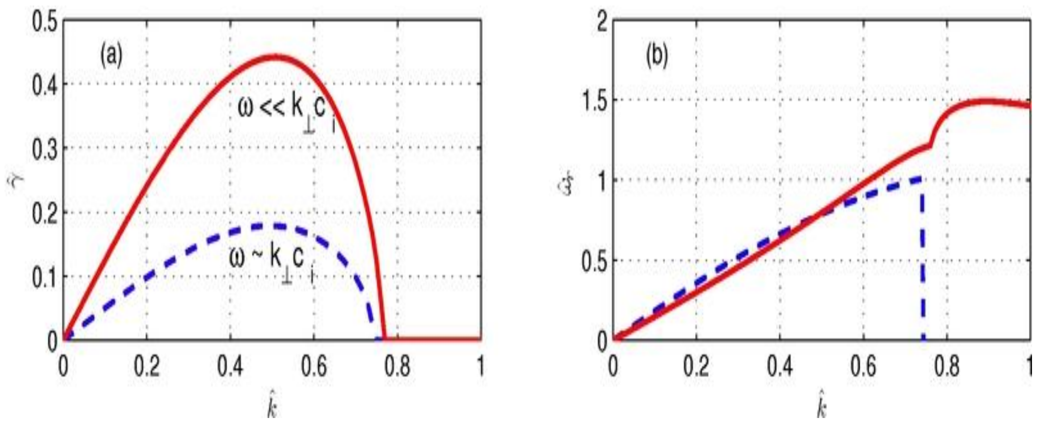

Figure 4.4: Growth ($\hat{\gamma}$) and frequency ($\hat{\omega}$) versus $\hat{k}$ when (a) ions are Boltzmann ($\omega / k_{\perp} << c_i$), and (b) ions are non-Boltzmann ($\omega / k_{\perp} \leq c_i$).

The effect of electron-neutral collision frequency ($\hat{\nu}_{en}$) on W-ETG mode is shown in Fig. 4.5. As it is clear from the analysis of W-ETG mode that mode is reactive like a toroidal ETG mode. In general the dissipation has the stabilizing effect on reactive mode. The profile shows that the growth rate of mode reduces for $\nu_e \neq 0$.

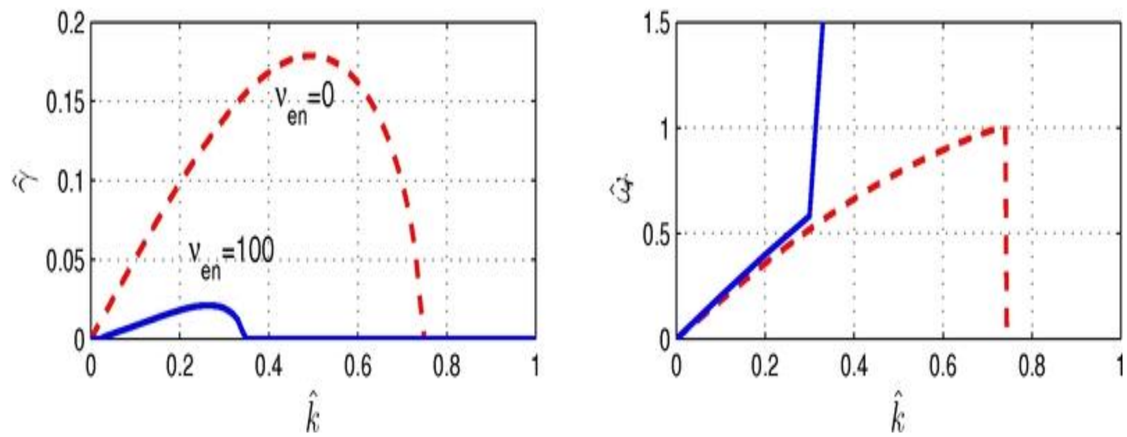

Figure 4.5: The growth ($\hat{\gamma}$) and frequency ($\hat{\omega}$) when (a) $\hat{\nu}_{en} (= \nu_{en} R / c_e) \neq 0$, and (b) $\hat{\nu}_{en} = 0$.

4.6.2 Estimation of Fluctuation Level and Beta Scaling

In this subsection, we attempt to explain some features of fluctuations as summarized in preceding section. We estimate saturated levels for the observed turbulence by using the simple mixing length argument since convective losses are not important in the present scenario. Comparing the convective energy loss with the linear growth rate of the mode, the ineffectiveness of convective losses in determining the saturation level can easily be shown. From Fig. 1, we observe the dimensionless $\hat{\omega}_r \sim 0.6$, $\hat{\gamma} = 0.35$ for $\beta_e = 0.6$, $\hat{k}_\perp = 0.4$ and $\partial\hat{\omega}_r / \partial\hat{k}_r \approx 1.5$. The group velocity and real frequency of W-ETG mode for LVPD plasma parameters are as follows:

$$\begin{aligned} V_{gy} &= \frac{\partial\omega_r}{\partial k_r} = \frac{\partial\hat{\omega}_r}{\partial\hat{k}_r}\frac{c_e\rho_e}{R} \approx 4.5\times10^5 cm/s \\ \omega &= \hat{\omega}\frac{c_e}{R} \approx 2\times10^5 \, rad/s \end{aligned} \tag{4.40}$$

The estimated value of velocity and frequency are in good agreement with experimental results summarized in section 4.5. The ratio of convective loss rate V_{gy}/L_{Te} and linear growth rate ($\gamma = \hat{\gamma}c_e/R$) is $(V_{gy}/L_{Te}\gamma) \sim (V_g\varepsilon_T/c_e\hat{\gamma}) \approx 0.04 << 1$). This shows weak stabilization due to convective process. The saturation must therefore come only through nonlinear effects. Note that the $E\times B$ rotation shear has weak effect on ETG mode since the observed shearing rate is much smaller than growth rate of ETG mode due to negligible electric field in core plasma. To estimate the fluctuation levels at saturation, we note that for $k_\| / k_\perp << 1$, the perpendicular electron current $J_\perp = -en_e(v_{E\times B} + v_{*e})$ yields $\delta B_z / B = \tilde{B} \approx (\beta_e/2)(\tilde{\phi} - \tilde{n}_e - \tilde{T}_e)$ [Eq. 4.26]. Hence the fluctuation amplitudes of $\tilde{n}$, $\tilde{B}$ and $\tilde{T}$ can be expressed in term of $\tilde{\phi}$ (using linear relations)

$$\begin{aligned} \langle\tilde{n}\rangle &= -\left|\tau_e^*\right|\langle\tilde{\phi}\rangle \\ \langle\tilde{B}\rangle &= \hat{\beta}\left|[(1+5\tau_e^*/3) - (\varepsilon_T - 2\varepsilon_n/3)(\hat{k}_y/\hat{\omega})]\right|\langle\tilde{\phi}\rangle \\ \langle\tilde{T}\rangle &= \left|[(\varepsilon_T - 2\varepsilon_n/3)(\hat{k}_y/\hat{\omega}) - 2\tau_e^*/3]\right|\langle\tilde{\phi}\rangle \end{aligned} \tag{4.41}$$

In order to calculate fluctuation level of above parameters, we approximate saturated values of $\tilde{\phi}$ using the mixing length estimates $\langle \tilde{\phi} \rangle \approx 1/k_x L_T = \varepsilon_T \rho_e / \hat{k}_\perp R$ [94]. Figure 4.6 shows the comparison of experimentally observed and theoretically estimated $\delta B_Z / B_Z$, $\delta n_e / n_e$, $\delta T_e / T_e$ and ratio of normalized temperature to density fluctuations as function of β_e. In the experiment, the ambient magnetic field remains constant and plasma beta is varied by only changing the plasma density via changing filament current.

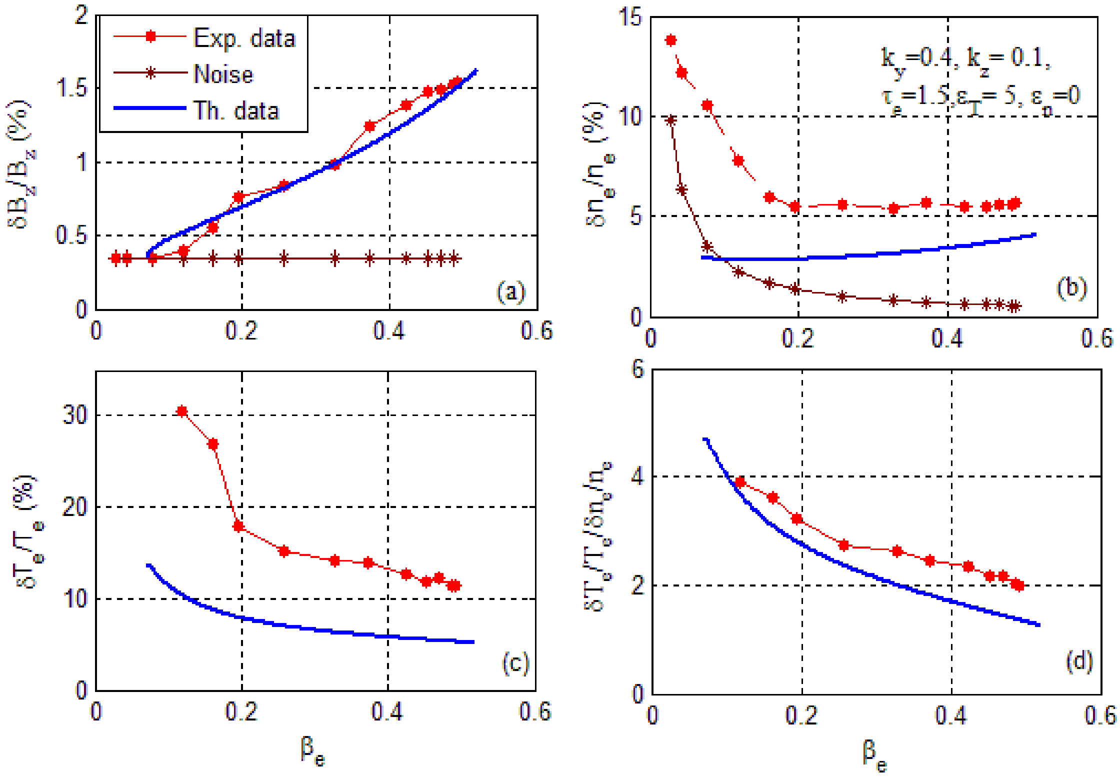

Figure 4.6: The profiles represent the comparison between theoretically estimated (continuous line) and experimental observed (filled circle) fluctuations with beta. The beta scaling is compared for normalized fluctuations of (a) magnetic field (b) density (c) electron temperature and (d) ratio of electron temperature to density fluctuations.

In figure 4.6(a), the comparison of magnetic fluctuation shows good agreement for β_e scaling in both cases. Results show that magnetic fluctuation increases with β_e because δB_Z contributions leading to additional plasma compression effect and destabilization of the mode. For $\beta_e < 0.1$, the nature of fluctuations becomes electrostatic because the effect of $\delta B_\perp$ largely dominates over δB_Z perturbation and fluctuation estimation is consistent with the numerical results of stabilization of the ETG mode [Fig. 4.2]. On the other hand, density fluctuation, temperature fluctuation decreases with β_e [Fig. 4.6(b-c)]. In the figure 4.6(d), the estimated ratio of $\delta T_e / T_e$ and $\delta n_e / n_e$ amplitudes decreases with β_e and found very close to the experimental observations for $\beta_e = 0.1 - 0.3$. We also found that the density and temperature perturbations are also out of phase with potential perturbations for typical values $\varepsilon_T = 5, \hat{k}_y = 0.4, \varepsilon_n = 0, \tau_e = 1.5, \hat{k}_z = 0.1$. The theoretical estimated value of phase angles between $\hat{n} - \hat{\phi}_f$, $\hat{n} - \hat{B}_z$ and $\hat{T}_e - \hat{\phi}_f$ for the observed frequency of the mode are 159^0, 108^0 and 134^0 whereas experimentally obtained phase angles are 152^0, 132^0 and 127^0 respectively. These theoretical findings are also in good agreement with experimental results.

4.7 Conclusions

In the present chapter, the basic fluid equations describing W-ETG mode in finite β_e plasma are derived and analytical solutions for different cases are presented. The theory is validated by comparing the results of linear dispersion relation with experimental observations of laboratory plasma in linear device. Theoretical results based on general mixing length arguments are found to be in reasonable agreement with the experimental results, in terms of fluctuation magnitude, correlations, phase angle, beta scaling and parametric dependence of growth rates and observed frequencies. It is interesting to note that the mixing length argument for predicting the level of fluctuations for ETG modes is supported by our experimental observations in LVPD. It is, however, widely known that the mixing length estimates of electron transport due to ETG turbulence in a tokamak are too small (i.e. typically $\sqrt{m_e / m_i}$ times ion gyro Bohm diffusion coefficient) to explain the observations. To understand the magnitude of high anomalous electron transport in tokamaks, it has been argued recently [12-13, 54] that the ETG modes are nonlinearly dominated by radially elongated modes known as "streamers" which are generated by a cascade process towards longer scales. These streamers saturate by tertiary instability like Kelvin-Helmholtz instability and yield the transport much larger than mixing length estimates, which is close to the observations. The implication of this discussion is that for obtaining the large transport from ETG mode in tokamak we rely on nonlinear cascades of ETG mode to longer wavelength streamers and its saturation to tertiary wave and whereas in LVPD plasma, ETG mode saturates before the formation of streamers. This observation may be indicative of a very significant limitation to the range of applicability of mixing length argument. We note that the ratio ρ_e / L_{Te} is $\sim 10^{-2}$ for LVPD plasma parameters whereas the ratio ρ_e / L_{Te} is $\sim 10^{-5}$ for tokamaks. The ratio ρ_e / L_{Te} of tokamak plasma is $\sim 10^{3}$ times smaller than ρ_e / L_{Te} for LVPD plasma. It would then seem that flattening of electron temperature by excursions of electron gyro orbit could occur only when electron can sweep across a significant length of gradient in electron temperature. This also suggests that the mixing length theory to determine fluctuation level may be valid only for values of ρ_e / L_{Te} larger than a critical value. In order to verify such a hypothesis one needs a large data base from various machines that is beyond the scope of this thesis. It is also shown that the finite β_e effects associated with parallel magnetic field perturbation δB_z have the destabilization effect on W-ETG mode whereas β_e effect due to magnetic flutter $\delta B_\perp$ perturbation stabilizes the mode. The effects of non-adiabatic ions and electron collision are shown to be stabilizing for W-ETG mode in lower-hybrid regime. Moreover, it is also shown that the non-adiabatic ion response is important in determining the ratio of density fluctuation and potential fluctuation amplitudes. From experimental observation it has been seen that correlations among fluctuations of density, potential and magnetic fields are matches well with theoretical investigations. Present extension of the conventional theory of ETG instability in an entirely different high beta regime can be of use such as in magnetospheric plasma during sub storm [100, 101] as well as in alternative magnetic confinement concepts [86, 87, 88] and fusion devices [89].

The present theoretical investigation is based on linear calculations and does not include the nonlinear terms in derived dispersion relation. The nonlinear effects play the significant role in saturation mechanism of the turbulence. Therefore, a detail study of secondary instability is necessary to understand the actual physics of the turbulence spectrum. In next chapter, theoretical model for electromagnetic secondary instability of coupled Whistler-Electron Temperature Gradient is presented by deriving the dispersion relations for long scale mode like zonal flows and streamers. Moreover, the numerical results for zonal flows, zonal field, electromagnetic streamers and magnetic streamers have also been discussed.

Chapter 5

Electromagnetic Secondary Instabilities of Coupled Whistler-ETG Turbulence

5.1 Introduction

In the previous chapter, we studied the linear features of coupled W-ETG mode and a comparison was made with experimental results of the electromagnetic ETG turbulence in the LVPD plasma [33]. The nonlinear terms of the fluid equations were completely ignored during the derivation of dispersion relation of W-ETG mode [53]. In general, the effect of nonlinear terms determines the saturation mechanism of the turbulence by exciting secondary instabilities associated with large scale modes [3]. In the case of ETG turbulence, two dominant nonlinear drift modes that would be excited are zonal flows [3, 13, 55-57, 86] and streamers [12, 51, 54]. The role of these nonlinear modes is found to be very crucial in determining the evolution of short scale drift instabilities. The earlier results support the argument that zonal flows like structure suppresses the turbulent heat transport whereas streamers like structures enhance the radial heat transport in plasma [12]. In this regard, a detail study related to the generation mechanism of zonal flows and streamers becomes necessary to understand the exact nature of turbulent anomalous transport in finite beta plasma.

This chapter investigates excitation of nonlinear structures like zonal flows and steamers in ETG turbulence at finite beta in cyclindrical plasma device like LVPD [33, 61]. Linear characteristics of ETG mode in finite beta, dubbed as Whistler-ETG, has been well studied by

Singh et al., [53]. The present chapter is a follow-up nonlinear extension of the previous chapter. Complete set of nonlinear equations describing the W-ETG turbulence has been derived considering adiabatic ion response. Zonal flows and steamers excitation has been studied as a modulational instability process of the host W-ETG turbulence. Equations for the long scale modes have been derived using appropriate space-time averaging of the nonlinear set of equations where the nonlinear terms are evaluated in quasilinear limit from the linear responses. Here, long scale means greater than elecron gyro scale but less than the radial gradient scale length. Short scale turbulence is described by Wave Kinetic Equation (WKE) for the wave action density [3]. It is shown that electromagnetic zonal flows, zonal fields, electromagnetic streamers and magnetic streamers can be excited. It is seen that the zonal perpendicular magnetic field evolves independent of zonal electrostatic potential (or flow) while for streamers perpendicular magnetic field evolves in coupling with potential and temperature fields but gets decoupled for axially smooth perturbations i.e., when parallel wave number $q_z = 0$. The dispersion relations for zonal flows and streamers are solved numerically and growth rates and real frequencies are calculated with respect to different parameters like poloidal and parallel wave numbers, plasma beta and temperature gradient length scale. Zonal flows and fields are found to grow at different rates. Similarly electromagnetic and pure magnetic streamers show different growths. The backreaction of secondary structures on the host turbulence and its self-consistent evolving characteristic has been studied. The competition between Reynolds and Maxwell stresses together with non-monotonic behavior of linear W-ETG growth spectra with respect to beta leads non monotonic behavoir of zonal flows and streamers growth rate with beta. This can be expected to make important impact on turbulent transport of heat and particles.

The organization of the chapter is as follows. In the section **5.2,** the model equations of W-ETG are given and a brief summary of linear physics of W-ETG modes is given in section **5.3**. Section **5.4** describes nonlinear model for zonal flows and section **5.5** represents the mechanism of streamers excitation in the background of W-ETG turbulence. The numerical results and discussion for zonal flows and streamers are presented in section **5.6**. The chapter will conclude in section **5.7**.

5.2 Model Equations for W-ETG Turbulence

We present the basic equations for governing the W-ETG mode turbulence in shearless magnetic field for finite beta plasma which contain the effects of magnetic flutter perturbations ($\delta B_\perp$) and parallel magnetic field perturbations (δB_z) as discussed in previous chapter. The space time ordering of W-ETG are $k_\perp \rho_i \gg 1$, $k_\perp \rho_e \le 1$, $\Omega_i < \omega << \Omega_e$, $k_\perp c_i > \omega$, $\omega_{*T} > \omega$ and $k_z R \sim 1$. Here $k_\perp (k_z)$ are perpendicular (parallel) wave number of the mode, ω is the mode frequency, ρ_j is Larmor radius, c_j is thermal speed, Ω_j is cyclotron frequency; $\rho_j = c_j / \Omega_j$, $\Omega_j = eB / m_j c$, T_j and m_j being temperature and mass of the electron(e) and ion(i) species(j). R is the length of the plasma along the axial magnetic field. We consider fully adiabatic ion response

$$n_{i,k} = -\tau_e \phi_k \tag{5.1}$$

The perpendicular magnetic field fluctuations $\delta B_\perp$ are driven purely by the current arising from fluctuating electron parallel velocity v so that $v = \nabla_\perp^2 A_z$. The perturbed equations for electron dynamics are the continuity equation

$$\frac{\partial n_e}{\partial t} + \frac{\partial \phi}{\partial y} - \frac{\beta}{2}\left(\frac{\partial}{\partial t} + K\frac{\partial}{\partial y}\right) b_z + \left(\frac{\partial}{\partial t} + K\frac{\partial}{\partial y}\right)\nabla_\perp^2 \phi + \nabla_\perp^2 \nabla_z^0 A_z$$

$$= -[\phi, n_e] - \vec{\nabla}\cdot\left[\phi, \vec{\nabla}_\perp(\phi + p_e)\right] + \frac{\beta}{2}\left[A_z, \nabla_\perp^2 A_z\right] + \frac{\beta}{2}[\phi - p_e, b_z] - \rho_e^* \frac{\beta}{2} b_z \nabla_\perp^2 \nabla_z^0 A_z \tag{5.2}$$

Parallel electron momentum equation or Ohm's law

$$\left(\left(\frac{\beta}{2} - \nabla_\perp^2\right)\frac{\partial}{\partial t} - \nu\nabla_\perp^2 + \frac{\beta}{2}K\frac{\partial}{\partial y}\right)A_z + \nabla_z^0(\phi - p_e)$$

$$= -\frac{\beta}{2}[\phi - p_e, A_z] + \left[\phi, \nabla_\perp^2 A_z\right] - \rho_e^* \frac{\beta}{2} b_z \nabla_z^0 (\phi - p_e) \tag{5.3}$$

And the temperature equation

$$\frac{\partial}{\partial t}\left(T_e - \frac{2}{3}n_e\right) + \left(\eta_e - \frac{2}{3}\right)\frac{\partial \phi}{\partial y} = -\left[\phi, T_e - \frac{2}{3}n_e\right] \tag{5.4}$$

The parallel magnetic fluctuations b_z are generated by the perpendicular current fluctuations due to $E \times B$ and electron diamagnetic velocity fluctuations.

$$\nabla_\perp^2 \vec{A}_\perp = \hat{z} \times \vec{\nabla} b_z = \hat{z} \times \vec{\nabla}\left(\phi - p_e\right) \tag{5.5}$$

The above model equations (5.1-5.5) for W-ETG turbulence are modifications of the model equations for ETG turbulence in the Ref. [13] to include coupling to Whistler mode. However they are similar to the set of model equations of previous chapter except the nonlinear terms proportional to ρ_e^* in equations (5.2) and (5.3) originating from parallel magnetic fluctuations b_z (whistler coupling). The third linear term on the left hand side and the fourth nonlinear term on the right hand side in the equations (5.2) results from effective incompressibility of the fluctuating $E \times B$ particle flux $\vec{\nabla} \cdot \left[(nv_{E\times B})(1 - \delta B_z / B_0)\right]$ and electron diamagnetic flux $\vec{\nabla} \cdot \left[(nv_{*pe})(1 - \delta B_z / B_0)\right]$ due to whistling of magnetic field. The Poisson's brackets are defined as $\left[f, g\right] = \hat{z} \times \vec{\nabla} f \cdot \vec{\nabla} g$. The various quantities are normalized as $x = (x - x_0)/\rho_e$, $y = y/\rho_e$, $z = z/L_n$, $t = tc_e/L_n$, $\phi = (e\delta\phi/T_e)(L_n/\rho_e)$, $n_i = (\delta n_i/n_0)(L_n/\rho_e)$, $v = (\delta v_{\|e}/c_e)(L_n/\rho_e)$, $p_e = (\delta p_e/P_{e0})(L_n/\rho_e)$, $L_n \nabla_\| \equiv \nabla_\| = \frac{\partial}{\partial z}$, $A_{\perp,z} = (2L_n c_e/\beta\rho_e c)(e\delta A_{\perp,z}/T_{e0})$, $b_z = 2L_n \delta b_z / B_0 \rho_e \beta$ with the nondimensional parameters: $\eta_e = L_{n_{e0}} / L_{T_{e0}}$, $K = (1 + \eta_e)$, $\tau_e = T_{e0}/T_{i0}$, $\beta = 8\pi P_{0e}/B_0^2$, $L_f = -\mathrm{d}lnf/\mathrm{d}x$, $\nu = \nu_e L_n / c_e$, $\rho_e = c_e/\Omega_{ce}$ and $\rho_e^* = \rho_e / L_n$. In the above the field quantities are normalized to the mixing length level and so $\phi,\ p_e,\ A_\|,\ A_\perp \sim 1$ in this normalization. The nonlinearities in the above equations originate mainly from $E \times B$ drift nonlinearity i.e., $\vec{v}_{E\times B} \cdot \vec{\nabla} f = \left[\phi, f\right]$, polarization drift nonlinearity $\vec{v}_{E\times B} \cdot \vec{\nabla}\nabla_\perp^2 f = \left[\phi, \nabla_\perp^2 f\right]$ and parallel operator nonlinearity from $\nabla_z = \nabla_z^0 + \tilde{\delta}\vec{B}_\perp \cdot \vec{\nabla} + \tilde{\delta}\vec{B}_\| \cdot \vec{\nabla} = \nabla_z^0 - (\beta/2)\left[A_z, \quad\right] + \rho_e^*(\beta/2) b_z \nabla_z^0$. The form of directional derivative along the net magnetic filed $\vec{B} = \vec{B}_0 + \vec{\delta} B$ shows that parallel magnetic compression induced nonlinearity is one order higher than magnetic flutter induced nonlinearity and other $E \times B$ and polarization nonlinearities in the parameter ρ_e^*. Hence the nonlinear contribution from parallel magnetic field fluctuations can be safely ignored in the preceeding calculations.

5.3 A Brief Summary of Linear Physics of W-ETG Mode

The linear physics of the W-ETG mode has been investigated extensivley in the previous chapter. However it will be useful here to reconsider some aspects of it because some linear physics information, such as real frequency ω_r and growth rate γ symmetry properties for $\vec{k} \to -\vec{k}$ and linear amplitude relations among various fields, goes into the nonlinear calculations done in Section 3. The linear relations among Fourier amplitudes of various fields are obtained and defined by following parameters.

$$T_{e,k} = \left[\left(\eta_e - \frac{2}{3}\right)\frac{k_y}{\omega} - \frac{2}{3}\tau_e\right]\phi_k \equiv R_T\phi_k \tag{5.6}$$

$$p_{e,k} = \left[\left(\eta_e - \frac{2}{3}\right)\frac{k_y}{\omega} - \frac{5}{3}\tau_e\right]\phi_k \equiv R_p\phi_k \tag{5.7}$$

$$A_{z,k} = \left[\frac{k_z}{\omega}\frac{(1+5/3\tau_e)\omega - \left(\eta_e - 2/3\right)k_y}{\left(\beta/2 + k_\perp^2\right)\omega + i\nu k_\perp^2 - \beta/2Kk_y}\right]\phi_k \equiv R_A\phi_k \tag{5.8}$$

$$b_{z,k} = \left[\left(1 + \frac{5}{3}\tau_e\right) - \left(\eta_e - \frac{2}{3}\right)\frac{k_y}{\omega}\right]\phi_k \equiv R_b\phi_k \tag{5.9}$$

Fourier analysing in space and time, the set of equations (5.1-5.5) yields the linear dispersion relation [5.53] as discussed in previous chapter [Eqns. (5.32)],

$$\omega\tau_e + k_y + k_\perp^2\left(\omega - Kk_y\right) + \frac{\beta}{2}\left(\omega - Kk_y\right)R_b = k_\perp^2 k_z R_A \tag{5.10}$$

The above dispersion relation (Eq. 5.10) is plotted in figure 5.1, figure 5.2 and figure 5.3 with respect to k_x, k_y, k_z respectively keeping the other two wavenumbers fixed in time.

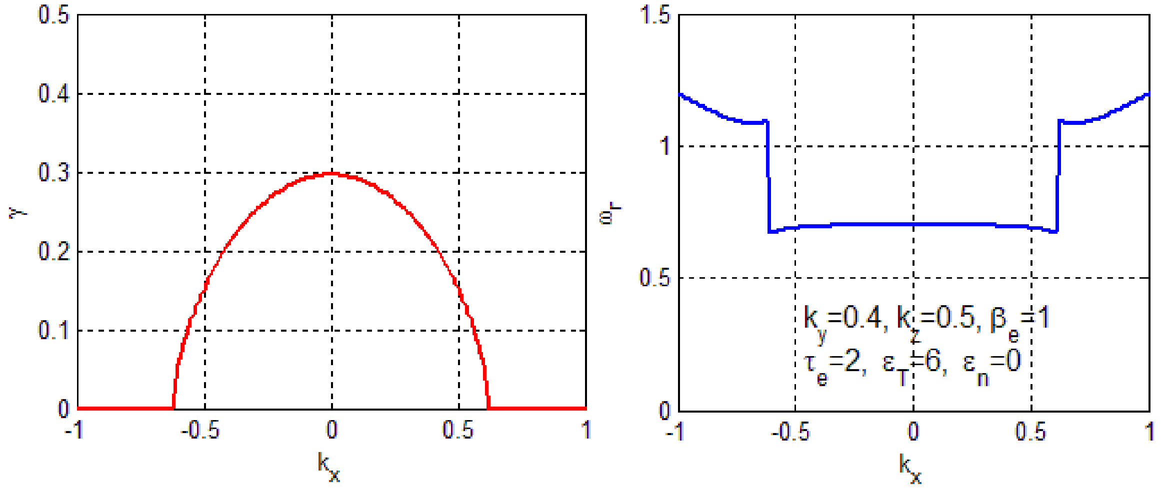

Figure 5.1: Growth rate and real frequency vs k_x. The figure shows that both the growth rate and the real frequency are symmetric with respect to the transformation $k_x \to -k_x$.

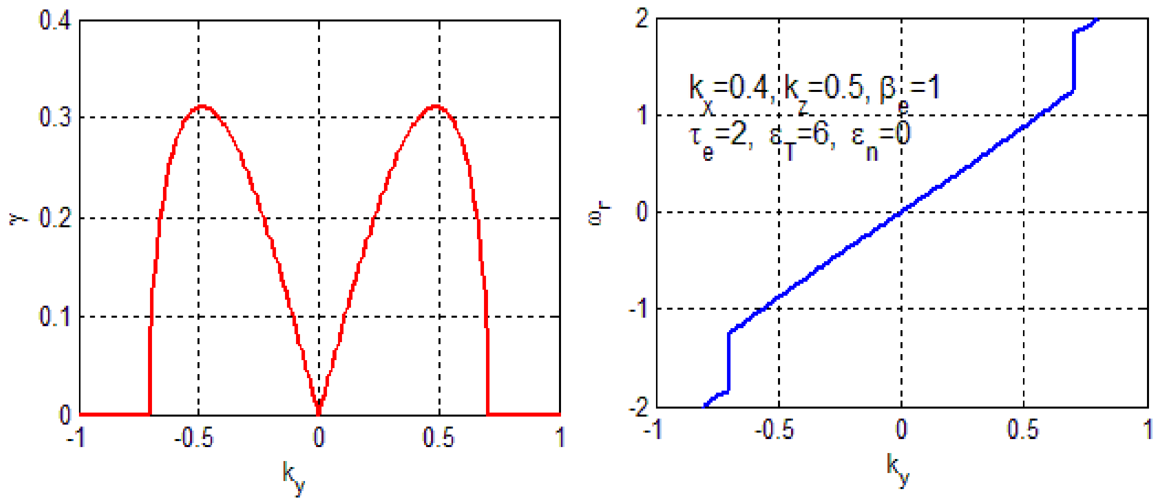

Figure 5.2: Growth rate and real frequency vs k_y. The figure shows that the growth rate is symmetric whereas the real frequency is anti-symmetric with respect to the transformation $k_x \to -k_x$.

The figures reveal the following symmetry properties of $\omega_{r,k}$ and γ_k for $\vec{k} \to -\vec{k}$.

$$\omega_{r,k_x} = \omega_{r,-k_x}, \quad \omega_{r,k_y} = -\omega_{r,-k_y}, \quad \omega_{r,k_z} = \omega_{r,-k_z}, \tag{5.11}$$

and

$$\gamma_{k_x} = \gamma_{-k_x}, \quad \gamma_{k_y} = \gamma_{-k_y}, \quad \gamma_{k_z} = \gamma_{-k_z}, \tag{5.12}$$

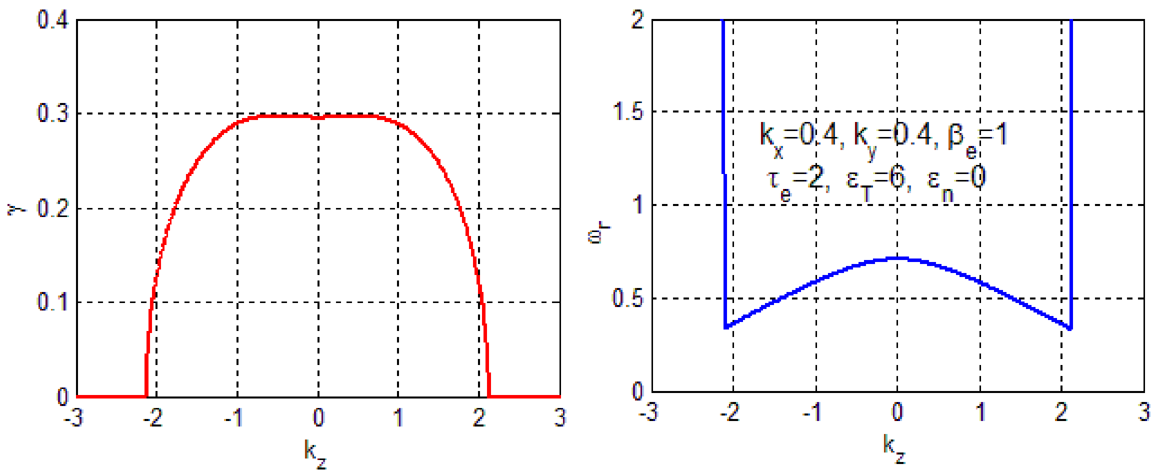

Figure 5.3: Growth rate and real frequency vs k_z. The figure shows that both the growth rate and the real frequency are symmetric with respect to the transformation $k_x \to -k_x$.

Table 5.1: Symmetry properties of varoius responses

Responses	Symmetries w.r.t k_x	Symmetries w.r.t k_y	Symmetries w.r.t k_z
$\mathrm{Re}\, R_T$	symmetric	symmetric	symmetric
$\mathrm{Re}\, R_p$	symmetric	symmetric	symmetric
$\mathrm{Re}\, R_A$	symmetric	anti-symmetric	anti-symmetric
$\mathrm{Re}\, R_b$	symmetric	symmetric	symmetric
$\mathrm{Im}\, R_T$	symmetric	anti-symmetric	symmetric
$\mathrm{Im}\, R_p$	symmetric	anti-symmetric	symmetric
$\mathrm{Im}\, R_A$	symmetric	symmetric	anti-symmetric
$\mathrm{Im}\, R_b$	symmetric	anti-symmetric	symmetric

These in turn decide the symmetry of responses of other fields to the electrostatic potential perturbations. The symmetry properties of R_T, R_p, R_A and R_b are mentioned in table 5.1. This information plays vital role in calculating the nonlinear drivers in the zonal field and streamer equations.

5.4 Study of Zonal Flow Model

The zonal flow model equations are obtained by appropriate averaging of the nonlinear W-ETG model equations over turbulence space-time scale. Zonal flow is nothing but the $m=0, n=0$ or $q_y=q_z=0$ and $q_x \neq 0$ mode in the turbulence. Here q_x is the radial wave number. So zonal flow mode equations are consisting of coupled equations in various fields with vanishing poloidal and parallel wave number but finite radial wave number. For the zonal mode, the averaging yields

$$\left(-\tau_e+\nabla_X^2\right)\frac{\partial\langle\phi\rangle}{\partial t}-\frac{\beta}{2}\frac{\partial\langle b_z\rangle}{\partial t}=-\langle[\phi,n_e]\rangle-\left\langle\vec{\nabla}\cdot\left[\phi,\vec{\nabla}_\perp(\phi+p_e)\right]\right\rangle+\frac{\beta}{2}\left\langle\left[A_z,\nabla_\perp^2 A_z\right]\right\rangle$$
$$+\frac{\beta}{2}\langle[\phi-p_e,b_z]\rangle-\rho_e^*\frac{\beta}{2}\left\langle b_z\nabla_\perp^2\nabla_z^0 A_z\right\rangle \tag{5.13}$$

$$\left(\left(\frac{\beta}{2}-\nabla_X^2\right)\frac{\partial}{\partial t}-\nu\nabla_X^2\right)\langle A_z\rangle=-\frac{\beta}{2}\langle[\phi-p_e,A_z]\rangle+\left\langle\left[\phi,\nabla_\perp^2 A_z\right]\right\rangle$$
$$-\rho_e^*\frac{\beta}{2}\left\langle b_z\nabla_z^0(\phi-p_e)\right\rangle \tag{5.14}$$

$$\frac{\partial}{\partial t}\left(\langle T_e\rangle+\frac{2}{3}\tau_e\langle\phi\rangle\right)=-\left\langle\left[\phi,T_e-\frac{2}{3}n_e\right]\right\rangle \tag{5.15}$$

and

$$\langle b_z\rangle=\langle\phi\rangle-\langle p_e\rangle \tag{5.16}$$

The terms on the left hand side with $\langle\ \rangle$ represents zonal components and that on the right hand side are averaged nonlinear drives which has $k_y=k_z=0$. Explicit forms of all the right hand side nonlinear terms as a function of $|\phi_k|^2$ using the linear responses equations (5.6 - 5.9) are derived in the appendix using quasilinear approximation. Using the results in the 8 we get

$$\left(-\tau_e+\nabla_X^2\right)\frac{\partial\langle\phi\rangle}{\partial t}-\frac{\beta}{2}\frac{\partial\langle b_z\rangle}{\partial t}=\nabla_X^2 Re\int d\vec{k}k_y k_x\left(1-\frac{\beta}{2}|R_A|^2+R_p\right)|\phi_k|^2 \tag{5.17}$$

$$\left(\left(\frac{\beta}{2}-\nabla_X^2\right)\frac{\partial}{\partial t}-\nu\nabla_X^2\right)\langle A_z\rangle=-i\nabla_X Re\int \mathrm{d}\vec{k}k_y\left(k_\perp^2+\frac{\beta}{2}\left(1-R_p^*\right)-i\nabla_X k_x\right)R_A\,|\,\phi_k\,|^2 \tag{5.18}$$

$$\frac{\partial}{\partial t}\left(\langle T_e\rangle+\frac{2}{3}\tau_e\langle\phi\rangle\right)=-\nabla_X Re\int \mathrm{d}\vec{k}ik_y R_T\,|\,\phi_k\,|^2 \tag{5.19}$$

$$\langle b_z\rangle=\langle\phi\rangle-\langle p_e\rangle=\left(1+\tau_e\right)\langle\phi\rangle-\langle T_e\rangle \tag{5.20}$$

Here Re stands for the real part of the integral and gradient in X acts on the spatial scale of the zonal flow. In a coexisting system of disparate scales such as small microturbulence scale W-ETG and zonal flow modulations of microscale fields by macroscale fields conserve wave action or quanta ($N_k = E_k / \omega_{r,k}$,where E_k is energy of mode $\vec{k}$) of the microscale fields. Generically, there will be an adiabatic invariant of the form $N_k = N_k(|\phi_k|^2, |A_{z,k}|^2, |b_{z,k}|^2, |T_{e,k}|^2)$ which, by the use of linear equations (5.6 - 5.9), can be written as $N_k = N_k(|\phi_k|^2)$. This allows us to write the modulated nonlinear drive terms as a function of N_k via $\delta|\phi_k|^2 = C_k \delta N_k$. Next the wave kinetic equation for the adiabatic invariant N_k is used to couple the turbulence to the zonal flow [3].

$$\frac{\partial N_k}{\partial t}+\frac{\partial\omega_{r,k}}{\partial\vec{k}}\cdot\frac{\partial N_k}{\partial\vec{X}}-\frac{\partial\omega_{r,k}}{\partial\vec{X}}\cdot\frac{\partial N_k}{\partial\vec{k}}=\gamma_k N_k-\Delta\omega N_k^2 \tag{5.21}$$

where $\omega_{r,k}$ and γ_k are respectively the real frequency and growth rate of the underlying turbulence in the presence of the slowly varying long scale zonal fields. The first term on the right hand side is the linear growth of the turbulence and the second term is the pull back due to nonlinear interactions. The set of equations (5.13-5.21) now form a closed system. We assume the equilibrium as state of stationary turbulence. This allows us to find the equilibrium turbulence spectrum $\langle N_k\rangle$ by letting the right hand side of equation (5.21) to vanish i.e., $\gamma_k\langle N_k\rangle-\Delta\omega\langle N_k\rangle^2=0$. To study the stability of such an equilibrium we can make Chapman-Enskog expansion of N_k; $N_k=\langle N_k\rangle+\delta N_k$, where $\langle N_k\rangle$ is the slowly varying ``mean" wave action density, and δN_k is the coherent perturbation to it induced by gradients of $\langle N_k \rangle$ in radius $\vec{X}$ and $\vec{k}$. Then the perturbed linearized wave kinetic equation takes the form

$$\left(\frac{\partial}{\partial t} + \vec{v}_g \cdot \frac{\partial}{\partial \vec{X}} + \gamma_k\right)\delta N_k = \frac{\partial \delta\omega_{r,k}}{\partial \vec{X}} \cdot \frac{\partial \langle N_k \rangle}{\partial \vec{k}} + \delta\gamma_k \langle N_k \rangle \tag{5.22}$$

In the above equation (5.22), the contribution of turbulence intensity gradient (i.e., $\vec{\nabla}_X \langle N_k \rangle$) has not been considered for simplicity. Assuming $\Psi = \Psi_q \exp(-i\Omega t + iq_X X)$ for $\Psi = \left(\delta N_k, \langle\phi\rangle, \langle p_e\rangle, \langle T_e\rangle, \langle A_z\rangle, \langle b_z\rangle\right)$ the wave kinetic equation (5.22) yields

$$\delta N_{k,q} = R_{k,q}\left[\frac{\partial \delta\omega_{r,k}}{\partial \vec{X}} \cdot \frac{\partial \langle N_k \rangle}{\partial \vec{k}} + \delta\gamma_k \langle N_k \rangle\right] \tag{5.23}$$

where the propagator $R_{k,q}$ is given by

$$R_{k,q} = \frac{i}{\left(\Omega_q - \vec{q}\cdot\vec{v}_g + i\gamma_k\right)} \tag{5.24}$$

Now we need to look for the ways in which the real frequency $\omega_{r,k}$ and growth rate γ_k can be modulated to find $\delta\omega_{r,k}$ and $\delta\gamma_k$ in the equation (5.23). The zonal flow being a long scale mode will convect the fast microturbulence modes. This effect is captured via $\partial_t \to \partial_t + \left[\langle\phi\rangle, \quad\right]$ and $k_z \to k_z - (\beta/2)\left[\langle A_z\rangle, \quad\right]$. Then, in general

$$\begin{aligned}\omega_{r,k} &\simeq \omega(k_\perp, k_z, \varepsilon_n, \varepsilon_T) + \vec{k}_\perp \cdot \langle V\rangle_{E\times B} \\ &= \omega_k^{lin} + v_{gz}\delta k_z + v_{g\perp}\delta k_\perp + \frac{\delta\omega_r}{\delta\varepsilon_n}\delta\varepsilon_n + \frac{\delta\omega_r}{\delta\varepsilon_T}\delta\varepsilon_T + \vec{k}_\perp\cdot\langle V\rangle_{E\times B}\end{aligned} \tag{5.25}$$

However $k_\perp$ is not modulated by zonal fields i.e., $\delta k_\perp = 0$. Also ignoring $\delta\omega_r/\delta\varepsilon_n$ and $\delta\omega_r/\delta\varepsilon_T$, as they enter through FLR effects, we get

$$\omega_{r,k} = \omega_k^{lin} - \vec{k}_\perp \cdot \left[\vec{\nabla}\left(\langle\phi\rangle - \frac{\beta}{2}v_{gz}\langle A_z\rangle\right)\times\hat{z}\right] \tag{5.26}$$

The modification of growth rate due to modulations of k_z, ε_n and ε_T by the zonal fields is given by

$$\gamma_k \equiv \gamma_k(k_\perp, k_z, \eta_e) \simeq \gamma_k + \frac{\partial \gamma_k}{\partial k_z}\delta k_z + \frac{\partial \gamma_k}{\partial \varepsilon_n}\delta\varepsilon_n + \frac{\partial \gamma_k}{\partial \varepsilon_T}\delta\varepsilon_T \tag{5.27}$$

$$= \gamma_k + \frac{\beta}{2}\frac{\partial \gamma_k}{\partial k_z}\vec{k}_\perp \cdot \left(\vec{\nabla}\langle A_z\rangle \times \hat{z}\right) - \left[-\frac{\partial \gamma_k}{\partial \varepsilon_n}\tau_e \nabla_X \langle\phi\rangle + \frac{\partial \gamma_k}{\partial \varepsilon_T}\nabla_X \langle T_e\rangle\right] \tag{5.28}$$

Note that the last term containing $\nabla_X \langle\phi\rangle$ in the above equation arises from zonal electron density perturbation via quasineutrality. Using equations (5.26) and (5.28) we get

$$\delta N_{k,q} = R_{k,q} k_y \nabla_X^2 \left(\langle\phi\rangle - \frac{\beta}{2} v_{gz}\langle A_z\rangle\right)\frac{\partial\langle N_k\rangle}{\partial k_x}$$

$$-R_{k,q}\left(\frac{\beta}{2}\frac{\partial \gamma_k}{\partial k_z}k_y \nabla_X\langle A_z\rangle + \left[-\frac{\partial \gamma_k}{\partial \varepsilon_n}\tau_e \nabla_X\langle\phi\rangle + \frac{\partial \gamma_k}{\partial \varepsilon_T}\nabla_X\langle T_e\rangle\right]\right)\langle N_k\rangle \tag{5.29}$$

Now using the above wke3 for $\delta N_{k,q}$ in equation (5.17) and then using the $\vec{k}$-space symmetry properties of ω_r and γ followed by fourier transformation in X yields

$$\left(\tau_e + q^2\right)\frac{\partial\langle\phi\rangle_q}{\partial t} + \frac{\beta}{2}\frac{\partial}{\partial t}\left(\left(1+\tau_e\right)\langle\phi\rangle_q - \langle T_e\rangle_q\right) = q^4 \int \mathrm{d}\vec{k} k_y^2 \left(1 - \frac{\beta}{2}|R_A|^2 + ReR_p\right)$$

$$\times R_{k,q} C_k \left(-k_x \frac{\partial\langle N_k\rangle}{\partial k_x}\right)\langle\phi\rangle_q \tag{5.30}$$

The second term in on the left hand side in the above equation is the additional effect of magnetic whistling b_z. Again using the equation (5.29) for $\delta N_{k,q}$ in equation (5.18) and then using the $\vec{k}$-space symmetry properties of ω_r and γ followed by fourier transformation in X yields

$$\left(\left(\frac{\beta}{2} + q^2\right)\frac{\partial}{\partial t} + \nu q^2\right)\langle A_z\rangle_q = \frac{\beta}{2} q^2 \int \mathrm{d}\vec{k} k_y^2 \left(k_\perp^2 ImR_A + \frac{\beta}{2} Im\left(R_A - R_p^* R_A\right)\right)$$

$$\times \langle A_z\rangle_q R_{k,q} C_k \frac{\partial \gamma_k}{\partial k_z}\langle N_k\rangle$$

$$+\frac{\beta}{2} q^4 \int \mathrm{d}\vec{k}\left(-k_y^2 ReR_A R_{k,q} C_k\right) v_{gz}\langle A_z\rangle_q \left(-k_x \frac{\partial\langle N_k\rangle}{\partial k_x}\right) \tag{5.31}$$

Similarly from equation (5.29) and equation (5.19) we get

$$\frac{\partial}{\partial t}\left(\langle T_e\rangle_q+\frac{2}{3}\tau_e\langle\phi\rangle_q\right)=q^2\int \mathrm{d}\vec{k}k_y ImR_T C_k R_{k,q}\left[-\frac{\partial\gamma_k}{\partial\varepsilon_n}\tau_e\langle\phi\rangle_q+\frac{\partial\gamma_k}{\partial\varepsilon_T}\langle T_e\rangle_q\right]\langle N_k\rangle \tag{5.32}$$

Equation (5.31) shows that the zonal perpendicular magnetic field (or A_z) dynamics is effectively decoupled from the dynamics of other zonal fields such as electrostatic field (or zonal flow) and zonal temperature. The root cause of this is the $\vec{k}$ space symmetry properties of the $\omega_{r,k}$ and γ_k and the responses of the fluctuation fields R_A and R_p. The dominant effect of the coupling of the Whistler mode to the ETG mode on the zonal flow excitation is the linear coupling term on the left hand side of the equation (5.30). Whistler coupling has no influence on poloidal zonal magnetic dynamics and zonal temperature dynamics as can be seen from equation (5.31) and equation (5.32) respectively. Using these equations, the general dispersion relation for zonal flow can be obtained as

$$\Omega_q\left[\left(\tau_e+q^2\right)+\frac{\beta}{2}\left\{\left(1+\tau_e\right)+\frac{\frac{2}{3}\tau_e\Omega_q+iq^2\tau_e S_n}{\Omega_q-iq^2 S_T}\right\}\right]=iq^4 S_R \tag{5.33}$$

where S_n, S_T and S_R are defined as

$$S_n=\int \mathrm{d}\vec{k}k_y ImR_T C_k R_{k,q}\frac{\partial\gamma_k}{\partial\varepsilon_n}\langle N_k\rangle \tag{5.34}$$

$$S_T=\int \mathrm{d}\vec{k}k_y ImR_T C_k R_{k,q}\frac{\partial\gamma_k}{\partial\varepsilon_T}\langle N_k\rangle \tag{5.35}$$

$$S_R=\int \mathrm{d}\vec{k}k_y^2\left(1-\frac{\beta}{2}|R_A|^2+ReR_p\right)R_{k,q}C_k\left(-k_x\frac{\partial\langle N_k\rangle}{\partial k_x}\right) \tag{5.36}$$

5.4.1 Backreaction of Zonal Flow Shear on W-ETG

The backreaction of zonal flow shear on turbulence can be studied by the taking the average of equation (5.21)

$$\frac{\partial\langle N_k\rangle}{\partial t}=\left\langle\frac{\partial\delta\omega_{r,k}}{\partial\vec{X}}\cdot\frac{\partial\delta N_k}{\partial\vec{k}}\right\rangle+\langle\delta\gamma_k\delta N_k\rangle-\Delta\omega\langle\delta N_k\delta N_k\rangle \tag{5.37}$$

Using the response of δN_k for zonal flow perturbation from equation (5.29) yields

$$\left\langle\frac{\partial\delta\omega_{r,k}}{\partial\vec{X}}\cdot\frac{\partial\delta N_k}{\partial\vec{k}}\right\rangle \tag{5.38}$$

$$=\frac{\partial}{\partial k_x}\left[\left\langle\left(\nabla_X\delta\omega_{r,k}\right)R_{k,q}\left(\nabla_X\delta\omega_{r,k}\right)\right\rangle\frac{\partial\langle N_k\rangle}{\partial k_x}+\left\langle\left(\nabla_X\delta\omega_{r,k}\right)R_{k,q}\delta\gamma_{r,k}\right\rangle\langle N_k\rangle\right] \tag{5.39}$$

$$=\frac{\partial}{\partial k_x}\int \mathrm{d}\vec{q}R_{k,q}k_y^2q^4\,|\langle\phi\rangle-\frac{\beta}{2}v_{gz}\langle A_z\rangle|^2\,\frac{\partial\langle N_k\rangle}{\partial k_x}+\frac{\partial}{\partial k_x}Re\int\mathrm{d}\vec{q}iq^3k_yR_{k,q}$$

$$\times\left(\langle\phi\rangle_{-q}-\frac{\beta}{2}v_{gz}\langle A_z\rangle_{-q}\right)\left(\frac{\beta}{2}\frac{\partial\gamma_k}{\partial k_z}k_y\langle A_z\rangle_q+\left[-\frac{\partial\gamma_k}{\partial\varepsilon_n}\tau_e\langle\phi\rangle_q+\frac{\partial\gamma_k}{\partial\varepsilon_T}\langle T_e\rangle_q\right]\right)\langle N_k\rangle \tag{5.40}$$

Now consider

$$\langle\delta\gamma_k\delta N_k\rangle=\left\langle\left(\delta\gamma_{r,k}R_{k,q}\nabla_X\delta\omega_{r,k}\right)\right\rangle\frac{\partial\langle N_k\rangle}{\partial k_x}+\left\langle\delta\gamma_{r,k}R_{k,q}\delta\gamma_{r,k}\right\rangle\langle N_k\rangle \tag{5.41}$$

whose first term is similar to the second term on the right hand side bracket of the equation (5.40) and the second term is given as follows.

$$\left\langle\delta\gamma_{r,k}R_{k,q}\delta\gamma_{r,k}\right\rangle=Re\int\mathrm{d}\vec{q}q^2R_{k,q}\,|\,\frac{\beta}{2}\frac{\partial\gamma_k}{\partial k_z}k_y\langle A_z\rangle_q+\left(-\frac{\partial\gamma_k}{\partial\varepsilon_n}\tau_e\langle\phi\rangle_q+\frac{\partial\gamma_k}{\partial\varepsilon_T}\langle T_e\rangle_q\right)|^2 \tag{5.42}$$

The second term in equation (5.40) and the first term in equation (5.41) indeed vanish for the integrand being odd in q. The last term on the right hand side of the equation (5.37) is the self nonlinearity of the turbulence modulations, which being a higher order term can be safely ignored. This allows us to write the evolution equation for $\langle N_k\rangle$ as

$$\frac{\partial\langle N_k\rangle}{\partial t}=\frac{\partial}{\partial k_x}D\frac{\partial\langle N_k\rangle}{\partial k_x}+\Gamma\langle N_k\rangle \tag{5.43}$$

where the electromagnetic turbulence diffusion coefficient D is given by

$$D=\int\mathrm{d}\vec{q}R_{k,q}k_y^2q^4\,|\langle\phi\rangle-\frac{\beta}{2}v_{gz}\langle A_z\rangle|^2 \tag{5.44}$$

and the nonlinear growth Γ is given by

$$\Gamma=Re\int\mathrm{d}\vec{q}q^2R_{k,q}\,|\,\frac{\beta}{2}\frac{\partial\gamma_k}{\partial k_z}k_y\langle A_z\rangle_q+\left(-\frac{\partial\gamma_k}{\partial\varepsilon_n}\tau_e\nabla_X\langle\phi\rangle+\frac{\partial\gamma_k}{\partial\varepsilon_T}\nabla_X\langle T_e\rangle\right)|^2 \tag{5.45}$$

The equation (5.43) with equations (5.44) and (5.45) describes the backreaction of zonal flow on turbulence. The set of equations (5.30-5.32) and equations (5.43-5.45) describe the self-consistent evolution of WTEG turbulence and zonal flow and fields.

5.5 Stability of W-ETG Turbulence with respect to Streamer Excitation

Streamers are another long scale modes with $\nabla_X \ll \nabla_Y$. Alternatively they are the modes with $m \neq 0$, $n = 0$ or $q_X = 0$, $q_Y \neq 0$. Pictorially these modes are radially extended (or smooth) structures causing radially outward plasma flow. These modes spring up as a product (or by-product) of modulational instability of the ITG/ETG turbulence. In this section we will discover the effect of whistler coupling on the excitation of streamers which is relevant to high beta plasmas such as LVPD. The streamer equations are obtained by appropriate averaging of W-ETG model equations over turbulence space-time scale.

$$
\begin{aligned}
&-\tau_e \frac{\partial\langle\phi\rangle}{\partial t} + \frac{\partial\langle\phi\rangle}{\partial Y} - \frac{\beta}{2}\left(\frac{\partial}{\partial t} + K\frac{\partial}{\partial Y}\right)\langle b_z\rangle + \nabla_Y^2\nabla_Z^0\langle A_z\rangle + \left(\frac{\partial}{\partial t} + K\frac{\partial}{\partial Y}\right)\nabla_Y^2\langle\phi\rangle \\
&\quad = -\langle[\phi, n_e]\rangle - \left\langle\vec{\nabla}\cdot\left[\phi, \vec{\nabla}_\perp(\phi + p_e)\right]\right\rangle + \frac{\beta}{2}\left\langle\left[A_z, \nabla_\perp^2 A_z\right]\right\rangle \\
&\quad\quad + \frac{\beta}{2}\langle[\phi - p_e, b_z]\rangle - \rho_e^* \frac{\beta}{2}\left\langle b_z \nabla_\perp^2 \nabla_z^0 A_z\right\rangle
\end{aligned}
\tag{5.46}
$$

$$
\begin{aligned}
&\left(\left(\frac{\beta}{2} - \nabla_Y^2\right)\frac{\partial}{\partial t} - \nu\nabla_Y^2 + \frac{\beta}{2}K\frac{\partial}{\partial Y}\right)\langle A_z\rangle + +\nabla_z^0\langle\phi - p_e\rangle \\
&\quad = -\frac{\beta}{2}\langle[\phi - p_e, A_z]\rangle + \left\langle\left[\phi, \nabla_\perp^2 A_z\right]\right\rangle - \rho_e^* \frac{\beta}{2}\left\langle b_z \nabla_z^0(\phi - p_e)\right\rangle
\end{aligned}
\tag{5.47}
$$

$$
\frac{\partial}{\partial t}\left(\langle T_e\rangle + \tau_e \frac{2}{3}\langle\phi\rangle\right) + \left(\eta_e - \frac{2}{3}\right)\frac{\partial\langle\phi\rangle}{\partial Y} = -\langle[\phi, T_e]\rangle \tag{5.48}
$$

and

$$
\langle b_z\rangle = \langle\phi\rangle - \langle p_e\rangle \tag{5.49}
$$

Like the zonal case the terms on the left hand side with $\langle\,\rangle$ represents streamer components and that on the right hand side are averaged nonlinear drives which has $q_x = q_z = 0$. Explicit forms of all the right hand side nonlinear terms as a function of $|\phi_k|^2$ using the linear responses. Equations (5.6-5.9) are derived in the Appendix B by considering quasilinear approximation. Using the results in the appendix we get

$$-\tau_e \frac{\partial\langle\phi\rangle}{\partial t} + \frac{\partial\langle\phi\rangle}{\partial Y} - \frac{\beta}{2}\left(\frac{\partial}{\partial t} + K\frac{\partial}{\partial Y}\right)\langle b_z\rangle + \nabla_Y^2\nabla_Z^0\langle A_z\rangle$$
$$+\left(\frac{\partial}{\partial t} + K\frac{\partial}{\partial Y}\right)\nabla_Y^2\langle\phi\rangle = -\nabla_Y^2 Re\int \mathrm{d}\vec{k} k_y k_x\left(1 - \frac{\beta}{2}|R_A|^2 + R_p\right)|\phi_k|^2 \tag{5.50}$$

$$\left(\left(\frac{\beta}{2} - \nabla_Y^2\right)\frac{\partial}{\partial t} - \nu\nabla_Y^2 + \frac{\beta}{2}K\frac{\partial}{\partial Y}\right)\langle A_z\rangle + \nabla_Z^0\langle\phi - p_e\rangle$$
$$= i\nabla_Y Re\int \mathrm{d}\vec{k} k_x\left(k_\perp^2 + \frac{\beta}{2}\left(1 - R_p^*\right) - i\nabla_Y k_y\right)R_A|\phi_k|^2 \tag{5.51}$$

$$\frac{\partial}{\partial t}\left(\langle T_e\rangle + \frac{2}{3}\tau_e\langle\phi\rangle\right) + \left(\eta_e - \frac{2}{3}\right)\frac{\partial\langle\phi\rangle}{\partial Y} = \nabla_Y Re\int \mathrm{d}\vec{k} i k_x R_T|\phi_k|^2 \tag{5.52}$$

$$\langle b_z\rangle = \langle\phi\rangle - \langle p_e\rangle = \left(1 + \tau_e\right)\langle\phi\rangle - \langle T_e\rangle \tag{5.53}$$

Streamers being on a much larger scale compared to the underlying turbulence they form a coexisting desperate scale system where streamer modulations conserve wave action N_k. One can always get $|\phi_k|^2 = C_k N_k$. Since the nonlinear drivers in the above equations (5.50 - 5.53) are $\propto N_k$ the streamer equations can be closed by WKE. The coupling between mean field such as streamer and the turbulence is provided by the WKE (equation (5.21)) where now the $\omega_{r,k}$ and γ_k should be read as real frequency and growth rate in the presence of streamers. From equation (5.21) onwards and up to equation (5.24) all the descriptions for zonal flow can be applied to streamers just by replacing ``zonal flow"$\rightarrow$ ``streamers" consistently throughout. Now to get modulation of real frequency recall that $\delta k_\perp = 0$ always and $\delta\varepsilon_n = \delta\varepsilon_T = 0$ for streamers because streamers are radially smooth perturbations. So ω_r

can be modulated only via modulation of k_z and radial flow due to streamer potential $\langle\phi\rangle$. Hence

$$\delta\omega_{r,k} = v_{gz}\delta k_z + \vec{k}_\perp \cdot \langle V\rangle_{E\times B} = -k_x\left[\nabla_Y\left(\langle\phi\rangle - \frac{\beta}{2}v_{gz}\langle A_z\rangle\right)\right] \tag{5.54}$$

Similarly growth rate is modulated only via modulations of k_z

$$\delta\gamma_k \approx \frac{\partial\gamma_k}{\partial k_z}\delta k_z = \frac{\beta}{2}\frac{\partial\gamma_k}{\partial k_z}k_x\nabla_Y\langle A_z\rangle \tag{5.55}$$

Using equations (5.54) and (5.55) in equation (5.23) we get the modulation in N_k as

$$\delta N_{k,q} = -R_{k,q}k_x\nabla_Y^2\left(\langle\phi\rangle - \frac{\beta}{2}v_{gz}\langle A_z\rangle\right)\frac{\partial\langle N_k\rangle}{\partial k_y}$$
$$+R_{k,q}\left(\frac{\beta}{2}\frac{\partial\gamma_k}{\partial k_z}k_x\nabla_Y\langle A_z\rangle\right)\langle N_k\rangle \tag{5.56}$$

Now using equation (5.56) and the $\vec{k}$-space symmetry properties of $\omega_{r,k}$ and γ_k and then taking the fourier transform of the resulting equations in Y we get the following dynamical equations for streamers

$$\left(-\tau_e - (1+\tau_e)\frac{\beta}{2} - q_Y^2\right)\frac{\partial\langle\phi\rangle_q}{\partial t} + iq_Y\left(1 - \frac{\beta}{2}(1+\tau_e)K - q_Y^2K\right)\langle\phi\rangle_q$$
$$+\frac{\beta}{2}\left(\frac{\partial}{\partial t} + iq_YK\right)\langle T_e\rangle - iq_Y^2q_\parallel\langle A_z\rangle_q$$
$$= -q_Y^4\int d\vec{k}k_x^2\left(1 - \frac{\beta}{2}|R_A|^2 + ReR_p\right)R_{k,q}C_k\left(-k_y\frac{\partial\langle N_k\rangle}{\partial k_y}\right)\langle\phi\rangle_q \tag{5.57}$$

$$\left(\left(\frac{\beta}{2} + q_Y^2\right)\frac{\partial}{\partial t} + \nu q_Y^2 + i\frac{\beta}{2}Kq_Y\right)\langle A_z\rangle_q + iq_\parallel\left(\langle\phi\rangle_q - \langle p_e\rangle_q\right)$$
$$= \frac{\beta}{2}q_Y^2\int d\vec{k}k_x^2\left(k_\perp^2 ImR_A + \frac{\beta}{2}Im\left(R_A - R_p^*R_A\right)\right)\langle A_z\rangle_q R_{k,q}C_k\frac{\partial\gamma_k}{\partial k_z}\langle N_k\rangle$$
$$+\frac{\beta}{2}q_Y^4\int d\vec{k}\left(-k_x^2ReR_AR_{k,q}C_k\right)v_{gz}\langle A_z\rangle_q\left(-k_y\frac{\partial\langle N_k\rangle}{\partial k_y}\right) \tag{5.58}$$

$$\frac{\partial}{\partial t}\left(\langle T_e\rangle_q + \frac{2}{3}\tau_e\langle\phi\rangle_q\right) + i\left(\eta_e - \frac{2}{3}\right)q_Y\langle\phi\rangle_q$$

$$= -iq_Y^3 \int \mathrm{d}\vec{k} k_x^2 C_k R_{k,q} \left(-ImR_T \frac{\partial \langle N_k \rangle}{\partial k_y} \right) \langle \phi \rangle_q \tag{5.59}$$

It is clear from above equations that for streamers the perpendicular magnetic dynamics gets completely isolated from the other streamer fields dynamics in the limit when $q_\parallel = 0$. Thus in this limit the growth rates of electric and magnetic streamers should be calculated separately. From above streamer mode equations a linear relation among various streamer fields can be defined as follows.

$$\langle T_e \rangle_q = \left[\frac{q_y^3 \sigma_T}{\Omega_q} + \left(\eta_e - \frac{2}{3} \right) \frac{q_Y}{\Omega_q} - \frac{2}{3} \tau_e \right] \langle \phi \rangle_q \equiv R_{T,q} \langle \phi \rangle_q \tag{5.60}$$

$$\langle p_e \rangle_q = \left[\frac{q_y^3 \sigma_T}{\Omega_q} + \left(\eta_e - \frac{2}{3} \right) \frac{q_y}{\Omega_q} - \frac{5}{3} \tau_e \right] \langle \phi \rangle_q \equiv R_{p,q} \langle \phi \rangle_q \tag{5.61}$$

$$\langle A_z \rangle_q = \frac{q_\parallel}{\Omega_q} \frac{(1 + 5/3\tau_e)\Omega_q - (\eta_e - 2/3) q_y - q_y^3 \sigma_T}{(\beta/2 + q_y^2)\Omega_q + i\nu q_y^2 - \beta/2Kq_y - i\beta/2q_y^2 (\sigma_{A1} + q_y^2 \sigma_{A2})} \langle \phi \rangle_q$$
$$\equiv R_{A_z,q} \langle \phi \rangle_q \tag{5.62}$$

$$\langle b_z \rangle_q = \left[1 + \frac{5}{3} \tau_e - \left(\eta_e - \frac{2}{3} \right) \frac{q_y}{\Omega_q} - \frac{q_y^3 \sigma_T}{\Omega_q} \right] \langle \phi \rangle_q$$
$$\equiv R_{b,q} \langle \phi \rangle_q \tag{5.63}$$

From the above set the equations, on taking fourier transform in t, yields the dispersion relation for streamer

$$\Omega_q \left(\tau_e + (1+\tau_e) \frac{\beta}{2} + q_Y^2 \right) + q_Y \left(1 - \frac{\beta}{2} (1+\tau_e) K - q_Y^2 K \right)$$
$$- \frac{\beta}{2} (\Omega_q - q_Y K) R_{T,q} - q_Y^2 q_\parallel R_{A_z,q} = i q_y^4 \sigma_\phi \tag{5.64}$$

where

$$\sigma_\phi = \int \mathrm{d}\vec{k} k_x^2 \left(1 - \frac{\beta}{2} | R_A |^2 + ReR_p\right) R_{k,q} C_k \left(-k_y \frac{\partial \langle N_k \rangle}{\partial k_y}\right) \tag{5.65}$$

and

$$\sigma_T = -\int \mathrm{d}\vec{k} k_x^2 C_k R_{k,q} \left(-ImR_T \frac{\partial \langle N_k \rangle}{\partial k_y}\right) \tag{5.66}$$

$$\sigma_{A1} = \int \mathrm{d}\vec{k} k_x^2 \left(k_\perp^2 ImR_A + \frac{\beta}{2} Im\left(R_A - R_p^* R_A\right)\right) R_{k,q} C_k \frac{\partial \gamma_k}{\partial k_z} \langle N_k \rangle \tag{5.67}$$

$$\sigma_{A2} = \int \mathrm{d}\vec{k} \left(-k_x^2 ReR_A R_{k,q} C_k\right) v_{gz} \left(-k_y \frac{\partial \langle N_k \rangle}{\partial k_y}\right) \tag{5.68}$$

5.5.1 Backreaction of Streamers on the Host Turbulence

Equation (5.37) in its general form describes the backreaction of a slow-large scale mode on the host turbulence. So it is valid for streamers as well except that now $\partial / \partial \vec{X} \to \partial / \partial Y$ and $\partial / \partial \vec{k} \to \partial / \partial k_y$. Hence we can write

$$\left\langle \frac{\partial \delta\omega_{r,k}}{\partial \vec{X}} \cdot \frac{\partial \delta N_k}{\partial \vec{k}} \right\rangle \tag{5.69}$$

$$= \frac{\partial}{\partial k_y} \left[\left\langle \left(\nabla_Y \delta\omega_{r,k}\right) R_{k,q} \left(\nabla_Y \delta\omega_{r,k}\right) \right\rangle \frac{\partial \langle N_k \rangle}{\partial k_y} + \left\langle \left(\nabla_Y \delta\omega_{r,k}\right) R_{k,q} \delta\gamma_{r,k} \right\rangle \langle N_k \rangle \right] \tag{5.70}$$

$$= \frac{\partial}{\partial k_y} \int \mathrm{d}\vec{q} R_{k,q} k_x^2 q_Y^4 \, | \langle \phi \rangle - \frac{\beta}{2} v_{gz} \langle A_z \rangle |^2 \, \frac{\partial \langle N_k \rangle}{\partial k_x} + \frac{\partial}{\partial k_y} Re \int \mathrm{d}\vec{q} i q_Y^3 k_x^2 R_{k,q}$$

$$\times \left(\langle \phi \rangle_{-q} - \frac{\beta}{2} v_{gz} \langle A_z \rangle_{-q} \right) \frac{\beta}{2} \frac{\partial \gamma_k}{\partial k_z} \langle A_z \rangle_q \langle N_k \rangle \tag{5.71}$$

Similarly

$$\langle \delta\gamma_k \delta N_k \rangle = \left\langle \left(\delta\gamma_{r,k} R_{k,q} \nabla_Y \delta\omega_{r,k}\right) \right\rangle \frac{\partial \langle N_k \rangle}{\partial k_y} + \left\langle \delta\gamma_{r,k} R_{k,q} \delta\gamma_{r,k} \right\rangle \langle N_k \rangle \tag{5.72}$$

whose first term is similar to the second term on the right hand side bracket of the equation (5.71) and the second term is given as follows.

$$\left\langle \delta\gamma_{r,k} R_{k,q} \delta\gamma_{r,k} \right\rangle = Re\int \mathrm{d}\vec{q} k_x^2 q_Y^2 R_{k,q} \left| \frac{\beta}{2} \frac{\partial \gamma_k}{\partial k_z} \left\langle A_z \right\rangle_q \right|^2 \tag{5.73}$$

The second term in equation (5.71) and the first term in equation (5.72) indeed vanish for the integrand being odd in q. The last term on the right hand side of the equation (5.37) is the self nonlinearity of the turbulence modulations, which being a higher order term can be safely ignored. This allows us to write the evolution equation for $\left\langle N_k \right\rangle$ as

$$\frac{\partial \left\langle N_k \right\rangle}{\partial t} = \frac{\partial}{\partial k_y} D \frac{\partial \left\langle N_k \right\rangle}{\partial k_y} + \Gamma \left\langle N_k \right\rangle \tag{5.74}$$

where the electromagnetic turbulence diffusion coefficient D is given by

$$D = \int \mathrm{d}\vec{q} R_{k,q} k_x^2 q_Y^4 \left| \left\langle \phi \right\rangle - \frac{\beta}{2} v_{gz} \left\langle A_z \right\rangle \right|^2 \tag{5.75}$$

and the nonlinear growth Γ is given by

$$\Gamma = Re\int \mathrm{d}\vec{q} k_x^2 q^2 R_{k,q} \left| \frac{\beta}{2} \frac{\partial \gamma_k}{\partial k_z} \left\langle A_z \right\rangle_q \right|^2 \tag{5.76}$$

The equation (5.74) with equation (5.75) and (5.76) describes the backreaction of streamers on turbulence. The set of equations (5.57-5.59) and equations (5.74-5.76) describe the self-consistent evolution of W-ETG turbulence and streamers flow and fields.

5.6 Numerical Results and Discussion

The numerical results are independently discussed for zonal flows and streamers. For each nonlinear mode, the profiles of growth rate, real frequency are obtained as a function of wave number and plasma beta for different parameters as following.

5.6.1 Results for Zonal Flows

The numerical results for zonal flows has been discussed below using the dispersion relation (33) but for different normalization suitable for flat density profile case, i.e. $(\Omega_q, \omega_k) = (\Omega_q, \omega_k)/(c_e/R)$ and $(q_\parallel, k_\parallel) = (q_\parallel, k_\parallel)R$.

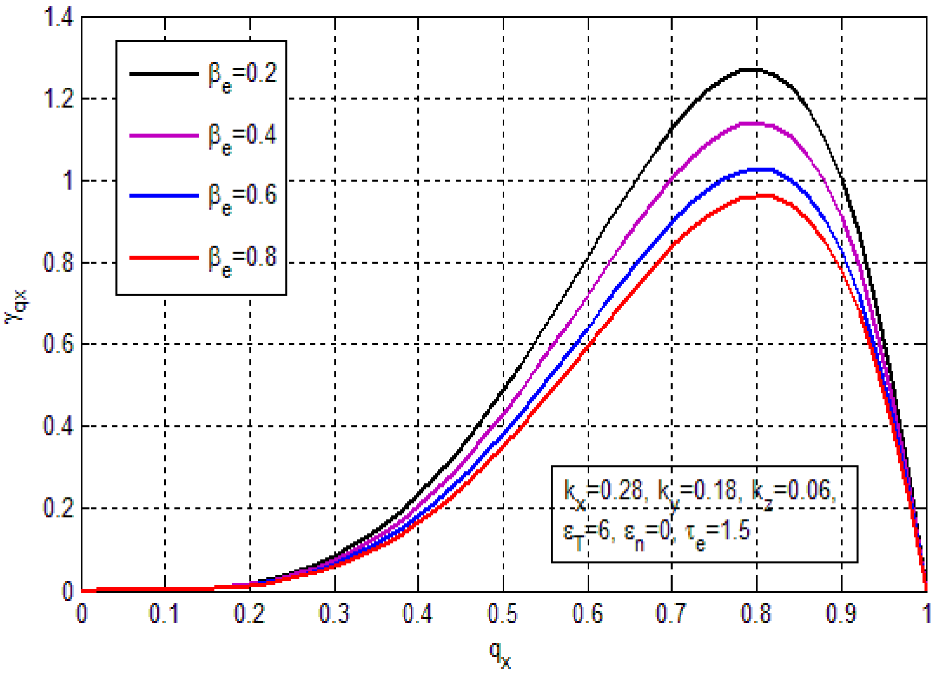

Figure 5.4: Growth rate of zonal flows vs q_x for different values of β_e.

Figure 5.4 shows the normalized growth rate (γ) as a function of wave-number (q_x) of zonal flows for different value of β_e at $k_x = 0.28$, $k_y = 0.18$, $k_z = 0.06$, $q_z = 0$, $\varepsilon_T = 6$, $\varepsilon_n = 0$, $\tau_e = 1.5$. The profile represents that growth of the zonal modes continuous increases as q_x increases and decreases with β_e. For higher value of $q_x > 0.7$ the growth gets stabilized due to FLR effect and peaks lie around $q_y = 0.8$. The numerical real frequency becomes zero for the zonal flow consistent with theoretical model.

Figure 5.5 illustrates the normalized growth rate (γ) of the mode as a function of β_e for various value of ε_T for $q_x = 0.1$ and other parameters remain fixed as above mentioned. With initial value of $\beta_e < 0.1$, growth of zonal mode decreases and it increases with increasing $\beta_e > 0.1$. For further higher value of β_e mode gets stabilized. For $0.1 < \beta_e < 0.2$, multiple peaks reflects due to inverse dependence of the growth due to primary mode of W-ETG instability. The characteristic of β_e scaling follows similar trend as for background turbulence.The growth rate of zonal flow increases with ε_T.

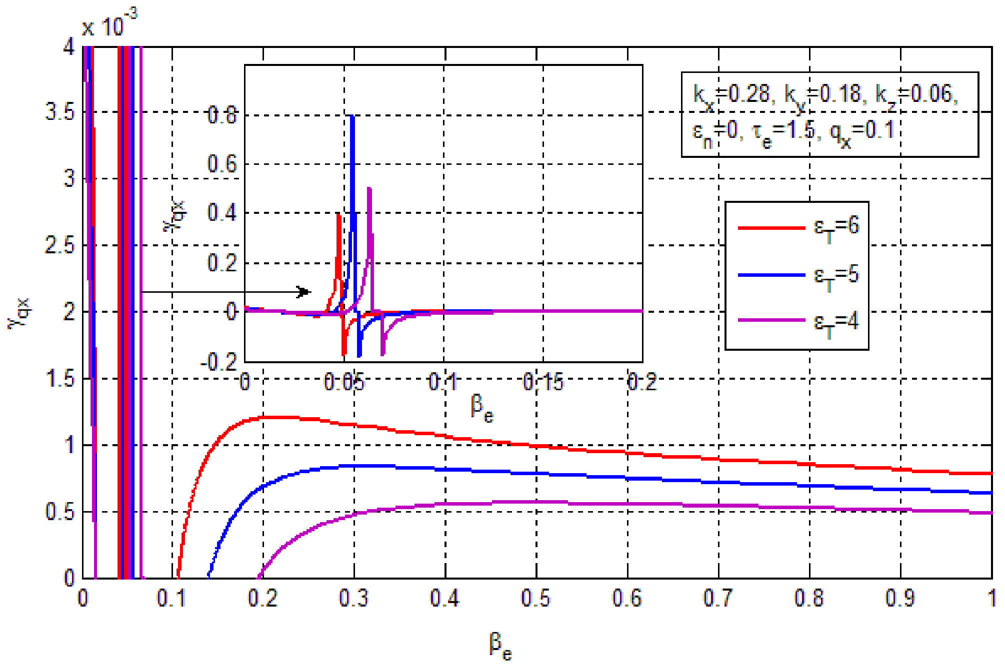

Figure 5.5: Growth rate of zonal flows vs β_e for different values of ε_T.

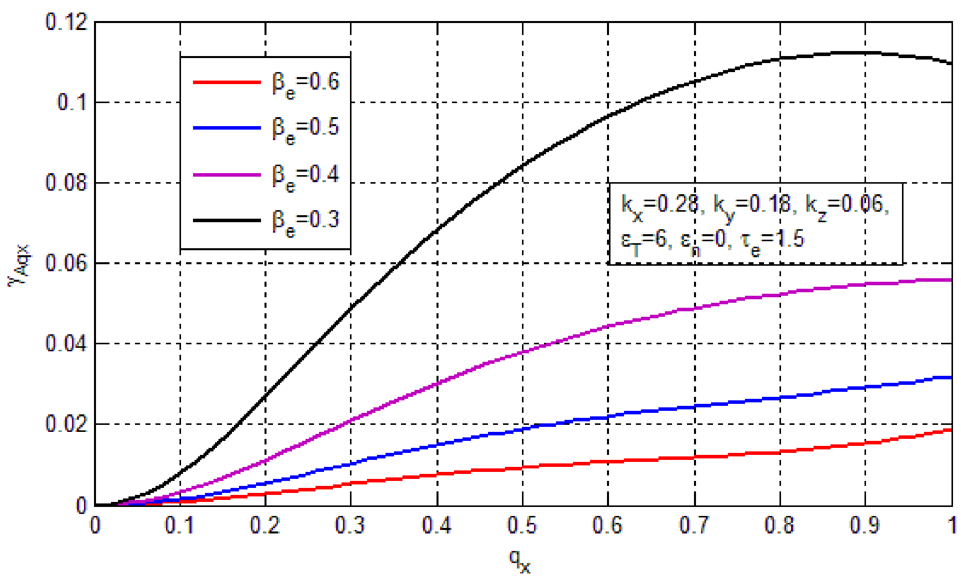

Figure 5.6: Growth rate of zonal field vs q_x for different values of β_e.

Figure 5.6 represents the normalized growth rate (γ) as a function of wave-number (q_x) of zonal field for different value of β_e at $k_x = 0.28$, $k_y = 0.18$, $k_z = 0.06$, $q_z = 0$, $\varepsilon_T = 6$, $\varepsilon_n = 0$, $\tau_e = 1.5$. The growth of the zonal modes decreases with β_e and increases with q_x similar as for zonal flow. For $q_x > 0.7$ the growth of the mode is getting saturated.

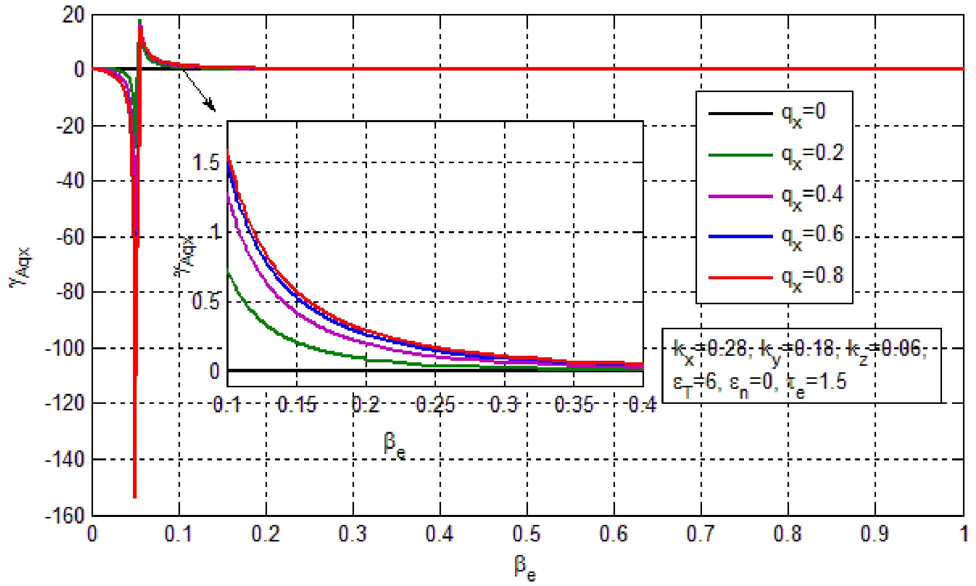

Figure 5.7: Growth rate of zonal field vs β_e for different values of q_x.

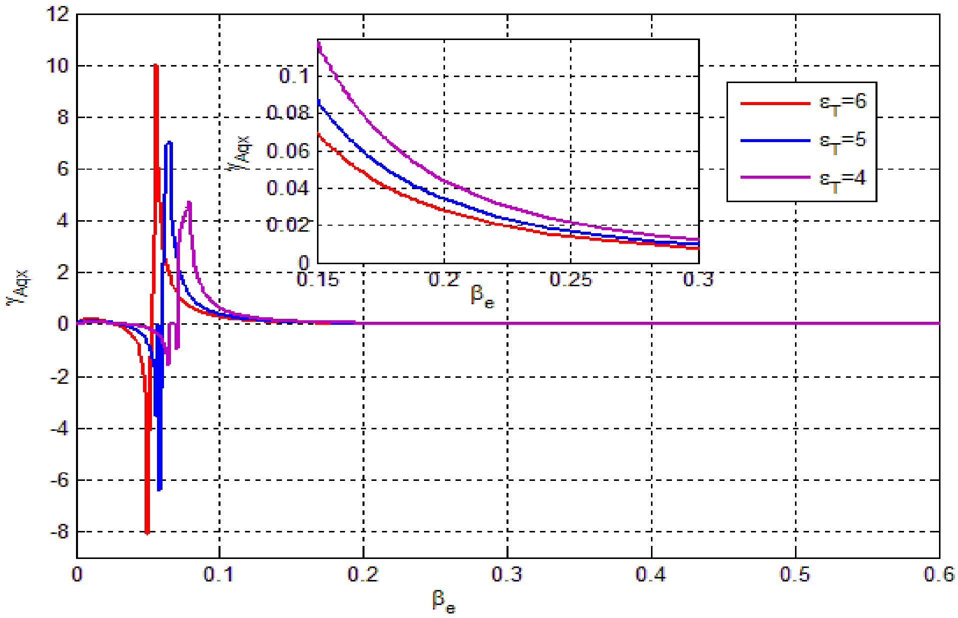

Figure 5.8: Growth rate of zonal field vs β_e for different values of ε_T. The other parameters remain fixed as mentioned in above figure with $q_x = 0.1$.

The growth rate (γ) of zonal fields as a function of β_e for various value of q_x has been represented in figure 5.7 keeping other parameters same. The mode having high value of q_x has more growth comparison to low q_x mode. In the electrostatic limit, the growth of zonal mode is zero and for $\beta_e > 0.1$, it decreases continuosly and becomes zero for higher value of

β_e. Similarly, figure 5.8 is the growth rate (γ) of the mode as a function of β_e for different value of ε_T and follows similar trend with beta as discussed above. The growth of zonal fields is smaller for higher value of ε_T.

5.6.2 Results for Streamers

In this section we present discussion of numerical solutions of the dispersion relation for streamers. The dispersion relation (equation 5.64) has been written in a normalization which is not suitable for flat density profile cases. Hence the dispersion relation is re-written in a more flexible normalization scheme suitable which can deal with flat density profile cases. Here $(\Omega_q,\omega_k) = (\Omega_q,\omega_k)/(c_e/R)$ and $(q_\parallel,k_\parallel) = (q_\parallel,k_\parallel)R$.

$$\Omega_q\left(\tau_e + \left(1+\tau_e\right)\frac{\beta}{2} + q_Y^2\right) + q_Y\left(1 - \frac{\beta}{2}\left(1+\tau_e - q_Y^2\right)\left(\varepsilon_n + \varepsilon_T\right)\right)$$
$$+\left(-\frac{\beta}{2}\left(\Omega_q - q_Y\left(\varepsilon_n+\varepsilon_T\right)\right) + \right)R_{T,q} - q_Y^2 q_\parallel R_{A_z,q} \;=\; iq_y^4\sigma_\phi \qquad (5.77)$$

where now the nonlinear terms given in equations (5.65-5.68) structurally remains as it is. The above equation is in general an integral eigenvalue equation due to the specific structure of the propagator $R_{k,q}$, which makes it very difficult to solve exactly. Hence to make progress, we assume that the primary modes are growing much faster than the secondary modes i.e., $\Omega_q - \vec{q}\cdot\vec{v}_{g,k} << \gamma_k$. This makes the propagator independent of Ω_q i.e. $R_{k,q} = 1/\gamma_k$ and the dispersion relation becomes purely algebraic. γ_k is obtained by solving the linear dispersion relation [Eqn. 5.10]. Moreover to evaluate the nonlinear terms the equilibrium action density $<N_k>$ has to be prescribed. Again for simplicity we assumed a monochromatic spectrum of $<N_k>$ i.e., $<N_k>= N_{k0}\delta(k_x-k_{x0})\delta(k_y-k_{y0})\delta(k_z-k_{z0})$ corresponding to a cold beam of quasi-particles. In all numerical calculations presented here we have set $C_k N_{k0} = |\phi_0|^2 = (2/\beta)\ \varepsilon_T^2$.

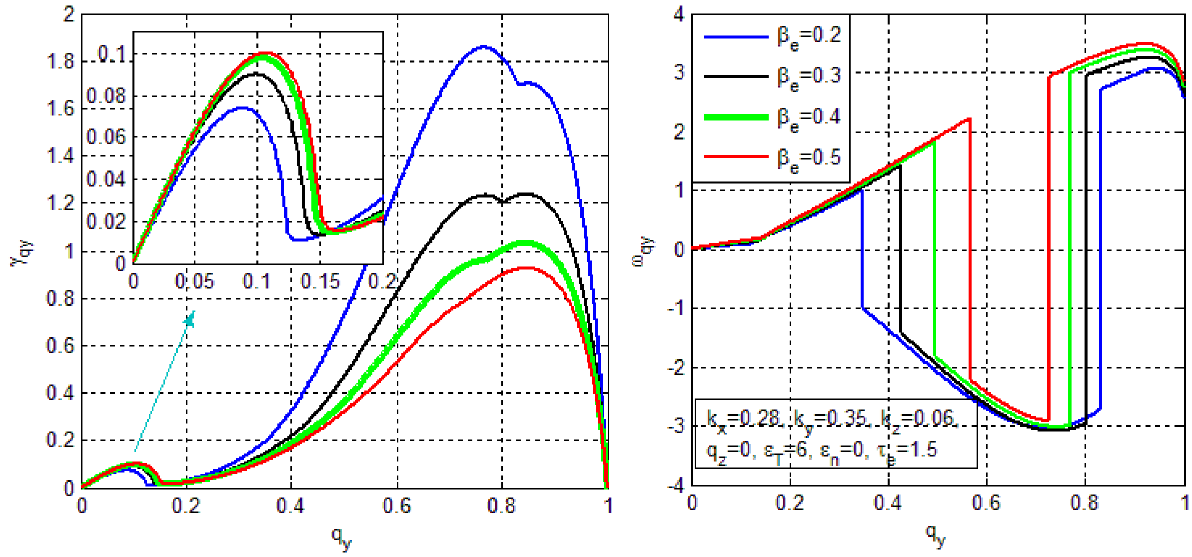

Figure 5.9: The growth rate and real frequency of electromagnetic streamers vs q_y for different value of β_e. The figure shows that the growth rate increase with β_e.

Figure 5.9 shows the normalized growth rate (γ) and real frequency(ω_r) as a function of wave-number (q_y) of secondary mode (streamer) of W-ETG instability for different value of β_e keeping other parameters fixed at $k_x = 0.28$, $k_y = 0.35$, $k_z = 0.06$, $q_z = 0$, $\varepsilon_T = 6$, $\varepsilon_n = 0$, $\tau_e = 1.5$. The profile represents that growth of the secondary instability increases with β_e for lower value of q_y and it peaks lie around $q_y = 0.1$ whereas for high value of $q_y > 0.15$, growth rate decreases with β_e. The second peak represents the maximum growth of primary mode of the instability. This result explains nonlinear features of W-ETG streamers such as inverse cascading because generation of secondary mode of low q_y at cost of high q_y.

Figure 5.10 shows the normalized growth rate (γ) and real frequency (ω_r) as a function of wave-number (q_y) for different value of q_z keeping other parameters fixed at $k_x = 0.28$, $k_y = 0.35$, $k_z = 0.06$, $\beta_e = 0.6$, $\varepsilon_T = 6$, $\varepsilon_n = 0$, $\tau_e = 1.5$. The figure represents that maximum growth of secondary mode decreases with increasing value of q_z for $q_y < 0.2$.

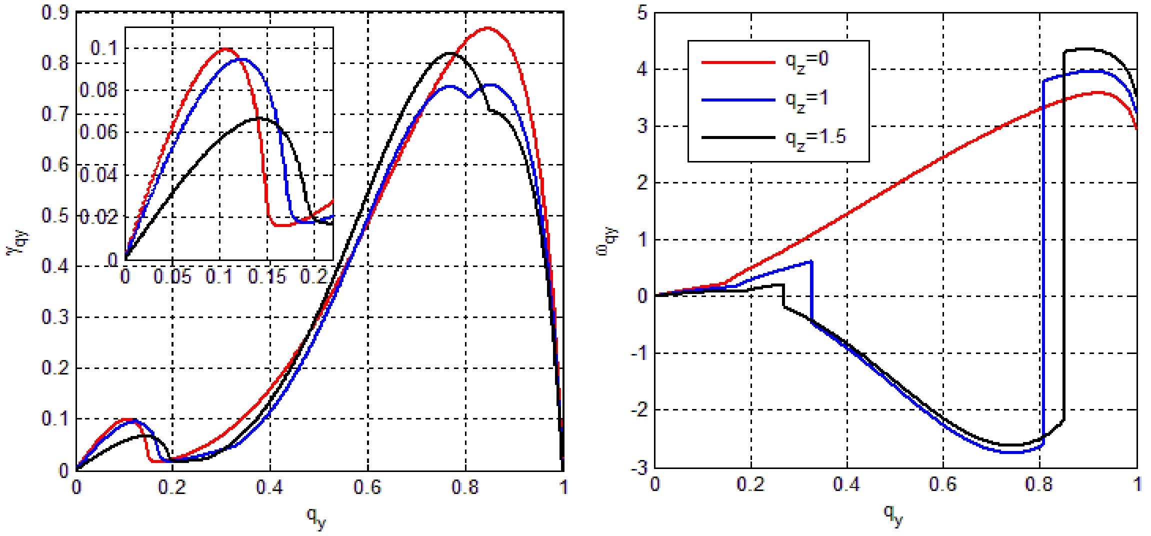

Figure 5.10: The growth rate and real frequency of magnetic streamers vs q_y for different value of q_z. The figure shows that the growth rate of the secondary mode decreases with q_z. The other parameters remains fixed as mentioned in above figure with β_e=0.5.

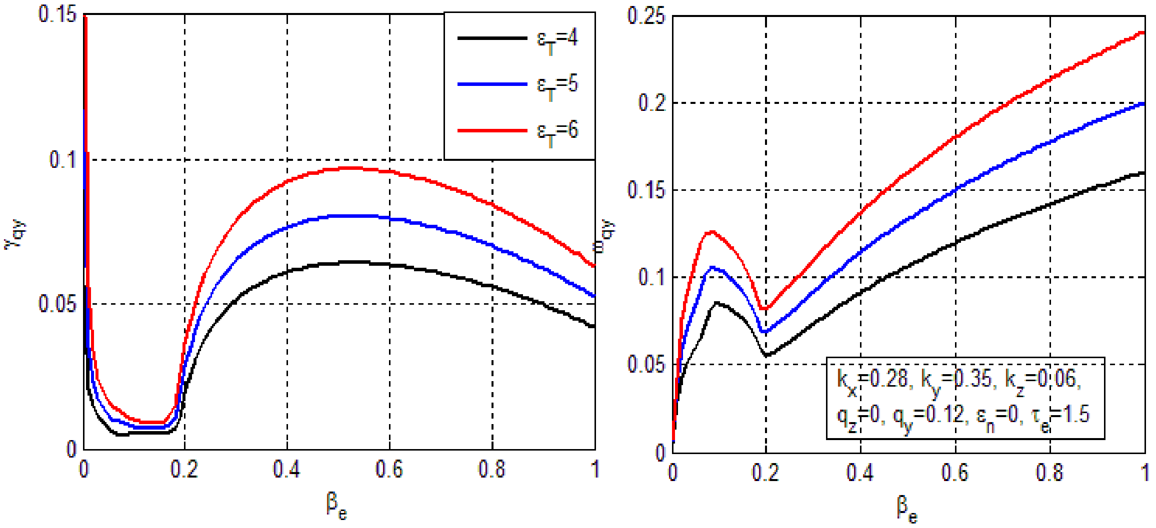

Figure 5.11: The growth rate and real frequency vs β_e for different value of ε_T. The two regions represent electrostatic and electromagnetic nature of the streamers.

Figure 5.11 illustrates the normalized growth rate (γ) and real frequency (ω_r) as a function of β_e for various value of ε_T for parameters $k_x = 0.28$, $k_y = 0.35$, $k_z = 0.06$, $q_z = 0$, $q_y = 0.1$, $\varepsilon_n = 0$, $\tau_e = 1.5$. In initial value of $\beta_e < 0.2$, growth of mode decreases and it increases with increasing $\beta_e > 0.2$. These two regions represent electrostatic and electromagnetic nature of the secondary mode respectively. In the electrostatic limit ($\beta_e < 0.2$), mode gets stabilized due to $\delta B_\perp$ perturbation whereas in the electromagnetic case ($\beta_e > 0.2$), coupling of δB_z perturbation with other fluctutaions of ETG mode give rise to Whistler-ETG mode and growth of the mode increases with ε_T. It is noted that for β_e greater than critical value there is threshold value of β_e for each ε_T before that value growth increases and after that growth decreases. For each ε_T, band of β_e changes so that before critical value mode is like electrostatic and after that it becomes electromagnetic.

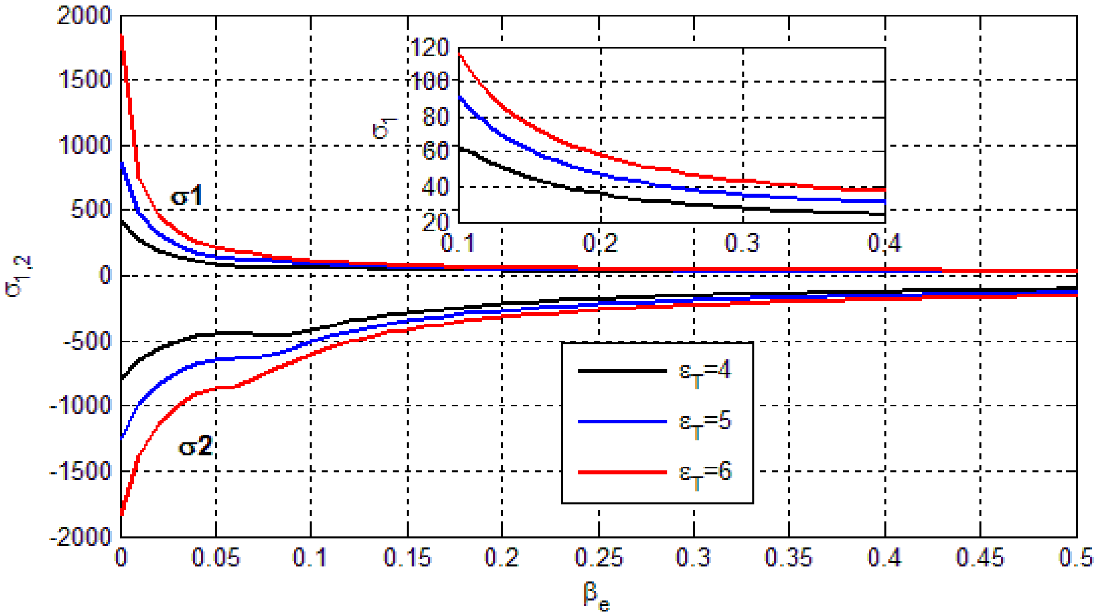

Figure 5.12: The nonlinear drives σ_1 and σ_2 vs β_e for different value of ε_T. The other parameters are similar as for above figure.

Figure 5.12 represents the variation of nonlinear drives (σ_1 and σ_2) of streamers as a function of β_e for different value of ε_T with parameters $k_x = 0.28$, $k_y = 0.35$, $k_z = 0.06$, $q_z = 0$, $q_y = 0.1$, $\varepsilon_n = 0$, $\tau_e = 1.5$. In initial value of $\beta_e < 0.2$ (electrostatic limit), σ_1 decreases and σ_2 increase very rapidly as compared to $\beta_e > 0.2$ (electromagnetic case). For higher value of β_e both σ_1 & σ_2 get saturated. It is also observed from profile that σ_1 increases and σ_2 decrease with increasing value of ε_T.

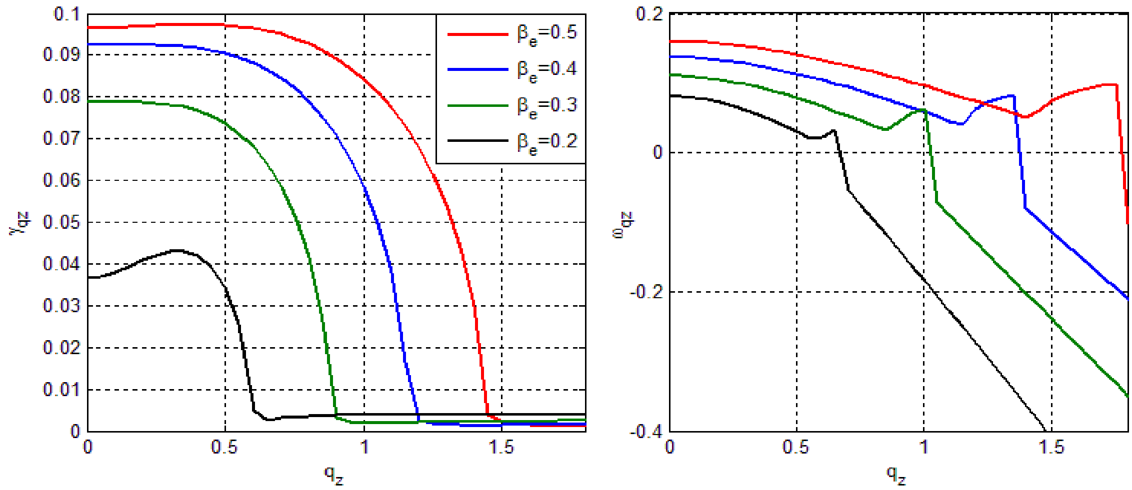

Figure 5.13: The growth rate and real frequency of electromagnetic streamers vs q_z for different value of β_e.

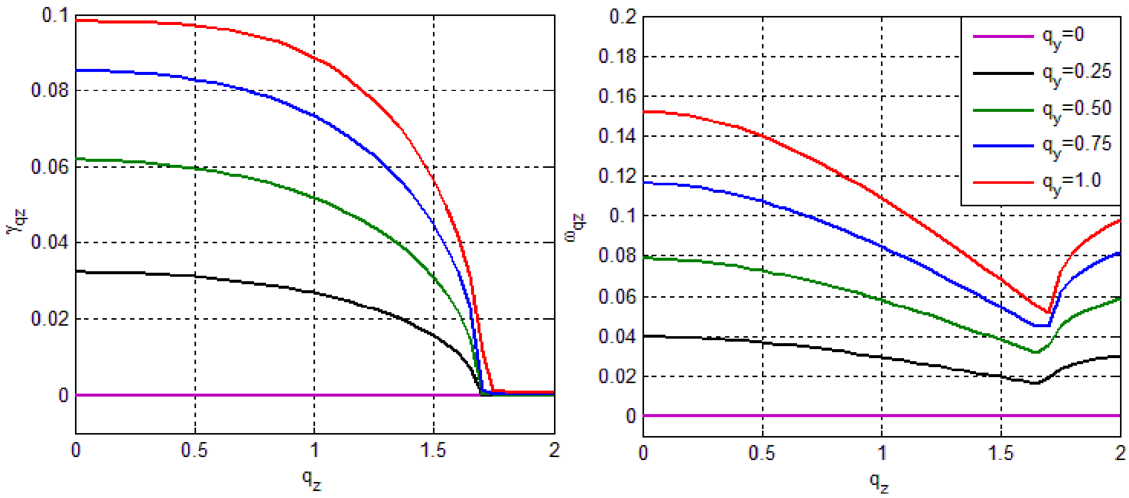

Figure 5.14: The growth rate and real frequency vs q_z for different value of q_y.

Figure 5.13 shows the normalized growth rate (γ) and real frequency (ω_r) as a function of wave-number (q_z) for different value of β_e at $k_x = 0.28$, $k_y = 0.35$, $k_z = 0.06$, $q_y = 0.1$, $\varepsilon_T = 6$, $\varepsilon_n = 0$, $\tau_e = 1.5$. The profile represents that, for small value of q_z does not effect the net growth of the mode except small beta ($\beta_e < 0.3$) but increase in value of q_z has stabilizing effect on growth due to parallel compression. It is also noticed that flat region in profile and growth of the mode increases with β_e. Similar stabilizing effect has been seen in the figure 5.14 for different value of q_y. The growth becomes zero for $q_z > 1.8$ for any value of q_y and modes get disappeared for $q_y = 0$.

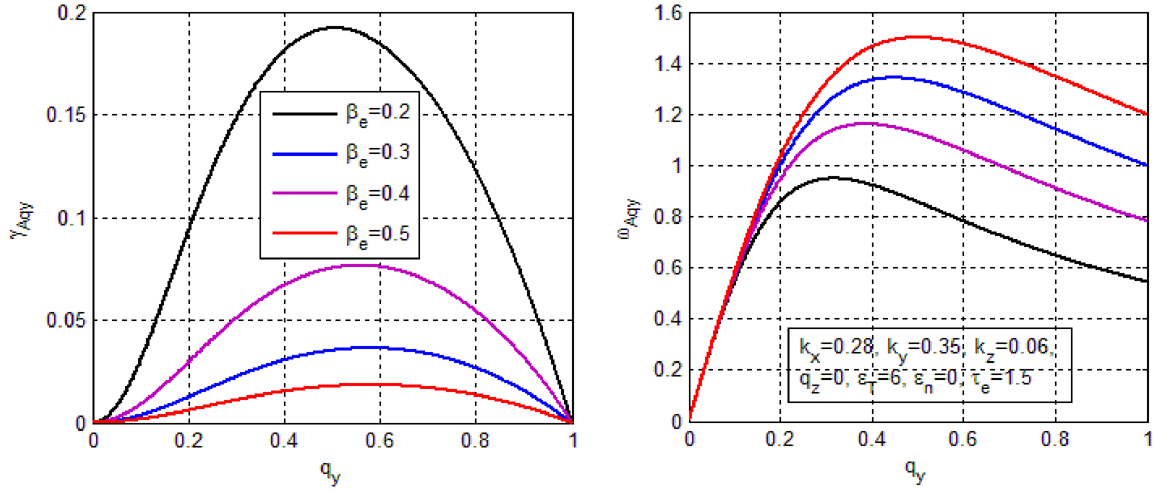

Figure 5.15: The growth rate and real frequency of magnetic streamer vs q_y for different value of β_e.

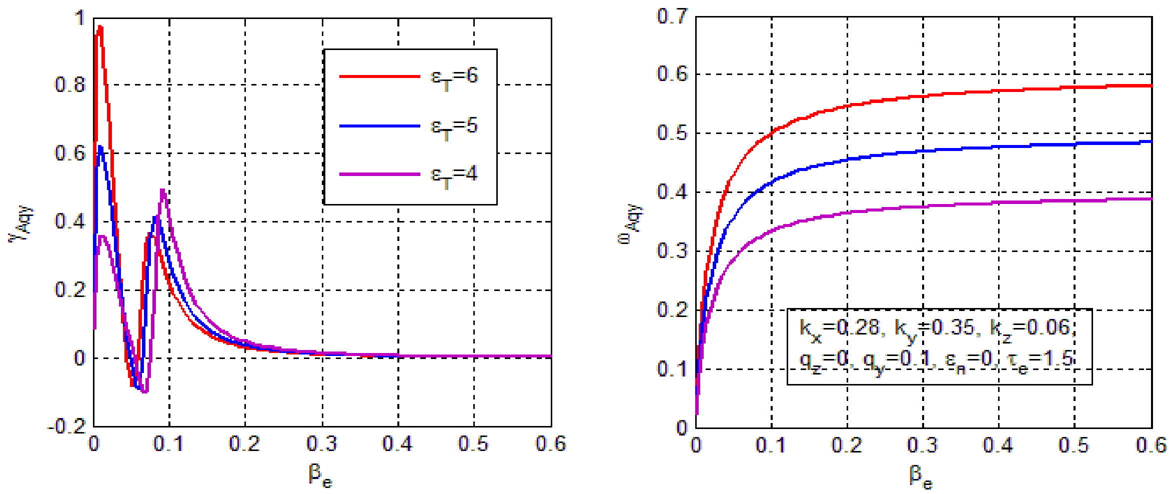

Figure 5.16: The growth rate and real frequency of magnetic streamer vs β_e for different value of ε_T.

By using equations (5.62) and (5.64) we try to look at the charcteristic of magnetic streamers at ($q_z = 0$) in figure 5.15. It shows the normalized growth rate (γ) and real frequency(ω_r) as a function of wave-number (q_y) for different value of β_e at $k_x = 0.28$, $k_y = 0.35$, $k_z = 0.06$,

$q_z = 0$, $\varepsilon_T = 6$, $\varepsilon_n = 0$, $\tau_e = 1.5$. The growth of magnetic streamers decreases whereas real frequency increases with increasing β_e. The maximum growth shifts towards high q_y for higher value of β_e and growth becomes zero at $q_y = 1$ due to FLR stabilisation for each value of β_e.

Figure 5.16 illustrates the normalized growth rate (γ) and real frequency (ω_r) of magnetic streamers as a function of β_e for various value of ε_T for parameters $k_x = 0.28$, $k_y = 0.35$, $k_z = 0.06$, $q_z = 0$, $q_y = 0.1$, $\varepsilon_n = 0$, $\tau_e = 1.5$. In the profile of growth rate, two peaks are observed where the value of first peak increases and second peak decreases with ε_T. The growth rate decreases with β_e and becomes zero for higher value of β_e. The real frequency increase in low β_e and got saturated in high β_e where whistler coupling is significant. On the other hand, real frequency increases with ε_T.

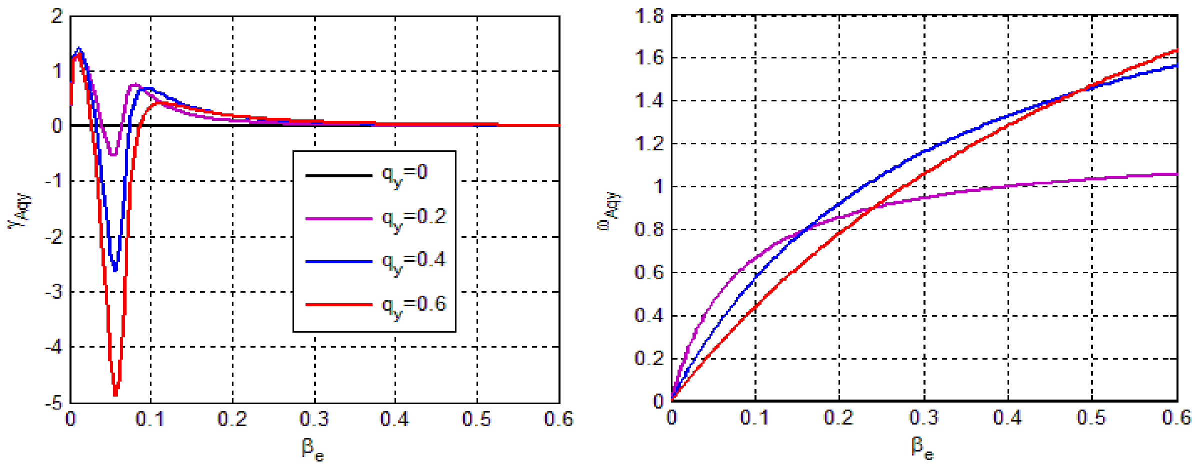

Figure 5.17: The growth rate and real frequency of magnetic streamer vs β_e for different value of q_y. The other parameters remain same as used for past figures of magnetic streamers.

Figure 5.17 represents the similar normalized growth rate (γ) and real frequency (ω_r) vs β_e but for different value of q_y. For high beta case, growth rate decreases and real frequency increases with q_y. For $q_y = 0$, the magnetic streamers are completely absent and real frequency becomes zero irrespective of any value of β_e.

5.7 Conclusions

Secondary instability of W-ETG turbulence is studied with respect to excitation of different long scale fluctuation patterns viz., poloidally smooth and radially oscillating zonal flows and poloidally oscillating and radially smooth streamers. Excitation of each pattern is studied independently of the other though the real pattern will be made of both of zonal flows and streamers interacting with each other.

Wave kinetic equation for the wave action density is used to describe the short scale background turbulence modulation by test long scale perturbation. Nonlinear evolution equations for long scale modes are written in terms of wave action density to form a self-consistent loop of evolution of turbulence and secondary modes. Actually the stress terms formed by averaging of nonlinear small scale fluctuating quantities are written in terms of wave action density. Then a linear stability analysis is done to obtain the dispersion relation of the secondary modes in which equilibrium action density distribution is considered independent of time. To study the backreaction of long scale modes on the host turbulence an equation for quasilinear evolution of mean wave action density is derived. The major findings of the chapter are as follows.

• Zonal flows get excited whenever $-k_x \partial < N > / \partial k_x > 0$ which is typically observed in experimental situations.

• Maxwell stress competes with the Reynolds stress and tend to reduce the zonal flow growth with increasing β. Magnetic whistlering do not produce a nonlinear stress term at $\mathcal{O}((\rho_s^*)^2)$. However the magnetic whistlering scales down the zonal flow growth rate further with increasing β.

• Parallel zonal magnetic vector potential dynamics is independent of the dynamics of the other zonal components.

• Zonal potential diffuses turbulence in towards high k_x which is further enhanced by finite beta effect since $v_{gz} < 0$. The excited zonal temperature and potential causes modulation in η_e which leads to a nonlinear growth of turbulence, which is further enhanced or reduced by finite β effect depending on whether $\partial \gamma_k / \partial k_z > 0$ or < 0.

• The q_y and β spectrum of the growth rate for zonal flows are also discussed. The growth rate increases with q_x and decreases with β. Similar spectrum is also discussed for zonal fields for different parameters and results follow similar characteristic as for zonal flows.

• The growth rate of zonal flow increases with increasing value of ε_T whereas in high beta case ($\beta > 0.2$), it decreases for zonal fields.

• Streamers get excited whenever $-k_y \partial < N > / \partial k_y > 0$ which is also typically observed in experimental situations.

• Parallel streamer magnetic vector potential dynamics is independent of the dynamics of the other streamer components only when $q_{\|} = 0$. Otherwise the streamers are electromagnetic in character.

• Streamer potential diffuses turbulence in towards high k_y which is further enhanced by finite beta effect since $v_{gz} < 0$. The excited streamer vector potential at finite β causes a nonlinear growth of turbulence which is independent of sign of $\partial \gamma_k / \partial k_z$. This behavior of the nonlinear growth is different from that in the zonal flow case due to the fact that streamer perturbations are radially smooth which do not modulate η_e.

• The q_y spectrum of the growth rate shows double hump character with a peak at $q_y < 0.1$ characteristic of streamers apart from another peak at high q_y (~ 0.7). Streamer growth rate increases with β while the growth of background turbulence at high q_y reduces with β.

• Fully electromagnetic streamers with finite q_z shows lower growth compared with the streamers with $q_z = 0$. Moreover increasing β and increasing q_z increases the maximum growing streamer's poloidal wave number.

• For small value of q_z, growth rate of the streamers remains constant but after critical value of $q_z > 0.4$,4 it has stabilizing effect on the growth of the streamers. The critical value of q_z increases with β but independent of q_y.

• The real frequency of streamers decreases with q_z.

• Axially smooth streamer's growth rate shows a non-monotonic behavior with β, goes through a minimum in low β range and then a maximum in high beta range which shows systematic increase with ε_T.

• For $q_z = 0$, magnetic streamers show maximum growth at $q_y = o.5$ which depend on values of β. Higher β reduces the growth of the magnetic streamers and peak of the growth shifts towards higher q_y.

• For $\beta < 0.1$, the growth rate of magnetic streamers increases with increasing value of ε_T but it decreases for $\beta > 0.1$. The real frequency of magnetic streamers increases with β and ε_T.

Appendix A: Evaluation of Nonlinear Terms in the Zonal Mode Equations

Using the general properties of the Poisson brackets given in Ref. [13], the nonlinear terms appearing on the right hand side of the zonal mode equations (5.13-5.15) are evaluated as follows. The dominant nonlinear terms are of the two generic types viz., $\left[f,g\right]$ and $\left[f,\nabla_{\perp}^{2}g\right]$. Hence it is sufficient to show corresponding zonal averaged forms.

$$\langle[f,g]\rangle=\left\langle\nabla_{y}\left(\frac{\partial f}{\partial x}g\right)\right\rangle-\left\langle\nabla_{x}\left(\frac{\partial f}{\partial y}g\right)\right\rangle \tag{A.1}$$

$$=-\nabla_{X}\left\langle\left(\frac{\partial f}{\partial y}g\right)\right\rangle \tag{A.2}$$

where now ∇_X represents the radial derivative on zonal mode scale. The right hand side term can further be expressed in terms of fourier amplitudes f_k and g_k of the respective fields, giving

$$\langle[f,g]\rangle=-\nabla_{X}Re\int\mathrm{d}\vec{k}\left(-ik_{y}\right)f_{k}^{*}g_{k}=-\nabla_{X}Re\int\mathrm{d}\vec{k}\left(ik_{y}\right)f_{k}g_{k}^{*} \tag{A.3}$$

Similarly

$$\left\langle\left[f,\nabla_{\perp}^{2}g\right]\right\rangle=-\nabla_{X}^{2}\left\langle\frac{\partial f}{\partial y}\frac{\partial g}{\partial x}\right\rangle+\nabla_{X}\left\langle\frac{\partial^{2}f}{\partial x\partial y}\frac{\partial g}{\partial x}+\frac{\partial^{2}f}{\partial y^{2}}\frac{\partial g}{\partial y}\right\rangle \tag{A.4}$$

$$=-\nabla_{X}^{2}Re\int\mathrm{d}\vec{k}k_{y}k_{x}f_{k}^{*}g_{k}+\nabla_{X}Re\int\mathrm{d}\vec{k}\left(-ik_{y}\right)k_{\perp}^{2}f_{k}^{*}g_{k} \tag{A.5}$$

Appendix B: Evaluation of Nonlinear Terms in the Streamer Mode Equations

The dominant nonlinearities in the streamer equations are also of the same generic form as that in zonal flow equations. Hence again using the poisson bracket properties given in Ref. [13] gives the following streamer averaged terms.

$$\langle[f,g]\rangle=\left\langle\nabla_{y}\left(\frac{\partial f}{\partial x}g\right)\right\rangle=\nabla_{Y}Re\int\mathrm{d}\vec{k}\left(-ik_{x}\right)f_{k}^{*}g_{k} \tag{B.1}$$

$$= \nabla_X Re\int \mathrm{d}\vec{k}\left(ik_x\right) f_k g_k^* \tag{B.2}$$

Similarly

$$\left\langle\left[f, \nabla_\perp^2 g\right]\right\rangle = \nabla_Y^2 \left\langle \frac{\partial f}{\partial x}\frac{\partial g}{\partial y}\right\rangle - \nabla_Y \left\langle \frac{\partial^2 f}{\partial x^2}\frac{\partial g}{\partial x} + \frac{\partial^2 f}{\partial x \partial y}\frac{\partial g}{\partial y}\right\rangle \tag{B.3}$$

$$= \nabla_Y^2 Re\int \mathrm{d}\vec{k} k_x k_y f_k^* g_k - \nabla_Y Re\int \mathrm{d}\vec{k}\left(-ik_x\right) k_\perp^2 f_k^* g_k \tag{B.4}$$

Appendix C: Model Equations for W-ETG Secondary Instability in Tokamak

In this section, the general equations of W-ETG mode are discussed where additional effect of magnetic field curvature has been included in the calculations for tokamak applications. The modified dispersion relations for linear W-ETG mode and for streamers are discussed as following.

Appendix C.1: Derivation of Linear Dispersion Relation of W-ETG Mode

The perturbed continuity equation for electron dynamics can be written as

$$\frac{\partial n_e}{\partial t} + \left(1-\varepsilon_n\left(1+\tau_e\right)\right)\frac{\partial \phi}{\partial y} - \frac{\beta}{2}\left(\frac{\partial}{\partial t} + K\frac{\partial}{\partial y}\right)b_z + \left(\frac{\partial}{\partial t} + K\frac{\partial}{\partial y}\right)\nabla_\perp^2\phi + \varepsilon_n\frac{\partial T_e}{\partial y} + \nabla_\perp^2\nabla_z^0 A_z$$
$$= -\left[\phi, n_e\right] - \vec{\nabla}\cdot\left[\phi, \vec{\nabla}_\perp(\phi + p_e)\right] + \frac{\beta}{2}\left[A_z, \nabla_\perp^2 A_z\right] + \frac{\beta}{2}\left[\phi - p_e, b_z\right] - \rho_e^*\frac{\beta}{2} b_z \nabla_\perp^2 \nabla_z^0 A_z \tag{C.1.1}$$

Here $\varepsilon_n = 2L_n / R$ is the additional term associated with curvature in magnetic field lines where L_n is the density gradient scale length and R is the radius of curvature of magnetic field. The second and fifth terms associated with ε_n result from the effective compression of $E \times B$ and diamagnetic particle flux modified by curvature in magnetic field. The parallel electron momentum equation or Ohm's law can be written as

$$\left(\left(\frac{\beta}{2}-\nabla_\perp^2\right)\frac{\partial}{\partial t}-\nu\nabla_\perp^2+\frac{\beta}{2}K\frac{\partial}{\partial y}\right)A_z+\nabla_z^0\left(\phi-p_e\right)$$

$$=-\frac{\beta}{2}\left[\phi-p_e,A_z\right]+\left[\phi,\nabla_\perp^2A_z\right]-\rho_e^*\frac{\beta}{2}b_z\nabla_z^0\left(\phi-p_e\right) \tag{C.1.2}$$

and finally electron temperature equation is following

$$\frac{\partial}{\partial t}\left(T_e-\frac{2}{3}n_e\right)+\frac{5}{3}\varepsilon_n\frac{\partial T_e}{\partial y}+\left(\eta_e-\frac{2}{3}\right)\frac{\partial\phi}{\partial y}=-\left[\phi,T_e-\frac{2}{3}n_e\right] \tag{C.1.3}$$

Here second term result from the additional compression in diamagnetic heat flow modified due to curvature effect of magnetic field. The linear relations among fourier amplitudes of various fields are obtained as follows.

$$T_{e,k}=\left[\left(\eta_e-\frac{2}{3}\right)\frac{k_y}{\omega-\omega_D}-\frac{2}{3}\tau_e\frac{\omega}{\omega-\omega_D}\right]\phi_k\equiv\mathcal{R}_T\phi_k \tag{C.1.4}$$

$$p_{e,k}=\left[\left(\eta_e-\frac{2}{3}\right)\frac{k_y}{\omega-\omega_D}-\tau_e\frac{5/3\omega-\omega_D}{\omega-\omega_D}\right]\phi_k\equiv\mathcal{R}_p\phi_k \tag{C.1.5}$$

$$A_{z,k}=\frac{k_z}{\omega-\omega_D}\frac{\omega-\omega_D+\tau_e\left(5/3\omega-\omega_D\right)-\left(\eta_e-2/3\right)k_y}{\left(\beta/2+k_\perp^2\right)\omega+i\nu k_\perp^2-\beta/2Kk_y}\phi_k\equiv\mathcal{R}_A\phi_k \tag{C.1.6}$$

$$b_{z,k}=\left[1+\tau_e\frac{5/3\omega-\omega_D}{\omega-\omega_D}-\left(\eta_e-\frac{2}{3}\right)\frac{k_y}{\omega-\omega_D}\right]\phi_k\equiv\mathcal{R}_b\phi_k \tag{C.1.7}$$

where $\omega_D=5/3\varepsilon_n k_y$ is the curvature drift frequency. Fourier analysing in space and time the set of Equations (C.1.1-C.1.3) yields the linear dispersion relation,

$$\omega\tau_e+\left(1-\varepsilon_n\left(1+\tau_e\right)\right)k_y+k_\perp^2\left(\omega-Kk_y\right)+\frac{\beta}{2}\left(\omega-Kk_y\right)\mathcal{R}_b+\varepsilon_n k_y\mathcal{R}_T=k_\perp^2k_z\mathcal{R}_A \tag{C.1.8}$$

Appendix C.2: Derivation of Nonlinear Dispersion Relation of W-ETG Mode and Excitation of Streameres in Tokamak

Following the procedures as used in section (5) the streamer equations of W-ETG turbulence for tokamak plasma are obtained as following.

$$-\tau_e \frac{\partial\langle\phi\rangle}{\partial t} + \left(1-\varepsilon_n\left(1+\tau_e\right)\right)\frac{\partial\langle\phi\rangle}{\partial Y} - \frac{\beta}{2}\left(\frac{\partial}{\partial t} + K\frac{\partial}{\partial Y}\right)\langle b_z\rangle + \nabla_Y^2\nabla_Z^0\langle A_z\rangle$$

$$+\left(\frac{\partial}{\partial t} + K\frac{\partial}{\partial Y}\right)\nabla_Y^2\langle\phi\rangle + \varepsilon_n\frac{\partial\langle T_e\rangle}{\partial Y} = -\nabla_Y^2 Re\int \mathrm{d}\vec{k}k_y k_x\left(1-\frac{\beta}{2}|\mathcal{R}_A|^2 + \mathcal{R}_p\right)|\phi_k|^2 \qquad \text{(C.2.1)}$$

$$\left(\left(\frac{\beta}{2} - \nabla_Y^2\right)\frac{\partial}{\partial t} - \nu\nabla_Y^2 + \frac{\beta}{2}K\frac{\partial}{\partial Y}\right)\langle A_z\rangle + \nabla_Z^0\langle\phi - p_e\rangle$$

$$= i\nabla_Y Re\int \mathrm{d}\vec{k}k_x\left(k_\perp^2 + \frac{\beta}{2}\left(1-\mathcal{R}_p^*\right) - i\nabla_Y k_y\right)\mathcal{R}_A|\phi_k|^2 \qquad \text{(C.2.2)}$$

$$\frac{\partial}{\partial t}\left(\langle T_e\rangle + \frac{2}{3}\tau_e\langle\phi\rangle\right) + \frac{5}{3}\varepsilon_n\frac{\partial\langle T_e\rangle}{\partial Y} + \left(\eta_e - \frac{2}{3}\right)\frac{\partial\langle\phi\rangle}{\partial Y} = \nabla_Y Re\int \mathrm{d}\vec{k}ik_x\mathcal{R}_T|\phi_k|^2 \qquad \text{(C.2.3)}$$

$$\langle b_z\rangle = \langle\phi\rangle - \langle p_e\rangle = \left(1+\tau_e\right)\langle\phi\rangle - \langle T_e\rangle \qquad \text{(C.2.4)}$$

The terms on the left hand side with $\langle\ \rangle$ represents streamer components and that on the right hand side are averaged nonlinear drives which has $q_x = q_z = 0$.

Now using the $\vec{k}$-space symmetry properties of real frequency ($\omega_{r,k}$) and growth rate (γ_k) and then taking the fourier transform of above equations in Y, we get

$$\left(-\tau_e - \left(1+\tau_e\right)\frac{\beta}{2} - q_Y^2\right)\frac{\partial\langle\phi\rangle_q}{\partial t} + iq_Y\left(1-\varepsilon_n\left(1+\tau_e\right) - \frac{\beta}{2}\left(1+\tau_e\right)K - q_Y^2 K\right)\langle\phi\rangle_q$$

$$+\left[\frac{\beta}{2}\left(\frac{\partial}{\partial t}+iq_Y K\right)+i\varepsilon_n q_Y\right]\langle T_e\rangle - iq_Y^2 q_\parallel \langle A_z\rangle_q$$

$$= -q_Y^4\int \mathrm{d}\vec{k}k_x^2\left(1-\frac{\beta}{2}|\mathcal{R}_A|^2+Re\mathcal{R}_p\right)\mathcal{R}_{k,q}C_k\left(-k_y\frac{\partial\langle N_k\rangle}{\partial k_y}\right)\langle\phi\rangle_q \tag{C.2.5}$$

$$\left(\left(\frac{\beta}{2}+q_Y^2\right)\frac{\partial}{\partial t}+\nu q_Y^2+i\frac{\beta}{2}Kq_Y\right)\langle A_z\rangle_q + iq_\parallel\left(\langle\phi\rangle_q-\langle p_e\rangle_q\right)$$

$$=\frac{\beta}{2}q_Y^2\int \mathrm{d}\vec{k}k_x^2\left(k_\perp^2 Im\mathcal{R}_A+\frac{\beta}{2}Im\left(\mathcal{R}_A-\mathcal{R}_p^*\mathcal{R}_A\right)\right)\langle A_z\rangle_q\mathcal{R}_{k,q}C_k\frac{\partial\gamma_k}{\partial k_z}\langle N_k\rangle$$

$$+\frac{\beta}{2}q_Y^4\int \mathrm{d}\vec{k}\left(-k_x^2 Re\mathcal{R}_A\mathcal{R}_{k,q}C_k\right)v_{gz}\langle A_z\rangle_q\left(-k_y\frac{\partial\langle N_k\rangle}{\partial k_y}\right) \tag{C.2.6}$$

$$\frac{\partial}{\partial t}\left(\langle T_e\rangle_q+\frac{2}{3}\tau_e\langle\phi\rangle_q\right)+i\frac{5}{3}\varepsilon_n q_Y\langle T_e\rangle_q+i\left(\eta_e-\frac{2}{3}\right)q_Y\langle\phi\rangle_q$$

$$=-iq_Y^3\int \mathrm{d}\vec{k}k_x^2C_k\mathcal{R}_{k,q}\left(-Im\mathcal{R}_T\frac{\partial\langle N_k\rangle}{\partial k_y}\right)\langle\phi\rangle_q \tag{C.2.7}$$

From above streamer mode equations a linear relation among various streamer fields can be obtained as follows.

$$\langle T_e\rangle_q=\left[\frac{q_y^3\sigma_T}{\Omega_q-\Omega_D}+\left(\eta_e-\frac{2}{3}\right)\frac{q_Y}{\Omega_q-\Omega_D}-\frac{2}{3}\tau_e\frac{\Omega_q}{\Omega_q-\Omega_D}\right]\langle\phi\rangle_q\equiv\mathcal{R}_{T,q}\langle\phi\rangle_q \tag{C.2.8}$$

$$\langle p_e\rangle_q=\left[\frac{q_y^3\sigma_T}{\Omega_q-\Omega_D}+\left(\eta_e-\frac{2}{3}\right)\frac{q_y}{\Omega_q-\Omega_D}-\tau_e\frac{5/3\Omega_q-\Omega_D}{\Omega_q-\Omega_D}\right]\langle\phi\rangle_q\equiv\mathcal{R}_{p,q}\langle\phi\rangle_q \tag{C.2.9}$$

$$\langle A_z\rangle_q=\frac{q_\parallel}{\Omega_q-\Omega_D}\frac{\Omega_q-\Omega_D+\tau_e\left(5/3\Omega_q-\Omega_D\right)-\left(\eta_e-2/3\right)q_y-q_y^3\sigma_T}{\left(\beta/2+q_y^2\right)\Omega_q+i\nu q_y^2-\beta/2Kq_y-i\beta/2q_y^2\left(\sigma_{A1}+q_y^2\sigma_{A2}\right)}\langle\phi\rangle_q\equiv\mathcal{R}_{A_z,q}\langle\phi\rangle_q \tag{C.2.10}$$

$$\langle b_z\rangle_q=\left[1+\tau_e\frac{5/3\Omega_q-\Omega_D}{\Omega_q-\Omega_D}-\left(\eta_e-\frac{2}{3}\right)\frac{q_y}{\Omega_q-\Omega_D}-\frac{q_y^3\sigma_T}{\Omega_q-\Omega_D}\right]\langle\phi\rangle_q\equiv\mathcal{R}_{b,q}\langle\phi\rangle_q \tag{C.2.11}$$

where $\Omega_D = 5/3\varepsilon_n q_y$ is the curvature drift frequency at streamer wavelength. From the above set the equations, the dispersion relation for streamer in tokamak can be written as

$$\Omega_q\left(\tau_e+(1+\tau_e)\frac{\beta}{2}+q_Y^2\right)+q_Y\left(1-\varepsilon_n(1+\tau_e)-\frac{\beta}{2}(1+\tau_e)K-q_Y^2K\right)$$
$$+\left(-\frac{\beta}{2}\left(\Omega_q-q_YK\right)+\varepsilon_n q_Y\right)\mathcal{R}_{T,q}-q_Y^2q_\parallel\mathcal{R}_{A_z,q}=iq_y^4\sigma_\phi \qquad \text{(C.2.12)}$$

where

$$\sigma_\phi=\int \mathrm{d}\vec{k}k_x^2\left(1-\frac{\beta}{2}|\mathcal{R}_A|^2+Re\mathcal{R}_p\right)\mathcal{R}_{k,q}C_k\left(-k_y\frac{\partial\langle N_k\rangle}{\partial k_y}\right) \qquad \text{(C.2.13)}$$

$$\sigma_T=-\int \mathrm{d}\vec{k}k_x^2C_k\mathcal{R}_{k,q}\left(-Im\mathcal{R}_T\frac{\partial\langle N_k\rangle}{\partial k_y}\right) \qquad \text{(C.2.14)}$$

$$\sigma_{A1}=\int \mathrm{d}\vec{k}k_x^2\left(k_\perp^2Im\mathcal{R}_A+\frac{\beta}{2}Im\left(\mathcal{R}_A-\mathcal{R}_p^*\mathcal{R}_A\right)\right)\mathcal{R}_{k,q}C_k\frac{\partial\gamma_k}{\partial k_z}\langle N_k\rangle \qquad \text{(C.2.15)}$$

and

$$\sigma_{A2}=\int \mathrm{d}\vec{k}\left(-k_x^2Re\mathcal{R}_A\mathcal{R}_{k,q}C_k\right)v_{gz}\left(-k_y\frac{\partial\langle N_k\rangle}{\partial k_y}\right) \qquad \text{(C.2.16)}$$

where $\mathcal{R}_{k,q}$ is same as $R_{k,q}$ as defined in equation (5.24) but now contains the effect of magnetic curvature as well.

Chapter 6

Conclusions and Future Outlook

To summarize, we have presented the experimental evidence and theory of Electron Temperature Gradient driven turbulence in finite beta plasma in LVPD. A summary of each chapter of this thesis and direction of future research are as follows:

6.1 Summary and Conclusions

1. The experiment is carried out in LVPD argon plasma. We have designed and installed a rectangular solenoid (EEF) across the axis of LVPD to control energetic electrons, which enable us to control electron temperature and density profiles, all across the target plasma. Three significant changes in the characteristics of the plasma are observed by varying current in EEF: (i) energetic electrons are scavenged from the target region and constrained to remain in the source and EEF region; (ii) the electron temperature is reduced in the target region because the energetic electron are trapped in high magnetic field of EEF region whereas thermal electron diffused out from this region via classical processes; (iii) a significant gradient in the electron temperature and density profiles are produced by controlling current density along the length of solenoid for different EEF configurations. Furthermore, a capacitor bank based 5 kA current power supply has been made for providing different current density in EEF. In diagnostic front, an electronically compensated Langmuir probe technique has been developed to measure electron temperature fluctuations with good accuracy and exhibits a distinct advantage over uncompensated technique of the probe.

2. First unambiguous experimental demonstration of ETG turbulence is established in finite beta laboratory plasma in absence of energetic electrons. The excitation and confirmation of the ETG mode are made by suitable control of the equilibrium plasma profile using two optimized configurations of EEF. Observations reveal that δT_e, δn_e and δB_Z exhibit strong signature when temperature gradient, $\nabla_r T_e$ is finite and reduce to noise level when $\nabla_r T_e \simeq 0$. The experimental results conclude that observed turbulence lies in lower hybrid range of frequencies. The correlation coefficient exhibits strong anti-correlation between various physical parameters like electron temperature, plasma density, magnetic field and floating potential. The observed wave-numbers are consistent with the scale length ($k_\perp \rho_e \leq 1$) of ETG turbulence and also satisfies the condition $k_z / k_\perp << 1$. The joint wave-number frequency spectrum shows that the observed mode propagates in the electron diamagnetic drift direction and is of same order in magnitude. The observed mode is electrostatic for $\beta_e < 0.1$ and it becomes electromagnetic for $\beta_e > 0.1$. In addition to linear observations, the vortex like nonlinear coherent structures is also investigated by using conditional averaging technique in the background of ETG turbulence. Observations indicate that structures for ion saturation current and floating potential are anti-correlated. These coherent structures exhibit weak nonlinearity because of their elongated shape. Observations speculate that the nonlinear modes, having alternative dipole structures, would be streamers dominated structures excited by tertiary instability like Kelvin-Helmholtz (K-H) modes. The detail investigation of the exact nature of nonlinear structures over full poloidal cross-section of the plasma is an open problem for future studies.

3. Theoretical model to describe the coupled W-ETG mode in finite β_e plasma have been developed and analytical solutions for different cases are presented. The theoretical estimation of fluctuation level and the linear plots of W-ETG dispersion relation are compared with experimental observations of LVPD plasma for various plasma parameters. The comparison between experimental and theoretical results related with frequency, wave-number, phase velocity, phase angle, correlation, parametric dependence of growth rates and beta scaling of fluctuation level estimated from mixing length argument are in good agreement. The physics and some other aspects of ETG, Whistler and W-ETG modes have also been discussed.

4. Electromagnetic secondary instability of W-ETG turbulence is studied with respect to excitation of mesoscale [i.e., $(\rho_e L_T)^{1/2}$ or $(\rho_e^2 L_T)^{1/3}$] fluctuation patterns namely, poloidally smooth and radially oscillating zonal flows and poloidally oscillating and radially smooth streamers. The zonal flows, zonal magnetic field, electromagnetic streamers and pure magnetic streamers are shown to get excited by ETG turbulence with effect of finite beta. Excitation of each pattern is studied independently of the other, though the real pattern will be made from both of zonal flows and streamers interacting with each other. The dispersion relations for zonal flows and streamers are derived using wave kinetic formalism. The numerical results including growth rate with wave-number spectrum for different parameters are discussed. The interpretations of the results and mode characteristic for both nonlinear structures are also concluded.

6.2 An Outlook for Future Studies

1. The successful demonstration of ETG turbulence can be expanded in future towards identifying the ETG threshold in LVPD. This will provide to characterize the ETG turbulence in finite beta plasma and its impact on plasma transport. The transport estimation would provide the scaling between heat flux and typical scale lengths for LVPD plasma conditions. For carrying out this investigation, the EEF magnetic field is required to ramp up to achieve the variation in equilibrium profiles. This can be established by increasing the pulse plasma duration, by enhancing capacity of discharge power supply, EEF power supply, source function and versatility of our data acquisition system regarding data resolution and record length. After making the measurements on plasma transport, a theoretical model can be developed to explore the physics behind transport mechanism and would be scaled up to understand the physics of tokamak plasma.

2. In this thesis, the investigation of nonlinear structures is constrained in slab region because of diagnostic limitations and this poses difficulty in making a distinct conclusion about actual nature of structures. The detailed study of nonlinear structures over entire cross-section of core plasma may provide a clear overview of ETG turbulence. In future, we would like to measure nonlinear structures over entire cross-section. These

observations may also be helpful to speculate some crucial nonlinear phenomenon such as zonal flows, electromagnetic and magnetic streamers in the background of ETG turbulence. This experiment can be undertaken by developing suitably diagnostic like rotatable probe drive for scanning the whole poloidal cross-section of plasma.

3. It is well known that the shear electric field and magnetic shear play crucial role in controlling particle and thermal transport in plasma. In future, we would like to do experiments by introducing electric and magnetic shears in LVPD. The electric field shear in plasma can be generated by installing the biased poloidal ring at the edge whereas magnetic field shear can be generated by current carrying wire passing through axis of the plasma column of LVPD.

4. It would be interesting to investigate the physics behind modification in equilibrium profiles in target plasma due to changing EEF magnetic field configurations because it is still not understood how this happens. The different plasma equilibrium can be understood through the correlation with magnetic field geometry, role of leakage energetic electron through EEF and equilibrium plasma evolution in the target chamber of the device. This problem can be addressed by proper modelling of the plasma using thermal balance equations along with law of charge and mass conservations.

Bibliography

[1] O. Gruber, H.U. Fahrbach, O. Gehre et al., Plasma Phys. Control. Fusion **30**, 1611(1988).

[2] K. H. Burrell, S. L. Allen, G. Bramson et al., Plasma Phys. Control. Fusion **31**, 1649 (1989).

[3] P. H. Diamond, S. I. Itoh, K. Itoh and T. S. Hahm, Plasma Phys. Control. Fusion **47**, R35 (2005).

[4] R. R. Parker, M. Greenwald, S. C. Luckhardt et al., Nucl. Fusion **25**, 1127 (1985).

[5] R. J. Goldston, Plasma Phys. Control. Fusion **26**, 87 (1984).

[6] G. S. Lee and P. H. Diamond, Phys. Fluids **29**, 3291 (1986).

[7] P. N. Guzdar, C. S. Liu, J. Q. Dong et al., Phys. Rev. Lett. **57**, 2818 (1986).

[8] W. Horton, B. G. Hong, and W. M. Tang, Phys. Fluids **31**, 2971 (1988).

[9] W. Dorland, F. Jenko, M. Kotschenreuther et al., Phys. Rev. Lett. **85**, 5579 (2000).

[10] F. Jenko and W. Dorland Phys. Rev. Lett. **89**, 225001 (2002).

[11] W. M. Nevins, J. candy, S. Cowley et al., Phys. Plasmas **13**, 122306 (2006).

[12] R. Singh, P. K. Kaw and J. Weiland, Nucl. Fusion **41**, 1219 (2001).

[13] C. Holland and P. H. Diamond, Phys. Plasmas **9**, 3857 (2002).

[14] R. Singh, V. Tangri, H. Nordman et al., Phys. Plasmas **8**, 4340 (2001).

[15] Y. C. Lee, J. Q. Dong, P. N. Guzdar and C. S. Liu, Phys. Fluids **30,** 1331 (1987).

[16] J. Kim and W. Horton, Phys. Fluids **B 3,** 1167 (1991).

[17] W. Horton, P. Zhu, G. T. Hoang, T. Aniel, M. Ottaviani and X. Garbet, Phys. Plasmas **7,** 1494 (2000).

[18] W. Horton, G. T. Hoang, C. Bourdelle et al., Phys. Plasmas **11**, 2600 (2004).

[19] Y. Ren, S. M. Kaye, E. Mazzucato et al., Phys. Rev. Lett. **106**, 165005(2011).

[20] E. Mazzucato, D. R. Smith, R. E. Bell et al., Phys. Rev. Lett. **101,** 075001 (2008).

[21] X. Wei, V. Sokolov, and A. K. Sen, Phys. Plasmas **17**, 042108 (2010).

[22] X. R. Fu, W. Horton, Y. Xiao, Z. Lin, A. K. Sen, and V. Sokolov, Phys. Plasmas **19**, 032303 (2012).

[23] L. M. Awasthi, S. K. Mattoo, R. Jha et al , Phys. Plasmas **17**, 42109 (2010).

[24] S. K. Mattoo, V. P. Anita, L. M. Awasthi, and G. Ravi, Rev. Sci. Instrum.**72**, 3864 (2001).

[25] T. A. Santhosh Kumar, S. K. Mattoo, and R. Jha, Phys. Plasmas **11**, 1735 (2004).

[26] R. Limpaecher, K. R. Mackenzie, Rev. Sci. Instrument, **44**, 726 (1973).

[27] Ehlers and Leung, Rev. Sci. Instrum. **52**, 1452 (1982).

[28] A. J. T. Holmes, Rev. Sci. Instrum. **53**, 1517 (1982).

[29] C. Koch and G. Matthieussent, Phys. Fluids **26,** 545 (1983).

[30] N. Hershowitz and T. Intrator, Rev. Sci. Instrum. **52**, 1629 (1981).

[31] J. L. Ferreira, G. D. Ludwig, and A. Montes, Plasma Phys. Control. Fusion **33,** 297 (1991).

[32] K. N. Leung, N. Hershkowitz, and T. Romesser, Physics Letters **53 A,** 264 (1975).

[33] S. K. Singh, L. M. Awasthi, S. K. Mattoo, P. K. Srivastava, R. Singh and P. K. Kaw, Plasma Phys. Control. Fusion **54**, 124015 (2012).

[34] Ronald J. Adrian, Phys. Fluids **22** , 2065 (1979).

[35] S. J. Zweben and R. W. Gould, Nucl. Fusion **25**, 171 (1985).

[36] R. Jha, P. K. Kaw, S. K. Mattoo, C. V. S. Rao, Y. C. Saxena, and the ADITYA Team, Phys. Rev. Lett. **69**, 1375 (1992).

[37] S. Benkadda, T. Dudok de Wit, A. Verga, A. Sen, ASDEX Team, and X. Garbet, Phys. Rev. Lett. **73**, 3403 (1994).

[38] A. K. Singh and Y. C. Saxena, Phys. of Plasmas, **1**, 2926 (1994).

[39] B. K. Joseph, R. Jha, P. K. Kaw, S. K. Mattoo, C. V. S. Rao, Y. C. Saxena and the Aditya Team, Phys. Plasmas **4,** 4292 (1997).

[40] Lifang Dong, Long wang, Chunhua Feng, et al, Phys. Rev. E **57,** 5929 (1998).

[41] O. D. Gurcan and P.H. Diamond, Phys. Plasmas **11**, 4973 (2004).

[42] D. A. D'lppolito, J. R. Myra and S. J. Zweben, Phys. Plasmas **18**, 060501 (2011).

[43] P. K. Kaw, R. Singh, and P. H. Diamond, Plasma Phys. Controlled Fusion **44**, 51 (2002).

[44] J. M. Beall, Y. C. Kim and E. J. Powers, J. Appl. Phys. **53**, 3933 (1982).

[45] I. Langmuir and H. M. Mott-Smith, Gen. Elec. Rev **27**, 449 (1924).

[46] F. F. Chen, Plasma Diagnostics Techniques, edited by R. H. Huddlestone and S. L. Leonard, Chapter-4, New York (1965).

[47] I. H. Hutchinson, Principles of Plasma Diagnostics, Cambridge University Press, Chapter-3 (1987).

[48] Yuri P. Raizer, "Gas Discharge Physics", Springer Verlag Heidelberg, New York (1991).

[49] Bon-Woong Koo and Naoh Hershkowitz, J. Applied Physics **86,** 1213 (1999).

[50] Robert L. Merlino, Am. J. Phys. **75,** 1078 (2007).

[51] J. F. Drake, P. N. Guzdar and A. B. Hassam, Phys. Rev. Lett. **61**, 2205 (1988).

[52] O. D. Gurcan and P.H. Diamond, Phys. Plasmas **11**, 512 (2004).

[53] S. K. Singh, L. M. Awasthi, R. Singh et al., Phys. Plasmas, **18,** 102109 (2011).

[54] F. Jenko, W. Dorland, M. Kotschenreuther, and B. N. Rogers, Phys. Plasmas **7,** 1904 (2000).

[55] Z. Lin, T. S. Hahm, W.W. Lee, W. M. Tang and R. B. White, Science **281**, 1835 (1998).

[56] M. A. Malkov and P. H. Diamond, Phys. Plasmas **8**, 3996 (2001).

[57] A. I. Smolyakov, P. H. Diamond, and M. V. Medvedev, Phys. Plasmas **7**, 3987 (2000).

[58] M. A. Makowski and G. A. Emmart, Rev. Sci. Instrum. **54**, 830, (1983).

[59] R. H. Huddlestone and S. L. Leonhard. Plasma Diagnostic Techniques, chapter 3: Magnetic probes (R. H. Lovberg). Academic Press, (1965).

[60] P. K. Srivastava, S. K. Singh, L. M. Awasthi, and S. K. Mattoo, Rev. Sci. Instrum. **83**, 093504 (2012).

[61] S. K. Mattoo, S. K. Singh, L. M. Awasthi et al., Phys. Rev. Lett. **108**, 255007 (2012).

[62] Rudolf Limpaecher and K. R. Mackenzie, Rev. Sci. Instrument, **44**, 726 (1973).

[63] A. J. T. Holmes, Rev. Sci. Instrum. **53,** 1523 (1982).

[64] K. Toi, K. Kawahata, S. Morita, T. Watari et al., Phys. Rev. Lett. **64,** 1895 (1990).

[65] Y. Kawai, Ch. Hollenstein, and M.Guyot, Phys. Fluids **21**, 970 (1978).

[66] C. Gauthereu and G. Matthieussent, Phys. Lett. A **121,** 342 (1987).

[67] B. E. Cherrington, Plasma Chem. Plasma Process. **2**, 113 (1982).

[68] S. Pfau and M. Tichy, Low Temperature Plasma Physics, edited by R. Hippler, S. Pfau, Schmidt and K. H. Schoenbach, Wiley-VCH, Chapter-6 (2001).

[69] W. E. Yao, T. Intrator and N. Hershkowitz, Rev. Sci. Instrum. **56**, 519, (1985).

[70] J. R. Smith, N. Hershkowitz and P. Coakley, Rev. Sci. Instrum. **50**, 210 (1979).

[71] A. Siebenförcher and R. Schrittwieser, Rev. Sci. Instrum. **67**, 849 (1996).

[72] H. Himura, M. Fukao, H. Wakabayashi and Z. Yoshida, Rev. Sci. Instrum. **74**, 4658 (2003).

[73] G. B. Patel, P. K. Srivastava, L. M. Awasthi, V. P. Anitha, G. Ravi, P. J.Patel, U. K. Baruah, and S. K. Mattoo, Rev. Sci. Instrum. **73**, 1779 (2002).

[74] C. Hidalgo, R. Balbín, M. A. Pedrosa, I. García-Cortés, and M. A. Ochando, Phys. Rev. Lett. **69**, 1205 (1992).

[75] R. Balbín, C. Hidalgo, M. A. Pedrosa, I. García-Cortés, and J. Vega. Rev. Sci.

Instrum. **63**, 4605 (1992).

[76] PH. Verplancke(A), R. Chodura, J.-M. Noterdaeme, M. Weinlich, Cotrib. Plasma Phys. **36**, 145 (1996).

[77] L. Giannone, R. Balbin, H. Niedermeyer, M. Endler, G. Herre, C. Hidalgo, A. Rudij, G. Theimer, Ph. Verplanke, and the W7-AS Team, Phys. Plasmas **1**, 3614 (1994).

[78] S. K. Singh, P. K. Srivastava, L. M. Awasthi, S. K. Mattoo, A. K. Sanyasi, R. Singh and P. K. Kaw, Rev. Sci. Instrum, [Under Review, # RSI A131004].

[79] Okamoto, K. Hara, K. Nagaoka, S. Yoshimura, J.Vranjes, M.ono and M. Y. Tanaka, Phys. Plasmas, **10,** 2211 (2003).

[80] R. Jha and Y. C. Saxena, Phys. Plasmas **3**, 2979 (1996).

[81] Marklund G., Blomberg L., Faltammar C.-G.,and Lindqvist P. A., Geophys. Res. Lett. **2,** 1862 (1994).

[82] P. K. Shukla, R. Bingham, R. Dendy, H. Pecseli and L. Stenflo, J. Phys. IV France **5,** C6-19, (1995), Physique IV, http://dx.doi.org/10.1051/jp4:1995604.

[83] Christian Brandt, Olaf Grulke, Thomas Klinger et al., Phys. Rev. E **84**, 56405 (2011).

[84] J. Q. Dong, H. Sanuki and K. Itoh, Phys. Plasmas **8**, 3635 (2001).

[85] J. Oynes, H. L. Pecseli, and K. Rypdal, Phys. Rev. Lett. **75,** 81 (1995).

[86] S. C. Cowley, P. K. Kaw, R. S. Kelly and R. M. Kulsrud, Phys. Fluid **B 3**, 2066 (1991).

[87] R. Srinivasan, K. Avinash and P. K. Kaw, Phys. Plasmas **8**, 4483 (2001).

[88] O. Motojima e*t al.*, Proc. 21st IAEA Fusion Energy Conf., **OV/2-1**, (Chengdu, 2006).

[89] H. A. B. Bodin and A. A. Newton, Nucl. Fusion **20**, 1255 (1980).

[90] R. A. Truemann, L. Brostrom, J. LaBelle et al., J. Geophys. Res. **95**, 19099 (1990).

[91] J. P. Boeuf, G. J. M. Hagelaar, P. Sarrailh et al., Plasma Sour. Sc. Technol. **20**, 015002 (2011).

[92] Yu. A. Zaliznyak1, A. I. Yakimenko and V. M. Lashkin, J. Plasma Physics **74,** 381 (2008).

[93] M. Nakata, T. H. Watanabe, H. Sugama and W. Horton, Phys. Plasmas **18**, 12303 (2011).

[94] F. Jenko, W Dorland and G. W. Hammet, Phys. Plasmas **8**, 4096 (2001).

[95] V. Tangri, R. Singh and P. Kaw, Phys. Plasmas **12**, 072506 (2005).

[96] V. Tangri, P. Kaw, A. Das et al., Phys. Rev. Lett. **91**, 025001 (2003).

[97] F. Ryter, F. Leuterer, G. Pereverzev et al., Phys. Rev. Lett. **86**, 2325 (2001).

[98] J. Weiland, *"*Collective Modes in Inhomogeneous Plasmas*"*, IOP Publishing Ltd,

Bristol, UK, p. 45 – 81 (2000).
[99] L. M. Awasthi, G. Ravi, V. P. Anita et al., Plasma Source Sci. Technol. **12**, 158 (2003).
[100] M. Bruchhausen, R Burhenn, M. Endler et al., Plasma Phys. Control. Fusion **46**, 489 (2004).
[101] Truemann, L. Brostrom, J. LaBelle et al., J. Geophys. Res. **95**, 19099 (1990).